TRINITY COLLEGE DUBLIN
COLÁISTE NA TRÍONÓIDE
THE UNIVERSITY OF DUBLIN

Quantum Dots and Quantum Dot Based Polymer Composites

Cormac Hanley

A thesis submitted to the University of Dublin, Trinity College for the degree of Doctor of Philosophy.

School of Chemistry and CRANN

Trinity College Dublin

Dublin 2

Ireland

2013

Declaration

This thesis is submitted by the undersigned to the University of Dublin, Trinity College for the examination of Doctorate of Philosophy.

I declare that this thesis has not been submitted as an exercise for a degree at this or any other university and it is entirely my own work. I agree to deposit this thesis in the University's open access institutional repository or allow the library to do so on my behalf, subject to Irish Copyright Legislation and Trinity College Library conditions of use and acknowledgement.

Summary

The main aim of this thesis is to develop a range of new nanomaterials and composite materials based on fluorescent semiconducting nanoparticles (quantum dots). The work involves the synthesis and characterisation of various cadmium containing quantum dots (QDs), along with the investigation of interactions of QDs with various species.

Chapter 1 provides an overview of nanotechnology and introduces the relevant nanomaterials, with particular focus given to fluorescent semiconducting nanoparticles and their properties, and some details of relevant characterisation techniques important to this work. We cover the basic properties of both whispering gallery mode optical microcavities and dielectric elastomers. This chapter also outlines the motivation for our research, and sets out our aims.

Chapter 2 describes the details of experimental procedures and techniques used for synthesis of the materials. The characterisation techniques used are also detailed here.

Chapter 3 details the aqueous synthesis of organic cadmium selenide, cadmium zinc selenide and cadmium sulfide quantum dots (CdSe, CdZnSe, CdS QDs) prepared *via* microwave irradiation and hot-injection synthesis, and a comprehensive characterisation thereof using a range of steady state and time resolved techniques. Subsequently, this chapter focuses on the characteristics between binary CdSe QD and ternary CdZnSe QDs, along with an in-depth analysis of optical and electronic properties of this system. The investigation of QDs and optical microcavities is described in Chapter 4. Doping of polymer microspheres with QDs, as well as synthesis of a range of PMMA microspheres and their optical properties is investigated.

Chapter 5 details the preparation of novel Dielectric Elastomer (DEA) systems with QDs. The emission properties of these QDs are examined in detail, with both steady state and time resolved methods employed to gain a deeper understanding of the nature of these QDs while undergoing actuation in the elastomer film. The development of transparent compliant and highly conductive electrodes for these DEAs is also undertaken.

Finally, Chapter 6 provides the conclusions of this work, summarising the main achievements, and outlines the aims and avenues of research that are planned for the future.

We expect that the new nanomaterials developed in this project will find a broader range of potential applications. We also believe that this research will contribute to further progress of relevant areas of nanotechnology, chemistry, biosciences and solar technology.

Acknowledgements

First and foremost I would like to thank my supervisor, Prof. Yurii Gun'ko. He has given me the opportunity to pursue a challenging and rewarding project in a field I am passionate about. His ideas and guidance were the most important factors in submitting this work. Without it, this project would have been possible. His encouragement and insight into hurdles during the project were invaluable, giving me the motivation to continue through the four years.

I must also extend my genuine gratitude to the members of the Gun'ko group, past and present. Thank you to Prof. John Donegan and his group in physics for all their ideas and support. Thanks also go to Dr. Yury Rakovich, in San Sebastian, Spain for having me over in his lab and teaching me about FLIM. Thank you to Prof. Ferderico Carpi for hosting me in his lab in Pisa, Italy.

Thanks to the school of chemistry and SFI Ireland for making this project possible. Thank you to CMA and AML facilities and also CRANN for their facilities.

A big thank you too to my family, to Mum, Dad, John and Anne for your constant love and support.

Abbreviations

Abs	Absorption
AIBN	Azobisisobutyronitrile
a.u.	Arbitrary units
B	Relative contribution
X	Chi
°C	degrees Celsius
Cd	Cadmium
CdO	Cadmium Oxide
CdS	Cadmium Sulphide
CdSe	Cadmium selenide
CdTe	Cadmium telluride
CdZnSe	Cadmium Zinc Selenide
cm^{-1}	wavenumbers
CNT	Carbon Nanotube
DEA	Dielectric Elastomer Actuator
DEZn	DiethylZinc
DMAP	4-Dimethylaminopyridine
e^-	Electron
E	Energy
EAP	Electroactive Polymers
Em	Emission
FIB	Focused Ion Beam
FLIM	Fluorescence Lifetime Imaging Microscopy
FRET	Forster Resonance Energy Transfer

FWHM	Full Width Half Maximum
g	grams
GaAs	Gallium Arsenide
GPa	Giga Pascal
h^+	Hole
HDA	Hexadecylamine
HPA	Hexyl Phosphonic Acid
HRTEM	High Resolution Transmission Electron Microscopy
InP	Indium Phosphide
Int.	Intensity
IR	Infrared
λ_{em}	Emission wavelength
λ_{ex}	Excitation wavelength
LED	Light Emitting Diode
M	Molar concentration
mL	millilitre
µL	microlitre
mM	millimolar
µM	micromolar
MBE	Molecular Beam Epitaxy
MPA	Mercaptopropionic acid
NMR	Nuclear Magnetic Resonance
MWNT	Multi Walled Carbon Nanotube
NIR	Near Infrared
nm	nanometre
OA	Oleic Acid

ODA	Octadecylamine
ODPA	Octadecyl Phosphonic Acid
ODE	Octadecene
PEDOT:PSS	Poly(3,4-ethylenedioxythiophene) poly(styrenesulfonate)
PEI	Polyethylenimine
PMMA	Polymethylmethacrylate
PL	Photoluminescence
PLQY	Photoluminescence Quantum Yield
ps	picosecond
PTFE	Polytetrafluoroethylene
PS	Polystyrene
PVDF	Polyvinylidene Floride
QD	Quantum Dot
SA	Steric Acid
Si	Silicon
SILAR	Successive Ion Layer Adsorption and Reaction
SDBS	Sodium dodecylbenzenesulfonate
SEBS	Poly(styrene-ethylene/butylene-styrene)
SEM	Scanning Electron Microscope
SWNT	Single Walled Nanotube
τ	Lifetime
TBP	Tributylphosphine
TCSPC	Time Correlated Single Photon Counting
TEM	Transmission Electron Microscope
TGA	Thermogravimetric Analysis
$(TMS)_2S$	Bis(trimethylsilyl)sulfide

TOP	Trioctyl phosphine
TOPO	Trioctyl phosphine oxide
UV-vis	Ultraviolet-visible
WGM	Whispering Gallery Mode
XRD	X-Ray Diffraction
ZnS	Zinc Sulphide

Table of Contents

List of Figures and Tables

Chapter 1: Introduction

Chapter 2: Experimental

Chapter 3: QDs

Chapter 4: Quantum Dots and Optical Microcavities

Chapter 5: Quantum Dots and Dielectric Elastomers

Chapter 6: Conclusions and Future Work

Figure 6.3 Silica microspheres imaged by optical microscopy (50x mag). An aluminosilicate sol-gel was used to infiltrate our porous Ni template.

Figure 6.4 Q-factor for the WGM peaks from the microsphere emission. The peaks were labelled TE, TM and TM2.

Figure 6.5 SEBS dried on a silicon wafer (left), with 1% silicone oil and doped with QDs (right, top) and spin coated (right, bottom) with carbon black electrodes

Figure 6.6 Alternative Actuator design for UV-VIS absorption measurements -it is shown at the voltage of 0, 2 kV and under UV light

References:

(1) Museum, B. http://www.britishmuseum.org/research/collection_online/collection_object_details.aspx?objectId=61219&partId=1 **1958**, *Object number 1958,1202.1*.

(2) Cathedral, N. D. http://szou.cos.ucf.edu/outreach/webpage/image3311.jpg **1260**.

(3) Alivisatos, A. P. *Science* **1996**, *271*, 933.

(4) Murray, C. B.; Kagan, C. R.; Bawendi, M. G. *Annual Review of Materials Science* **2000**, *30*, 545.

(5) Washington, A. L.; Strouse, G. F. *Chemistry of Materials* **2009**, *21*, 2770.

(6) Zhang, Y.; Schnoes, A. M.; Clapp, A. R. *ACS Applied Materials & Interfaces* **2010**, *2*, 3384.

(7) Green, M. *Journal of Materials Chemistry* **2010**, *20*, 5797.

(8) Halpert, J. E.; Porter, V. J.; Zimmer, J. P.; Bawendi, M. G. *Journal of the American Chemical Society* **2006**, *128*, 12590.

(9) Shieh, F.; Saunders, A. E.; Korgel, B. A. *The Journal of Physical Chemistry B* **2005**, *109*, 8538.

(10) Murray, C. B.; Norris, D. J.; Bawendi, M. G. *Journal of the American Chemical Society* **2002**, *115*, 8706.

(11) Wang, X.; Ren, X.; Kahen, K.; Hahn, M. A.; Rajeswaran, M.; Maccagnano-Zacher, S.; Silcox, J.; Cragg, G. E.; Efros, A. L.; Krauss, T. D. *Nature* **2009**, *459*, 686.

(12) Arnold, S.; Khoshsima, M.; Teraoka, I.; Holler, S.; Vollmer, F. *Opt. Lett.* **2003**, *28*, 272.

(13) Bawendi, V. I. K. a. M. G. *MRS Bull.* **2001**, *26*, 998.

(14) Ha, S. M.; Park, I. S.; Wissler, M.; Pelrine, R.; Stanford, S.; Kim, K. J.; Kovacs, G.; Pei, Q. 2008; Vol. 6927, p 69272C.

(15) Shian, S.; Diebold, R. M.; McNamara, A.; Clarke, D. R. *Appl. Phys. Lett.* **2012**, *101*, 061101.

(16) Agilent **2013**.

(17) Jacobkhed http://en.wikipedia.org/wiki/File:Jablonski_Diagram_of_Fluorescence_Only.png#filehistory **2012**.
(18) Skoog, D. L., JJ *Fort Worth* **1992**.
(19) Markus Sauer, J. H., Jörg Enderlein *Wiley* **2010**, 4.
(20) *http://3dsciencepics.com/latest-transmission-electron-microscope-diagram/*.
(21) Holodiag http://www.holodiag.com/tga.php.
(22) Diffraction, X.-R. http://web.pdx.edu/~pmoeck/phy381/Topic5a-XRD.pdf.
(23) Cambridge, U. o. *Inroduction to mechanical testing* **2012**, http://www.doitpoms.ac.uk/tlplib/mechanical-testing/theory1.php.

Quantum Dots and Quantum Dot Based Composites

Cormac Hanley

This project develops a range of new nanomaterials based on fluorescent semiconducting nanoparticles (quantum dots).

Organic TOPO/HDA stabilised cadmium selenide and ternary core Cadmium Zinc Selenide are synthesised by microwave heating and hot-injection synthesis, and investigated using various spectroscopic techniques to gain insight into the nature of blinking in quantum dots.

High aspect ratio CdS quantum rods are synthesised and characterised. The addition of Cd and Se precursors to the CdS rods at high temperatures is investigated and growth mechanisms for new nanostructures are proposed.

Quantum dots are added to optical microcavities and their optical characteristics elucidated using emission spectroscopy. A range of microspheres are synthesised using microemulsion techniques and spray drying. Polymer microcylinder arrays are synthesised for various applications.

Dielectric elastomers are doped with quantum dots for the first time by swelling in organic solvents. The optical properties of the elastomer-QD composites are studied

under actuation of the elastomer. New PEDOT:PSS transparent electrodes are made, as well as a fluorescent QD variable lens.

We expect that the new nanomaterials developed here will find a range of potential applications. We also believe that this research will contribute to further progress of relevant areas of nanotechnology, chemistry, biosciences and solar technology.

Chapter 1: Introduction

1.1. General introduction

Nanoscience has become an increasingly important field in the last two decades, with many of the advancements in materials science due to the development of novel nano-scale materials such as carbon nanotubes, graphene, carbon composites, metal nanoparticles and semiconducting quantum dots[1-3]. These materials whose mechanical and optical properties differ significantly from their bulk counterparts have already been utilised in many applications including every day products. For example, quantum dots have been incorporated into solar cells, flat TV screens, used in lasing devices and in new light sources that can dramatically improve performance and reduce energy costs[2,4,5].

Over the last thirty years the area of nanomaterials have been developed due to the advancements in imaging using electron microscopy (TEM, SEM) and new synthetic techniques[6-8]. Nanomaterials differ from their bulk counterparts at the nanoscale level which give them unique electrical, mechanical and optical properties.

Nanomaterials are not a recent discovery however. In 1857 Michael Faraday presented colloidal gold nanoparticles with changing florescent wavelengths dependant on the source of illumination[9]. This optical effect was not explained until the appearance of Einstein's paper on colloids in 1905 which was accompanied by the development of quantum theory in the early 1900s[10]. It also led us to study how nanomaterials have been used throughout history, where for example, metallic nanoparticles have made appearances in 4th century Rome through the Lycurgus cup and in Medieval Europe in the decoration of stained glass windows (Fig. 1.1)[11,12].

Fig. 1.1 The use of Gold and silver nanoparticles have been in use as early as the 4th century[13,14]

Since then, the development of knowledge on metallic and semiconducting nanomaterials resulted in a range of novel composite materials and devices with many important applications in modern science and technology.

In this chapter we will provide an overview of quantum dots, their polymer composites, optical microcavities and potential applications of these materials.

1.2. Semiconducting nanocrystals (quantum dots)

1.2.1. Structure and properties of QDs

Semiconductor quantum dots are unique nanoscale particles which exhibit different optical properties to their bulk counterpart due to their small size (quantum confinement effect) [8]. The small size results in the confinement of the semiconductors electron hole pair, or exciton, when the semiconductor is smaller than its Bohr radius in all three dimensions. The exciton is therefore confined to a smaller space and the exciton confinement energy changes according to equation (1)[6]:

$$E = \frac{\hbar^2}{2}\left(\frac{1}{m_e} + \frac{1}{m_h}\right)\frac{\pi^2}{R^2} - 1.786\frac{e^2}{\epsilon R} - 0.248R^*_{ry} \qquad (1.1)$$

Where m_e and m_h are the electron and hole effective masses, e is the elementary charge, ϵ is the dielectric constant, R is the nanoparticle radius, $\hbar$ is Plank's constant and E^*_{ry} is the Rydberg constant defined as (2):

$$E_{ry}^{*} = 13605.8\frac{1}{\epsilon^2}\left(\frac{m_o}{m_e} - \frac{m_o}{m_h}\right)^{-1} \qquad (1.2)$$

Where m_o is the free electron mass. The first term in (1.1) corresponds to the ground state energies of the particles, while the second term represents the Coulomb attractive forces and the third term the spacial correlations between them. Thus it can be seen that with decreasing nanoparticle radius, the exciton energy increases.

The electron hole pair may recombine radiatively, resulting in the emission of a photon across the discrete bands of the semiconductor. Non-radiative decay may also occur, especially when an exciton interacts with a surface defect or capping ligand at the nanocrystal surface which increases the chance of surface recombination processes or Auger transitions (Fig. 1.2)[15,16].

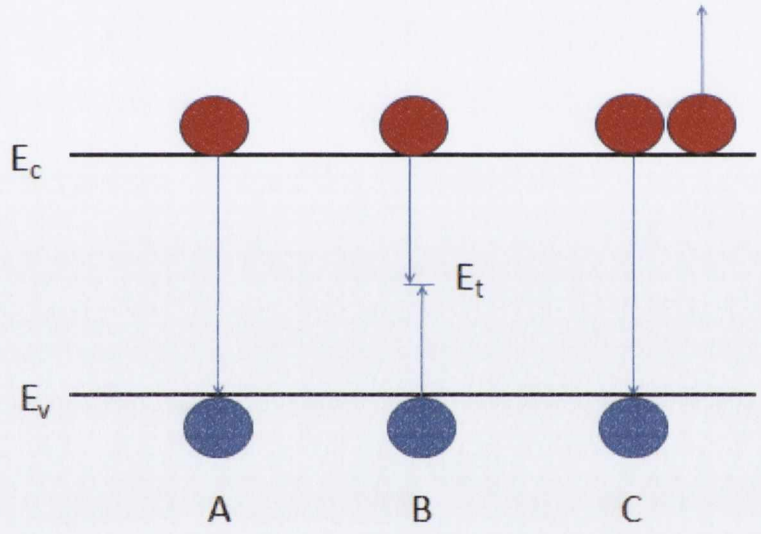

Fig. 1.2 Transitions of electron hole pairs from the valence band to the conduction band showing (A) band to band recombination, (B) trap assisted recombination and (C) Auger recombination

Because of their small size and discrete energy levels due to quantum confinement (Fig. 1.3), semiconductor nanocrystals are often called artificial atoms. Quantum dots are considered 0-D materials, because the Bohr radius is confined in all three dimensions, unlike 2-D confined quantum wires or 1-D confined quantum wells. To be confined

quantum dots therefore must have a radius smaller than that of the material Bohr radius, which is given as 5.8 nm for bulk cadmium selenide[17]. Bulk cadmium selenide consists of Cd^{2+} ions bound to Se^{2-} in a zinc blend structure. When heated above 100^0C the zinc blend structure transforms into a hexagonal wurtzite structure, which is the typical crystal structure for CdSe quantum dots. By varying the nanocrystal diameter, it is possible to control the emission and absorbance wavelength of the nanocrystal as the bandgap increases in energy with decreasing nanocrystal radius. As a result the nanocrystal absorbance and emission can be tuned to any wavelength in the visible spectrum (depending on the Bohr radius) to make fluorescent nanoparticles that can emit from UV to deep red.

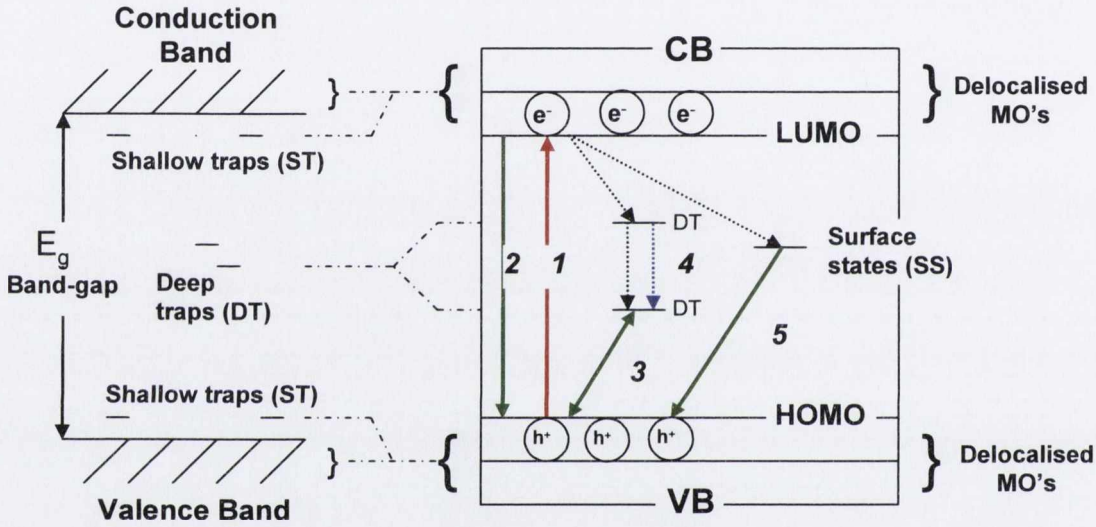

Fig 1.3. Schematic presentation of the band gap (E_g) structure of a semiconducting material and the change in that structure on going from the bulk to the nanoscale. The absorption and subsequent emission pathways upon excitation by a photon are also shown. Adapted from literature[18]. 1: hυ induced excitation ($E > E_g$) 2:Exciton recombination: luminescence3: Deep trap (defect) emission 4: Radiationless transition 5: Surface state emission

Optical excitations across the gap depend strongly on the size, even for crystallites as large as 10000 atoms. At 0 K the valence band of the semiconductor will be full, and the conduction band empty. When the temperature is increased an electron may receive enough energy to be promoted to the conduction band, leaving a positive hole in the valence band. The electron-hole pair can form a bound state called an exciton, with a Bohr radius for bulk materials given as:

$$a_b = \frac{\hbar^2 \epsilon}{e^2}\left[\frac{1}{m_e^*} + \frac{1}{m_h^*}\right] \quad (1.3)$$

Where ϵ is the bulk optical dielectric constant, e is the elementary charge and m* are the effective masses. When an electron-hole pair is created in a nanocrystal of radius smaller than that of the Bohr radius the exciton is confined in three dimensions. This results in a larger Columbic attraction between them and therefore a higher kinetic energy. The higher kinetic energy may be released in the form of a photon, resulting in the blue shift of the emission spectra of the nanocrystal when compared to its bulk value. For bulk CdSe the bohr radius is 5.6 nm[19], so any nanocrystal of radius smaller than this should display quantum confinement effects.

Confining the charge carriers in all three dimensions results in the density of states splitting up to form a discrete set of energy states. Solving the Eigen energies of the Schrodinger equation for the carriers in a confined space, a relationship between the size of the confined system and its energy levels can be calculated. This was done by Brus et al which resulted in the Brus equation relating particle size to the change in energy levels of the quantum dot [20,21]:

$$E'_g = E_g + \frac{h^2}{8R^2}\left(\frac{1}{m_e} + \frac{1}{m_h}\right) \quad (1.4)$$

where m_e and m_h are the mass of the excited electron and hole respectively, E_g is the band gap of the material and R the radius of the nanocrystal. In the medium confinement regime, this formula is approximately valid, when the reduced mass is replaced by the electron mass. This formula also does not take into account coupling of electronic states or surface related effects but is a good approximation.

Quantum dots are commonly made out of II-VI materials, such as CdSe, CdTe, ZnS or III-V materials such as GaAs and InP. III-V QDs can be synthesised using organometallic chemical vapour deposition[22], while a range of organic and aqueous colloid synthetic procedures are used to make II-VI colloidal QDs[7,23].

1.2.2. Main approaches for preparation of QD nanocrystals

QD nanostructures have been prepared by various top down approaches, such as lithography, and bottom up approaches such as molecular beam epitaxy (MBE) and colloidal chemistry.

Lithography uses polymer masks and etching to create QDs on a substrate such as silicon and Gallium Arsenide. Limitations of this technique include edge effects, defects in the QDs, low PLQY and it is prone to contamination[24,25]. Quantum dots can be made into well-defined highly uniform and dense arrays for next generation optoelectronic devices using this method. MBE has been a successful approach to creating monodisperse QDs of high quality[26]. Typically InAs QDs are grown on a thin layer of GaAs by depositing the metal in its gaseous phase[27]. These dots are self-assembled and can be easily incorporated into photonic devices. These QDs can be blue shifted by etching to control their size. The main drawback of this method is the high cost of MBE machine and materials. I will not consider the top down approaches here in detail as I have not used these techniques in my work. Therefore I would like to focus on the preparation of colloidal solutions of quantum dots using bottom up approaches.

The first controlled synthesis of colloidal semiconducting quantum dots was done by Brus et al in 1983 at Bell labs where they synthesised and characterised the first Cadmium-Sulphide crystallite[28]. A few years later in 1987 Mark Reed coined the term "quantum dot"[29]. After Iijima elucidated carbon nanotubes in 1991[30] a worldwide interest in nanoscale research began and in 1993 the first high quality colloidal QDs were synthesised by Murray et al using the pyrolysis of organic reagents by injection into a hot coordinating solvent[23]. These dots were characterised by photoluminescent spectroscopy, UV-Vis spectroscopy and TEM imaging. The synthesis lead to low size distribution, size tuneable QDs with high PLQY.

In our work here I mostly used high temperature and microwave synthesis of II-VI QDs, utilising organic ligands and stabilisers to control nucleation and crystal growth of the nanocrystals therefore I am going to consider these techniques in more details below.

1.2.3. High temperature synthesis of QDs

CdSe quantum dots were among the first synthesised at high temperatures using selenium and cadmium precursors to initiate nucleation by the formation of a CdSe seed that proceeds to use up the precursors during the growth of the nanocrystal. Growth is controlled by a number of factors, including monomer concentration, temperature of reaction and stabilisers present[31]. While aqueous synthesis is usually carried out at low temperatures, with growth being controlled by a thermodynamic reaction at the boiling

point of water, organic nucleation and growth occurs by the injection of room temperature selenium or cadmium precursors into a hot coordinating solvent.

Initially dimethyl cadmium ($(CH_3)_2Cd$) and tri-*n*-octylphosphine selenide [TOPSe][32], were used as precursors which were injected into a solution of the coordinating solvent tri-*n*-octylphosphine oxide (TOPO) at a high temperature (over 180 °C). Slow growth and annealing in the coordinating solvent resulted in uniform surface derivatization and regularity in the core structure, yielding CdSe nanocrystals with broad size ranges (1.2 – 11.5 nm). Further modification of the hot injection approach was developed by heating the TOPO up to 350° C under argon before injection [33]. It was found that this temperature was well above the flash point for TOPO and all manipulations were undertaken with extreme care and after injection, the temperature was reduced to yield monodisperse ensembles. This change in temperature was utilised to distinctly separate both the nucleation and growth phases and resulted in high quality crystalline, nearly monodisperse QD nanocrystals.

Technically, the hot injection method can be considered as a chemical co-precipitation, which involves a temporally discrete nucleation followed by slower controlled growth on the existing nuclei (Fig. 1.4). The colloidal system can also undergo so called Ostwald ripening, when the high surface energy of the small particles promotes their dissolution, then re-deposition of the material onto the larger particles enabling their further growth. This is a competing process where the smaller nanocrystals are absorbed by the larger, more stable nanocrystals, often leading to a high size distribution in the sample. Thus the nucleation and growth processes dictate the final particle size and morphology.

Ostwald ripening can be controlled by the strong coordinating ligands present in solution, while the high temperature induced rapid growth ensures highly crystalline, defect free nanocrystals are formed. As reagents are used up and the surface area to volume ratio decreases the QD surface energy decreases, slowing growth and allowing precise control of nanocrystal size. Smaller nanocrystals with a higher surface area may be incorporated into larger more stable nanocrystals at high temperatures leading to a large size distribution. Therefore, to ensure a narrow size distribution the reaction must be stopped before the monomer concentration falls below the level where Ostwald ripening occurs.

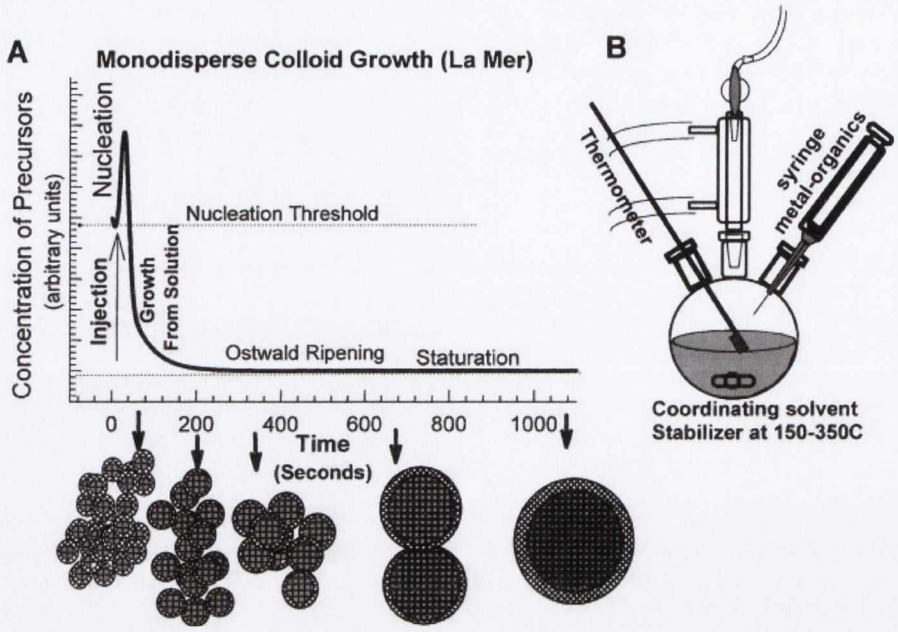

Figure 1.4. (A) The stages of nucleation and growth for the preparation of monodisperse NCs in the framework of the La Mer model. (B) Representation of the simple synthetic apparatus employed in the preparation of monodisperse NC samples. [Reproduced from [34]].

Sung et al's work on the studies of growth kinetics of CdSe and CdSe/ZnSe core shell QDs resulted in an Arrhenius-type analysis of the ripening of the nanocrystals that can be used to predict growth kinetics of the system for better control of nanocrystal synthesis[35]. Peng et al[36] suggested three regimes of nanocrystal development during the synthesis: The first stage is growth of all nanoparticles, where monomers are in excess and growth of the nanocrystals depends on the reactivity of the precursors, temperature and surface ligands; The second stage is the focusing regime - this is when monomer concentration drops and nanocrystals are focused into one size. After time we come to the defocusing stage - when monomer concentration drops below a critical value and Ostwald ripening occurs.

1.2.4 Microwave synthesis of QDs

Microwave synthesis of nanoparticles has been extensively used lately with advances in quantum dot synthesis as well as exfoliation of graphene[37], preparation of gold and silver nanoparticles[38] and magnetite synthesis[39]. Microwave heating is an attractive alternative to conventional thermal heating for a number of reasons. High heating rates means that high temperature reactions that typically take hours can be completed within minutes[40]. Microwave chemistry offers unique opportunities to significantly increase the rate of nanoparticle formation, while not compromising on the high quality and narrow size

distributions needed for these nanomaterials to be further utilised in other areas. Microwave heating is achieved through polar bonds in materials absorbing microwave energy and converting it into thermal energy through dielectric heating. This can lead to several different heating effects depending on the polarisability of your materials[41].

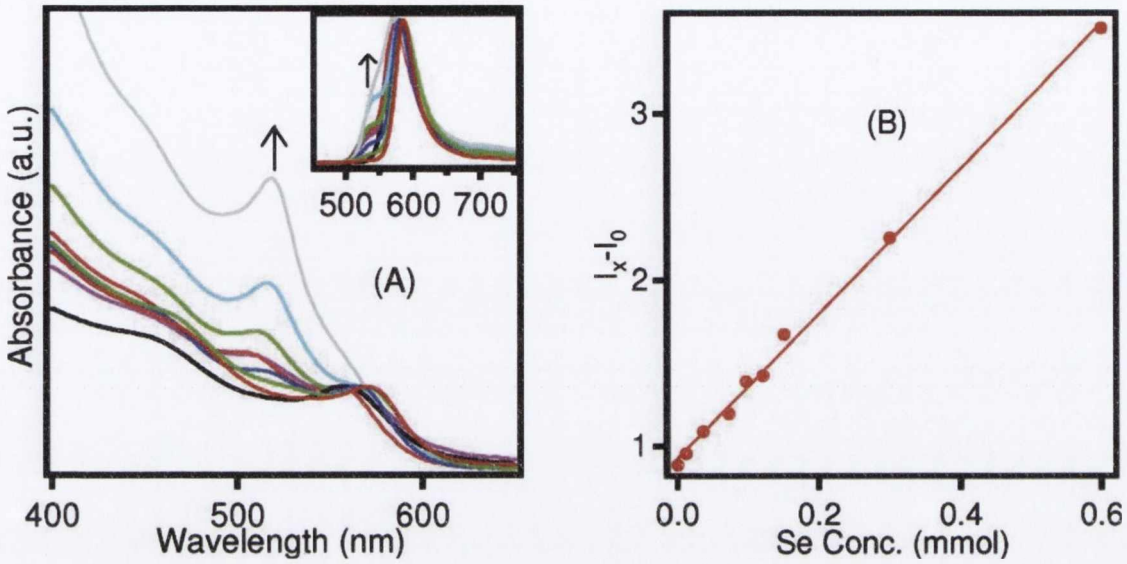

Fig. 1.5 Absorption and emission (inset) spectra for reaction with increasing concentration of TOPSe in a microwave reaction (left) and plot of the relative intensity of the absorption contributions for the two independent QDs generated in the two step reaction as a function of added TOPSe monomer[42]

For example, an aqueous solution with highly polar bonds in water can absorb the microwave energy evenly, which will therefore result in uniform heating of the solution[42]. Strouse et al showed how the selective absorption of TOPSe in microwave synthesis of CdSe QDs can affect the reaction rates of the system (Figure 1.5). This is in contrast to a solution in non-polar solvent containing polar reagents or precursors. In this case the microwave irradiation is absorbed by polar bonds of selected components and heating should affect selected polar bonds, rather than non-polar media. This can allow to eliminate unwanted side reactions and produce higher purity products[43]. The microwave approach also provides the potential for a scale-up of the QD synthesis without the potential hindrance due to thermal gradient effects; something that is particularly important for further industrial large scale production of nanoparticles. The utilisation of these techniques allowed for the preparation of high quality, nearly monodisperse InGaP, InP, CdS, CdSe, CdTe and other QDs from appropriate molecular precursors in non-microwave absorbing alkane solvents[42,44-46].

Aqueous CdSe quantum dots have also been synthesised using microwave irradiation to induce nucleation and growth of the cadmium and selenium precursors[47]. These QDs have also been capped with an inorganic shell of semiconductor of a higher bandgap to increase the PLQY and stability of the QD via both single and two pot processes[48]. Although CdSe quantum dots with high PLQY and good stability have been made in the aqueous phase by microwave heating, literature is still rare in regards to the synthesis of QDs in the organic phase prepared by a similar method.

In 2005 Strouse et al. used a CEM microwave to produce high quality CdSe quantum dot in non-absorbing long chain alkanes[44,46]. These QDs had high PLQYs of 40% were produced by dielectric heating through the selenium precursor. More recently Strouse has adopted the system to CdS QDs, leading to a narrow size distribution synthesis with highly emissive defect PL QDs[45].

1.2.5 Capping ligands for QD synthesis

As I mentioned above coordinating ligands in the solution during growth also play a significant role in determining QD size, shape and growth parameters. Yu et al studied the effects of TOP and TBP in the growth of CdTe nanocrystals[49]. They found that the steric hindrance of ligands and monomer activity, instead of monomer concentration are more relevant factors to predict QD growth in colloidal systems. Kalyuzhny et al have shown that surface ligands can also influence the emission properties of QDs[50]. TOP capped CdSe QDs were studied using NMR to observe ligand attachment to the QDs, as well as finding that the addition of HDA and metal acetates increased the PLQY of the QDs, while dilutions of the QD solutions resulted in a decrease in PLQY and a red shift in the emission spectra as ligands were detached from the surface of the QDs. Bullen et al demonstrated the effects of chemisorption of amines on CdSe QDs, showing that ligand absorption is temperature dependant and follows a Lagmuir Isotherm in nonpolar solvents[51].

CdSe solubility and stability in organic solvents is achieved by using organic capping ligands with long chained aliphatic tails. Trioctylphosphine (TOP) and primary amines bind to the surface of the QD through the strong phosphine or nitrogen lone pairs[52], effectively pacifying the surface of the QD. These ligands eliminate the dangling bonds on the surface of the nanocrystal, removing non-radiative pathways and creating a strong

potential barrier to confine the exciton. As well as making the QD soluble and stable in solution, the ligands may be used for functionalization by further reactions.

In addition, if necessary phase transfer of organic phase QDs into aqueous medium can be performed by a biphasic ligand exchange for potential biological applications of QDs (Figure 1.6)[53,54]. However these phase transfer processes frequently result in the significant drop of stability and quantum efficiency of QDs. For example, Smith et al showed that the effects of removing the organic ligands such as TOPO and ODA and replacing them with water soluble ligands such as mercaptopropionic acid (MPA) and Polyethylenimine (PEI) can reduce the effectiveness of the QD as fluorophores in biological systems as their surface is more open to oxidation after the phase transfer[55].

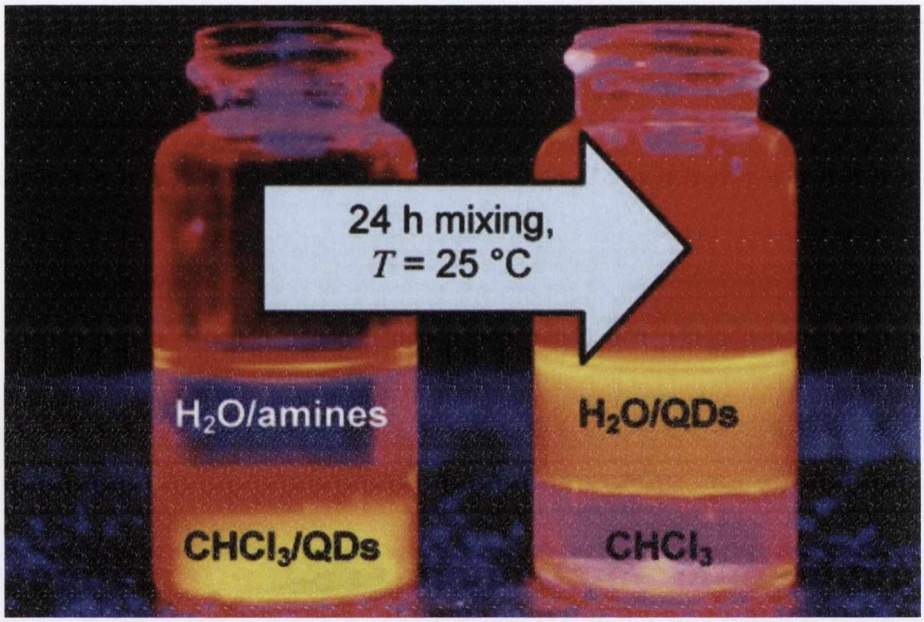

Fig. 1.6 An example of phase transfer by Biphasic Ligand Exchange on CdSe QDs[56]

The first capping agents were used by Fendler, who used sodium bis-2-ethylhexylsulfosuccinate (AOT) to passivate some CdS quantum dots[57]. Then, he added to his reaction some sodium hexametaphosphate as another stabiliser. These experiments can be considered as the firsts additions of capping agents on such nanoparticles, and have been followed by other studies, which resulted in the use of trioctylphosphine oxide (TOPO) as the standard capping agent for the synthesis of quantum dots, because of its numerous advantages[58].

TOPO is suggested to bind preferentially to the $(01\bar{1}0)$ and $(11\bar{2}0)$ facets on the short axis of the CdSe particle, with binding energies of 1.23 and 1.37 eV respectively (Figure 1.7)[58]. TOPO binds to the cadmium terminated (000) face (top) with a binding energy of 0.85 eV, but significantly less tightly to the selenium terminated (0001) face (bottom) as demonstrated by the smaller binding energy of 0.63 eV (assuming a relaxed cluster of wurtzite $Cd_{33}Se_{33}$ as a model).

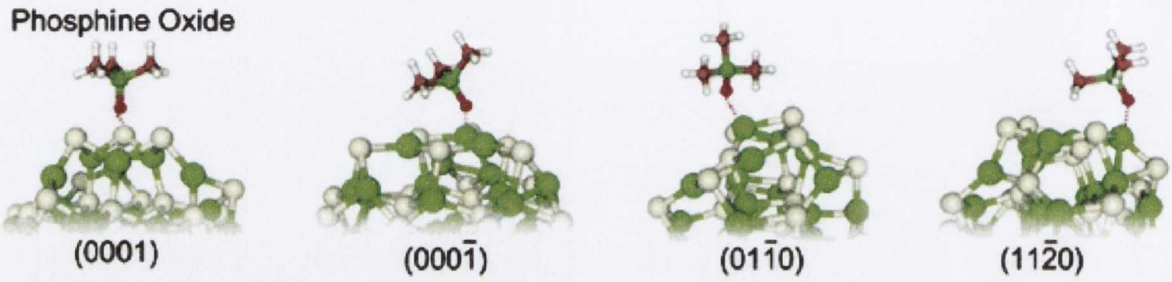

Fig. 1.7 Capping of CdSe quantum dot by TOPO. The organic ligand can bind to the quantum dot in several ways. Preferential binding is through the $(01\bar{1}0)$ facet with a binding energy of 1.23 eV[58].

There were some reports that the use of pure TOPO was not suitable as a surfactant because the particles grew too quickly to control their size, and became insoluble at high concentrations. This is why the ligand is used at technical grade, with the large amount of impurities retarding the growth of the QDs and the impurities binding strongly to the surface to give higher photoluminescent quantum yields[8].

CdSe QDs which are prepared using long chain primary amines are generally found to have emission quantum yields of 60% without the need for an inorganic shell[59]. This has been attributed to the closer packing of the ligands on the nanoparticle surface and the etching of surface defects, whilst amines have also been shown to contribute to the oxygen etching process. The use of amines as capping agents on CdSe particles has also been shown to result in a surface reconstruction, specifically a lattice contraction during growth, which may contribute to higher PLQYs. Further evidence for a ligand-directed reconstructed surface was obtained by measuring the surface strain of CdSe capped with differing capping agents, where TOPO capped CdSe exhibited tensile stress, whilst amine capped CdSe exhibited compressive stress. Ab initio calculations suggest that the mode of bonding is through the lone pair of electrons on the nitrogen atom, and in the case of CdSe, the amine binds to both selenium sites and cadmium sites[58]. Surprisingly, amines are

expected to bind to selenium sites preferentially over cadmium sites (binding energy of 1.05 eV for selenium terminated (0001) as compared to 0.91 eV for cadmium terminated $(000\bar{1})$ face).

1.2.6. QD core-shell nanostructures

Quantum Dot core shell nanocrystals have attracted a great attention due to their superior PLQY, resistance to photobleaching and oxidation. One of the first CdSe based core-shell QDs were synthesised by Dabbousi et al, by forming a Zinc Sulphide shell around a CdSe core[60]. Highly reactive diethyl zinc and hexamethyldisilathiane precursors were added to CdSe core particles at high temperatures to create a shell around the core CdSe. The use of higher bandgap material around the core resulted in a gradient in the bandgap between the CdSe and the outer ligands, which passivated the reactive surface of the particle and eliminated residual electron traps that could not be achieved by passivating the surface by organic ligands alone. The core shell nanocrystals demonstrated an increase in PLQY as less defect states on the surface were available for electron trapping. It was found that the absorbance and emission of the QDs was red shifted due to the larger particle size and the ability of the exciton to extend further into the ZnS shell. Further work was done to improve the quality of ZnS shell coating and the accuracy of the control of shell thickness. However, due to some lattice mismatch between the CdSe and ZnS crystals, the thicker shell could result in some defects at the interface between the core and shell. Peng et al were among the first who to successfully produced a CdS shell onto a CdSe core, with PLQYs of the new core-shell QDs reaching up to 50 % and their emission and absorbance red shifted due to the increase of the particle size [61]. Li et al introduced a new technique using Successive Ion Layer Adsorption and Reaction (SILAR) to coat a CdSe core with a CdS shell[62]. This new method was adopted from thin layer film LbL technique, where the shell thickness could be grown layer-by-layer onto the nanoparticle to minimise lattice mismatch between the core and shell to increase the PLQY even further. Reiss et al used ZnSe as a shell onto CdSe cores, with even higher PLQYs reaching up to 85 %[63]. The increase in PLQY was thought to be due to the lattice mismatch in ZnSe being lower than either ZnS or CdS with CdSe. The ZnSe shell was also found to preserve the optical properties of the core CdSe QDs when follow on ligand exchange with MPA was performed, showing only a slight decrease in PLQY after the phase transfer.

To provide better confinement of the exciton and less lattice strain between the core and shell of the nanoparticle, Reiss et al used a 3 pot synthesis to prepare CdSe/ZnSe/ZnS

nanoparticles[64]. The function of the outer ZnS shell was to deliver an effective potential barrier to confine the exciton, while the ZnSe shell provided a layer to reduce lattice strain which is commonly seen in CdSe/ZnS QDs. This was expanded upon by Tapalin et al, who developed the CdSe/CdS/ZnS core-shell-shell system[65].

Kim et al were among the first to cap a CdTe QD with an inorganic shell of lower bandgap than that of its core[66]. Typically, a type I QD has a band offset between the core and the shell, with the shell having a larger bandgap than the core. This results in confinement of the electron and hole in the lower bandgap core material. In type II QDs however, such as CdTe/CdSe core-shell nanostructures, the charge is separated with hole residing in the core, and the electron in the shell (Figure 1.8). This approach resulted in longer lifetimes of excited electrons, indicating that the exciton recombines through non-radiative decay paths and that electron-hole separation was more easily achieved using the type II QDs.

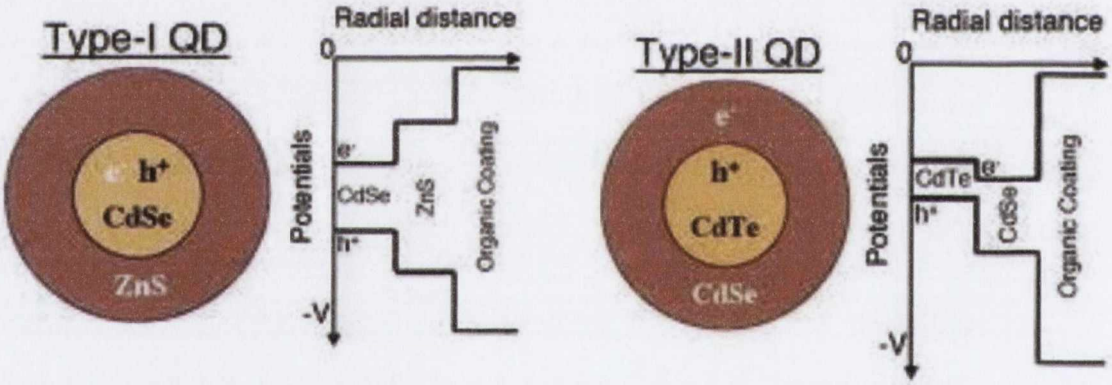

Fig. 1.8 Bandgap engineering of CdSe/ZnS (Type I) and CdTe/CdSe (Type II) Quantum Dots[67]

1.2.7. Anisotropic quantum nanostructures

Peng et al showed that the morphologies of quantum dot systems could be manipulated by the addition of short chain phosphonic acids to the colloidal system during nanocrystal growth. Using CdSe core QDs and small amounts of HPA it was found that the spherical nanocrystals had a preferential growth along one axis, leading to a rod like morphology. Interestingly, these new quantum rods were found to have polarised emission. Manna et al later showed increasing morphology control of CdSe nanostructures when they

produced quantum rods, tetrapods and teardrop like structures[68]. They found that starting with zinc blend CdSe QDs that the (001) face had 3 dangling bonds that needed to be passivated, so it was of higher energy and growth was preferred along that direction. Wurzite phase CdSe QDs however had three (111) facets of equal energy, leading to a tetrapod structure, instead of a rod. Hu et al studied CdSe quantum rod nanostructures and found that their emission is linearly polarised along the z axis, in line with their empirical pseudopotential calculations[69]. Other studies of CdSe quantum rods have found differences between spherical QDs and quantum rods emission[70]. Advances in methods of shape controlled synthesis led to rod and tetrapod structures in CdTe, CdS, ZnS and core-shell rods and dot-rod structures[49,71,72]. Shieh et al have shown how a range of CdTe, CdSe and CdS heterostructures can be synthesised by a single reaction scheme dependent on the rate of precursor injection[73]. They used coordinated cadmium oxide (CdO) with *n*-tetradecylphosphonic acid (TDPA) as their starting precursor to form a variety of heterogeneous structures such as CdTe/CdSe/CdTe and CdS/CdTe/CdS rods (Figure 1.9).

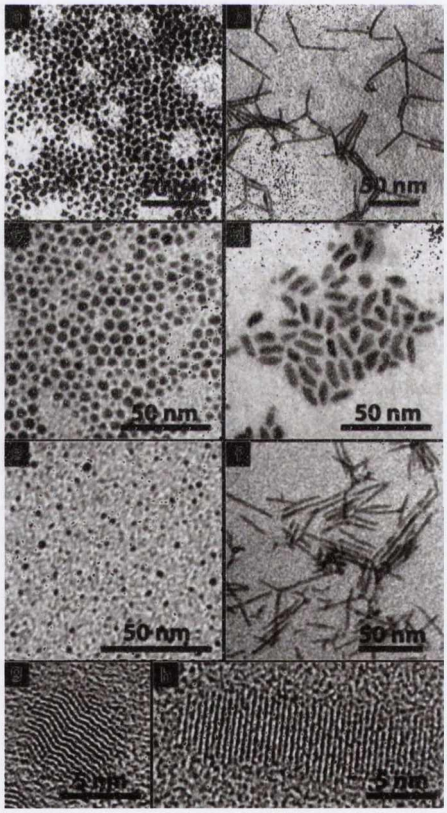

Fig. 1.9. A range of quantum rods have been made starting from spherical quantum dots. (a,b – CdTe dots and rods; c,d – CdSe dots and rods, e,f – CdS dots and rods; g,h – HRTEM of stacking faults in the spherical QD, but none in the rod[73]

A range of semiconducting quantum rods and with metal nanoparticle tips have also been synthesised by Mokari et al using CdSe quantum rods and gold nanoparticles [74]. It was found that the interaction between the semiconducting rod and the metal nanoparticle tips enhances new nonradiative pathways created by the proximity of metal, likely leading to electron transfer to the Au. As a result, quenching of the emission was observed with increasing Au nanoparticle size. Costi et al reviewed advances in development of hybrid nanostructures such as CdSe-Au, CdSe-Pt, CdS-Fe_3O_4 and others as well as their optical and electronic properties and applications [75]. CdS nano tetrapods with defect chiral emission are one of a new kind of high aspect ratio semiconducting nanostructure with interesting optical properties[76]. CdSe/CdS heterostructure have also been synthesised to give a dual emitting species when the CdS arms of a tetrapod with a CdSe core is more than 55 nm in length[77]. Not only does the single structure give well defined dual emission peaks, the peaks appear to be of equal intensity. The relative intensities of the dual emission, originating from exciton phase-space filling and reduced Auger recombination, can be effectively modulated by the photon fluence of the pump laser. Ultrafast carrier dynamics have been studied in a ZnSe/CdS/ZnSe "nanobarbell" structures also[78]. The type II quantum heterostructure would be ideal in photovoltaics for its fast and efficient charge separation characteristics. Halpert et al had already synthesised a similar barbell like structure using CdSe rods with CdTe tips (Figure 1.10) [67]. HRTEM images clearly show the CdSe and CdTe domains of the nanostructures, with clear separation of CdSe rods and the CdTe tips.

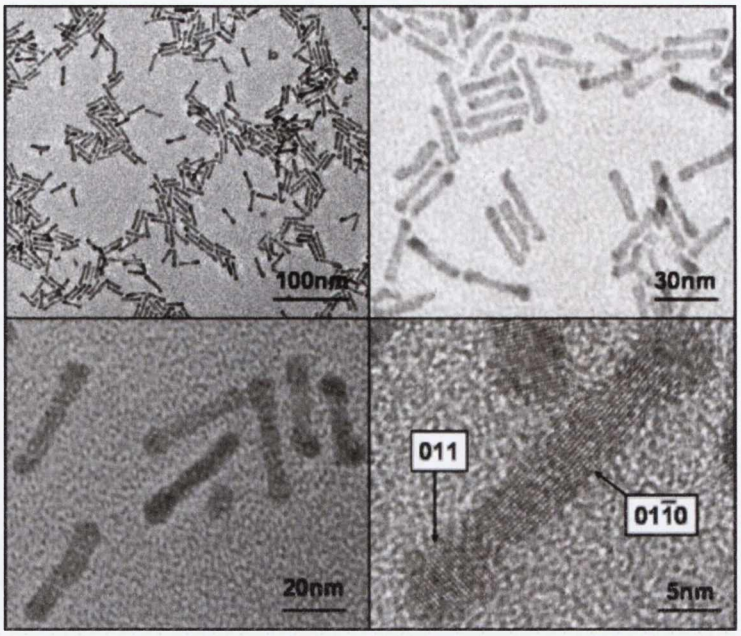

Fig.1. 10. A Type II "nanobarbell" structure - CdSe rods with CdTe tips show promising characteristics for charge separation applications[67].

1.2.8. QD fluorescence and blinking phenomena

Due to the quantum confinement effect QDs have spectra with well-defined absorption and emission bands (Fig. 1.11, left). The absorption peak corresponds to the 1s-1s electronic transition, while the emission results from radiative recombination of the photoexcited carriers.

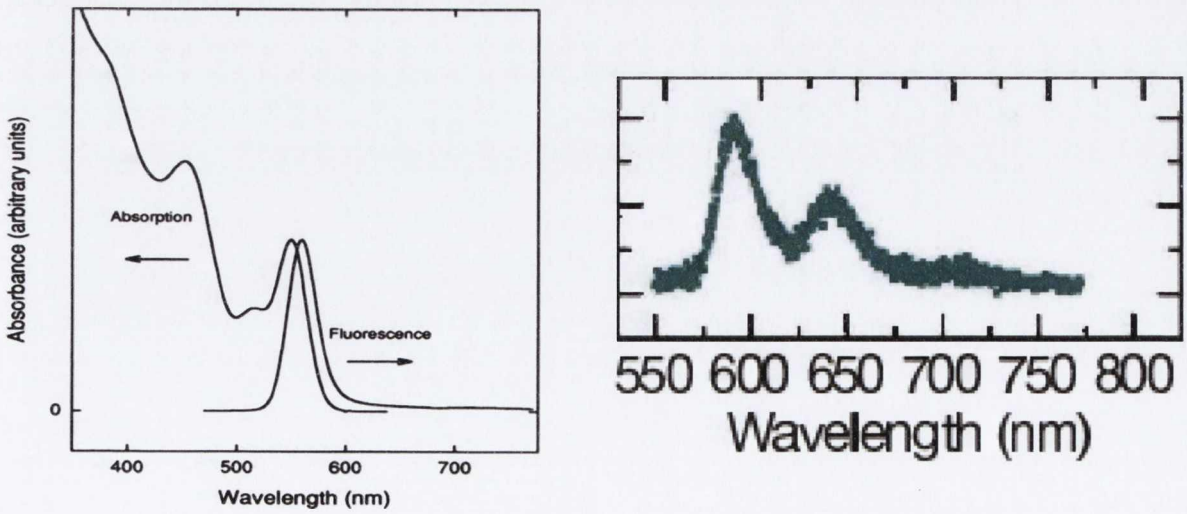

Fig. 1.11 Typical absorption and emission spectra of a CdSe QD (left)[23] and emission of a single non-blinking CdZnSe/ZnSe QD (right)[79]

Because of the extremely high surface area of semiconducting quantum dots surface reconstruction occurs to reduce the free energy at the surface of the dot. The rearrangement in the atomic positions of these surface atoms results in energy levels within the energetically forbidden band gap of the bulk material. When an electron is excited from the valence band these energy levels can act as traps, keeping the electron from decaying back to the valence band and emitting a photon. This leads to the degradation of the optical properties of the material and a reduced quantum yield as the electron recombines through non-radiative pathways[80]. The luminescent quantum yield of a fluorophore is given as the ratio of the number of photons emitted to the number of photons absorbed by the sample:

$$Q = \frac{photon_{ems}}{photon_{abs}} \qquad (1.5)$$

PLQY of QDs are calculated by comparing the photoluminescent emission spectra of the QD against a fluorophore of known QY [81]. The trapping of the electron on the surface by unpassivated ligands can also lead to a phenomenon known as blinking, where the QD does not fluoresce for a certain period of time[82]. This intermittent behaviour in QDs results in photoluminescence 'off' periods with the limited number of photons that can be detected in a given time period and also makes the photon arrival times from a single nanocrystal highly unpredictable. The blinking in QDs can happen in a number of ways, with the electron residing in a "deep trap" from a defect in the crystal lattice or an unpassivated dangling bond. During this time another exciton may transfer its energy to this excited electron and eject it from the nanocrystal. This results in the nanocrystal becoming charged, and resultant excitons decay non-radiatively, resulting in the nanocrystal being in an "off-state"[52,83]. Wang at al showed that alloyed QDs with a graded core-shell were non-blinking using a point scan of individual QDs (Fig 1.12) [79].

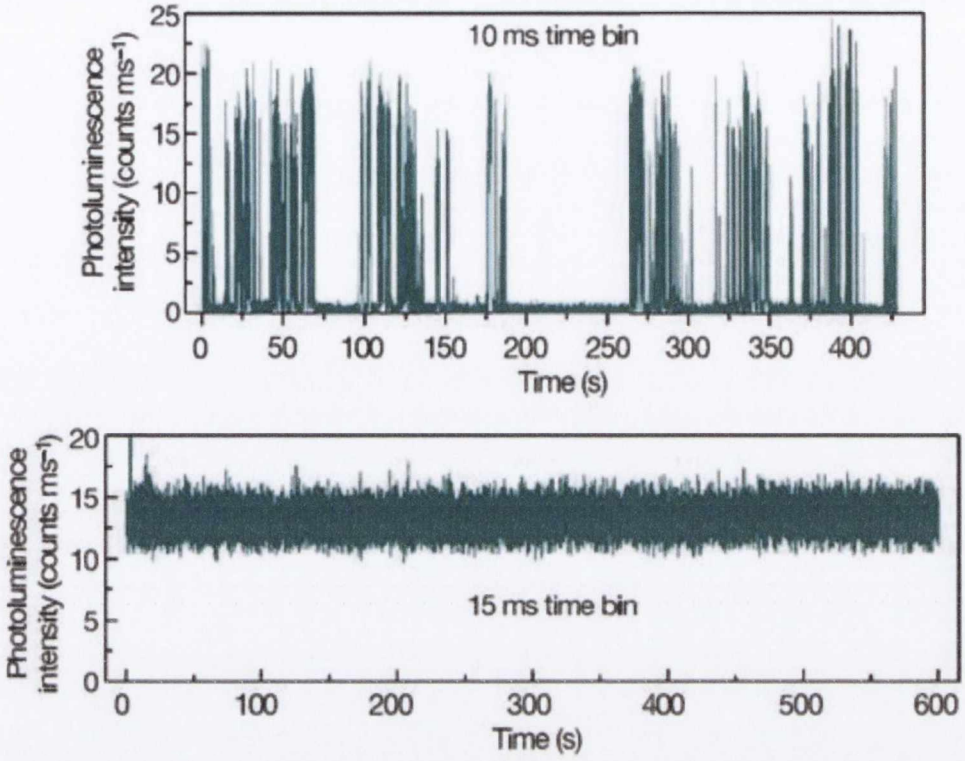

Fig. 1.12. Above – a typical blinking CdSe QDs with on/off states, and below – continuous emission from a CdZnSe/ZnSe QD[79]

Recently there was a report on ternary alloy based QDs that do not have blinking effects [83]. In this case the ternary alloy QD structure results in a graded junction between the core and the shell that leads to a lower lattice strain and therefore less defect traps as well as a graded energy junction, so the electron hole pair can recombine more efficiently. An excited electron may then recombine with either its own point positive charge, or the other one left behind from the ejected electron. Since both holes must have opposite spin, the electron will not be optically forbidden to recombine with one of the holes, thus shorter lifetimes are seen for this process. Hence, non-blinking quantum dots should exhibit shorter lifetimes that can be investigated by Time Correlated Single Photon Counting (TCSPC). The theoretical aspects of blinking in QDs have been considered by several recent of papers[84,85]. However despite the studies these phenomena are still unclear and poorly understood. Several reviews in this area take into consideration multiphoton excitation, charging of the nanocrystal and Auger-assisted recombination[86,87]. Others have shown that "Giant" CdSe/CdS core-shell QDs have supressed blinking, as the thick shell shields the core from any surface defects that can induce charging of the QD[88]. The production of non-blinking QD nanostructures is very important as these continuously

emitting nanomaterials are extremely important for further development of QD based lasers and biological probes. However this is still quite challenging and poorly explored area and further research is necessary to address these issues.

1.3. Optical Microcavities

Optical microcavites are used in many fields, providing multiple recirculation of light to maintain laser oscillation[89], high power densities[90] and long paths lengths for spectroscopic measurements, sensing devices[91] and micro-lasers[92]. Open dielectric resonators can trap light inside a cavity by total internal reflection at the interface of two media of different refractive index. For example spherical microcavities like this are attractive alternative to Fabry-Perot resonators due to their small size, high quality factor (Q factor, related to the loss of light in a resonator) values of up to $Q \sim 10^7$ and mechanical stability[93].

Mie and Debye were the first to study scattering and resonant eigenfrequencies of spheres in 1908[92], with Lord Rayleigh investigating the propagation of sound waves along the curved surface of St. Pauls Cathedral[94] leading to the term whispering gallery modes (WGMs).

The coupling of light to achieve effective WGM resonant effects is an important issue[95]. Free beam coupling uses an external beam to couple to the evanescent field of the resonator, which extends slightly outside of its body by a few wavelengths[96]. This can be an inefficient process and the positioning of the beam close to the edge of the resonator results in the most effective coupling. Once light is coupled to the resonator, the light is totally internally reflected (TIR) at the air/boundary interface, setting up a standing wave inside. Loss of light and therefore effectiveness of the resonator is due to scattering and absorption of the light by the material. This results in the effective Q-factor (quality factor) of the resonator, which takes into account propagation effects within the cavity. Shape and surface roughness also play a large part in determining the Q-factor[5], with a smooth surface reducing scattering effects. Q-factor is given as $Q = \omega\tau$, where ω is the frequency of the mode and τ the lifetime of the photon.

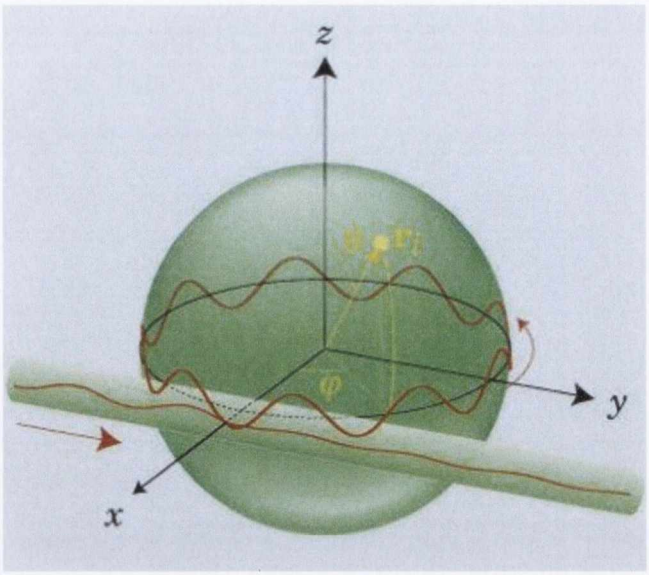

Fig 1.13. A standing wave is set up in a spherical microcavity. Light can be coupled in and out of the cavity via an optical taper[97].

When a standing wave is set up inside the cavity with an integer number of modes the microcavity will be in resonance with that particular mode (Figure 1.13). Modes are characterised by their quantum numbers *n, l* and *m*, where *n* represents the radial number giving the number of peaks in the radial direction inside a sphere, *l* is the angular mode number giving the number of wavelengths that fit into the circumference and *m* is the azimuthal mode number equal to *–l*....0....+*l*. WGMs are observed in the PL spectra of the microresonators by a series of periodical sharp peaks, resulting from the increased probability transition when emission wavelength couples to the spectral mode of the microcavity when in resonance.

Over last two decades hollow microspheres have attracted a great interest due their unique properties and numerous potential applications ranging from drug delivery to gas storage[98-102]. Various hollow microspheres from organic polymers and inorganic materials have been produced and investigated[103-106]. Hollow polymer microspheres are of particular importance as these materials have been envisaged for drug delivery, cosmetics preservation, catalysis, smart coatings and various encapsulation applications. Hollow polymer microspheres can be prepared by a variety of methods involving microencapsulation, liquid droplet methods, self-assembly techniques, emulsion polymerization, templating, microfluidic and a number of other approaches[105,107-118]. For example, a new electrohydrodynamic atomization (EHDA) method has been used recently to create a range of biocompatible hollow microspheres for drug delivery systems[117,119]. Using a 2-syringe system, a polymethylsilsesquioxane shell and

perflurohexane core microspheres were produced, although precise conditions are needed to form hollow spheres in the majority and cross-linking of polymer spheres can occur during synthesis. In another work the use of water-oil-water emulsions of polystyrene and acrylonitrile-butadiene-styrene/polycarbonate in combination with solvent evaporation techniques enabled to produce hollow microspheres[111,120]. This method typically results in spheres with diameters of 100 μm. Hollow polyaniline/Fe_3O_4 composite microspheres were also produced by emulsion polymerisation in a multistep process giving spheres of diameter ~1 μm[109].

Although the preparation of hollow polymer microspheres by methods above are well known, these techniques often involve multipot synthesis, expensive equipment, high temperatures (furnaces), long reaction times and stabilising ligands that makes them costly and hard to scale up to industrial scale[106,110,121-124]. One of the simple and efficient methods to produce microspheres is a spray drying technology. This method is based on the atomization of a solution through a spray nozzle. The solute may then be separated from the solution as the solvent is vaporized and removed, leaving behind a solid microsphere. The use of spray drying of polymer solutions has previously been used for production of a range of polymer microspheres for biological applications[125,126]. For example, polysaccharide microspheres were formed by spray drying a solution of chitosan, hyrdoxypropyl-B-cyclodextrin and polyethelyene glycol to form spherical microspheres to study the release of bovine serum[127]. Manitol, trehalose and insulin solutions have also been used in spray-freeze-drying methods to create spherical shapes showing that a range of solutions may be used to form microspheres[128,129]. The easy addition of biological agents to these systems can lead to potential applications of microcavities as possible lab on a chip and sensing candidates. However, so far it has not been shown that these methods can manufacture polymer microspheres with hollow cavities and of sufficient quality for optical applications.

Previously QDs have been incorporated into solid (non-hollow) polymer microspheres by swelling in organic solvents, or by layer by layer (LbL) deposition onto the surface [5,130-133]. The QD loaded microspheres have been proposed for potential applications as optical microresonators, single-photon emitters, nanojets, optical sensors and low-threshold micro-lasers. Klimov et al have shown how lasing from QDs on a polystyrene sphere increases the PL emission when increasing the laser pump fluence (Fig. 1.14). However, a large scale production of these microstructures is still very technically challenging that limits further development of this area.

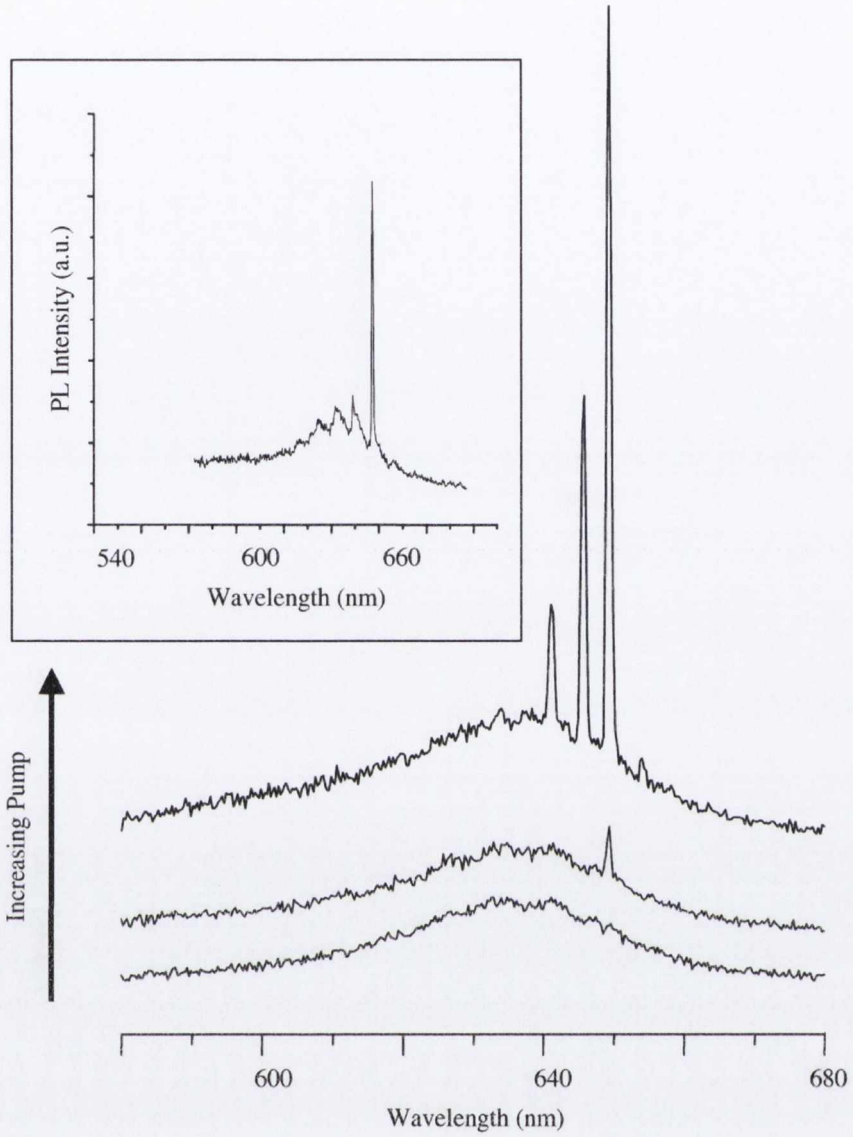

Fig. 1.14. WGM emission from CdSe QDs on the surface of polystyrene spheres[134].

Microcylinders are interesting as optical microcavities as their length makes them ideal to couple to other systems that can change their optical properties. For example, Chantada postulates that microcylinders would be ideal for biosensing applications, as they can be coupled to a substrate which would widen the WGM resonance peaks, as well as still being able to interact with other systems[135]. Gun'ko et al demonstrated how such micocylinders could be produced by infiltrating an alumino-silicate sol-gel through a porous glass membrane[136]. The thermal treatment of the aluminosilicate gel resulted in a broad defect emission that show light confinement in the form of well-defined WGM peaks. The defect emission was caused by the presence of interstitial carbon defects. Fluorescent Lifetime

Imaging Microscopy (FLIM) was used to image the microtubes and measure the lifetimes of the microtubes (Figure 1.15)

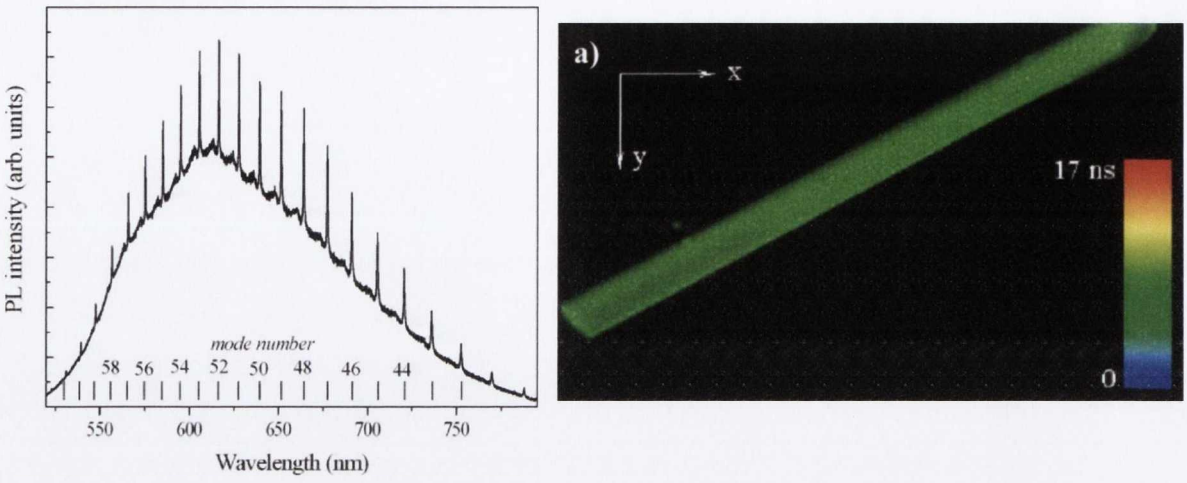

Fig. 1.15. WGM resonance peaks from a microcylinder (left) and the same microcylinder imaged using FLIM (right). [136]

1.4. Electroactive Dielectric Elastomers

Electroactive Polymers (EAPs) are polymers that can respond to electrical stimulation with the result being a change in the polymers shape or size. Because of their similarities, EAPs can be compared to McKibben and Shape Memory alloys (SMAs) in their properties[137,138]. Although EAPs are considered superior to both, as McKibben actuators rely on heavy electric motors and pneumatics and SMAs have slow response times and speeds. EAPs can be divided into two types: ionic actuators where actuation involves the diffusion or mobility of ions and electronic actuators where an electric field or Coulomb forces drive the actuation. Ionic EAPs include carbon nanotubes (CNTs), conducting polymers such as polypyrrole and ionic polymer-metal composites (IPMCs) and can actuate at low voltages compared to electronic EAPs although they have lower actuation strain (Fig. 1.16)[139].

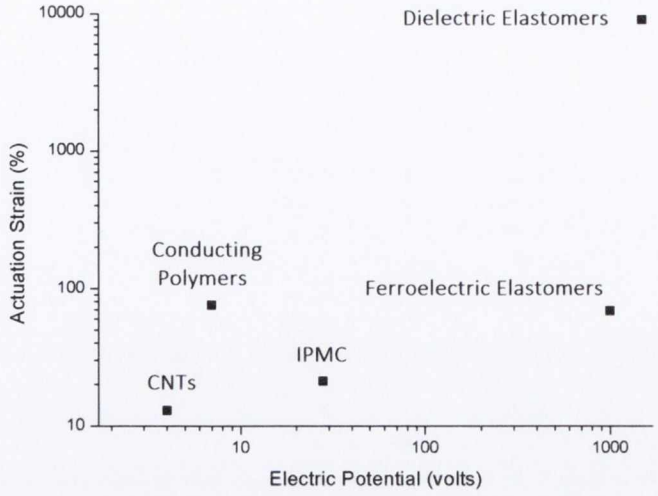

Fig. 1.16 Comparison of actuation strain and voltages needed for Ionic and electronic elastomers.

Electronic EAPs can be separated into two categories: Ferroelectric Polymers[140,141] and Dielectric Elastomers[142-145]. Ferroelectric materials such as polyvinylidene difluoride (PVDF) are materials whose dielectric properties change when electrostriction occurs. Due to the high voltages and lower actuation strain than dielectric elastomers, I will concentrate on the properties of dielectric elastomer actuators (DEAs). DEAs are a new EAP technology for light-weight, compact, energy-efficient and large-displacement electromechanical transducers, currently being studied and developed for several possible applications. The term dielectric was first coined by William Whewell in a letter to Michael Faraday in 1836[146] to describe the effect of current flow in a capacitor, where current at one plate charges another plate through an insulator. The result of having a static external field across the capacitor is that charged species in the dielectric become polarised, which Maxwell formed equations to describe:

$$S_{Maxwell} = -s\varepsilon_o\varepsilon_r\frac{E^2}{2} \qquad (1.6)$$

Where s is the elastic compliance, ε_0 is the permittivity of free space, ε_r the relative permittivity and E the electric field. $S_{Maxwell}$ gives us a relation of the strain in the thickness direction of the film using these parameters. An elementary DEA consists of a thin elastomeric layer with compliant electrodes on each side. When an electric potential difference is applied between the electrodes, an electrostatic stress (Maxwell stress) causes the film thickness to reduce and the electrode area to expand (Fig. 1.17)[144,147].

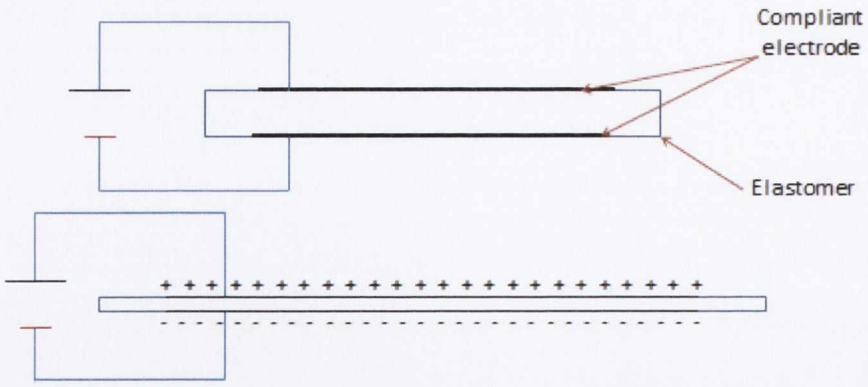

Fig. 1.17 Dielectric Elastomer undergoing actuation through Maxwell stress

The first demonstration of an EAP properties was done by Wilhelm Roentgen in 1880, where he showed the effect of an elastic bands change in length in an electric field[148]. The biggest breakthrough from then was in 1969, when Kawai demonstrated the piezoelectrical effects of the highly processable PVDF, which had substantial actuation activity compared to other materials at the time[149]. Piezoelectrical materials can accumulate charge when a mechanical stress is applied, whereas dielectric elastomers do not. Since then a wide range of compliant elastomers have been synthesised and used, with strains of $\leq$300 % achievable[150]. The most widely used dielectric elastomers used today are silicone, acrylic and polyurethane elastomers[142,145,150-153].

For a ceramic glassy polymer that has a high stiffness, deformation of actuation is limited by electrical breakdown, when the voltage mobilizes charged species in the dielectric to produce a path of electrical conduction. In compliant acrylic elastomers however, such as VHB elastomer, the actuation is limited by electromechanical instability, where the voltage can causes the dielectric to thin as it expands due to Maxwell forces. VHB is an acrylic elastomer synthesised by 3M and is widely used as an adhesive tape. After electromechanical instability, the electric field increases as the membrane thins until the dielectric fails by electrical breakdown. To counter this, efforts have been made to enhance the elastomer to improve its mechanical properties. Strategies to do this have started with the elastomer composition itself, by adding fillers to increase the elastomers dielectric constant or mechanical properties or using blends of elastomers and high dielectric polymers. This has been particularly prevalent in acrylic and silicone elastomers. Jiang Yu Li added a high dielectric filler, copper-phthalocyanine (CuPc) to P(VDF-TrFE) and

measured a sizable increase in its dielectric properties and strain response[154]. Unfortunately, adding high dielectric filler can often reduce the mechanical properties of the elastomer, as the filler has a much higher stiffness and lower elastomer strain than the polymer it's added to. Ha et al demonstrated high elastomer strain with a VHB-based IPN film with other additives (Fig. 1.18)[155].Carpi et al used a blend of poly(dimethylsiloxane) and poly(3-hexylthiophene) to yield an increase of the relative dielectric permittivity and a reduction of the tensile elastic modulus of the siloxane compound on its own[151], while in other work a dispersion of TiO_2 particles in a silicone elastomer enhanced the elastomers stress and strain by up to four times of the pure silicone by dramatically increasing the dielectric constant[156]. Unfortunately, the large TiO_2 particles in the elastomer often results in the usually transparent elastomer film to turn opaque due to efficient scattering of light by TiO_2 particles

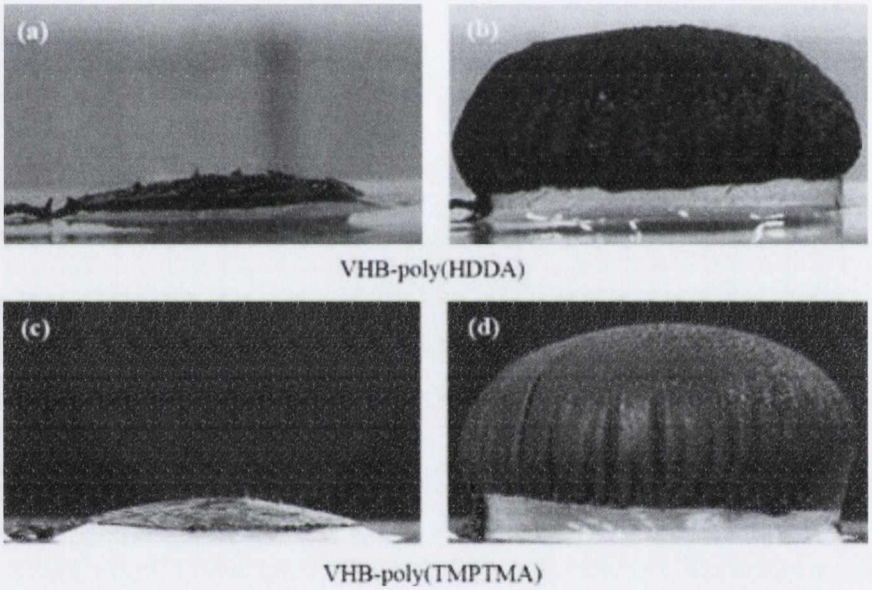

Fig. 1.18 VHB-based IPN films before and after actuation for films with HDDA (a and b) and TMPTMA (c and d) additives in a diaphragm configuration with no externally applied prestrain[155]

Because of the high actuation strain of DEAs, suitable compliant electrodes must also be used to supply the high voltages needed for actuation to occur. Metallic electrodes are not suitable as compliant electrodes for elastomers that can biaxially strain up to 380 %. Some work on zig-zag shapes and thin layers for metallic electrodes has been done, showing strains of up to 80 %. For the acrylic elastomer VHB, the most common compliant electrode is made up of carbon black or carbon graphite in silicone grease, which is easily painted onto the films and can accommodate strains in excess of 300 %. The high surface

area of carbon black, easy to process, low cost and good conductivity makes it an ideal electrode for use in DEAs. Yuan et at have used single walled CNTs as an alternative to the carbon black paste, for use in transparent, flexible electodes on VHB elastomer. SWCNTs were spray dried onto VHB elastomer and showed promising results with biaxial strains reaching 200 %, (after prestretch of 300 %) although the transparency of the films was still poor[157](Fig. 1.19).

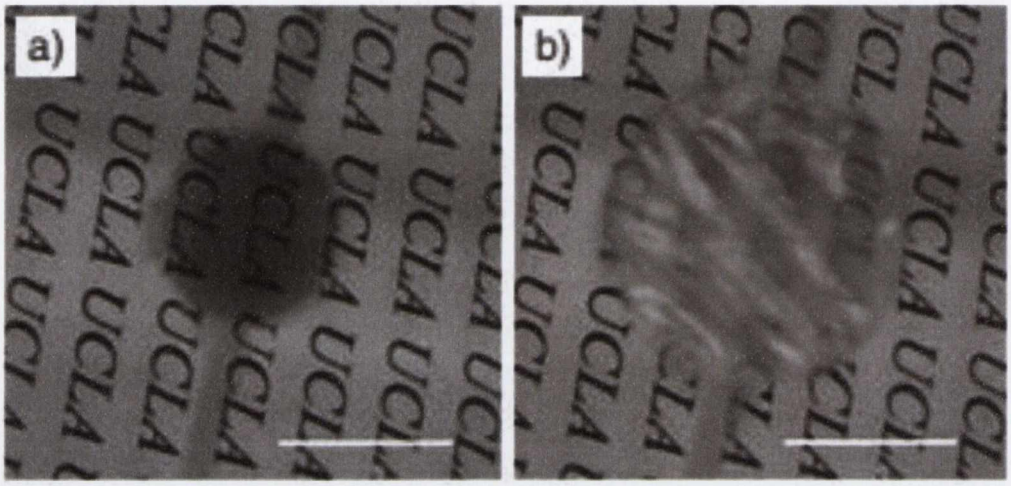

Fig. 1.19 SWCNT electrodes showing a 200% biaxial strain[158].

Son et al demonstrated an electromechanically driven variable lens using cured silicone rubber and PEDOT as a transparent electrode[159]. The electrode was applied to the silicone rubber by swelling the elastomer in a toluene/PEDOT solution, with transparency of up to ~70 %. Hwang et al have demonstrated a transparent multi-layer graphene lens with similar properties[160]. Other lens configurations which was developed by Carpi et al use a silicone gel sandwiched between two elastomer films for greater control of the lens for applications in magnification, projection and tactile feedback devices[161].

1.5. Aims and objectives of the project

The main goal of this project is to develop new quantum dot nanostructures and corresponding quantum dot based composite materials for potential applications in optoelectronics and photonics.

My primary objective is to develop good quality QD nanocrystals with high quantum yields. I plan to focus on CdSe and CdSe/ZnSe based QDs due to their superior luminescent properties. I also plan to develop nanocrystals with high aspect ratios and

robust optical properties for doping of polymer materials. Particular attention is to be paid to non-blinking QDs with continuous emission. I aim to prepare CdSe and $Cd_xZn_{x-1}Se$ quantum dots using both microwave heating and classical hot injection synthesis to make highly fluorescent, non-blinking QDs. These materials are to be characterised by absorption and PL emission spectroscopy, lifetime emission spectroscopy and, SEM, TEM, TGA and FLIM.

Another technical objective involves the incorporation of quantum dot emitters into 3D microcavities and the utilisation of such microcavities to build novel photonic structures which could be potentially used as microlasers and micro-optical sensors. I plan to introduce QDs into polymer based optical microcavities. QDs are good candidates for a fluorescent emitter to observe WGMs in microcavities as they provide high QYs, are stable, easily processable and have narrow emission spectra that can be tuned over a variety of wavelengths. Spherical optical microcavities are to be synthesised using a polymer microemulsion and QDs can be incorporated into these by the swelling of the polymer in organic solvents. I also plan to develop the fabrication of QD containing microcylindrical arrays that may also show WGM resonance effects. Finally one of our major aims is to incorporate QDs into acrylic dielectric elastomers. I plan to use both Type I and Type II (CdTe/CdSe) quantum dots for loading into DE to see if the charge separation in type II quantum dots can affect the elastomers actuation abilities. I plan to load VHB elastomer with quantum dots and test its optical properties when undergoing actuation at high voltages.

Overall I anticipate that the successful realisation of this project should result in the development of new nanocomposite materials with a range of potential applications in new optoelectronic and photonic devices.

References:

(1) Coleman, J. N.; Khan, U.; Gun'ko, Y. K. *Advanced Materials* **2006**, *18*, 689.
(2) Milliron, D. J.; Gur, I.; Alivisatos, A. P. *Mrs Bulletin* **2005**, *30*, 41.
(3) Michalet, X.; Pinaud, F. F.; Bentolila, L. A.; Tsay, J. M.; Doose, S.; Li, J. J.; Sundaresan, G.; Wu, A. M.; Gambhir, S. S.; Weiss, S. *Science* **2005**, *307*, 538.
(4) Sun, Q.; Wang, Y. A.; Li, L. S.; Wang, D. Y.; Zhu, T.; Xu, J.; Yang, C. H.; Li, Y. F. *Nature Photonics* **2007**, *1*, 717.
(5) Rakovich, Y. P.; Yang, L.; McCabe, E. M.; Donegan, J. F.; Perova, T.; Moore, A.; Gaponik, N.; Rogach, A. *Semiconductor Science and Technology* **2003**, *18*, 914.
(6) Einevoll, G. T. *Phys. Rev. B* **1992**, *45*, 3410.

(7) Rogach, A. L.; Katsikas, L.; Kornowski, A.; Su, D. S.; Eychmuller, A.; Weller, H. *Berichte Der Bunsen-Gesellschaft-Physical Chemistry Chemical Physics* **1996**, *100*, 1772.
(8) Peng, X. G.; Manna, L.; Yang, W. D.; Wickham, J.; Scher, E.; Kadavanich, A.; Alivisatos, A. P. *Nature* **2000**, *404*, 59.
(9) Faraday, M. *Philosophical Transactions of the Royal Society of London* **1857**, *147*, 145.
(10) Einstein, A. *Annalen der Physik* **1905**, *322*, 549.
(11) Barber, D. J.; Freestone, I. C. *Archaeometry* **1990**, *32*, 33.
(12) Daniel L. Schodek, P. F., Michael F. Ashby *Butterworth-Heinemann* **2009**, *Chapter 2*, 30.
(13) Museum, B. http://www.britishmuseum.org/research/collection_online/collection_object_details.aspx?objectId=61219&partId=1 **1958**, *Object number 1958,1202.1*.
(14) Cathedral, N. D. http://szou.cos.ucf.edu/outreach/webpage/image3311.jpg **1260**.
(15) Klimov, V. I.; McBranch, D. W.; Leatherdale, C. A.; Bawendi, M. G. *Physical Review B* **1999**, *60*, 13740.
(16) Wang, X. Y.; Qu, L. H.; Zhang, J. Y.; Peng, X. G.; Xiao, M. *Nano Letters* **2003**, *3*, 1103.
(17) Biju, V.; Itoh, T.; Anas, A.; Sujith, A.; Ishikawa, M. *Analytical and Bioanalytical Chemistry* **2008**, *391*, 2469.
(18) Alivisatos, A. P. *Science* **1996**, *271*, 933.
(19) Kiyoshi Takahashi, A. Y., Adarsh Sandhu *Springer* **2007**, 25.
(20) Brus, L. E. *The Journal of Chemical Physics* **1984**, *80*, 4403.
(21) E. Chukwuocha, M. O. a. T. H. *World Journal of Condensed Matter Physics* **2012**, *2*, 96.
(22) Marzin, J. Y.; Gerard, J. M.; Izrael, A.; Barrier, D.; Bastard, G. *Physical Review Letters* **1994**, *73*, 716.
(23) Murray, C. B.; Norris, D. J.; Bawendi, M. G. *Journal of the American Chemical Society* **2002**, *115*, 8706.
(24) Ouk Kim, S.; Solak, H. H.; Stoykovich, M. P.; Ferrier, N. J.; de Pablo, J. J.; Nealey, P. F. *Nature* **2003**, *424*, 411.
(25) Chou, S. Y.; Krauss, P. R.; Renstrom, P. J.; AVS: 1996; Vol. 14, p 4129.
(26) Petroff, P. M.; DenBaars, S. P. *Superlattices and Microstructures* **1994**, *15*, 15.
(27) Leonard, D.; Fafard, S.; Pond, K.; Zhang, Y. H.; Merz, J. L.; Petroff, P. M.; AVS: 1994; Vol. 12, p 2516.
(28) Rossetti, R.; Beck, S. M.; Brus, L. E. *Journal of the American Chemical Society* **1984**, *106*, 980.
(29) Reed, M. A.; Randall, J. N.; Aggarwal, R. J.; Matyi, R. J.; Moore, T. M.; Wetsel, A. E. *Phys. Rev. Lett.* **1988**, *60*, 535.
(30) Iijima, S. *Nature* **1991**, *354*, 56.
(31) Bullen, C. R.; Mulvaney, P. *Nano Letters* **2004**, *4*, 2303.
(32) Murray, C. B.; Norris, D. J.; Bawendi, M. G. *J. Am. Chem. Soc.* **1993**, *115*, 8706.
(33) Bowen Katari, J. E.; Colvin, V. L.; Alivisatos, A. P. *J. Phys. Chem.* **1994**, *98*, 4109.
(34) Murray, C. B.; Kagan, C. R.; Bawendi, M. G. *Annual Review of Materials Science* **2000**, *30*, 545.
(35) Sung, Y.-M.; Park, K.-S.; Lee, Y.-J.; Kim, T.-G. *The Journal of Physical Chemistry C* **2006**, *111*, 1239.
(36) Peng, Z. A.; Peng, X. *Journal of the American Chemical Society* **2001**, *123*, 1389.
(37) Murugan, A. V.; Muraliganth, T.; Manthiram, A. *Chemistry of Materials* **2009**, *21*, 5004.
(38) Liu, F. K.; Huang, P. W.; Chang, Y. C.; Ko, F. H.; Chu, T. C. *Journal of Materials Research* **2004**, *19*, 469.

(39) Correa-Duarte, M. A.; Giersig, M.; Kotov, N. A.; Liz-Marzan, L. M. *Langmuir* **1998**, *14*, 6430.
(40) Caddick, S. *Tetrahedron* **1995**, *51*, 10403.
(41) de la Hoz, A.; Diaz-Ortiz, A.; Moreno, A. *Chemical Society Reviews* **2005**, *34*, 164.
(42) Washington, A. L.; Strouse, G. F. *Chemistry of Materials* **2009**, *21*, 2770.
(43) Liao, X. H.; Chen, N. Y.; Xu, S.; Yang, S. B.; Zhu, J. J. *Journal of Crystal Growth* **2003**, *252*, 593.
(44) Washington Ii, A. L.; Strouse, G. F. *Journal of the American Chemical Society* **2008**, *130*, 8916.
(45) Washington, A. L.; Strouse, G. F. *Chemistry of Materials* **2009**.
(46) Gerbec, J. A.; Magana, D.; Washington, A.; Strouse, G. F. *Journal of the American Chemical Society* **2005**, *127*, 15791.
(47) Qian, H.; Qiu, X.; Li, L.; Ren, J. *The Journal of Physical Chemistry B* **2006**, *110*, 9034.
(48) He, Y.; Sai, L.-M.; Lu, H.-T.; Hu, M.; Lai, W.-Y.; Fan, Q.-L.; Wang, L.-H.; Huang, W. *Chemistry of Materials* **2007**, *19*, 359.
(49) Yu, W. W.; Wang, Y. A.; Peng, X. *Chemistry of Materials* **2003**, *15*, 4300.
(50) Kalyuzhny, G.; Murray, R. W. *The Journal of Physical Chemistry B* **2005**, *109*, 7012.
(51) Bullen, C.; Mulvaney, P. *Langmuir* **2006**, *22*, 3007.
(52) Nirmal, M.; Dabbousi, B. O.; Bawendi, M. G.; Macklin, J. J.; Trautman, J. K.; Harris, T. D.; Brus, L. E. *Nature* **1996**, *383*, 802.
(53) Smith, A. M.; Duan, H.; Rhyner, M. N.; Ruan, G.; Nie, S. *Physical Chemistry Chemical Physics* **2006**, *8*, 3895.
(54) Pellegrino, T.; Manna, L.; Kudera, S.; Liedl, T.; Koktysh, D.; Rogach, A. L.; Keller, S.; Rädler, J.; Natile, G.; Parak, W. J. *Nano Lett.* **2004**, *4*, 703.
(55) Smith, A. M.; Duan, H.; Mohs, A. M.; Nie, S. *Advanced Drug Delivery Reviews* **2008**, *60*, 1226.
(56) Zhang, Y.; Schnoes, A. M.; Clapp, A. R. *ACS Applied Materials & Interfaces* **2010**, *2*, 3384.
(57) Tricot, Y. M.; Fendler, J. H. *Journal of the American Chemical Society* **1984**, *106*, 7359.
(58) Green, M. *Journal of Materials Chemistry* **2010**, *20*, 5797.
(59) Talapin, D. V.; Rogach, A. L.; Shevchenko, E. V.; Kornowski, A.; Haase, M.; Weller, H. *Journal of the American Chemical Society* **2002**, *124*, 5782.
(60) Dabbousi, B. O.; Rodriguez-Viejo, J.; Mikulec, F. V.; Heine, J. R.; Mattoussi, H.; Ober, R.; Jensen, K. F.; Bawendi, M. G. *The Journal of Physical Chemistry B* **1997**, *101*, 9463.
(61) Peng, X.; Schlamp, M. C.; Kadavanich, A. V.; Alivisatos, A. P. *Journal of the American Chemical Society* **1997**, *119*, 7019.
(62) Li, J. J.; Wang, Y. A.; Guo, W.; Keay, J. C.; Mishima, T. D.; Johnson, M. B.; Peng, X. *Journal of the American Chemical Society* **2003**, *125*, 12567.
(63) Reiss, P.; Bleuse, J.; Pron, A. *Nano Lett.* **2002**, *2*, 781.
(64) Reiss, P.; Carayon, S.; Bleuse, J.; Pron, A. *Synthetic Metals* **2003**, *139*, 649.
(65) Talapin, D. V.; Mekis, I.; Götzinger, S.; Kornowski, A.; Benson, O.; Weller, H. *The Journal of Physical Chemistry B* **2004**, *108*, 18826.
(66) Kim, S.; Fisher, B.; Eisler, H.-J.; Bawendi, M. *Journal of the American Chemical Society* **2003**, *125*, 11466.
(67) Halpert, J. E.; Porter, V. J.; Zimmer, J. P.; Bawendi, M. G. *Journal of the American Chemical Society* **2006**, *128*, 12590.
(68) Manna, L.; Scher, E. C.; Alivisatos, A. P. *Journal of the American Chemical Society* **2000**, *122*, 12700.
(69) Hu, J.; Li, L.-s.; Yang, W.; Manna, L.; Wang, L.-w.; Alivisatos, A. P. *Science* **2001**, *292*, 2060.
(70) Mohamed, M. B.; Burda, C.; El-Sayed, M. A. *Nano Lett.* **2001**, *1*, 589.

(71) Neeleshwar, S.; Chen, C. L.; Tsai, C. B.; Chen, Y. Y.; Chen, C. C.; Shyu, S. G.; Seehra, M. S. *Physical Review B* **2005**, *71*, 201307.
(72) Chen, M.; Xie, Y.; Lu, J.; Xiong, Y.; Zhang, S.; Qian, Y.; Liu, X. *Journal of Materials Chemistry* **2002**, *12*, 748.
(73) Shieh, F.; Saunders, A. E.; Korgel, B. A. *The Journal of Physical Chemistry B* **2005**, *109*, 8538.
(74) Mokari, T.; Rothenberg, E.; Popov, I.; Costi, R.; Banin, U. *Science* **2004**, *304*, 1787.
(75) Costi, R.; Saunders, A. E.; Banin, U. *Angewandte Chemie International Edition* **2010**, *49*, 4878.
(76) Govan, J. E.; Jan, E.; Querejeta, A.; Kotov, N. A.; Gun'ko, Y. K. *Chemical Communications* **2010**, *46*, 6072.
(77) Lutich, A. A.; Mauser, C.; Da Como, E.; Huang, J.; Vaneski, A.; Talapin, D. V.; Rogach, A. L.; Feldmann, J. *Nano Lett.* **2010**, *10*, 4646.
(78) Hewa-Kasakarage, N. N.; El-Khoury, P. Z.; Tarnovsky, A. N.; Kirsanova, M.; Nemitz, I.; Nemchinov, A.; Zamkov, M. *ACS Nano* **2010**, *4*, 1837.
(79) Wang, X.; Ren, X.; Kahen, K.; Hahn, M. A.; Rajeswaran, M.; Maccagnano-Zacher, S.; Silcox, J.; Cragg, G. E.; Efros, A. L.; Krauss, T. D. *Nature* **2009**, *459*, 686.
(80) Verberk, R.; van Oijen, A. M.; Orrit, M. *Physical Review B* **2002**, *66*, 4.
(81) Yu, W. W.; Qu, L.; Guo, W.; Peng, X. *Chemistry of Materials* **2003**, *15*, 2854.
(82) Hamada, M.; Nakanishi, S.; Itoh, T.; Ishikawa, M.; Biju, V. *ACS Nano*, *4*, 4445.
(83) Ha, T. *Nature* **2009**, *459*, 649.
(84) Gómez, D. E.; van Embden, J.; Jasieniak, J.; Smith, T. A.; Mulvaney, P. *Small* **2006**, *2*, 204.
(85) Morello, G.; Anni, M.; Cozzoli, P. D.; Manna, L.; Cingolani, R.; De Giorgi, M. *The Journal of Physical Chemistry C* **2007**, *111*, 10541.
(86) Kuno, M.; Fromm, D. P.; Johnson, S. T.; Gallagher, A.; Nesbitt, D. J. *Physical Review B* **2003**, *67*, 125304.
(87) Efros, A. L. *Nat Mater* **2008**, *7*, 612.
(88) Chen, Y.; Vela, J.; Htoon, H.; Casson, J. L.; Werder, D. J.; Bussian, D. A.; Klimov, V. I.; Hollingsworth, J. A. *Journal of the American Chemical Society* **2008**, *130*, 5026.
(89) Fujiwara, S.; Bando, K.; Masumoto, Y.; Sasaki, F.; Kobayashi, S.; Haraichi, S.; Hotta, S. *Applied Physics Letters* **2007**, *91*, 3.
(90) Hill, M. T.; Dorren, H. J. S.; de Vries, T.; Leijtens, X. J. M.; den Besten, J. H.; Smalbrugge, B.; Oei, Y. S.; Binsma, H.; Khoe, G. D.; Smit, M. K. *Nature* **2004**, *432*, 206.
(91) Vollmer, F.; Arnold, S.; Keng, D. *Proceedings of the National Academy of Sciences of the United States of America* **2008**, *105*, 20701.
(92) Mie *Ann. Phys* **1908**, *1*, 377.
(93) Cai, M.; Painter, O.; Vahala, K. J. *Phys. Rev. Lett.* **2000**, *85*, 74.
(94) Rayleigh, L. *Philos Mag* **1910**, *20*.
(95) Bayer, M.; Forchel, A.; Reinecke, T. L.; Knipp, P. A.; Rudin, S. *physica status solidi (a)* **2002**, *191*, 3.
(96) Huang, G.; Bolanìfos Quinìfones, V. A.; Ding, F.; Kiravittaya, S.; Mei, Y.; Schmidt, O. G. *ACS Nano* **2010**, *4*, 3123.
(97) Arnold, S.; Khoshsima, M.; Teraoka, I.; Holler, S.; Vollmer, F. *Opt. Lett.* **2003**, *28*, 272.
(98) Kawashima, Y.; Niwa, T.; Takeuchi, H.; Hino, T.; Itoh, Y. *Journal of Pharmaceutical Sciences* **1992**, *81*, 135.
(99) D Gagnebien, B. D. *US Patent 5,219,561 Google Patents*

1993.
(100) Cochran, J. K. *Current Opinion in Solid State and Materials Science* **1998**, *3*, 474.
(101) Zhu, H.; Wang, J.; Xu, G. *Crystal Growth & Design* **2008**, *9*, 633.
(102) Soppimath, K. S.; Kulkarni, A. R.; Aminabhavi, T. M. *Drug Development and Industrial Pharmacy* **2001**, *27*, 507.

(103) Hu, C. Y.; Xu, Y. J.; Duo, S. W.; Li, W. K.; Xiang, J. H.; Li, M. S.; Zhang, R. F. *Journal of the Chinese Chemical Society* **2010**, *57*, 1091.
(104) Bertling, J.; Blömer, J.; Kümmel, R. *Chemical Engineering & Technology* **2004**, *27*, 829.
(105) Wei, B.; Wang, S. J.; Song, H. G.; Liu, H. Y.; Li, J.; Liu, N. *Petroleum Science* **2009**, *6*, 306.
(106) Liu, B. Y.; Jia, D. C.; Dong, L. H.; Yin, Y. S. *Progress in Chemistry* **2009**, *21*, 1450.
(107) Vladisavljevic, G. T.; Williams, R. A. *Advances in Colloid and Interface Science* **2005**, *113*, 1.
(108) Han, J.; Song, G.; Guo, R. *Advanced Materials* **2006**, *18*, 3140.
(109) Yang, C.; Li, H.; Xiong, D.; Cao, Z. *Reactive and Functional Polymers* **2009**, *69*, 137.
(110) Liu, H. R.; Hu, X.; Yang, S.; Miao, W. F.; Li, Z. C.; Zhang, W. *Progress in Chemistry* **2009**, *21*, 672.
(111) Jie, L.; Hongyan, L.; Shujun, W. *Materials Letters* **2011**, *65*, 2696.
(112) Ma, G. H. *Colloid and Polymer Science* **2013**, *291*, 53.
(113) Sukhorukov, G. B.; Fery, A.; Brumen, M.; Mohwald, H. *Physical Chemistry Chemical Physics* **2004**, *6*, 4078.
(114) De Geest, B. G.; De Koker, S.; Sukhorukov, G. B.; Kreft, O.; Parak, W. J.; Skirtach, A. G.; Demeester, J.; De Smedt, S. C.; Hennink, W. E. *Soft Matter* **2009**, *5*, 282.
(115) De Cock, L. J.; De Koker, S.; De Geest, B. G.; Grooten, J.; Vervaet, C.; Remon, J. P.; Sukhorukov, G. B.; Antipina, M. N. *Angewandte Chemie-International Edition* **2010**, *49*, 6954.
(116) Duncanson, W. J.; Lin, T.; Abate, A. R.; Seiffert, S.; Shah, R. K.; Weitz, D. A. *Lab on a Chip* **2012**, *12*, 2135.
(117) Vladisavljevic, G. T.; Kobayashi, I.; Nakajima, M. *Microfluidics and Nanofluidics* **2012**, *13*, 151.
(118) Pich, A.; Richtering, W. In *Chemical Design of Responsive Microgels*; Pich, A., Richtering, W., Eds. 2010; Vol. 234, p 1.
(119) Sanson, N.; Rieger, J. *Polymer Chemistry* **2010**, *1*, 965.
(120) Cai, P.-j.; Tang, Y.-j.; Wang, Y.-t.; Cao, Y.-j. *Materials Chemistry and Physics* **2010**, *124*, 10.
(121) Fu, Q. T.; He, T. T.; Yu, L. Q.; Liu, Y. J.; Chai, Y. M.; Liu, C. G. *Progress in Chemistry* **2010**, *22*, 1116.
(122) Purcell-Milton, F.; Gun'ko, Y. K. *Journal of Materials Chemistry* **2012**, *22*, 16687.
(123) Huang, P.; Chai, S. G.; Yuan, J. J.; Lu, G. H.; Yang, T. T.; Cheng, S. Y. *Progress in Chemistry* **2012**, *24*, 31.
(124) Roques-Carmes, T.; Marchal, P.; Gigante, A.; Corbel, S. *Russian Chemical Reviews* **2009**, *78*, 375.
(125) Bose, S.; Bogner, R. H. *Pharmaceutical Development and Technology* **2007**, *12*, 115.
(126) Lee, K. W.; Viehbeck, A. *Ibm Journal of Research and Development* **1994**, *38*, 457.
(127) Gayakwad, S. G.; Bejugam, N. K.; Akhavein, N.; Uddin, N. A.; Oettinger, C. E.; D'Souza, M. J. *Journal of Microencapsulation* **2009**, *26*, 692.
(128) Rochelle, C.; Lee, G. *Journal of Pharmaceutical Sciences* **2007**, *96*, 2296.
(129) Schiffter, H.; Condliffe, J.; Vonhoff, S. *Journal of the Royal Society Interface* **2010**, *7*, S483.
(130) Meissner, K. E.; Allen, A. In *Sensors, 2005 IEEE* 2005, p 4 pp.
(131) Rakovich, Y. P.; Gerlach, M.; Bradley, A. L.; Donegan, J. F.; Connolly, T. M.; Boland, J. J.; Przyjalgowski, M. A.; Ryder, A.; Gaponik, N.; Rogach, A. L. *Journal of Applied Physics* **2004**, *96*, 6761.
(132) Rakovich, Y. P.; Donegan, J. F.; Gerlach, M.; Bradley, A. L.; Connolly, T. M.; Boland, J. J.; Gaponik, N.; Rogach, A. *Physical Review A* **2004**, *70*.
(133) Rakovich, Y. P.; Donegan, J. F. *Laser & Photonics Reviews* **2010**, *4*, 179.

(134) Bawendi, V. I. K. a. M. G. *MRS Bull.* **2001**, *26*, 998.
(135) Chantada, L.; Nikolaev, N. I.; Ivanov, A. L.; Borri, P.; Langbein, W. *J. Opt. Soc. Am. B* **2008**, *25*, 1312.
(136) Rakovich, Y. P.; Balakrishnan, S.; Donegan, J. F.; Perova, T. S.; Moore, R. A.; Gun'ko, Y. K. *Advanced Functional Materials* **2007**, *17*, 1106.
(137) Klute, G. K.; Czerniecki, J. M.; Hannaford, B. In *Advanced Intelligent Mechatronics, 1999. Proceedings. 1999 IEEE/ASME International Conference on* 1999, p 221.
(138) Sozinov, A.; Likhachev, A. A.; Lanska, N.; Ullakko, K. *Appl. Phys. Lett.* **2002**, *80*, 1746.
(139) Shahinpoor, M.; Bar-Cohen, Y.; Simpson, J. O.; Smith, J. *Smart Materials and Structures* **1998**, *7*, R15.
(140) Zhang, Q. M.; Bharti, V.; Zhao, X. *Science* **1998**, *280*, 2101.
(141) Lovinger, A. J. *Science* **1983**, *220*, 1115.
(142) Pelrine, R.; Kornbluh, R.; Pei, Q.; Joseph, J. *Science* **2000**, *287*, 836.
(143) Pelrine, R.; Kornbluh, R.; Joseph, J.; Heydt, R.; Pei, Q.; Chiba, S. *Materials Science and Engineering: C* **2000**, *11*, 89.
(144) Kofod, G.; Sommer-Larsen, P.; Kornbluh, R.; Pelrine, R. *Journal of Intelligent Material Systems and Structures* **2003**, *14*, 787.
(145) Brochu, P.; Pei, Q. *Macromolecular Rapid Communications* **2010**, *31*, 10.
(146) Yeo, R. R. *Cambridge University Press* **1993**.
(147) McMeeking, R. M.; Landis, C. M. *Journal of Applied Mechanics* **2004**, *72*, 581.
(148) Bar-Cohen, Y. *Electrochemistry Encyclopedia* **2004**, *(http://electrochem.cwru.edu/encycl/)*.
(149) Kawai, H. *Japanese Journal of Applied Physics* **1969**, *8*, 975.
(150) Ha, S. M.; Yuan, W.; Pei, Q.; Pelrine, R.; Stanford, S. *Smart Materials and Structures* **2007**, *16*, S280.
(151) Carpi, F.; Gallone, G.; Galantini, F.; De Rossi, D. *Advanced Functional Materials* **2008**, *18*, 235.
(152) Behl, M.; Lendlein, A. *Materials Today* **2007**, *10*, 20.
(153) Takahashi, T.; Hayashi, N.; Hayashi, S. *Journal of Applied Polymer Science* **1996**, *60*, 1061.
(154) Li, J. *Phys. Rev. Lett.* **2003**, *90*, 217601.
(155) Ha, S. M.; Park, I. S.; Wissler, M.; Pelrine, R.; Stanford, S.; Kim, K. J.; Kovacs, G.; Pei, Q. 2008; Vol. 6927, p 69272C.
(156) Carpi, F.; Rossi, D. D. *Dielectrics and Electrical Insulation, IEEE Transactions on* **2005**, *12*, 835.
(157) Yuan, W.; Hu, L. B.; Yu, Z. B.; Lam, T.; Biggs, J.; Ha, S. M.; Xi, D. J.; Chen, B.; Senesky, M. K.; Grüner, G.; Pei, Q. *Advanced Materials* **2008**, *20*, 621.
(158) Shian, S.; Diebold, R. M.; McNamara, A.; Clarke, D. R. *Applied Physics Letters* **2012**, *101*, 061101.
(159) Son, S.-i.; Pugal, D.; Hwang, T.; Choi, H. R.; Koo, J. C.; Lee, Y.; Kim, K.; Nam, J.-D. *Appl. Opt.* **2012**, *51*, 2987.
(160) Hwang, T.; Kwon, H.-Y.; Oh, J.-S.; Hong, J.-P.; Hong, S.-C.; Lee, Y.; Choi, H. R.; Kim, K. J.; Bhuiya, M. H.; Nam, J.-D. *Applied Physics Letters* **2013**, *103*, 023106.
(161) Carpi, F.; Frediani, G.; Turco, S.; De Rossi, D. *Advanced Functional Materials* **2011**, *21*, 4152.

Chapter 2: Experimental

2.1 Starting Materials and General Procedures

All starting materials were purchased from Sigma-Aldrich and used without further purification unless otherwise stated. These included: Cadmium Oxide (CdO, 99.99 %), Selenium (Se, 99.99 %), Trioctylphosphine (TOP 90 %), Trioctylphosphine oxide (TOPO, 99 %), Polymethylmethacrylate (PMMA, 95 % M.W 120,000), Methyl methcrylate (MMA, 99 %), Sulfur powder (S, 99.99 %), Octadecene (ODE, 99%), Octadecane (ODA, 99 %), Stearic Acid (SA, 95 %), Octadecyl Phosphonic Acid (PCI Synthesis, ODPA – 97 %), Tellurium powder (Te, 99.99 %), Octadecylamine (ODA, 98 %), Hexadecylamine (HDA, 98 %), Bis(trimethylsilyl)sulfide ($(TMS)_2S$, 1 M in hexane), DiethylZinc (DEZn, 1 M in hexane), Azobisisobutyronitrile (AIBN, 70 %), Glass cover slips (VWR – 15 mm x 15 mm x 0.15 mm). All solvents were distilled and degassed under argon before use.

Air free manipulations were carried out under vacuum or argon by Schlenk techniques using Schlenk glassware and a vacuum manifold fitted with a liquid nitrogen trap. Deoxygenated under argon Millipore water of 18.2 MΩ was used. All solvents were purified by distillation, degassed by sonication while under vacuum and stored under argon. An ultrasonic bath (Grant XB6 at 50-60 Hz) was used for sonication of polymer solutions.

2.2 Experimental details for Chapter 3

2.2.1 Microwave synthesis of CdSe and CdZnSe QDs

CdSe QDs were synthesised using our modification of the microwave method which was previously reported by Strous et al[1].

A 1 M stock solution of TOPSe was prepared by dissolving selenium powder in TOP under argon in a sonic bath for 10 minutes. This resulted in a clear solution. Cadmium Stearate (CdSA) was synthesised by heating a CdO/SA in a ratio of 4:1 under argon to

200 °C until the solution turned from red to clear. 0.2 M of CdSA, 5 mL of octadecane, 3 g of hexadecylamine and 1g of TOPO was added to the CEM star system 6 microwave reaction flask that was flushed with argon. Then 5 mL of the 1 M TOPSe stock solution was added to the container and the container was closed. The reaction mixture was then microwaved at full power until the desired temperature was reached or for a desired time (80 s - 300 s). The heating was stopped by turning off the microwave and an excess of methanol was added to cool the solution and precipitate QDs. The resultant QDs were washed several times in methanol and ethanol solutions, redispersed in toluene and centrifuged at 2000 rpm to crash out excessive reagents.

For CdZnSe QDs, TOPO and HDA were replaced with equimolar amounts of Octadecylamine (ODA).The synthesis is then carried out by the same method as previously described. The resultant CdSe QDs were washed and redispersed in ODE. This solution was added to the reaction vessel with ODA, 5 mL of 1 M TOPSe and 1 M of ZnSA was added to the flask and microwaved at full power for 6 minutes to ensure alloying of the CdSe cores.

2.2.2 Hot injection synthesis of CdSe, CdSe/ZnSe and CdZnSe QDs

A 0.2 M solution of TOPSe and CdSA was made as described above. 0.001 M of CdSA, 5mL of ODE and 3 g of ODA were mixed in a 100mL round bottomed flask. Initially the mixture was heated to 150 °C under vacuum and kept under constant argon flow for the remainder of the experiment. The solution was then heated to 280 °C and 0.01 M of TOPSe was swiftly injected into the hot solution by glass syringe, while the solution temperature dropped to 260 °C. Aliquots were taken every 30 s to monitor the growth of the QDs. The resultant QDs were cleaned by precipitation with methanol using the method which was previously described in section 2.2.1.

$Cd_xZn_{x-1}Se$ alloyed dots were prepared in a similar fashion, using the appropriate amount of ZnSA to maintain a Cd/Zn:Se ratio of 1:10. These dots were redispersed in 5 mL of ODE and 3 g of ODA and heated to 200 °C under argon. A 0.01 M solution of ZnSA and Se in 5 mL of TOP was injected into this reaction mixture at a rate of 0.1 mL/min via a glass syringe using a syringe pump. Aliquots were taken periodically to monitor shell growth of these particles. Then the QDs were co-precipitated and washed in methanol and re-dispersed in toluene for further characterisation and studies.

2.2.3 Synthesis of CdS QDs

CdS seeds were synthesised with a solution of TOP$(TMS)_2S$ (2 mL of $(TMS)_2S$ in 2.5 mL of TOP, $5.6x10^{-3}$ m) was made by mixing $(TMS)_2S$ in TOP under argon in a sonic bath for 10 minutes approximately. This resulted in a clear solution. CdODPA was synthesised by heating a CdO/ODPA (0.100 g of CdO, $7.8x10^{-4}$ m, and 0.603 g of ODPA, $1.8x10^{-3}$ m) with TOPO (3.299 g, $8.5x10^{-3}$ m), under vacuum to 150 °C and under argon to above 320 °C until the dissolution of CdO. Then, the solution turned to clear. When the temperature was stabilized to 320 °C, 0.45 mL of TOP$(TMS)_2S$ was swiftly injected into the hot solution by glass syringe, while the solution temperature dropped to 260 °C. Then, nanocrystals were allowed to grow for between 30 s and 5 minutes, depending on the size of QD desired. Samples of the solution were taken every 2 minutes to monitor the growth of the CdS seeds. The reaction was stopped by turning off the heater and the addition of methanol to cool the solution. The resultant CdS seeds were washed several times in methanol solution redispersed in toluene and centrifuged at 2000 rpm to crash out excess reagents.

To prepare the CdS QDs with intrinsic emission 0.0128 g (0.00010 mol) of CdO was weighed into a round bottom flask, to this 0.093 g of OA (0.000332 mol) and 3.9 g of ODE were added. The flask was then put under vacuum to degas solutions for 20 minutes. The reaction was then heated to 300 °C to allow formation of Cd(OA) and then a solution of sulphur dissolved in ODE (0.0016 g (0.00005 mol) was injected and growth was allowed to proceed for 10 minutes. After that the reaction mixture was removed from the heat and the reaction was quenched using EtOH.

2.2.4 Synthesis of CdS rods

CdS rods were synthesised using a solution of TOPS (0.120 g of S, $3.7x10^{-3}$ m, in 1.8 mL of TOP, 2 M) which was made by dissolving solid sulphur under argon in a sonic bath for 10 minutes. This resulted in a clear solution. CdODPA was synthesised by heating a CdO/ODPA (0.057 g of Cd0, $4.4x10^{-4}$ m, and 0.290 g of ODPA, $8.7x10^{-4}$ m) with hexadecylamine (0.080 g) and TOPO (3 g) under vacuum to 150 °C and under argon to above 320 °C until the dissolution of CdO. Then, the solution turned to clear. When the temperature was stabilized to 350 °C, solutions of CdS + TOP (1.6-3.2 mL) with known CdS concentration (6 x 10^{-7} m) were injected into the solution of TOPS and

then, the mixture was swiftly injected into the hot solution by glass syringe, while the solution temperature dropped to 250 °C.The reaction was kept at 250 °C for 7 minutes before quenching with EtOH. The resultant QDs were washed several times in methanol solution redispersed in toluene and centrifuged at 2000 rpm to crash out excess reagents.

2.2.5 Synthesis of CdS based rod/dot nanostructures

Initially a mixture of 0.0552 g of CdO (4.3×10^{-4} m), 1.5 mL of OA and 1.5 mL of TOP was prepared in a 100 mL round bottomed flask and then the mixture was heated at 250 °C until it turned clear. This solution was then cooled to 60 °C and a 0.6 M solution of TOPSe (0.0340 g of Se, 4.3×10^{-4} m in 0.7 mL of TOP, 1.6×10^{-3} m) was added. In another flask, we added CdS rods in hexane to 1.5 g of ODA (5.6×10^{-3} m) and 6 mL of ODE, and placed under vacuum at 80 °C to remove all hexane. We then put the flask under argon and heated it to 250 °C. The Cd/Se solution was injected in aliquots to our CdS rods at 250 °C (every 2 minutes). The reaction mixture was removed from the heat and the reaction was quenched using EtOH. The residue was then washed with methanol and redispersed in toluene for further characterisation and studies.

2.3 Experimental details for Chapter 4

2.3.1 Microemulsion synthesis of PMMA microspheres

PMMA microspheres were synthesised using a modified method by Kliene et al[2]. Briefly, 100 mL of MeOH, 50 mL of H_2O, 2 g of PVA and 5 mL of MMA were added to a 250 mL round bottomed flask and flushed with argon. The solution was stirred at 100 rpm with a magnetic stirrer bar and heated to 75 °C. The solution was kept at this temperature for 1 hour to reach thermal equilibrium and then 0.1 g of AIBN was added in 1 mL of H_2O. After 8 hours the reaction mixture was taken off the heat and an excess of MeOH was added. The mixture was centrifuged at 2000 rpm for 10 minutes. This was carried out up to 3 times to ensure narrow microsphere size dispersity in the sample.

2.3.2 Incorporation of QDs into PMMA and PS microspheres

0.05 g of PMMA or PS polymer microspheres was weighed and dispersed in 4.5 mL of propanol. 0.5 mL of a 2×10^{-6} M solution of CdSe/ZnSe QDs in chloroform was then added to this solution. The solution was sonicated in a sonic bath for 10 minutes,

redispersed in methanol and centrifuged at 2000 rpm for 10 minutes. The particles were washed three more times in methanol to ensure all chloroform was removed.

2.3.3 Preparation of PMMA micropillars

A 10 % w/v PMMA toluene solution was prepared by sonication in an ultrasonic bath for 3 hours to fully dissolve the polymer. 0.5 mL of a 2 x 10^{-6} M solution of CdSe/ZnSe QDs in toluene was then added to the solution and further sonicated for 30 min to ensure a homogeneous solution. A porous Ni template with 10μm pores used as received from Tecan LTD. was placed upon a Buchner filter under vacuum (water jet pump) and the PMMA solution was drop casted onto the template using a pipette. When the pores were filled the template was removed and let to dry overnight under ambient conditions. The polymer pillars (microcylinders) were removed by peeling off the polymer using a SEM stub.

2.3.4 Synthesis of CdSe/CdS QDs

CdSe/CdS core-shell QDs were synthesized by a method adapted from Tapalin et al[3] using the noncoordinating solvent 1-octadecene (ODE). Briefly, 0.057 g of cadmium oxide (CdO) and 0.29 g of octadecyl phosphonic acid (ODPA) were mixed in a 50 ml three-neck flask containing 5 ml of ODE. This mixture was degassed under vacuum and then heated under a nitrogen atmosphere to 300 °C. The mixture was then cooled to 250 °C. The selenium (Se) precursor was prepared by mixing 0.016 g of Se powder with 0.75 ml trioctylphoshine (TOP), under inert atmosphere, followed by sonication until the solution became transparent. Once the temperature of CdO/ODPA/ODE mixture reached 250 °C, heating was turned off, and the solution of Se precursor was injected rapidly using a needled syringe. To make CdSe/CdS core/shell QDs, a CdSe/TOPS (Coordinated TOP and Sulfur) precursor was prepared as follows. 0.75 ml of TOP was combined with 0.032 g sulphur powder under inert atmosphere. This mixture was sonicated until a clear solution was formed. This precursor was added to 0.5 g of CdSe cores dispersed in 2 ml of TOP under argon. CdO, ODPA, Trioctylphosphine oxide (TOPO) and Steric Acid (SA) were degassed for an hour under vacuum and then heated to 320 °C. The CdSe/TOPS solution was rapidly injected into the Cd solution and was allowed to react for 7 minutes. The reaction was quenched by addition of methanol. To purify core or core/shell quantum dots, repeated extractions with equivolumes of

hexanes/methanol were performed. The purified QDs were finally stored in toluene at $+^{o}4$ C in the fridge until further use.

2.3.5. Preparation of glass substrates

Glass cover slips purchased from VWR with a thickness of 0.15 mm were used. Initially glass substrates were washed with Millipore water and dried for 2 hours in an oven. Piranha solution was prepared by combining 5 mL of 98 % H_2SO_4 and 5mL of H_2O_2 (50 % w/v). The washed glass slide was inserted into the freshly made solution of Piranha etch and left for 10minutes. After 10 minutes the glass slide was removed and dipped in pure Millipore water, then dipped in another clean Millipore water bath before finally rinsed with Millipore water. The slide was dried by heat gun and then sprayed with a polymer solution.

Sodium dodecylbenzenesulfonate (SDBS, 90 % Sigma Aldrich) glass slides were prepared in a similar way to above, with the inclusion of dipping the glass slide into a 1 % w/v solution of SDBS and water after cleaning and drying with a heat gun.

2.3.6. Preparation of Polymer/QD solution

PMMA was used without any further purification (99 % mw: 120,000) and dissolved in degassed toluene at w/v concentrations of 1 %, 2.5 %, 5 %, 7.5 % and 10 % by sonication. Solutions were sonicated in a sonic bath until the Toluene/PMMA solution was clear and homogeneous. Stock solutions of CdSe/CdS and CdSe/ZnSe quantum dots in toluene were added to the PMMA/Toluene solution to make a known concentration of Polymer/QD solution.

2.3.7. Preparation of hollow microspheres by spray drying

Glass substrates were placed on a clean flat surface and secured in place by masking tape. The evolution air gun was placed directly over the substrate at a fixed distance of 15 cm from the substrate. The evolution air gun was attached to a pressurised argon gas cylinder with constant pressure of 20 PSI. Nozzle aperture was adjusted by a screw at

the back of the gun, which was calibrated for 5 settings -1: closed, 2: 44 % of open aperture size, 3: 75 % of open aperture size, 4: 87 % of open aperture size, 5: Open (A = 0.1385 mm^2). Spraying for all samples was done at constant pressure and distance. Spray time for each sample was 500 ms. Samples were allowed dry for 5 minutes in atmosphere before sprayed again. 4 ml of a known concentration of polymer/QD solution was inserted into the airgun liquid holder.

Surface wetting of toluene droplets on glass slides were analysed using First Ten Angstrom 125 software and pictures were taken using a Cannon 5.5 mm telecentric lens with an APPR B/W camera.

2.4 Experimental details for Chapter 5

2.4.1 Actuator manufacturing and studies

The QD loaded strips were used to manufacture circular actuator samples, as follows. The QD loaded elastomeric film was stretched over a plastic ring of a 6.55 cm diameter. This provided the film with a biaxial pre-stretch of 3.43 times. Pre-stretching was necessary to allow the electrodes to radially expand upon electrical charging. Two circular concentric compliant electrodes were produced by smearing a carbon paste (CW7200, Chemtronics Circuit Works, USA) on either side of the film. Thin aluminium foil strips were then used as electrical contacts between the electrodes and the wires connecting the device to the power source.

Absorption spectra of the QD doped dielectric elastomer actuator were measured and compared to those of the pure elastomer film and the QDs in colloidal solution, using a Cary 50 UV-Vis spectrometer.

Photoluminescence (PL) spectra of the QD doped dielectric elastomer actuator were measured and compared to those of the pure elastomer film and the QDs in colloidal solution, using the instrumentation described below.

For colloidal QDs, a Perkin–Elmer LS 55 fluorescence spectrometer was used. For samples in the solid state, an Andor Samrock sr-303i imaging spectrograph coupled with an Andor Newton 970 EMCCD spectroscopy detector were used. A specific area of 80μmx80μm was used in the measurements.

Photoluminescence decays of the QD doped dielectric elastomer actuator were measured using time-correlated single-photon counting (time-Harp, PicoQuant). The sample was excited by using a 480 nm diode laser and was analysed with an Olympus IX71 inverted microscope over an area of 80 μm x 80 μm.

2.4.2 Preparation of stretchable transparent conductive electrodes by spray drying of PDOT:PSS onto VHB

A stock solution of PEDOT:PSS was diluted with Millipore water to a concentration of 1 mg/L. A 1 cm x 1 cm strip of VHB was prestretched over a PTFE ring of 6 cm in diameter and a circular mask was applied onto the top layer with an inside diameter of 4 cm. A heated substrate was set to 110 ^{o}C and the PTFE ring with VHB was placed onto it and allowed to heat for 10 minutes. An evolution paint airbrush was connected to a robotic arm that moved in a pre-programed pattern over the heated substrate. A set amount of PEDOT:PSS was sprayed onto the elastomer film (0.5 ml – 3 ml). The mask was then removed from the elastomer to give our PEDOT:PSS electrode on a VHB film. The electrode can be washed with methanol by simply rinsing the elastomer film in a beaker of methanol. After rinsing, the elastomer was dried quickly using a hair dryer to remove any residual solvent.

2.4.3 Fabrication of electrically tuneable lenses.

Tuneable lenses were made by making a dimple in an elastomer film using a plastic substrate with a hole and sucking the elastomer film into the dimple. Silicone gel was then placed into the cavity and another elastomer film placed on top to seal it (Fig. 2.1).

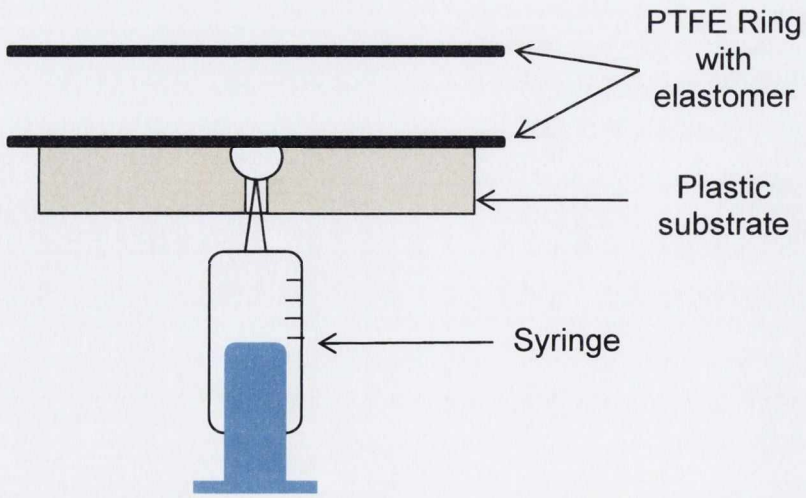

Fig. 2.1 Construction of elastomer lens using two elastomer films

2.4.4 Synthesis of CdTe/CdSe QDs

CdTe/CdSe QDs were made by a 1-pot hot injection synthesis. Initially a mixture of 0.0552 g of CdO (4.3×10^{-4} m), 1.5 ml of OA and 1.5 ml of TOP was prepared in a 100 ml round bottomed flask and then the mixture was heated at 250 °C until it turned clear. This solution was then cooled to 60 °C and a 0.6 M solution of TOPSe (0.0340 g of Se, 4.3×10^{-4} m in 0.7 ml of TOP, 1.6×10^{-3} m) was added. CdTe core QDs were synthesised by placing CdO (0.001 m), OA (0.004 m), TOPO (1 g) and HDA (3 g) into a round bottomed flask. The solution was degased for 1 hour under vacuum at 150 °C, then heated to 550 °C under argon where the solution turned clear, then cooled to 250 °C. TBPTe (5 ml, 0.1 M solution under argon) was then swiftly injected into the CdOA solution and allowed react for 2 minutes. The CdOA and TOPSe solution was then injected slowly over 10 minutes to form CdTe/CdSe core shell nanoparticles.

2.5 Characterisation techniques

2.5.1 UV-Vis absorption spectroscopy

A Cary 50 UV-Vis spectrometer and a Shimadzu UV-1601 UV - Visible Spectrophotometer were used to measure QD absorption. Most of the scans were carried out in the 300-800 nm range. Aggregation of QD particles can lead to scattering effects, resulting in higher absorbance values. Absorption spectroscopy measures the difference in the incident light and the transmitted light as it passes through a sample. When an atom or molecule absorbs energy, it promotes an electron from its ground state to an excited state. Energy can only be absorbed in discrete levels, which correspond to the difference in the ground and excited states according to the equation:

$$E = h\nu = \frac{hc}{\lambda} \qquad (2.1)$$

Where E is the energy, h is planks constant, ν is the frequency, c is the speed of light and λ is the corresponding wavelength. Rotational and vibrational absorbance can also occur for molecules, adding to the electronic absorption profile. Uv-Vis spectroscopy is mostly concerned with electronic transitions however, where the number of possible transitions include σ- σ^* (σ bonding to antibonding orbital), n- σ^*(saturated compounds with lone pairs- nonbonding electrons) and n-π^* transitions (n or π electrons to the π^*

excited state). Solvent absorption may also affect the end spectra, with n-π* transitions blue shifting, or red shifting for π-π* transitions with increasing solvent polarity due to solvation of the lone pair. Concentration may also be determined by absorbance spectroscopy by using the semi-empirical Beer Lambert Law:

$$A = \varepsilon bc \qquad (2.2)$$

Where A is the absorbance, ε is the constant of proportionality, b is the path length and c is the concentration. Concentration of QD solutions was done using a method developed by Peng et al using the first absorption peak to determine the size of the QD and another empirical function to determine the extinction coefficient to fit into (2.2)[4].

A Xenon Flash lamp is used as the UV-Vis light source in the Cary 50. The light may pass through a beam splitter to eliminate wavelength shift errors associated with traditional scanning methods. Schwartzwald collection mirrors collect the light from the Xenon lamp and focus it through a lens onto the excitation entry slit. The light passes through a monochrometer, then into the sample, with the remaining light being collected by a photomultiplier (2 silicone diode detectors) which give the intensity (Fig. 2.2).

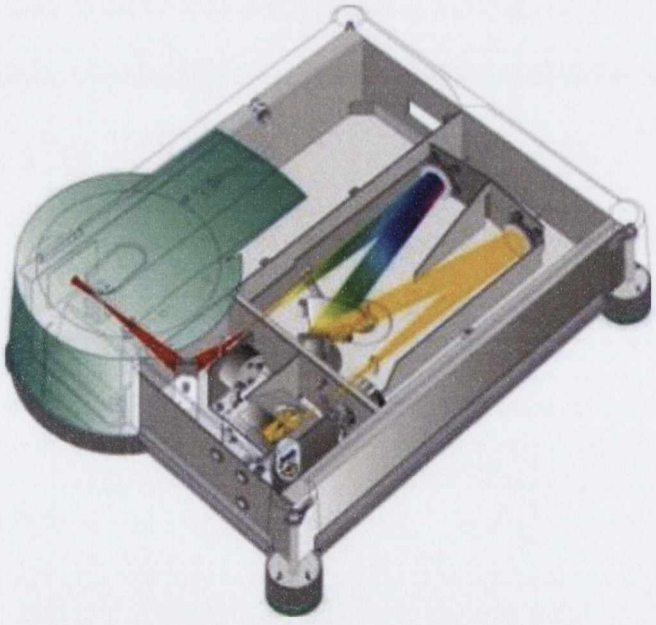

Fig. 2.2 Optics diagram of Cary 50 UV-Vis spectrometer[5].

2.5.2 PL spectroscopy

For PL studies of colloidal QDs, a Perkin–Elmer LS 55 and a Varian - Cary Eclipse fluorescence spectrometers were used with a 1cm x1cm quartz cuvette for the sample.

The excitation wavelength depends on particle size, and therefore the excitation was usually performed close to the band edge absorption of the particle. The emission was detected in the range 400-750 nm. The Quantum Yields (QY) were calculated from equation 2.3, using the area under the PL spectra, using Rhodamine 6G dye as a reference.

After excitation, the electron may lose some of its extra vibrational energy through intersystem crossing and collisions with other molecules. This is due to the electron having excess energy above its lowest excited state. After is decays to its lowest excited state, fluorescence may occur (Fig. 2.3). Tyndall scattering may affect the resultant spectra of a sample, where the incident light is scattered instead of to be absorbed by the sample and incorrectly interpreted as fluorescence.

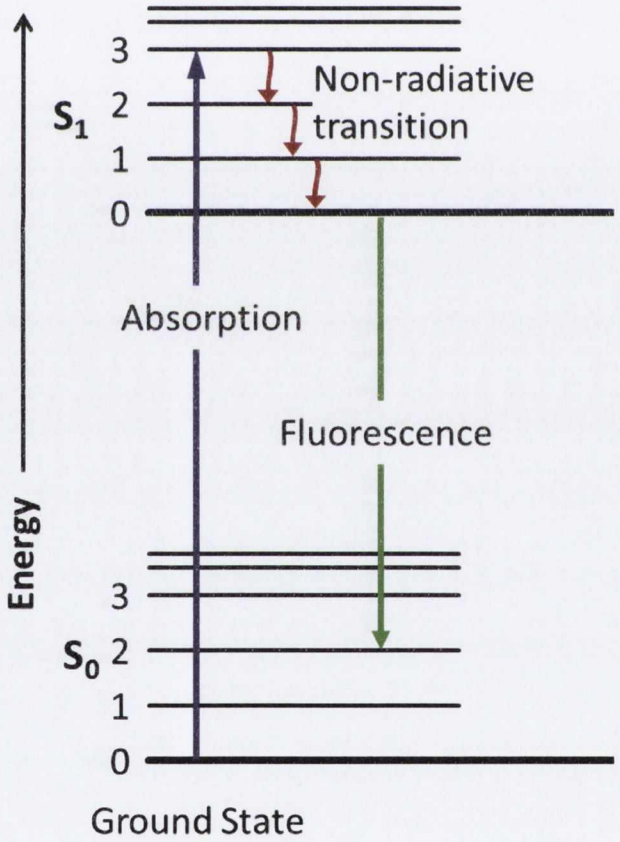

Fig. 2.3 Jablonski Diagram of an excited electron decaying through non-radiative transitions to its lowest excited energy state and then undergoing Fluorescence [6]

A Xenon flash lamp was used as an excitation source, with the light focused using Schwatzchild mirrors, focused with a lens and passed through a monochromator into the

sample (Fig. 2.4). An R928 PMT photomultiplier detector acts as the reference photomultiplier to provide a repeatable amount of illumination for the sample. The beam finally passes through an emission monochromator and into a photomultiplier to give a current signal.

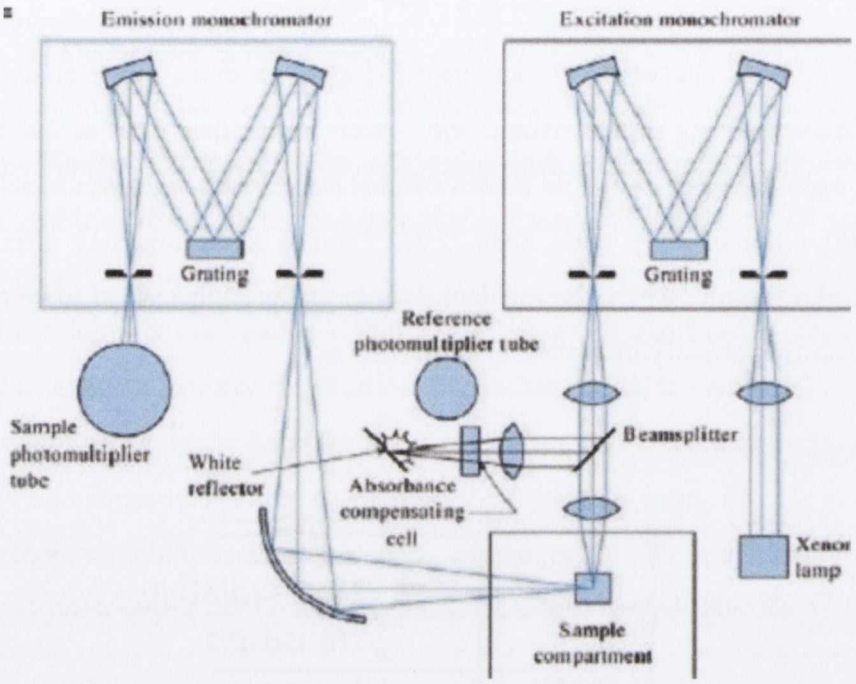

Fig. 2.4 General setup of a Florescence Spectrometer[7]

Samples were excited at a wavelength closest to their corresponding first exciton peak in their absorption spectra. When this was not possible, the wavelength selected was set at 350 nm, going up to 500 nm in 50 nm intervals to find the highest corresponding emission intensity of the sample. PLQYs were calculated using either Rhodamine 6G, suforhodamine 101 or Coumarin 153 dye as standard references. These dyes were used as their absorption and emission profiles closely resemble that of the QDs being measured. The absorption and emission profiles of these dyes in water were recorded (having a PLQY of 0.93 and 0.53 respectively) and excited at wavelengths between 450 nm and 600 nm. QD solutions were diluted so that their absorption band of the QD intersected that of the dye. This intersection point was used as the excitation wavelength of both the dye and the QD. The integrated area under the graph of the emission profiles of both the dye and the QD was inserted into (3) to calculate the QDs PLQY[4,8]:

$$QY_{QD} = \frac{\eta_S}{\eta_d}\frac{I_S}{I_d} \times QY_{DYE} \times 100 \qquad (2.3)$$

Where η_s is the sample refractive index, η_d is the dye refractive index, I_s is the integration value of the sample, and I_d is the integration value of the dye. Refractive index of solvents were taken from The CRC Handbook of Physics and Chemistry[9].

2.5.3 Steady state PL spectroscopy

Steady state PL of the polymer microspheres was measured using a Reinshaw micro-Raman setup, exciting the spheres with a 488 nm laser. An Olympus FV 1000 point-scanning confocal microscope with a multiline argon (453/488/515 nm) laser and 405, 543 and 633 nm diode lasers were used for the steady state PL studies.

Initially to perform steady state PL spectroscopy it is necessary to focus the microscope onto a sample, which is usually dried onto a glass slide. Before measurements begin, the instrument must be calibrated using a Si (100) wafer, with the peak centred at 514 nm. Emission signals are collected through a CCD detector (Fig. 2.5). Collection time was set to 10 s, with laser power varying from 0.1 % to 100 % depending on the PLQY of the sample, with collection centred on the PL maximum of the sample.

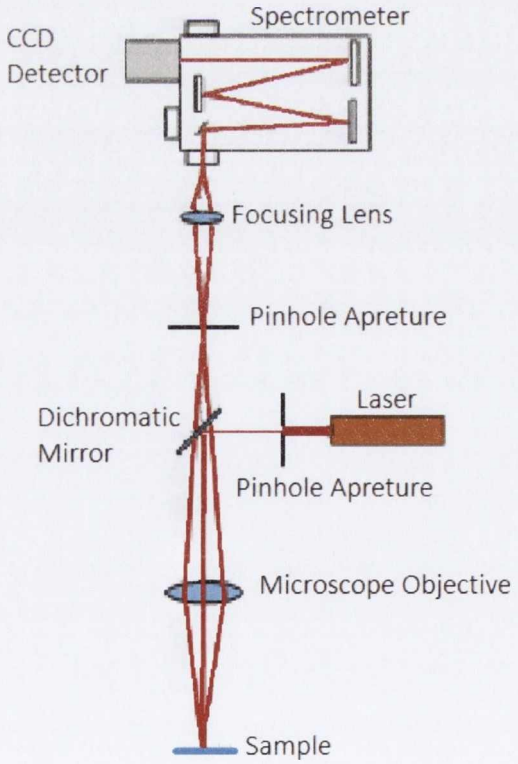

Fig. 2.5 Setup of Renishaw micro-Raman optics, adopted from

2.5.4 Photoluminescent lifetime measurements and time Correlated Single Photon Counting

Photoluminescence decays of the QD loaded microspheres were measured using time-correlated single-photon counting (time-Harp, PicoQuant). The sample was excited by using a 480 nm diode laser and was analysed with an Olympus IX71 inverted microscope over an area of 80 μm x 80 μm.

Photoluminescence lifetimes measurements were also performed using a time correlated single photon counting (TCSPC) spectrometer (Fluorolog 3 Horiba Jobin Yvon) and different semiconducting diode lasers (370 nm, 425 nm "Nanoled" – Horbia Jobin Yvon) with pulse duration shorter than 1ns for excitation.

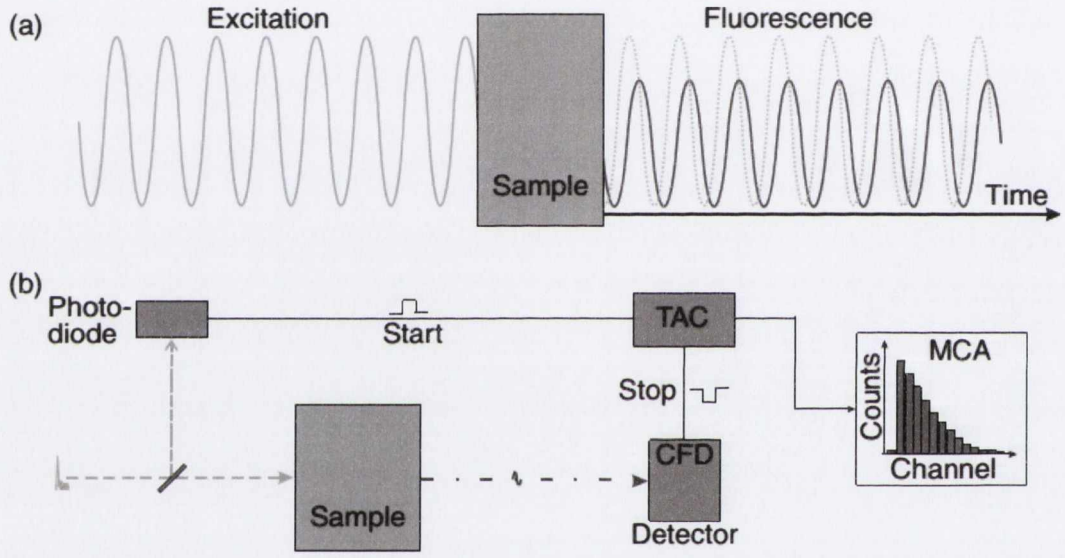

Fig. 2.6. The principle of phase modulation (a) and time correlated single photon counting (TCSPC) (b) for the measurement of fluorescent decays.[10]

With TCSPC (Fluorolog 3 Horiba Jobin Yvon) the excitation light pulse is split such that a photodiode is triggered at the same time that the sample is excited. When the first fluorescence photon is detected by an avalanche photodiode (APD) the time lag measured between the time when the sample is excited and when the first photon is collected. This experiment is repeated several times and the start/stop time lags are plotted as a histogram to chart the fluorescence decay (Fig. 2.6).

The phase modulation method allows to excite the sample with light which intensity is modulated sinusoidally. The forced fluorescence emission of the sample directly follows the excitation modulation. Because of the finite fluorescence lifetime, emission

modulation is delayed in phase by an angle relative to the excitation. In addition, fluorescence emission is demodulated due to the fact the fluorescence quantum yield of common samples if the forced ϕ_f is less than 100 %. Thus, fluorescence lifetime information can be extracted from both the degree of demodulation and the phase angle.

2.5.5 Fluorescent and Confocal microscopy

Confocal microscopy is an optical imaging technique which, by opposition to conventional optical microscopy, provides an image of the focal plane only and eliminates out of focus light from the rest of the sample. It achieves this by use of point illumination by laser source and a pinhole in an optically conjugated focal plane close to the detector to eliminate out of focus signal. An Olympus FV1000 Point-scanning Confocal Microscope equipped with a multiline argon (453/488/515 nm) laser was used in our studies.

Bright field and fluorescent confocal images were also obtained using an Olympus 51M fluorescent microscope, using a 350 nm light source for fluorescent imaging. Images were taken with a microscope objective of 10 x, 50 x and 150 x.

2.5.6 Transmission Electron Microscopy (TEM)

Transmission Electron Microscopy is an imaging technique that uses high a high energy electron beam to image samples at high resolutions. A field emission gun (FEG), such as tungsten FEG is placed under vacuum and a positive potential applied. Briefly, the electron beam is accelerated down the TEM column, and focused using condenser lenses onto a sample (Fig. 2.7). The electrons can interact with the sample, and detectors can use backscattered electrons as well as electrons that interact and pass through the sample to form an image. The electron beam, once past the sample, travels through a projector lens, undergoes a Fourier transform and finally interacts with a fluorescent screen and can be imaged using a CCD camera.

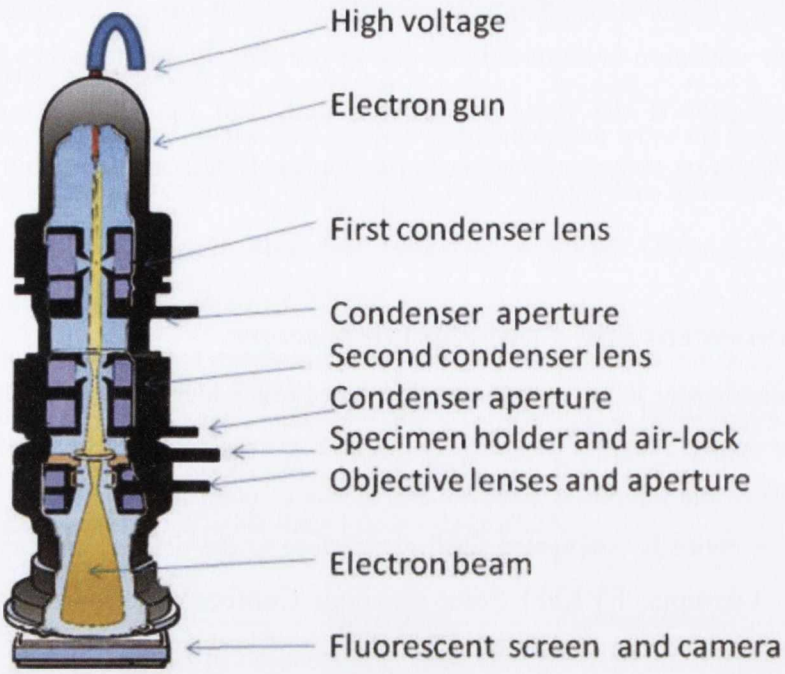

Fig. 2.7 TEM column showing the main components including the condenser lenses, objective aperture, objective lens and projection lens.[11]

A Jeol 2100 Transmission Electron Microscope (TEM) and a FEI TITAN Microscope were used to image all nanoparticles at 200 kV. Sizes of nanoparticles were calculated using ImageJ software. Samples were prepared by drop casting the particles onto lacey carbon grids and left to dry overnight.

2.5.7 Scanning Electron Microscopy (SEM)

SEM has similar principles to TEM, except is operates at lower electron voltages and images samples mainly by backscattered electrons. Because of the lower operating voltage, SEM has a lower resolution than TEM, and samples need to be conductive and grounded to avoid charge accumulation on the surface while imaging.

Field emission scanning electron microscopy (SEM) studies were performed using a Tescan Mira Variable Pressure Field emission SEM, which operated at 5.0 kV on gold coated surfaces. Further measurments were performed using a Hitachi s-4300, which operated at 5.0 kV, on gold coated surfaces and a Zeiss Auriga - Focused Ion Beam (FIB) with Cobra ion column.

2.5.8 Thermogravimetric Analysis

Thermogravimetric analysis (TGA) involves the measurements of the changes in the mass of a substance as a function of temperature. In order to determine mass changes in the sample we use a thermobalance which combine a microbalance with a furnace and temperature programmer. Small samples are preferred for TGA, as large masses can lead to non-homogeneous heating throughout the sample. The signal output, or TGA trace, may be electronically differentiated to give a derivative thermogravimetric (DTG) curve.

To perform the TGA studies the sample is normally placed in a ceramic holder and then the holder is placed into the TGA set up, where the weight of the boat is subtracted from the overall weight to give the weight of the sample. Usually the sample needs to be between 5-10 mg to reduce errors in weighing of the sample. The ceramic boat, connected to the precision balance is placed inside the furnace and is heated or cooled during the experiment. A flow of air or an inert gas controls the environment while heating. The mass of the sample is monitored as a function of temperature or time. These instruments can quantify loss of water, loss of solvent, loss of plasticizer, decarboxylation, pyrolysis, oxidation, thermal decomposition, weight % filler, amount of metallic catalytic residue remaining on carbon nanotubes, and weight % ash.

In our work TGA measurements were performed on QD loaded and pure samples to determine the percentage of QDs incorporated into the elastomer. In our work the measurements were carried out under nitrogen using a Perkin Elmer Pyris 1 TGA (Fig. 2.8) analyser with a temperature scan rate of 5 °C per minute.

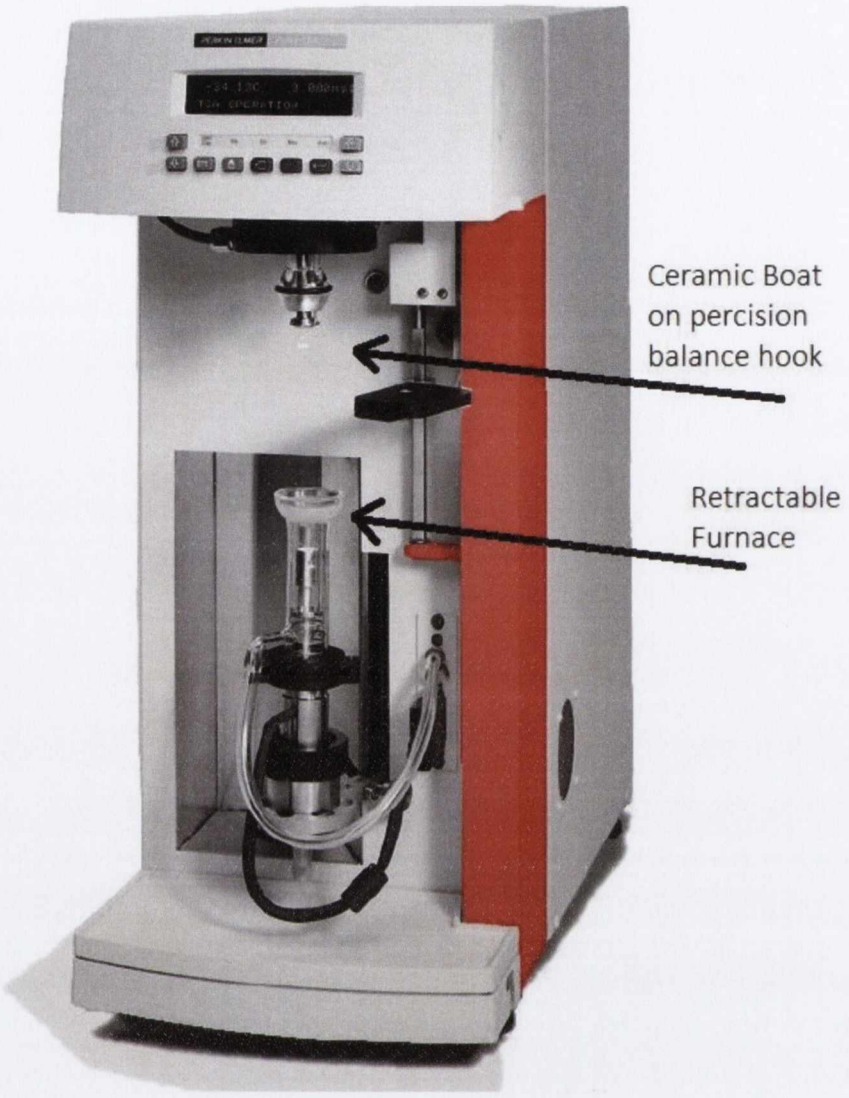

Fig. 2.8 Image of a typical TGA machine, highlighting the ceramic boat and retractable furnace[12]

2.5.9 X-Ray Diffraction

X-ray diffraction (XRD) involves the interaction of X-ray radiation with a wavelength (λ) of approximately 0.1 nm, with the atoms in the solid. Because the distances between the atoms in a crystal structure are comparable with the wavelength of the incoming radiation, crystals can diffract X-rays. The variation in the resulting intensities is caused by regions of constructive and destructive interference called a diffraction pattern. Depending on the interference conditions, each atom plane produces a series of

n reflections. From the patterns obtained, the interlayer spaces (dhkl) can be calculated using the Bragg equation below

$$\sin\theta = \frac{n\lambda}{2d} \quad \text{or} \quad n\lambda = 2d\sin\theta \qquad (2.4)$$

describes the diffraction of x-rays by a crystal as reflection from the net planes. θ is the glancing plane (2 θ is the diffraction angle) and d is the net plane spacing.

The x-ray diffraction pattern obtained is a plot of diffracted x-ray intensity against diffraction angle. The diffraction intensity is a function of the unit cell contents while the diffraction angle is function of the unit cell dimensions. The outcome of this is that identical unit cells with the same contents give the same diffraction pattern, i.e. each compound has its own set of characteristic d values and intensities which can be used for identification. Therefore, the diffraction pattern is like a fingerprint of the specimen. This fingerprint may exhibit slight changes between samples, however. The half widths of the reflections are inversely proportional to the crystallite sizes and directly proportional to the concentration and magnitude of structural defects. The cell constants, crystal system and space group of the specimen may be determined from the powder diffraction pattern. For a cubic crystal system,

$$\frac{1}{d^2} = \frac{h^2 + k^2 + l^2}{a^2} \qquad (2.5)$$

where a is a cell constant. From squaring the Bragg equation,

$$\sin^2\theta = \frac{\lambda^2}{4d^2} \qquad (2.6)$$

it may be taken that

$$\sin^2\theta = \frac{\lambda^2}{4a^2}(h^2 + k^2 + l^2) \qquad (2.7)$$

If cell constants have been worked out, all reflections can then be indexed. For X-rays, the crystallite size does not begin to affect the diffraction pattern until the crystallites

(or, more precisely, the coherent scattering domains) become smaller than 0.5 μm. Scherrer, in 1918, derived an equation to describe the broadening of a reflection in terms of the crystallite size:

$$D = \frac{K\lambda}{B\cos\theta} \qquad (2.8)$$

where D is the crystallite size, K is a constant (taken as 0.9), λ is the wavelength of the radiation employed (for all measurements in this thesis, λ = 1.5406 Å) and B is the line broadening. This broadening is measured from the increased peak width at half peak height, obtained from the Warren formula:

$$B = \sqrt{B_m^2 + B_s^2} \qquad (2.9)$$

where B_m is the measured peak width at half height and B_s is the standard peak width at half height obtained from a commercial sample. It should be noted that the error of determination is 20-30 %. For this reason, sizes determined from XRD will differ slightly from electron microscopy size analyses.

In order to produce an XRD pattern a monochromatic beam of X-rays is required. This is produced by hitting an anode of a pure sample of a particular metal with high energy electrons in a sealed vacuum tube. Once a pure metal is used, the wavelength of the X-ray beam produced may be known. Copper is the most commonly used metal for this purpose and the strongest wavelength produced is 1.5406 Å. The main aim of XRD analysis is to identify the crystalline phases present in the sample. The phases can be identified by comparison of the sample data (peaks and relative intensities) with a set of standard references provided by the Joint Committee on Powder Diffraction Standards (JCPDS) database.

X-ray analysis generally deals with crystalline matter, either single crystals or crystalline powders. A lattice is a repeating structure of points in space and the lattice constant refers to the distance between unit cells in a crystal lattice. Three dimensional lattices generally have three lattice constants, referred to as a, b and c. In the case of cubic crystal structures, all of the constants are equal and are only referred to as a.

A Phillips PW1710 Powder X-ray diffractometer (XRD) was used for qualitative phase identification of our nanoparticulate samples. Samples were prepared by placing our nanoparticles in a non-solvent solution and centrifuging for 10 minutes at 4,000 rpm. The excess solvent was decanted off and the sample was then allowed dry, then applied to a glass slide using silicone grease for analysis. XRD scans were taken over a 12 hour period starting at θ = 10and stopping at θ = 90.

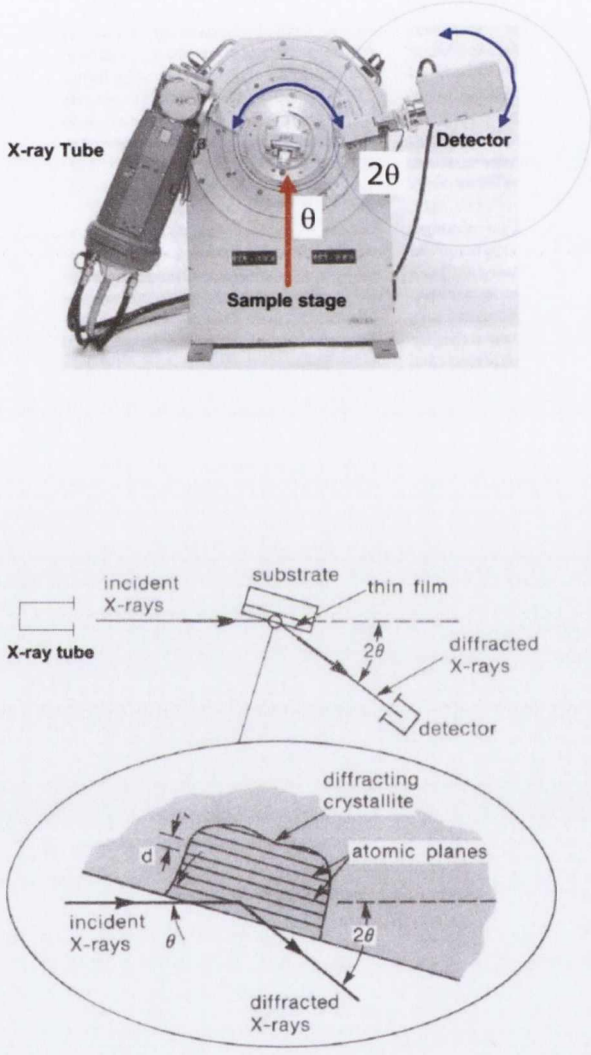

Fig. 2.9 A typical setup of an automated X-Ray Diffractometer (top) and how Braggs Law works on a crystalline substance (bottom)[13]

2.5.10 Mechanical testing

In a tensile test, a sample is extended at constant rate, and the load needed to maintain this is measured. The stress (ε) (calculated from the load) and strain (σ) (calculated from the extension) can either be plotted as nominal stress against nominal strain, or as true stress against true strain. The graphs in each case will be different[14]:

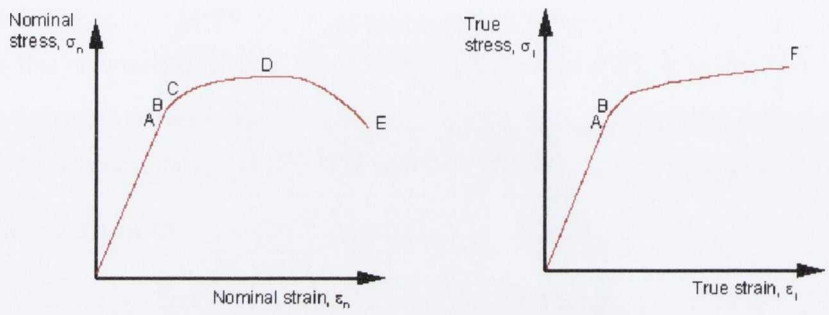

Fig. 2.10 Graphs illustrating the difference between nominal stress and strain and true stress and strain[14].

There are two main types of strain: elastic strain and plastic strain. Elastic strain is the stretching of atomic bonds, and is reversible. Elastic strain can be related to the stress by Hooke's law:

$$\sigma = E\varepsilon \qquad (2.10)$$

where E is the Young's modulus. For testing of our VHB acrylic elastomer, samples were cut into strips of 1 cm in width and 3.5 cm in length then clamped into the tensile tester on either end. Tensile test measurements were carried out using a Zwick Z100 tensile tester, with a cross head speed of 10 mm min^{-1}. The samples were pulled apart until the strip was broken, with the changing force being automatically recorded. From the stress/strain curve the ultimate tensile strength can also be measure, which is the point at which plastic deformation becomes unstable and a narrow region forms in the specimen.

References

(1) Washington Ii, A. L.; Strouse, G. F. *Journal of the American Chemical Society* **2008**, *130*, 8916.
(2) Klein, S.; Manoharan, V.; Pine, D.; Lange, F. *Colloid and Polymer Science* **2003**, *282*, 7.
(3) Talapin, D. V.; Mekis, I.; Götzinger, S.; Kornowski, A.; Benson, O.; Weller, H. *The Journal of Physical Chemistry B* **2004**, *108*, 18826.
(4) Yu, W. W.; Qu, L.; Guo, W.; Peng, X. *Chemistry of Materials* **2003**, *15*, 2854.
(5) University, K. C. http://www.kutztown.edu/acad/chem/instruments_html/uv_vis_absorbance.htm, 2012.
(6) Jacobkhed *http://en.wikipedia.org/wiki/File:Jablonski_Diagram_of_Fluorescence_Only.png#filehistory* **2012**.
(7) Skoog, D. L., JJ *Fort Worth* **1992**.
(8) Grabolle, M.; Spieles, M.; Lesnyak, V.; Gaponik, N.; Eychmüller, A.; Resch-Genger, U. *Analytical Chemistry* **2009**, *81*, 6285.
(9) Lide, D. R. *CRC Handbook of physics and chemistry*; The Chemical Rubber Company, 2001.
(10) Markus Sauer, J. H., Jörg Enderlein *Wiley* **2010**, 4.
(11) *http://3dsciencepics.com/latest-transmission-electron-microscope-diagram/*.
(12) Holodiag *http://www.holodiag.com/tga.php*.
(13) Diffraction, X.-R. *http://web.pdx.edu/~pmoeck/phy381/Topic5a-XRD.pdf*.
(14) Cambridge, U. o. *Inroduction to mechanical testing* **2012**, *http://www.doitpoms.ac.uk/tlplib/mechanical-testing/theory1.php*.

Chapter 3: Development and investigation of new QD nanostructures

3.1. Introduction

Quantum dots have been studied intensely over the past 20 years due to their unique photophysical properties, relative ease of synthesis and surface functionalization. Because of these properties QDs have become a versatile material for applications in biomedical research, electronics, sensing and photonics. However, fundamental studies are still required to completely understand the mechanisms of growth in semiconducting QD systems, their optical properties and how they change with morphology and when in contact with other nanoparticles, their effects of doping in materials, the toxicity of QDs in cells and their stability and effect on the environment.

The synthesis of QDs is constantly being refined and improved to create complex core-shell QDs with better stability, unique anisotropic structures that have different photonic applications than that of the typical spherical QD, faster reaction times with narrower size distributions and less environmental impact and non-blinking QDs for uses in biomedical and information technology.

The main aim of this part of my work is to develop new synthetic approaches for QDs using microwave heating, create stable core-shell QDs with high PLQY, explore ternary core QDs as non-blinking PL emitters and quantum dot-rod nanostructures and investigate their photophysical properties.

3.2- Synthesis and Characterisation of CdSe Quantum Dots

3.2.1 Microwave Synthesis and characterisation of CdSe QDs

Using my CEM 6 star microwave system I performed synthesis and optimisation of the conditions for nanocrystal growth, focusing on size control, narrow size distribution and high PLQYs of CdSe and CdSeZn ternary core QDs. The preparation process involved an addition of CdO along with an alkene (ODE), with capping ligands TOPO and HDA into a Pyrex reaction vessel along with TOPSe under argon (Fig. 3.1). Microwave times were varied to control the growth and size of the QDs.

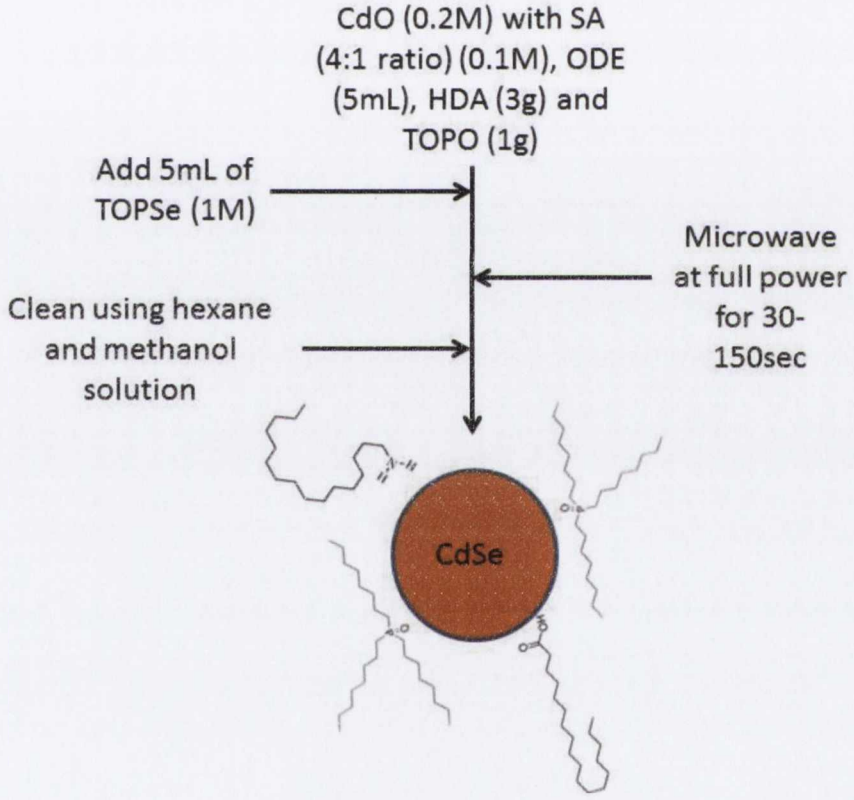

Fig. 3.1. Schematic presentation of CdSe synthesis by microwave heating.

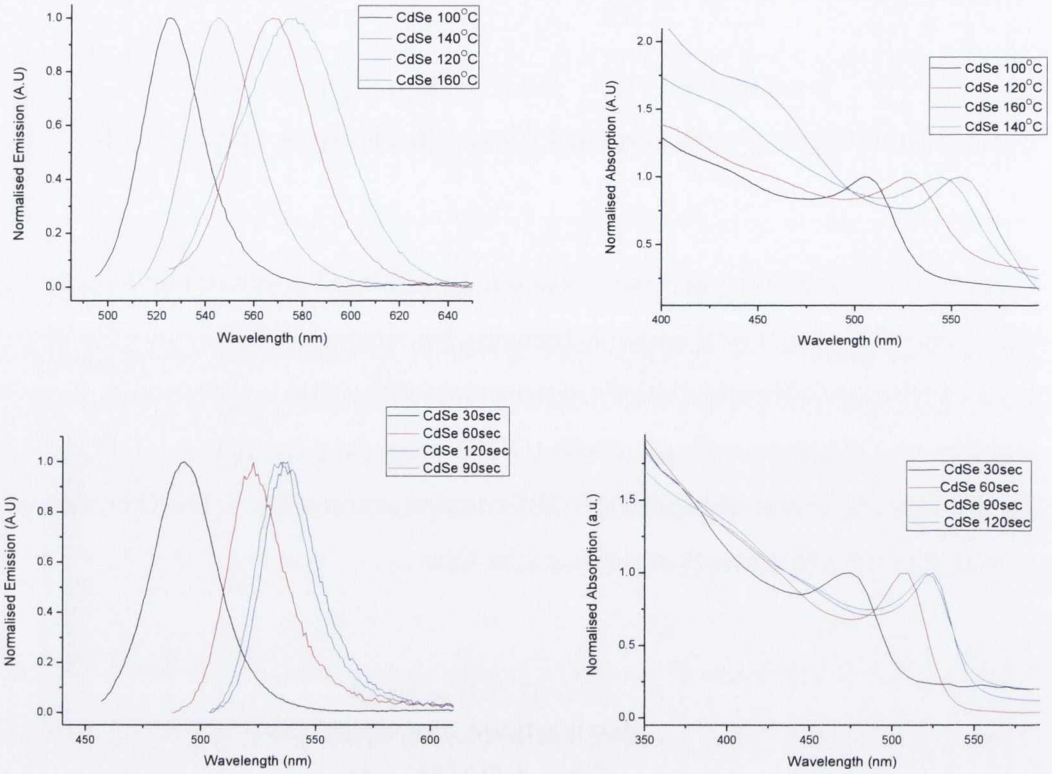

Fig. 3.2. Normalised absorbance and emission spectra for CdSe QDs with respect to emission max and the first absorption peak max. CdSe QDs were synthesised at different reaction temperatures (top) and for different times at 150 °C (bottom). Shifting of the absorbance band edge and emission spectra is due to an increase in QD size.

Photoluminescence and absorption spectra were recorded for CdSe QDs which were synthesised at different temperatures and reaction times. Samples were excited at wavelengths corresponding to their first absorption peak unless otherwise stated. Emission spectra were normalised with respect to their emission max and absorption spectra with respect to their first exciton peak to highlight the red shift of the spectra. Fig 3.2, bottom, shows that with increased reaction time at a reaction temperature of 150 °C, the absorption and emission spectra are red shifted, indicating nanocrystal growth as expected. Nanocrystal growth slows down significantly after 90 seconds as cadmium and selenium precursors completely reacted and are used up. The narrowing of the emission spectra is due a nanoparticle focusing regime as described in chapter 1, page 8. Increasing the reaction temperature and keeping the time constant at 120 s, I see a defocusing regime (Fig. 3.2, top). Ostwald ripening results in the broadening of absorption band edge of the

QDs and wider FWHM in the emission spectra. At higher temperature the emission peaks broaden quickly, with a FWHM of 28 nm at for a reaction at100 ^{o}C for 120 s to 50 nm for a reaction at 160 ^{o}C (Fig 3.2, top). It is thought that nucleation of the QDs begins purely from the selenium precursor, which has a polarisability value of 2.77 x 10^{-24} cm^3, compared to that of octadcane at 36.43 x 10^{-24} cm^{31}. This can lead to hot spots in the reaction, resulting in non-uniform heating. As the temperature increases, more nucleation points become available due to the increase in energy and competing processes start, leading to Ostwald ripening in the sample.

The PLQY of each sample was calculated using the method outlined in section, 2.5.2, and was found to increase with higher reaction temperature, up to 140 ^{o}C. An increase in reaction temperature allows the organic ligand to be distributed more freely onto the QD surface, increasing the surface coverage and hence the PLQY. After 140 ^{o}C however, PLQY drops. This may be due to the larger crystals developing more defects in the crystal lattice due to the slow, low temperature crystal growth, and poor surface coverage of ligands over the larger surface area.

Fluorescent lifetime measurements were carried out on all QD samples using TCSPC (Table 1). The exponential decay was fitted using a biexponential decay curve, giving us a long and short lifetime for each QD. The short lifetime is thought to be due to direct recombination of electron and hole, with little or no interaction with defects in the crystal or ligand on the surface[2,3]. The longer lifetime is due to the interaction of the exciton with defects in the crystal and binding ligand, which can create both deep and shallow energy traps that prolong the rate of decay back to the ground state. It was found that with increasing PLQY the longer lifetime contribution decreases slightly. This was thought to be due to better surface coverage of the QD by the capping ligands. By eliminating deep traps on the surface, there is less interaction of the exciton with these energy wells, leading to increased radiative recombination. The deep traps are not entirely eliminated however, and the exciton may still interact with them, resulting in a longer lifetime and decreased PLQY.

Table 3.1. Lifetime data of some of the CdSe QDs. X^2 is the fitting parameter of the biexponential, τ_1/ τ_2 is the first/second lifetime, β_1/ β_2 is the relative amount, and Φ is the PLQY.

SAMPLE	X^2	$\tau_{1(ns)}$	$\beta_{1(\%)}$	$\tau_{2(ns)}$	$\beta_{2(\%)}$	Φ (%)
150^0C 60s	1.03	13. ±2	21.86±2	45.±4	78.14±4	5.35
150^0C 120s	1.12	14. ±2	28.67±2	46.±4	71.33±3	9.84
80^0C 120s	1.06	14. ±2	24.70±2	43.±4	75.30±3	6.27
160^0C 120s	1.01	13.±2	18.28±2	43. ±4	80.72±4	10.79

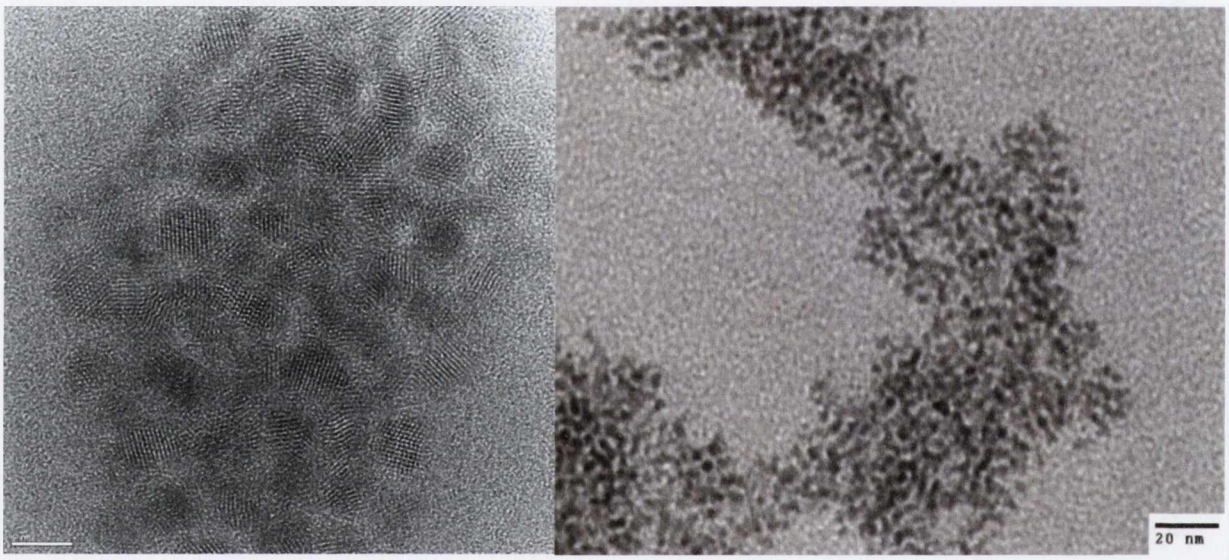

Fig 3.3. TEM images of CdSe QDs synthesised at 150 ^{0}C for 60 seconds (left) and 120 seconds (right). The lattice spacing of the CdSe QDs was found to be 4.4 Å.

TEM images of the CdSe QDs were obtained for each sample. Samples showed a size distribution of 4.6±0.32 nm and 5.1±0.81 nm for QDs synthesised at for 60 seconds and 120 seconds respectively. This was in agreement with the broadening of the emission spectra of the QDs. The nanocrystal samples were found to be quite uniform and spherical in shape. The lattice spacing of the HRTEM showed the CdSe nanocrystals have a lattice spacing of 4.4±0.2 Å, which corresponds to a crystal structure of wurtize CdSe[1]. My first TEM images were of QDs drop cast onto Formvar coated Cu TEM grids. The QDs had to be drop cast onto the TEM grids in an aqueous media, as organic solvents dissolve the formvar coating. This leads to the QDs coagulating in solution due to the hydrophobic

stabilising ligands, resulting in aggregates of QDs on the TEM grids (Fig. 3.3, right). This made it difficult to image individual QDs.

It was found that by fitting an equation developed by Yu et al[4] to my UV-Vis first absorption peaks and comparing it to the TEM images of the QDs that the formula did not take into account the strong binding effect of the capping ligands. This resulted in an error of +/-0.5 nm in this equation, which was subsequently adjusted for. For example, the diameter of CdSe is given as:

$$D = (1.6122\text{x}10^{-9})\lambda^4-(2.6575\text{x}10^{-6})\lambda^3+(1.6242\text{x}10^{-3})\lambda^2-(0.4277)\lambda+(41.57) \quad (1)$$

So for a QD with a first band edge exciton at λ = 500 nm, this would give D = 2.345 nm, a value lower than what I measure in TEM. I adjusted these formulas coefficients to get a better fit with accordance to my TEM results. This was done by adjusting the last coefficient to 38.90. Using this modified formula, and comparing my results to TEM images, we found that the modified formula had an error of +/-0.27 nm.

3.2.2 Synthesis and characterisation of CdSe/ZnSe and CdZnSe QDs

One of my goals was the development of non-blinking QDs. Therefore I have selected CdZnSe alloy as the core material for non-blinking QDs. Previously Wang et al have made ternary core QDs using highly reactive and dangerous metal organic Zn and Cd precursors in a multi-pot synthesis[5]. For my work I choose air-stable and safer Cd and Zn precursors in the form of ZnSA and CdSA (Fig. 3.4). Experiments were conducted to make a CdSeZn alloyed core using increasing Cd/Zn ratios (Fig. 3.5, left). However, an attempt of making ZnSe QDs was unsuccessful, due to the low reactivity of the ZnSA precursor.

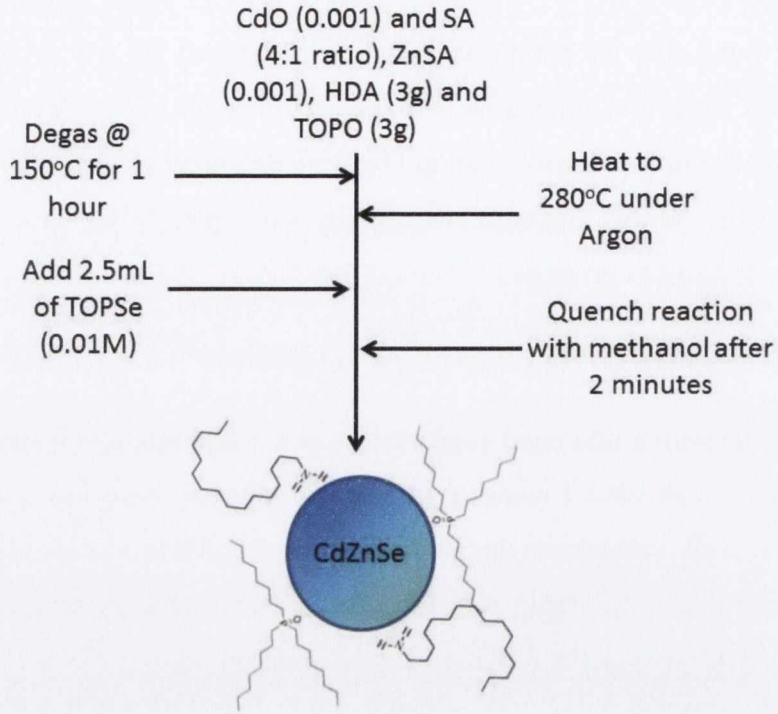

Fig. 3.4. Schematic diagram for the synthesis of CdZnSe QDs by microwave heating.

As seen in Fig 3.5, the QDs with the most defined band edge and highest PLQY contained a higher ratio of Cd to Zn precursor. These results indicate that the CdSe QDs are formed first in the reaction, acting as a seed for a ZnSe shell.

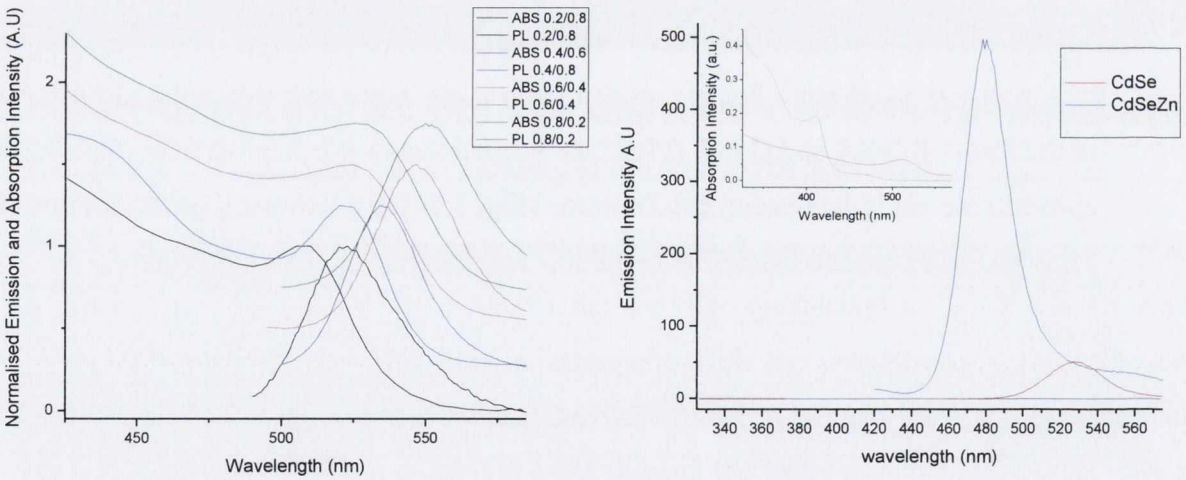

Fig 3.5. Emission and Absorbance spectra for CdSe QDs synthesised with varying ratios of zinc and cadmium stearate (left), and CdSe with CdSeZn alloyed QDs (right), absorption spectra inset.

Because of the low reactivity of the ZnSA it was decided to use ligands with a lower binding energy, so the ZnSA would need less energy to displace the strong binding such as

TOPO ligands which are attached to the surface. My procedure was modified by replacing HDA with ODA and taking TOPO out of the reaction. CdSe cores were prepared first, by microwaving at 150 ^{o}C for 120 seconds. These dots were purified by co-precipitation and washing with methanol and ethanol and then redispersed in octadecane. Excess of ZnSA and TOPSe was added into the reaction flask, along with ODA and the CdSe core dots. These were microwaved at full power for 6 minutes to ensure full alloying of the QDs. The resultant nanocrystals displayed a blue shift of 40nm, indicating a successful alloying of the QDs (Fig 3.5, right). The blue shift is due to the higher band gap energy of ZnSe, which is 2.7 eV compared to 1.73 eV for CdSe. An increased PLQY, from 21.1 % to 58.37 % indicated that not only has the CdSe core been alloyed, but that also some ZnSe shell formed and effectively passivated the surface, eliminating surface traps.

TCSPC was performed for each of the four samples. It was found that the lifetimes corresponded well for pure CdSe core QDs, with the lifetimes of the QDs with higher cadmium ratios being reduced slightly (Fig. 3.6). This may be due to some alloying effect between the CdSe core and ZnSe shell, producing more efficient relaxation pathways for the exciton to decay. Again, I see for the QDs of higher PLQY, the longer lifetime has a larger contribution. As seen before the CdSe QD core was fitted using a biexponential function, giving a long and short lived lifetime as expected. The ternary core however gave faster lifetimes of 3.71 ns and 10.83 ns compared to that of the CdSe core. This was previously reported by Wang et al after they observed similar results with ternary core QDs[5]. It was proposed that as the nanocrystal becomes excited, and electron may be trapped at the surface of the quantum dot and prevented from recombining with its hole, resulting in a charged nanocrystal. In this state, other excitons will recombine non-radiatively, effectively turning the nanocrystal "off". In an alloyed QD however, once the nanocrystal becomes charged another exciton may recombine with the spare hole left by the trapped electron. Since the two holes must have opposite spin as dictated by the quantum mechanics, the electron my recombine with greater efficiency, thus resulting in a shorter lifetime.

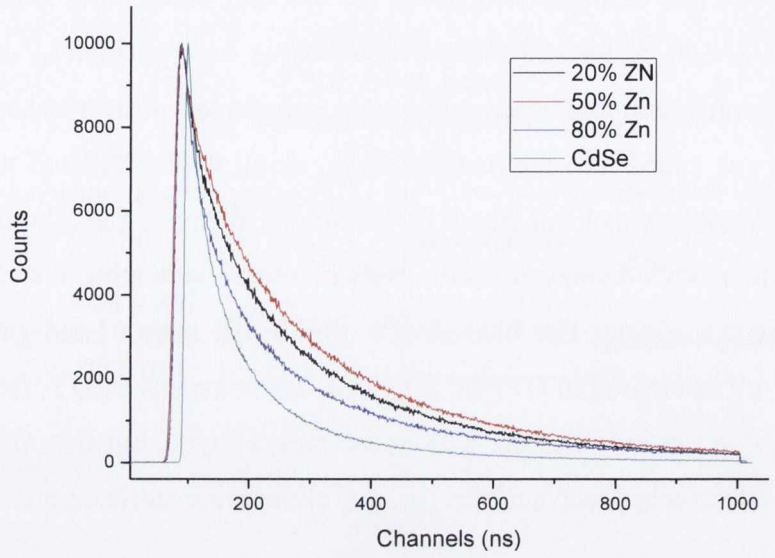

Fig. 3.6 Lifetime curves for CdSe and CdZnSe alloyed QDs.

Table 3.2. TCSPC lifetimes of CdSe QDs synthesised with varying Zn/Cd ratios, CdSe core and CdSeZn ternary core QDs.

SAMPLE	X^2	τ_1 (ns)	β_1 (%)	τ_2 (ns)	β_2 (%)	Φ (%)
Zn/Cd 0.2/0.8	1.057	16.66±2	27.58	42.±4	72.42	12.92
Zn/Cd 0.4/0.6	1.185	14.±2	33.67	46.±4	66.33	10.18
Zn/Cd 0.6/0.4	1.09	13.±1.5	10.35	36.±4	89.65	28.04
Zn/Cd 0.8/0.2	1.13	14.±2	8.67	35.±4	91.43	36.49
CdSe core	1.034	11. ±2	14.68	40.±4	75.32	21.1
CdSeZn	1.174	3.7±0.5	6.60	11.±3	93.4	58.37

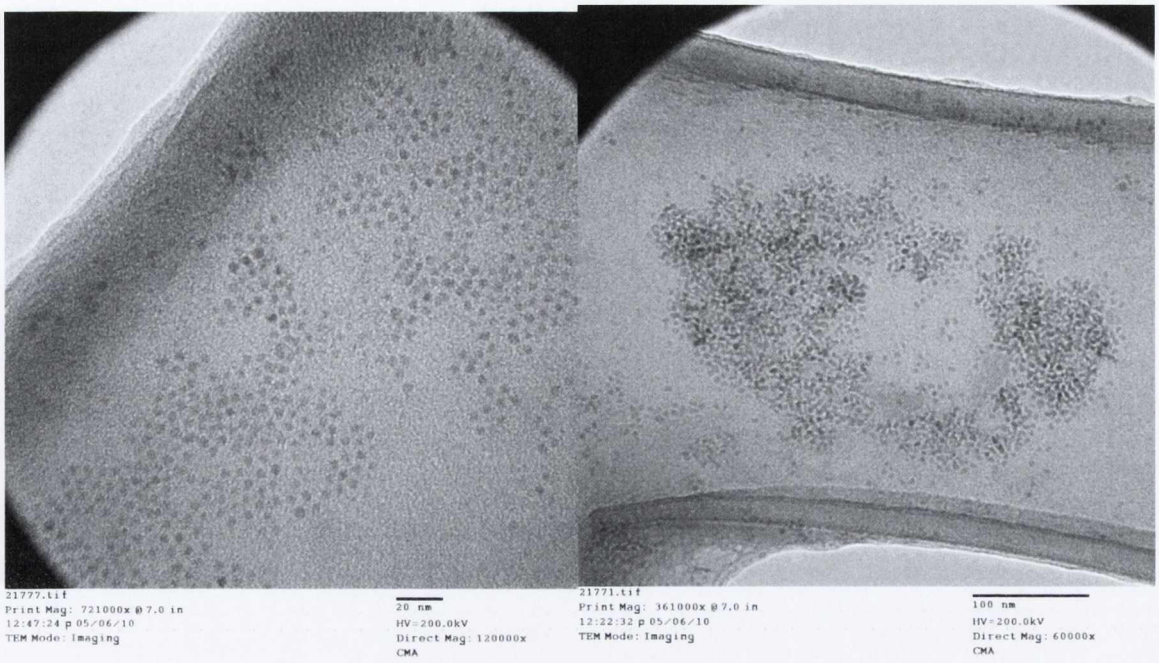

Fig. 3.7. TEM of CdSe/ZnSe QDs and CdSeZn ternary core QDs.

TEM images of CdSe/ZnSe and CdSeZn alloyed QDs are shown in Fig. 3.7. Particle size for all samples was averaged by counting the diameter of 200 individual QDs, giving a value of 3.56±0.6 nm for QDs synthesised with Zn/Cd ratio of 0.8/0.2 and 4.4±0.7 nm for QDs synthesised with a Zn/Cd ratio of 0.2/0.8. Using Yu et al[4] modified equation, the CdSe core size could be calculated and subtracted from the particle size to find the shell thickness. For samples with Zn/Cd ratios of 0.8/0.2 and 0.6/0.4, the average size was found to be 3.6±0.6 nm and 3.7±0.6 nm, which indicated that very little or no ZnSe shell had formed around the core. For samples with higher Cd ratios however my results indicated that a thin ZnSe shell was formed. The lack of a ZnSe shell around the smaller particles may be due to the small quantities of reactive cadmium species available to make CdSe cores.

3.3 Hot Injection Synthesis and Characterisation of CdSe QDs

Hot injection synthesis of semiconducting nanocrystals is now a well-defined field in materials chemistry. Murray et al[6] were among the first to use long chained phosphine ligands coordinated to a selenium precursor injected into a separate cadmium precursor at high temperatures. Nanocrystal growth was controlled by the strong capping ligands in the synthesis, leading to highly crystallinity, narrow size distribution and precise size control of the nanocrystals. Advances soon followed in the field, with high PLQY particles being regularly produced and greener precursors being used.

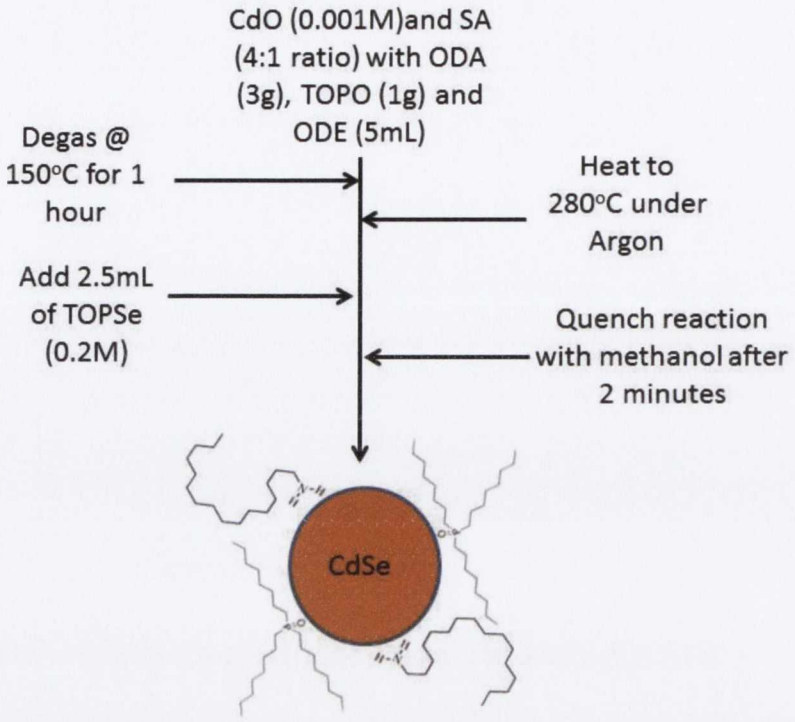

Fig. 3.8 Schematic presentation of CdSe synthesis by hot injection.

Synthesis of CdSe QDs was performed using TOPO and HDA as capping ligands (Fig. 3.8). PLQYs ranged from 11.3 % to 15.93 %. This was thought to be due to the oxidation of the CdSA and solvent when heated to temperatures of 250 °C. QD samples were extracted from the reaction mixture at 30 second intervals to monitor the growth of the QDs. After 150 seconds significant broadening of the PL emission is observed (Fig. 3.9), indicating Ostwald ripening. FWHM of 30 nm after 30 seconds and 60 seconds indicates a narrow size distribution, increasing to 42 nm at 150 seconds. Two peaks in the absorption spectra (Fig. 3.9, right) at 150 seconds indicated two sets of particle size emerging due to Ostwald ripening.

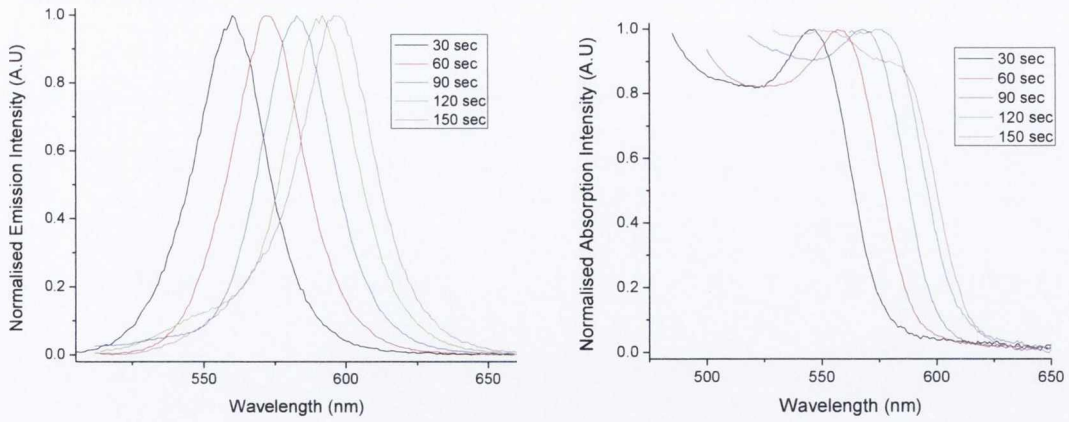

Fig. 3.9. PL emission spectra (left) and UV-visible absorbance spectra (right) of CdSe core QD's synthesized using hot injection method.

Fluorescent lifetime decay was performed by time correlated single photon counting for all samples. A typical exponential decay curve was found and fitted using a biexponential curve to give an average lifetime of give τ_1 = 14.7±2 ns and τ_2 = 43.3±4 ns, with relative amplitudes averaging 31.5 % and 68.5 % respectively.

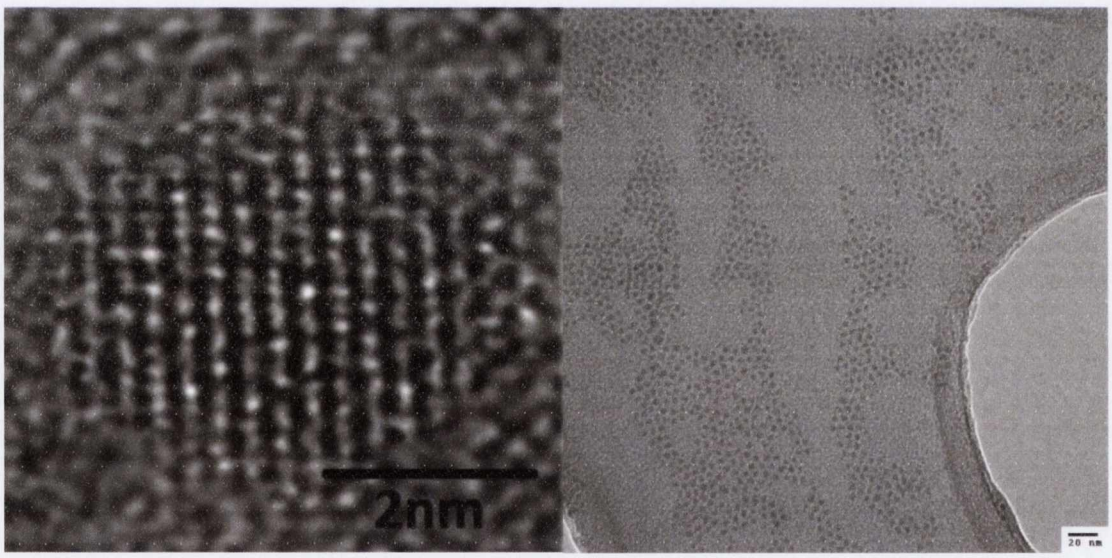

Fig. 3.10. HRTEM and panorama TEM image of CdSe quantum dots of diameter 4 +/-0.8 nm.

TEM analysis showed that I obtained well defined spherical QD with a relatively narrow size distribution (Fig. 3.10). The QD diameter was in close agreement with that of the calculated particle size found from applying the same modified equation previously used to calculate QD diameter from the absorbance spectra. These dots were drop casted onto lacey carbon TEM grids and the solvent left to evaporate over night. The drying effect

of the QDs can clearly be seen. The nanocrystals are closely packed on TEM grids, some regular spacing between individual QDs may be due to capping ligands. Using Image J tool to analyse particle size, I found that the particles had an average size of 4 +/-0.8 nm.

3.4 Hot injection synthesis and characterisation of CdSe/ZnSe core/shell quantum dots

Core CdSe QDs were synthesised by a similar method as in the previous section with a few modifications (Fig. 3.11). Firstly, the synthesis was performed under argon to ensure no oxidation of the precursors. This also eliminated oxygen species that could potentially interact with the nanocrystals during the synthesis and quench luminescence. TOPO was removed from the previous synthesis because of its strong bonding to zinc, making it difficult for the formation of ZnSe shell at temperatures below 300 ^{o}C. HDA was replaced with ODA as ODA can be used at higher temperatures and may give narrower size distribution of QDs. All precursors were degassed before use. The core CdSe QDs were then purified by the precipitation with methanol/ethanol and redispersed in ODE.

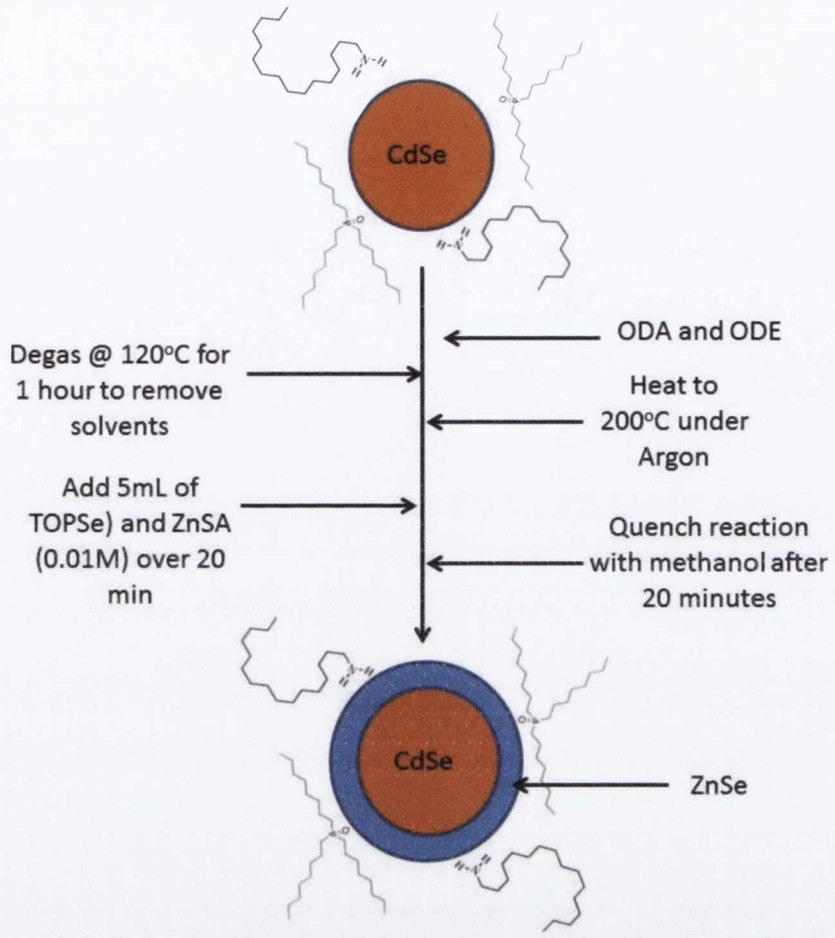

Fig. 3.11. Schematic diagram of CdSe/ZnSe core shell synthesis by hot injection method.

It was found that the ZnSe shell growth enhanced the PLQY of the core particles only when added over a period of time. When the ZnSe precursor was added swiftly into the CdSe cores ZnSe QDs formed alongside CdSe/ZnSe.

Two methods were used for a controlled addition of the ZnSe precursor: by cannula and by syringe pump. It was found that the syringe pump provide greater control over the addition of the precursor, although addition of the Zn and Se precursors by cannula ensured an oxygen free atmosphere.

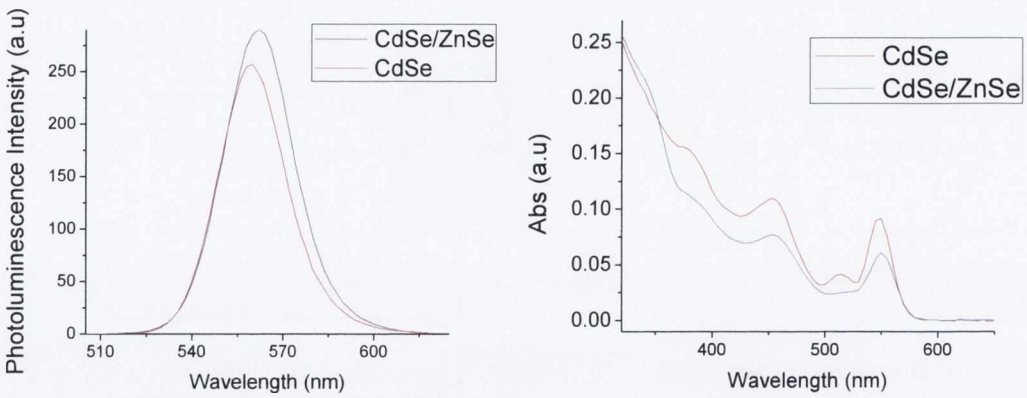

Fig. 3.12. UV-vis absorption spectra (right) and PL emission spectra (left) of CdSe/ZnSe quantum dots synthesized using the hot injection method with the cannula to inject the Zn precursor.

Fig 3.12 above shows the PL and absorbance spectra of CdSe and CdSe/ZnSe QDs. As I mentioned above, the synthesis was conducted under argon to avoid oxidation of the QDs and precursors. This also enabled us to increase the PLQY of the resulting samples. The core dots had a PLQY of 59.8 %, and the capped quantum dots had a maximum PLQY of 82.2 % after 10 minutes of growth after of Zn and Se precursors addition. Shell thickness is important for high PLQY. However, a thick shell may increase the lattice strain between the CdSe core and the ZnSe shell, leading to defects in the crystal lattice. The PLQY was seen to decrease after 10 minutes as a result of this. The FWHM was found to be 29 nm, increasing slightly to 32 nm after the addition of the ZnSe shell. The absorption peaks are much more defined compared to synthesis using HDA and TOPO, which would suggest far better size distribution using ODA and ODE. Large peaks in the absorption band at 465 nm are due to 1s to 1p transitions, which are indicative of high quality QDs with high symmetry[7]. The slight red shift of the CdSe/ZnSe compared to the core CdSe can be due to Ostwald ripening while putting on the ZnSe shell and also leakage of the exciton into the ZnSe shell[8].

Similar results were obtained using the syringe pump to inject 5 ml of TOPSe/Zn-SA with a rate of 0.1 ml per minute. The purified samples of core dots had a PLQY of 20 %, which increased up to 80 % after 10 minutes of shell growth. After this time the QY started to decrease similarly to the previous synthesis. The FWHM of these QDs after the ZnSe shell was 33 nm, so the synthesised particles were of a small size distribution. Using the syringe pump, these high quality CdSe/ZnSe QDs could be easily reproduced by the controlled addition of the ZnSe shell.

Lifetimes for CdSe/ZnSe were calculated in the same way for CdSe core QDs. The lifetimes were fitted with a biexponential function to give τ_1 = 15.±2 ns (33.2%) and τ_2 = 45±4 ns (66.8%). The lifetimes for the core-shell QD were slightly longer, and this may be due to capping of defects at the surface of CdSe QD eliminating faster non-radiative pathways. A point scan of a single CdSe QD using FLIM shows that the QD displays a characteristic on/off emission as the quantum dot charges (Fig. 3.13).

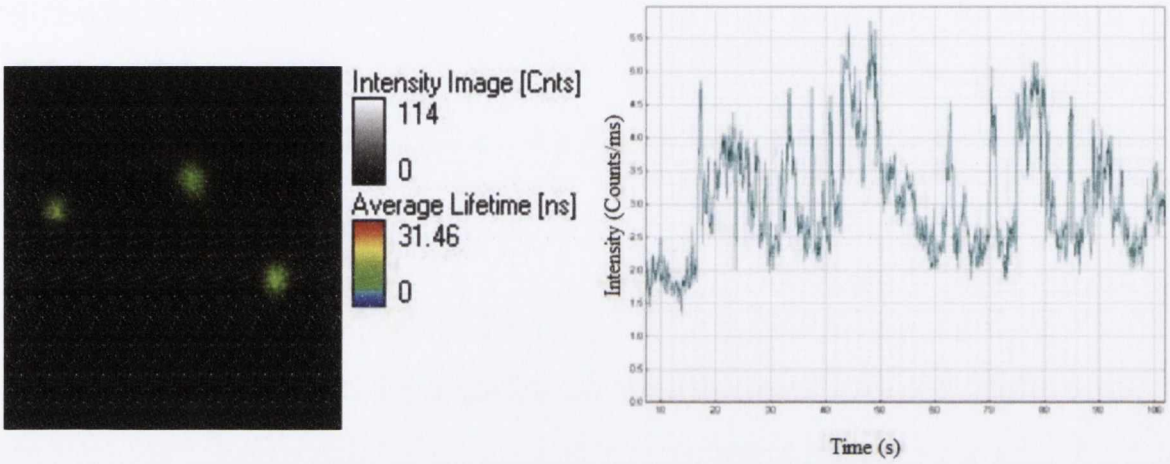

Fig. 3.13. FLIM of CdSe/ZnSe Quantum dots showing on/off blinking using a point trace.

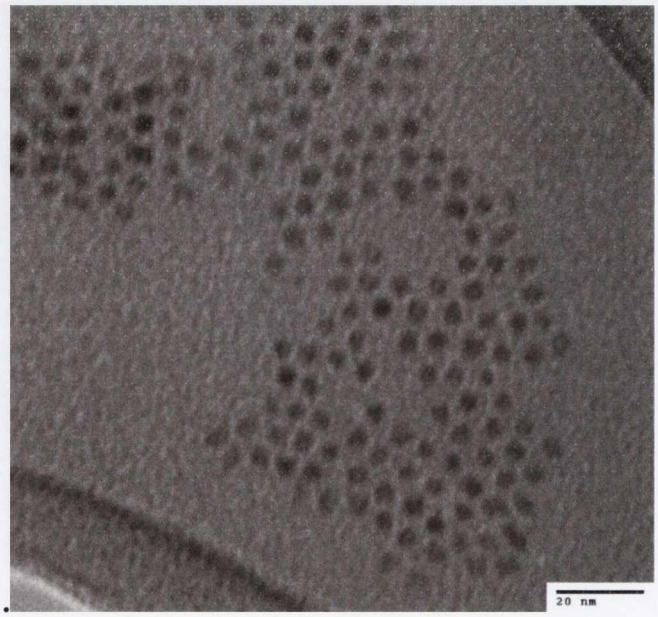

Fig. 3.14. TEM image of CdSe/ZnSe core/shell quantum dots.

TEM analyses (Fig. 3.14) showed that some particles had started deviating significantly in shape compared to pure CdSe QDs. This may be due to ZnSA having a preferential binding to a crystal facet. The QDs were found to have an average diameter of 4.8±0.8 nm. Some aggregates were found on the sample, possible due to unreacted organic ligands and stearic acid. These may be separated from the QD sample by further purification with methanol/ethanol mixtures.

Using both TEM images of CdSe and CdSe/ZnSe core shell dots I can estimate the thickness of the ZnSe shell to be 0.8 nm, which would correspond to 3-4 monolayers of a ZnSe shell[9].

3.5 Hot injection synthesis and characterisation of CdSeZn and CdSeZn/ZnSe alloyed quantum dots

The aim of this part was to develop ternary core and core/shell non-blinking quantum dots, using an alloyed core of $Cd_xZn_{x-1}Se$ which is expected to provide a graded potential barrier to eliminate surface traps and the blinking phenomenon. Synthesis was carried out as seen in Fig. 3.15.

During the synthesis of these ternary particles, a blue shift was induced as zinc was incorporated into CdSe particles. This is due to the band gap of zinc selenide being larger than that of cadmium selenide. As the zinc is incorporated into the CdSe QD, the band gap will shift to higher wavelengths due to the formation of Zn-Se bonds. Comparing to a CdSe dots synthesis I have to work at a higher temperature because of the low reactivity of the zinc precursor. CdSe dots are formed first, because of CdSA higher reactivity compared to ZnSA. At high temperatures the Zn diffuses into the formed CdSe core dots to make a ternary, inducing a blue shift in the emission spectra.

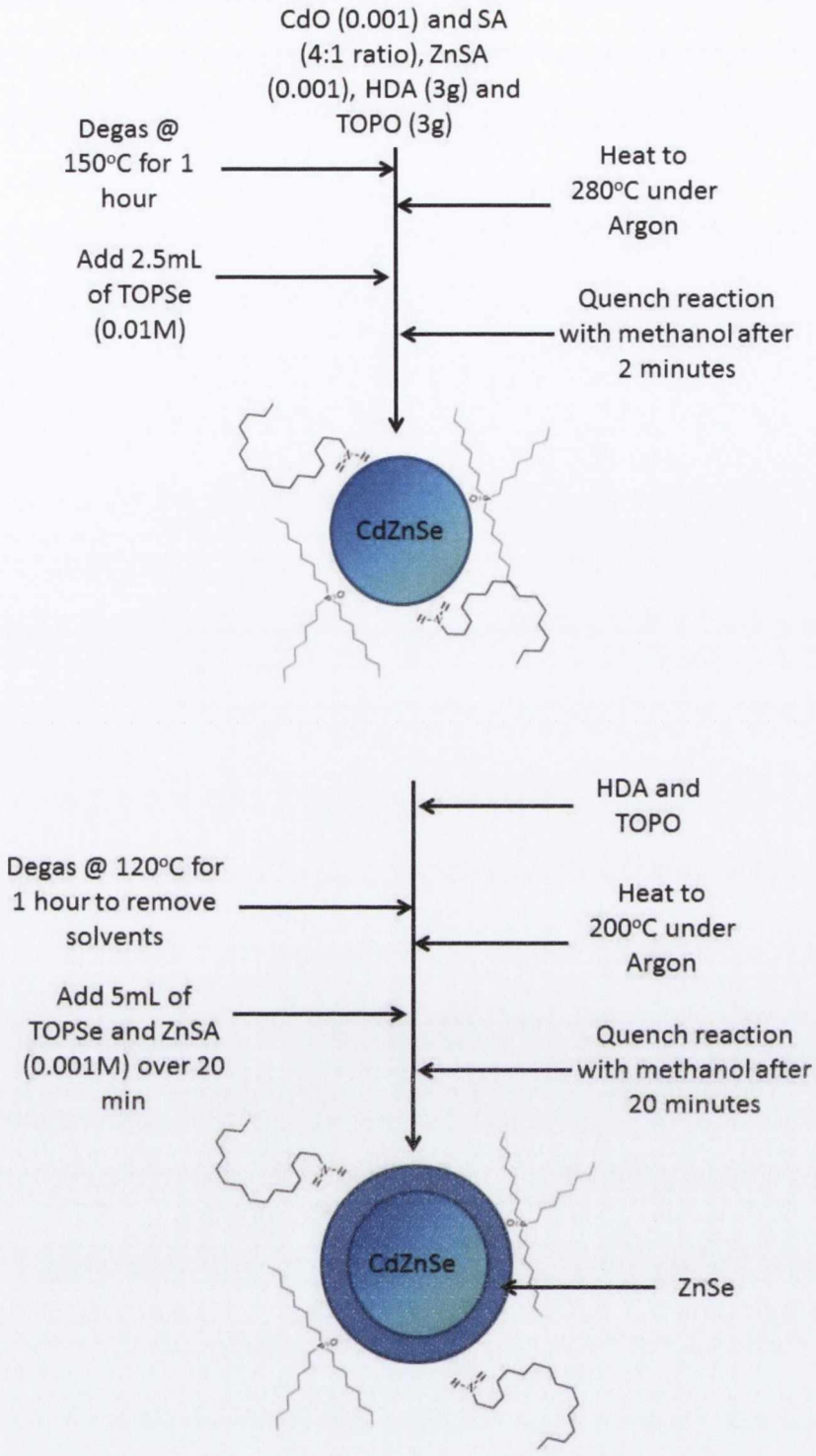

Fig. 3.15. Schematic diagram of CdZnSe/CdZe core-shell synthesis by hot injection method.

Ternary core QDs were synthesised with Cd/Zn ratios of 0.6/0.4 and 0.4/0.6. My first attempt was made by injecting the ZnSA precursor into the CdSe cores at 200 °C and taking aliquots every 120 seconds (Fig 3.16, a). The resultant emission spectra showed two peaks forming over time: one with blue shifting slightly from the CdSe cores and one with red shifting. It was thought that some CdSeZn alloyed dots were forming together with

Ostwald ripening of the CdSe cores. Unfortunately, it is difficult to distinguish between a ternary core and binary core QD. As the QD sample was very stable in solution, size selective precipitation of the QDs yielded no significant changes in the absorption or emission spectra. Because of the small scale of the reaction, XRD analysis of the QD sample at each stage is not possible, although this may have given us proof of the alloying of the sample. The experiment was then repeated with a longer timeframe and a higher reaction temperature of 250 ^{o}C (Fig 3.16, b).

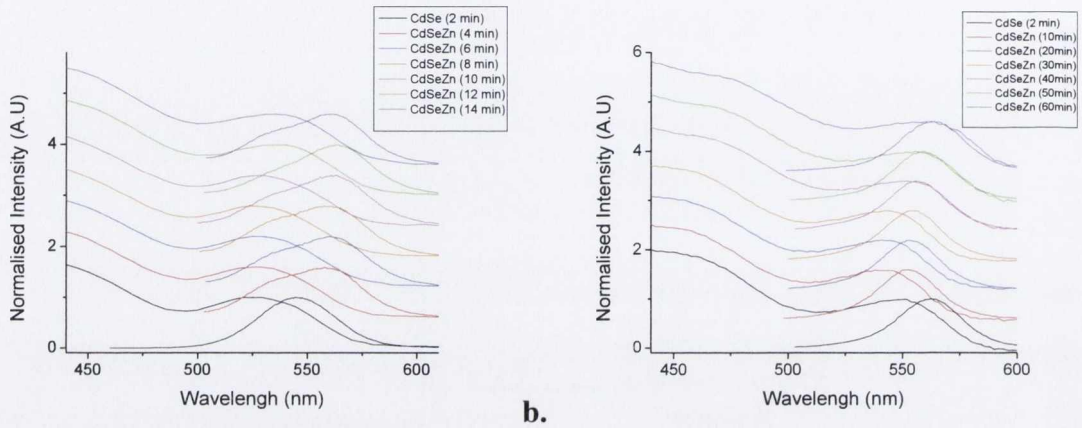

Fig. 3.16. UV-vis and PL spectra of CdSeZn quantum dots during 2 syntheses, (a) for 12 min and (b) for 45 min.

A shift in emission from 564 nm to 553 nm was observed after 10 minutes, with no double peak forming. This is due to the zinc alloying of the CdSe core, therefore the reaction was allowed to continue for a further 35 minutes to ensure a uniform ternary core was formed. PLQY of this alloyed core was found to be at 42 %, which would imply good surface passivation by the organic ligands and few crystal lattice defects.

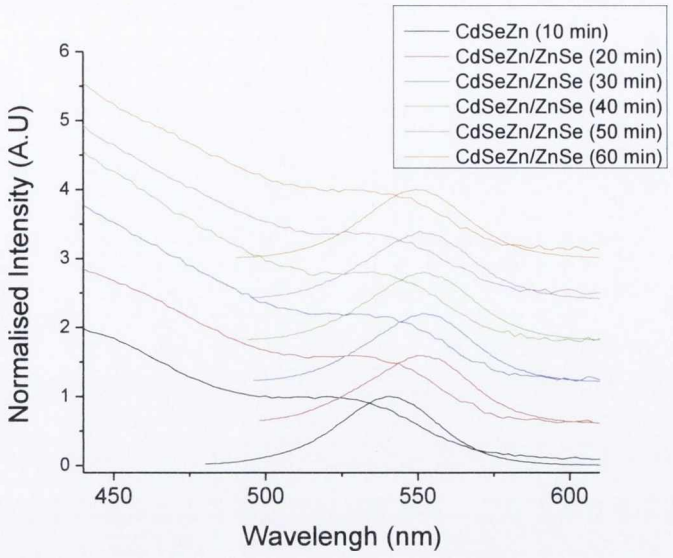

Fig. 3.17. PL and UV-vis spectra of CdSeZn/ZnSe quantum dots.

The CdSeZn ternary core QDs were capped with a ZnSe shell using a pump syringe to add the ZnSe solution to the alloyed cores at 250°C. The ZnSA and Se powder in 5 ml of TOP were injected into the QDs at a rate of 0.1 ml/min and allowed to react for a further 10 minutes. The larger FWHM of 40 nm is due to the exciton being able to propagate into the ZnSe cap (Fig. 3.17). This would also explain the slight red shift seen after 20 minutes. The PLQY was increased from 42 % to a maximum of 59.8 % after 30 minutes. This increase in PLQY may be in part to the annealing out of defects of the QDs at 250 °C as well as the ZnSe shell.

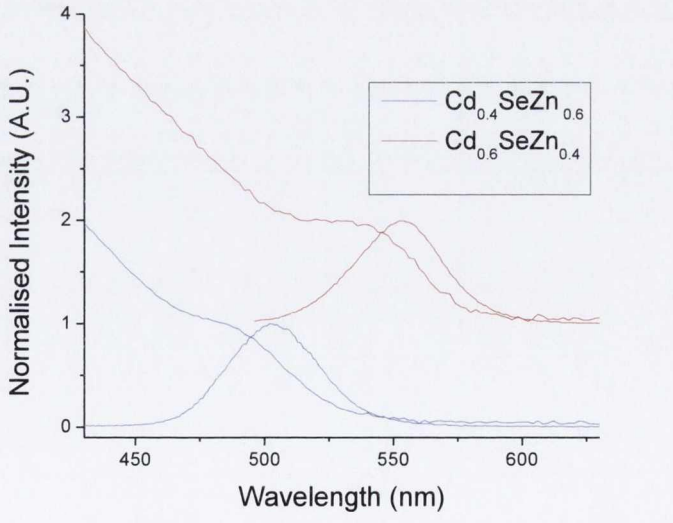

Fig. 3.18. PL and UV-vis spectra of CdSeZn/ZnSe alloyed quantum dots with Cd/Zn ratios of 0.6/0.4 and 0.4/0.6

It was also demonstrated that by varying the zinc content in the reaction the absorption and emission spectra could be tuned to a variety of wavelengths at ease (Fig. 3.18). Because of zincs stability, growth of the QDs is slow and so size distribution is narrow even after long reaction times. By using Vegard's law[10] it is possible to predict the absorbance and emission peaks of the QDs alloys for precise wavelength. Vegard's law states that there is a linear relationship between the lattice spacings of an alloy and that of the concentration of the constituent elements. This can be extended to the bad gap of the material to give an approximate empirical model for the band gap of an alloyed semiconductor.

Lifetimes for CdSeZn and for CdSeZn/ZnSe were calculated in the same way for CdSe core QDs. The lifetimes were fitted with a biexponential function to give τ_1 = 4.4±0.5 ns (7.4%) and τ_2 = 17.±2 ns (92.6%) for alloyed core particles, and τ_1 = 4.7±0.5 ns (8.9%) and τ_2 = 17±2 ns (91.1%) for alloyed core/shell particles. The lifetimes for the core shell particle are slightly longer, and this may be due to the capping of defects states at the surface of QDs by the shell, that results in eliminating faster non-radiative pathways.

This is in close agreement with literature values which found the shorter lifetime to be between 4.0-5.6 ns for CdSeZn/ZnSe particles[11], that can be explained by the existence of a trion in the QD. Below is a summary of lifetimes for all samples (τ), including relative amounts (β) and quantum yield (Ø):

Table 3.3 Optical characteristics of CdSe-ZnSe based QD structures.

QD sample	Φ (%)	χ^2	τ1	β1	τ2	β2
CdSe	60%	0.998	15.±2ns	26%	43.ns±4ns	74%
CdSe/ZnSe	82.6%	1.04	15. ±2ns	33.2%	45±4ns	66.8%
CdZnSe	42%	1.094	4.4s±0.5ns	7.4%	17. ±2ns	92.6%
CdZnSe/ZnSe	59.8%	1.0086	4.7±0.5ns	8.9%	17. ±2ns	91.1%

Using FLIM, I focused on a single CdZnSe/ZnSe quantum dot to perform a point trace of its emission intensity over time. QDs were embedded into a PMMA matrix to reduce oxidation of the QD during FLIM (Fig. 3.19). My point scan reveals that the emission is

continuous with no off states being observed, although the laser did quench the QD emission after 5 minutes of scan time.

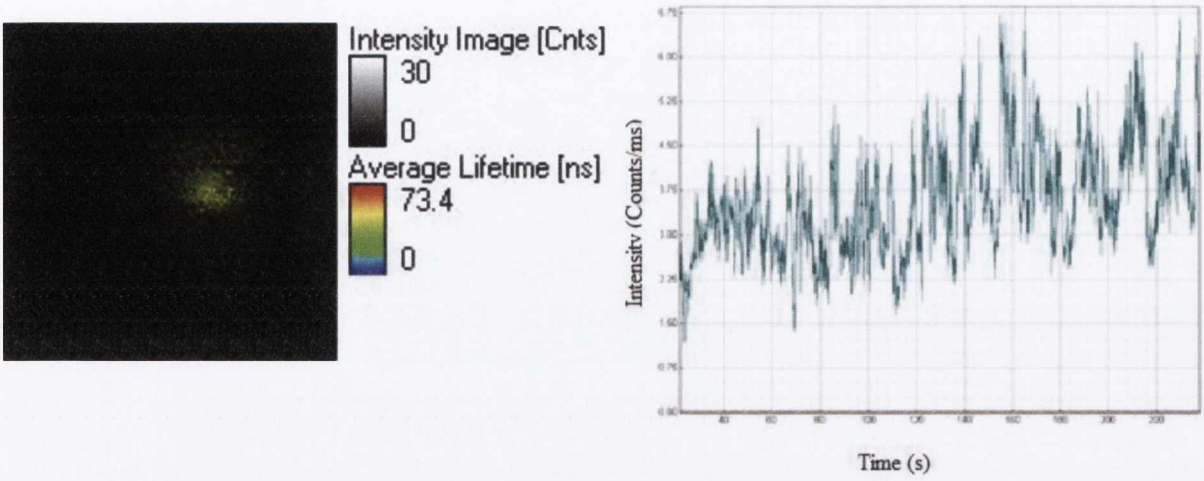

Fig. 3.19. FLIM image and point trace of single CdZnSe/ZnSe Quantum dot showing continuous emission.

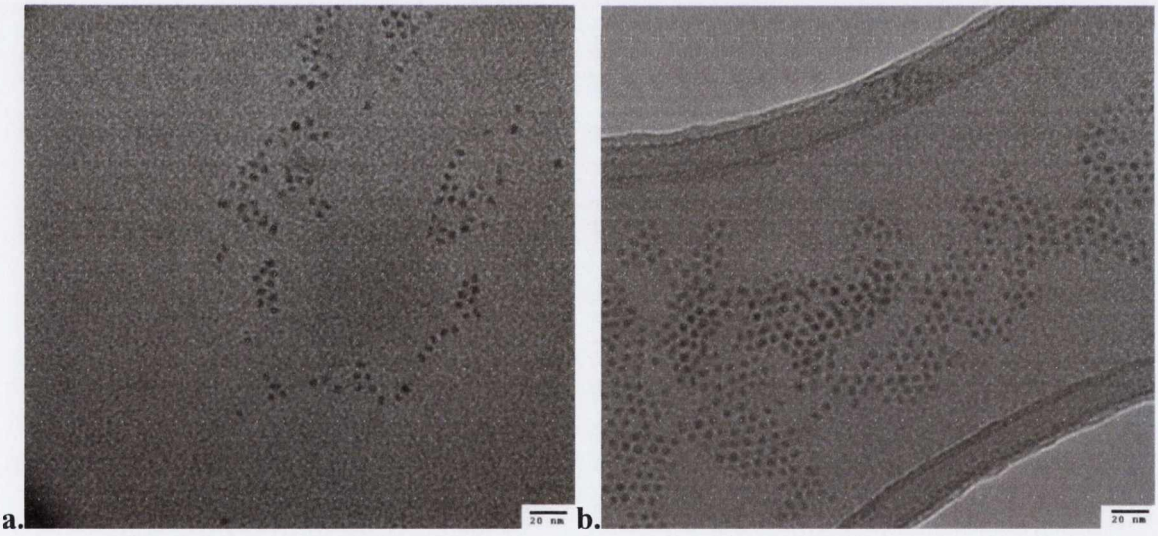

Fig. 3.20. TEM images of CdSeZn (a) and CdSeZn/ZnSe (b) QDs.

The average size of the core particles is 4.7+/-0.5 nm. The average size of the core/shell alloyed dots, synthesized using a 60:40 Cd:Zn ratio, is 5.0+/-0.6 nm (Fig. 3.20). HRTEM of the CdZnSe shows a crystalline structure and lattice fringes of 3.7 Å (Fig. 3.21), which is larger than that measured for my CdSe. This corresponds closely with the fact that ZnSe has a larger lattice spacing than that of CdSe [12]. If these were pure CdSe

particles, their absorption band edge would appear at 578 nm and 588 nm respectively[4]. Instead I see the absorbance peak at 536 nm, which gives further proof of a ternary alloyed structure.

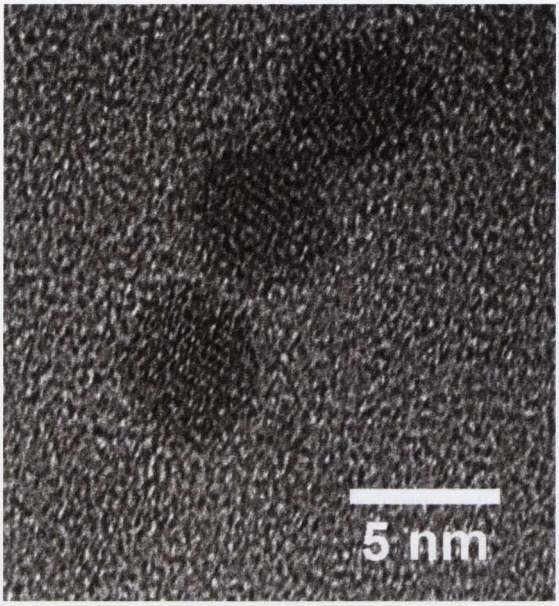

Fig. 3.21. HRTEM of CdZnSe QD cores showing lattice fringes of 3.7 Å

The absorbance and emission peaks may be calculated for ternary core structures using Vegard's law. I also performed powder diffraction XRD to compare my alloyed QDs with that of CdSe. I found that the XRD spectra changed accordingly for my alloyed samples, indicating a uniform CdZnSe alloy (Fig. 3.22)[13,14].

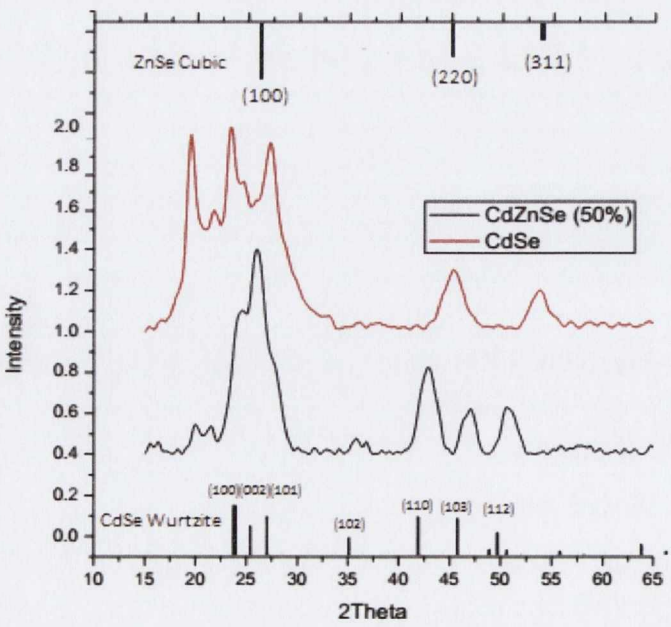

Fig. 3.22. XRD patterns of CdZnSe and CdSe QDs.

3.6 Synthesis and characterisation of CdS Quantum Dots, Rods and other nanostructures

Frequently QD morphology in colloidal synthesis can be controlled by using appropriate capping ligands that bind preferentially to a certain crystal surface of the QD during growth. By varying the ligands ratios, synthesis temperature and time I can control the morphology of certain QD systems. These may lead to unique structures with photonic properties well suited for charge separation, dual emitting nanostructures and large stokes shifts in the emission profiles. This section is dedicated to anisotropic CdS- CdSe based QD nanostructures.

3.6.1 Hot injection synthesis and characterisation of CdS QDs and Rods

The aim of this part was to create CdS seed particles as a stepping stone for CdS rods which are to be grown by preferential growth of the (002) crystal lattice surface. This was done by adding ligands that bind with different affinity to certain crystal facets to provide the directional growth. Changing the ligands and their ratios can form dots, rods, tetrapods and other high aspect ratio QD structures. These high aspect ratio QDs can have significant advantages over their spherical counterparts, including enhanced electron hole separation efficiencies for use in solar cells, polarized light emission and higher loading of polymer composites.

CdS seeds were made by methods previously reported in chapter 2, section 2.23 and as seen in Fig. 3.23. The reaction time was varied to obtain CdS dots of varying size. It was found that while initial nucleation and formation was quick, after 30 s particle growth slowed considerably. While growth of the particles was found to slow, the size distribution of the particles was found to increase, leading us to an optimal time for narrow size distribution after 2 minutes of growth.

The colloidal solution was cleaned by size selective precipitation using methanol and hexane and redispersed in toluene solution. The concentration of the CdS nanoparticles was calculated by absorbance of the solution using methods developed by Sun et al [15]. This was essential for my work to create rods of CdS of known length in the next stage of synthesis. Two types of CdS seed synthesis were produced and compared.

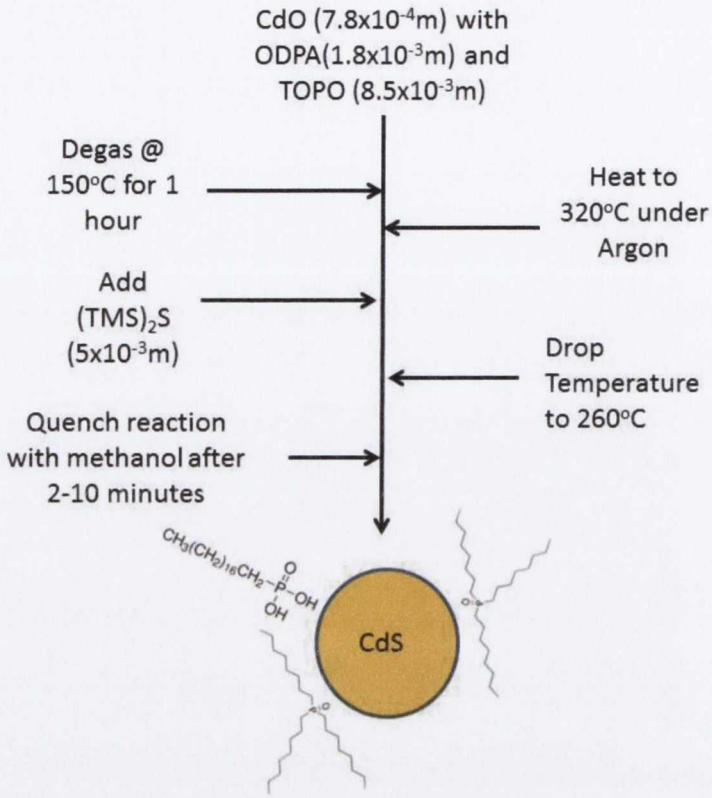

Fig. 3.23. Schematic of CdS seed synthesis by hot injection method.

CdS seeds were first made by injecting $(TMS)_2S$ in TOP into CdO solution at high temperatures. Aliquots were taken over a period of 10 minutes and UV-Vis and PL performed on each sample to monitor growth. As seen in Fig. 3.24, the initial attempt at the synthesis of CdS seeds resulted in a very weak PL emission and broad absorption band. The broad emission band could be annealed out by increasing the synthesis time to 25 minutes as the broad emission band is thought to be due to defects on the CdS nanocrystal surface (Fig. 3.25, left)[16]

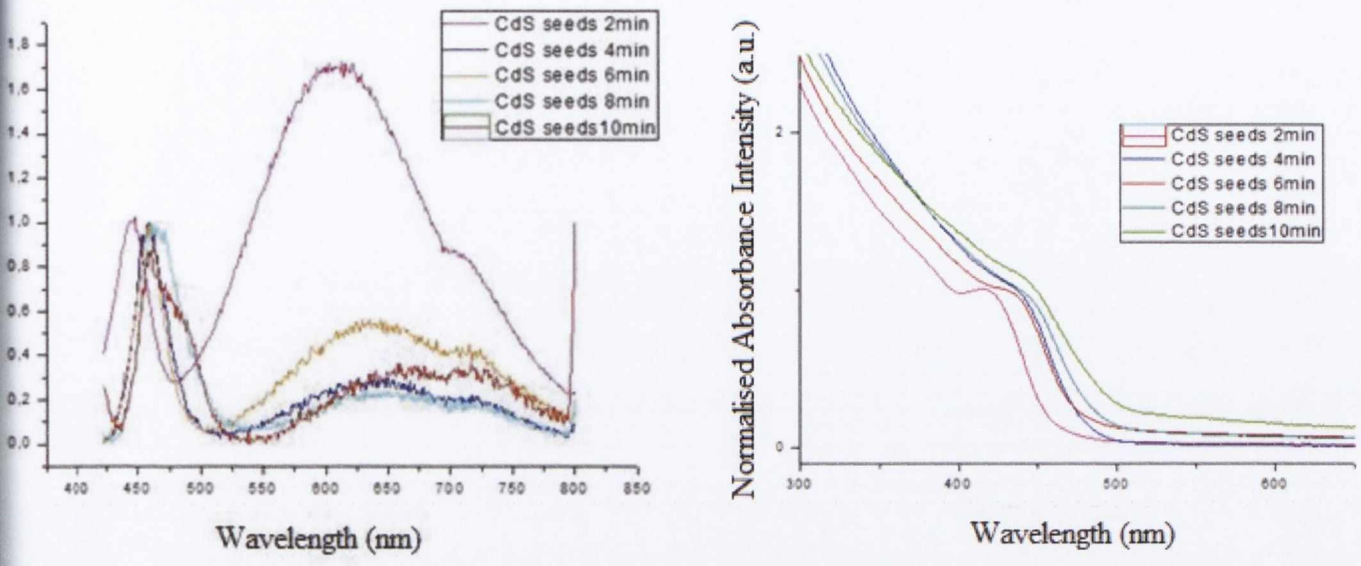

Fig. 3.24. Absorption (right) and PL spectra (left) of CdS seed made by TOPS and TMS hot injection (no oleic acid). The excitation wavelength used was 400 nm.

A second synthesis of the CdS QDs was attempted to achieve a sharper and high PL emission from the dots (Fig. 3.25, right). The synthetic procedure was changed according to method 2.23 in experimental. A more "intrinsic emission" (narrow FWHM, compared to a broad spectra seen from defect emission) was achieved at 400 nm, and no broad defect emission was seen, leading us to believe that the nanoparticles have less defects and narrower size distribution than that of the previous synthesis. Defect emission was reduced significantly at longer reaction times for CdS QDs synthesised using $(TMS)_2S$ as the defects were annealed at higher temperatures, although a widening of the absorbance band suggests that narrow size distribution is compromised as a result (Fig. 3.25, left).

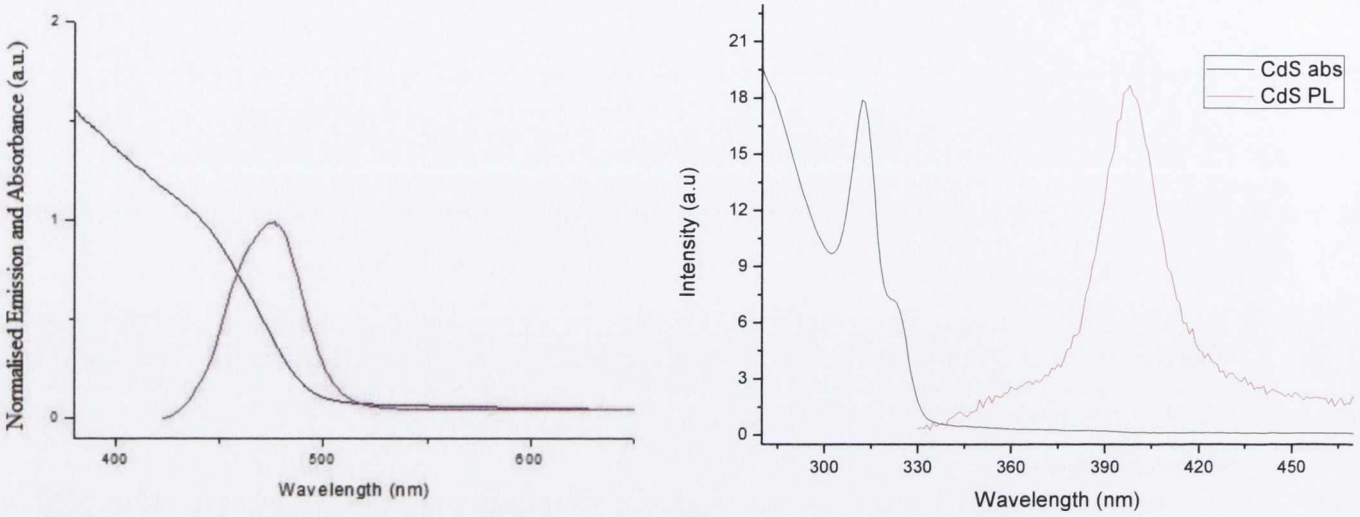

Fig. 3.25. PL of CdS seeds using $(TMS)_2S$ at longer reaction times (right)PL (left) and absorbance spectra of CdS seeds which were produced using oleic acid precursor.

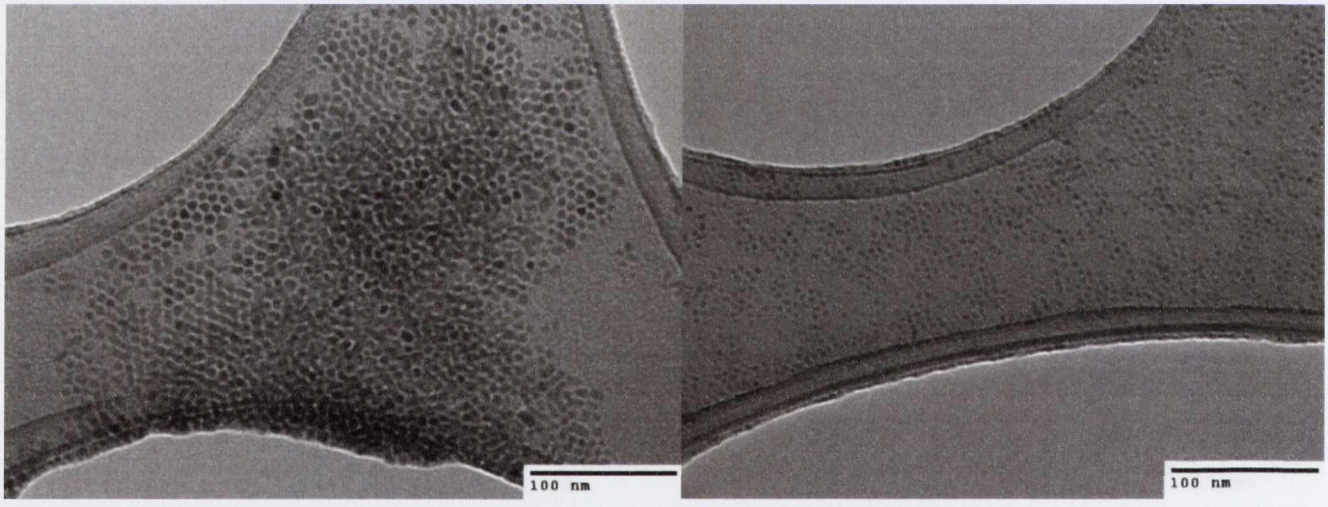

Fig. 3.26. TEM of CdS seeds on lacey carbon grids made using TMS as the sulphur precursor (left). Particles had a weak emission profile and broad size distribution. CdS particles made by CdOA and TOPS (right), show a narrower size distribution and more spherical particles. Particle size was calculated using image J software.

In my first synthesis my PL emission was very weak and broad, indicating a mostly defect origin of the PL. The absorbance was also broad and undefined, which is consistent with the large size distribution of the CdS particles (Fig. 3.26). Contrast between the carbon

substrate and quantum dots was hard to achieve, and therefore QDs were difficult to image compared to CdSe QDs, which is more crystalline and whose molecular weight is higher than that of CdS. A higher molecular weight will show more contrast in TEM images, as will nanocrystals with high crystallinity, compared to those that are more amorphous.

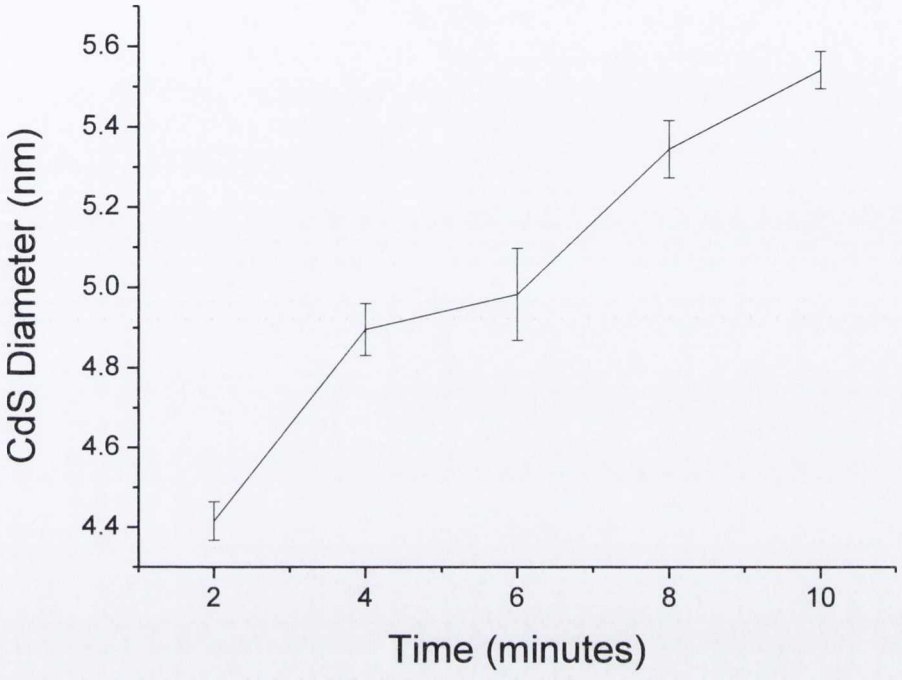

Fig. 3.27. Growth of CdS seed particles as a function of time. CdS seed particle size was calculated from TEM of samples. Errors were calculated by standard deviation of the data using Origin 8.

Using Image J software, CdS quantum dot diameters were found for a typical sample of QDs. For each sample size, a panorama view of CdS was used and between 500-1000 QDs measured to accurately determine the QD size per sample (Fig. 3.27). QD samples were measured at 2 minute intervals for 10 minutes.

CdS rods were made with varying length of between 10-50 nm. For this study, I used CdS rod lengths of 10 nm ± 1 nm, 22 nm ± 3 nm and 50 nm ± 4 nm for my reactions with Cd and Se. A known concentration of CdS rods was heated to 250 °C under argon and the Cd/Se precursor added dropwise to the solution over a period of 10 min (Fig. 3.28). Aliquots of the solution were taken every 30 s to observe changes in PL and absorption as well as for TEM analysis. Rod length was controlled by the concentration of seed particles and precursors added to the Cd/S solution. All reactions were maintained at 340 °C for 7

min to anneal the rods and maximise CdS rod formation from the seed particles. After 7 min rod growth ceased as monomer concentration was depleted

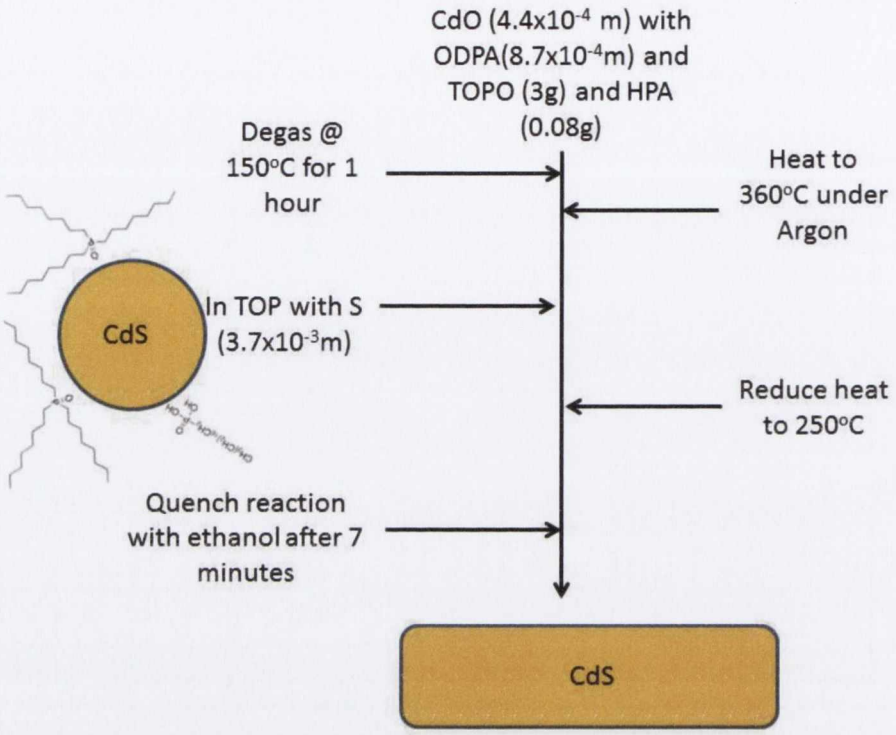

Fig. 3.28. Schematic of CdS rod synthesis by injection of CdS seeds into Cd precursor.

UV-Vis absorption spectroscopy was performed on CdS rods grown from CdS seed using 0.8, 1.6 and 3.2 ml of stock CdS seed solution (Fig. 3.29). Interestingly, when higher aspect ratio rods were grown, a sharper first exciton band appeared. This could be due to a focusing regime during growth, giving more a more uniform size of CdS rods. The reason for the lowest aspect ratio rod have an undefined first absorption peak is that CdS rod growth was fast, and Cd and S monomers were used up quickly in the reaction, resulting in a wider size distribution and shorter size focusing regime whilst growth occurred.

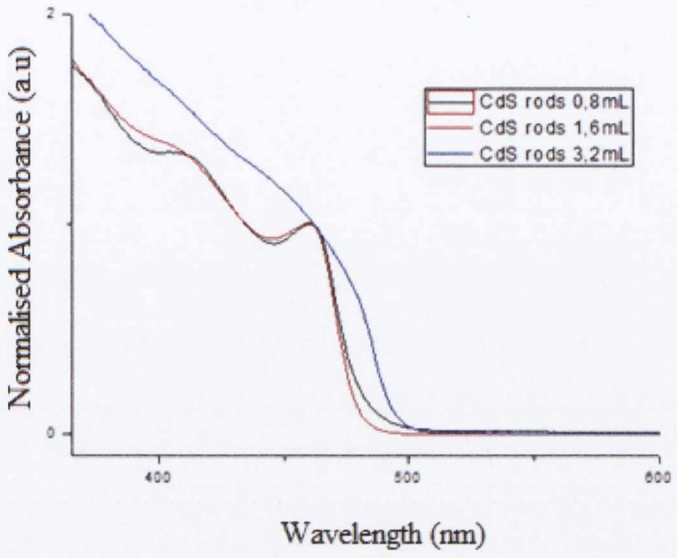

Fig. 3.29. UV-Vis absorbance spectra of CdS rods with increasing CdS seed particles. The increase in seed particles means a lowering in the aspect ratio of the resultant CdS rods.

Increasing CdS seed concentration to above the value used to create rods of 10 nm length resulted in a large size distribution and some aggregation of CdS seed particles which lead to the formation of large CdS clusters (Fig. 3.30, right). Decreasing CdS seed concentration to one below that used to create rods of 50 nm resulted in the formation of tetrapodal structures as well as the joining of adjacent rods (Fig 3.30 left).

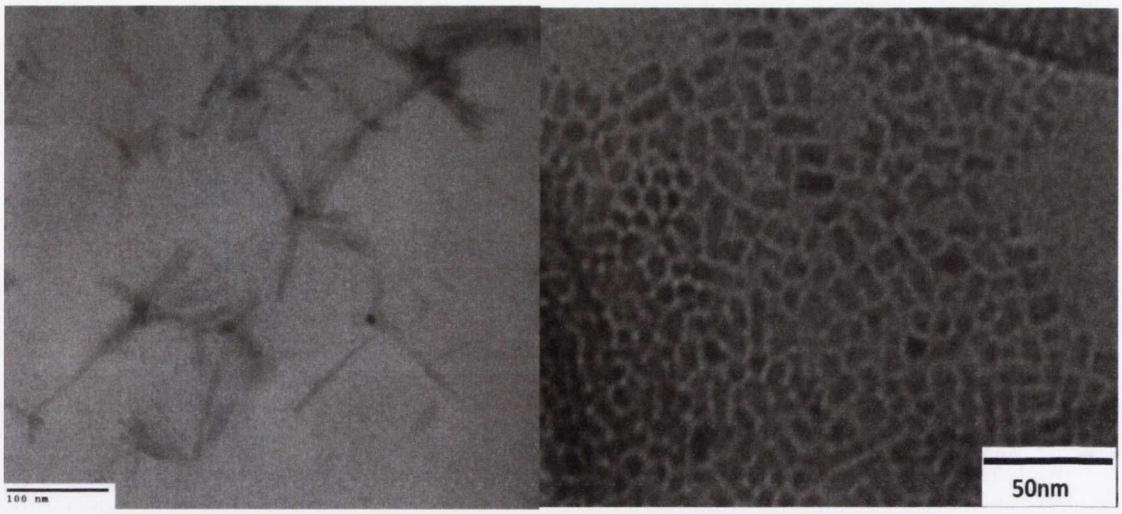

Fig. 3.30. Addition of too few CdS seed particles results in branched structures and aggregation of CdS rods (left), whereas excess CdS seed particles results in non-uniform low aspect ratio CdS nanostructures (right).

CdS rod length could be controlled with good precision with CdS seed concentrations between 1 ml and 2.5 ml using a stock concentration of CdS solution (6 x 10^{-7} m), giving us rod lengths between 20-50 nm. This also gave us the least amount of size distribution, and when imaged showed a high degree of alignment when dried on a lacey carbon grid (Fig. 3.31).

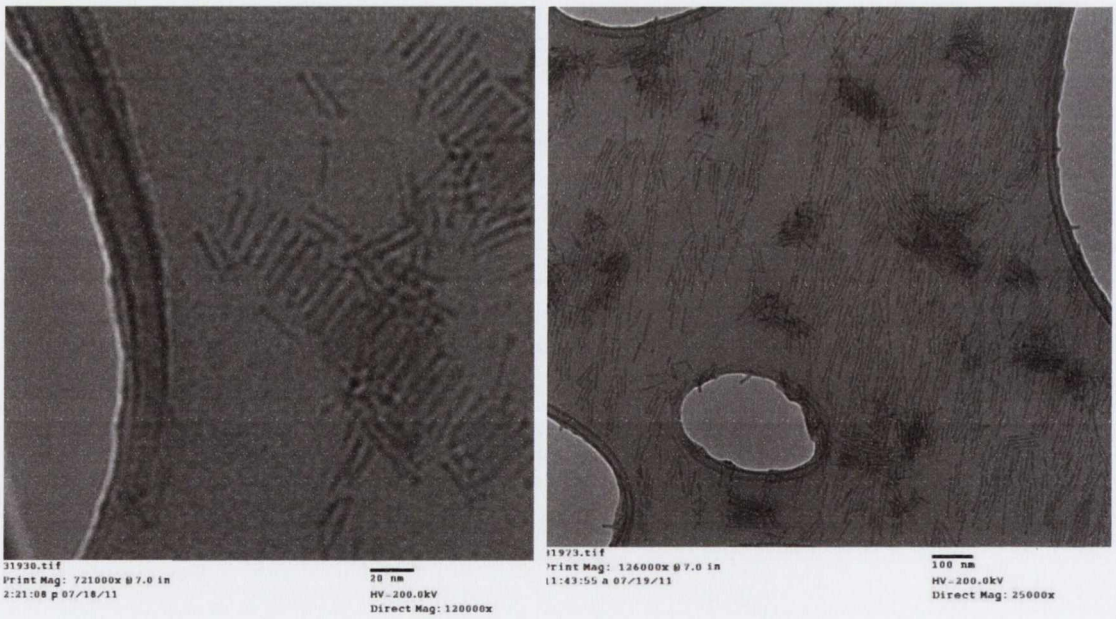

Fig. 3.31. TEM of CdS rods of varying aspect ratio. The rods are uniform in size and well dispersed on the grids.

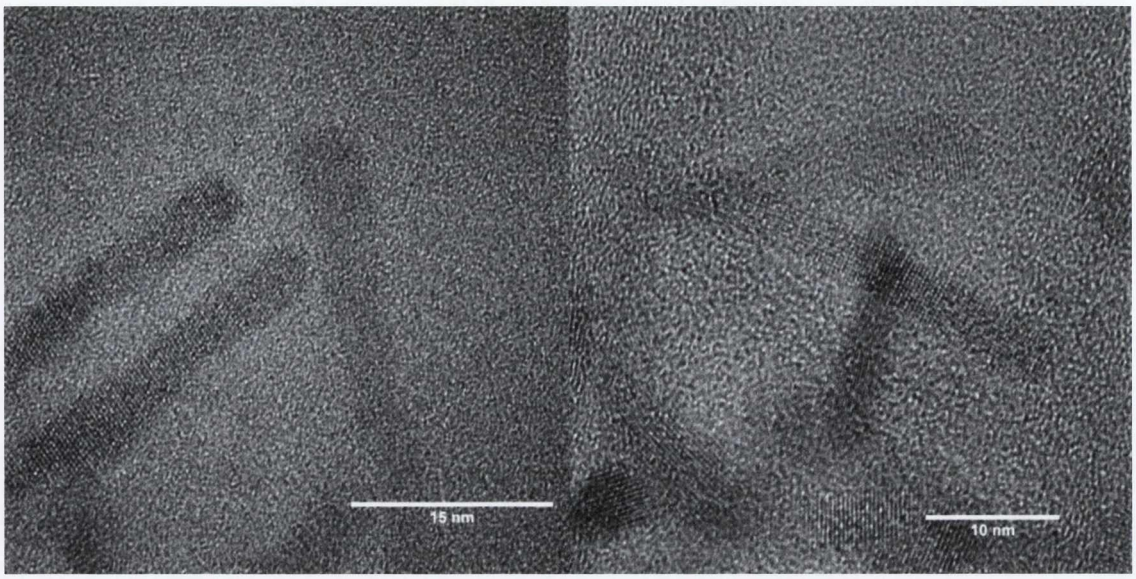

Fig. 3.32. HRTEM of CdS rods showing good crystallinity resulting from fast growth along the (002) axis.

HRTEM of these rods were also taken (Fig. 3.32). Highly uniform crystal lattices can be seen resulting in fast growth along the (002) axis. XRD of these CdS rods against CdS seeds showed sharper peaks and peaks arising between 42° and 55° from growth along the (110), (103) and (112) axis suggesting that the CdS seeds may be in the zinc blend phase, whereas the CdS rods are in the wurtzite phase (Fig. 3.33)[17].

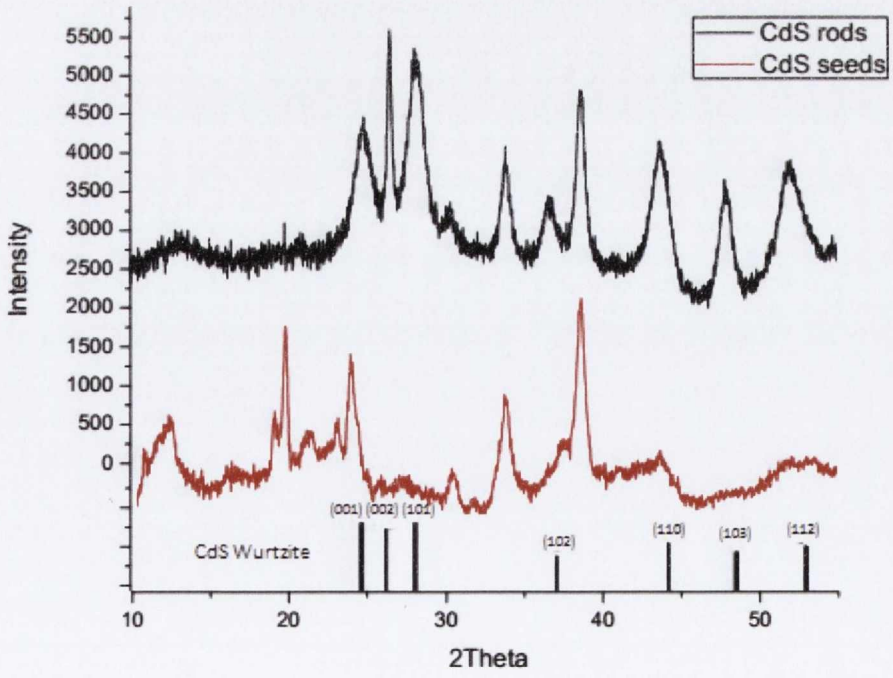

Fig. 3.33. Powder X-Ray diffraction of CdS dots (red) and CdS rods (black).

3.7.2 Preparation and characterisation of CdS-CdSe based heterostructures

CdS rods were isolated by removing the solvent by placing the solution under vacuum in a round bottomed flask at 80 °C and then by washing the residue with an excess of non-coordinating solvent. After 2 hours under vacuum, the flask was back filled with Argon and the temperature increased to 250 °C. At this temperature Se and Cd precursors were injected into the solution at timed intervals and aliquots taken every 2 min after each addition to monitor the reaction (Fig. 3.34).

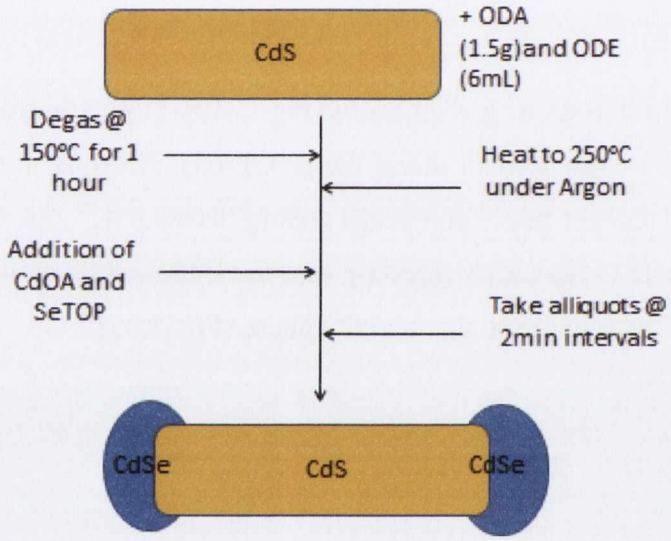

Fig. 3.34. Schematic presentation of CdS-CdSe heterostructure synthesis.

PL and UV spectra of the resulting solutions showed a peak with the fluorescence emission after 4 minutes, indicating the formation of CdSe QDs in the solution. After the second injection another peak was observed, indicating another growth regime of smaller QDs in the solution (Figure 3.35).

In a typical synthesis of CdSe QDs the addition of additional precursors usually leads to the growth of the QD particles already formed, resulting in a red shift of the PL when monitoring the reaction. As one can see two distinct and narrow PL emission bands here I could say that two growth regimes occur probably due to the influence of the CdS rods (Fig. 3.35, right). Further additions result in a third peak as growth of the new CdSe QDs are slowed significantly compared to the first and second additions. There is some red

shifting seen from the second peak at 645nm, but none for the first peak indicating high stability of the initial QDs formed. The stability may come from the QDs initially nucleating on the surface of the CdS rods. As the reaction continues, the CdS rods may rearrange to form a stable core shell CdSe/CdS particle, limiting the growth of the QD.

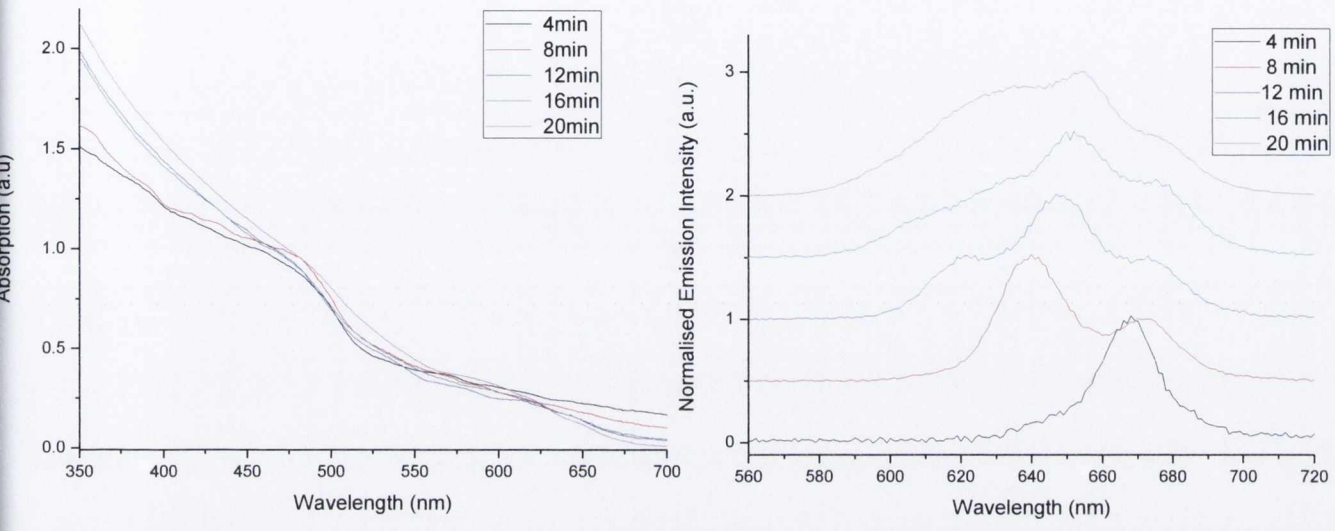

Fig 3.35. Monitoring of PL (right) and absorbance (left) spectra of CdS-CdSe structures over the reaction time with increasing CdSe precursors added.

The additional QDs formed are more likely to form free in solution as the first QDs formed have taken any high energy nucleation defect points on the CdS rods. This can be confirmed by the broadening of the peaks after further additions as a wide range of QDs are formed free in solution.

To test this further, I repeated the experiment with a single injection of the Cd and Se precursors in solution and took aliquots over a period of time. From the PL emission (Fig. 3.36) one can see that a single peak arises after the addition of the precursors. This peak does not show any red shifting over the reaction time, indicating that after these QD nanostructures are formed they are stable. Furthermore, the emission intensity increases over time. This is indicative of QDs with a high PLQY due to high crystallinity and low surface defect states that can quench emission. Long reaction times have been shown to anneal the surface defects from QDs to increase PLQY of the sample, although it often results in a broad size distribution of QDs due to Ostwald ripening.

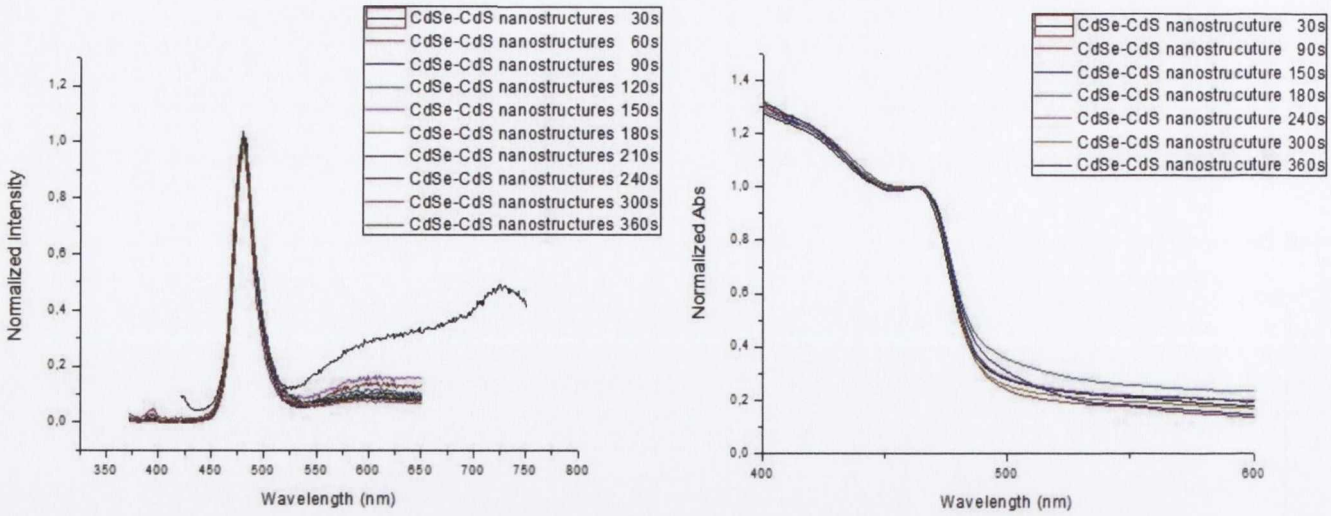

Fig. 3.36. Monitoring of photoluminescence (left) and absorbance (right) spectra of CdS-CdSe nanostructures over the reaction time.

TEM was performed on samples where multiple Cd/Se injections were given. This resulted in a sample where CdSe QDs formed in solution as well as on the CdS rods, leading to different size distributions (Fig. 3.37).

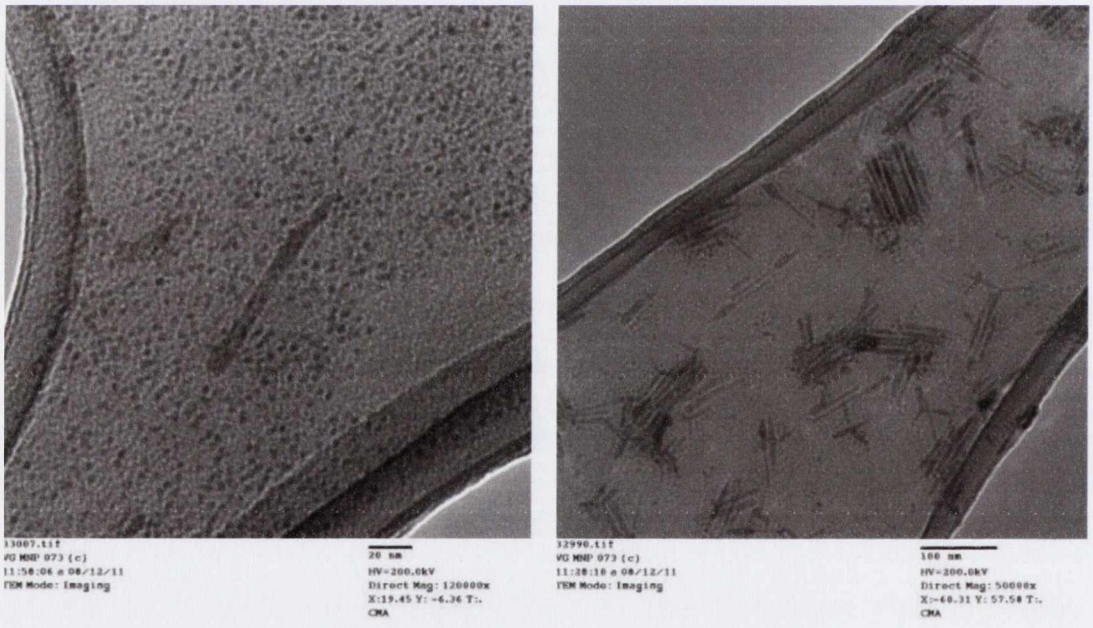

Fig. 3.37. Large amount of free CdSe QDs and CdSe QDs on CdS rods (left) and with lower concentration of Cd/Se precursors resulting in the deformation of the CdS rods.

One can see that from Fig. 3.37 (left) that CdSe QDs can form independently in the solution, but also on larger CdS rods, which can explain the emission spectra in Fig. 3.35.

For a single precursor addition more study of the CdS-CdSe was warranted as several unique structures were seen in TEM.

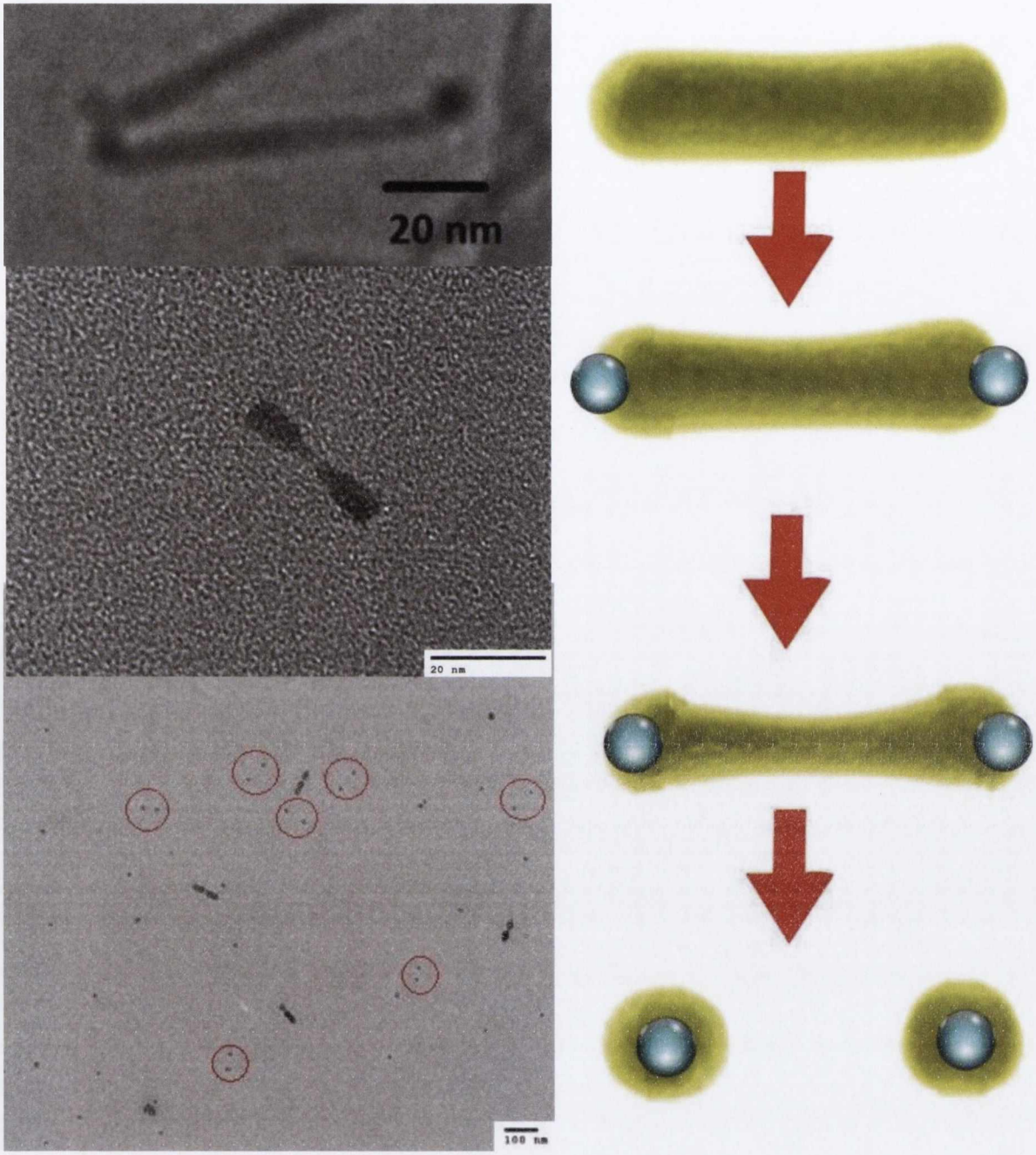

Fig. 3.38. Transformation of CdS rods into CdSe/CdS QDs. CdS is represented by yellow, and CdSe by blue dots (right). We can see the formation of CdSe tips on a CdS rod (left, top), the beginning of dissolution (left, middle), and the end result (left, bottom).

From the TEM we can see that the samples morphology greatly changes over the reaction time. I believe that with larger rods the CdSe QDs are nucleating on the defect sites of the CdS rods as well as forming free in solution with additional Cd/Se precursors. With smaller rods, the rods begin to rearrange to cover the high surface energy of the CdSe QDs, effectively creating a core-shell CdSe/CdS nanoparticle (Fig. 3.38). The suggested mechanism explains why I don't see a red shift in the CdSe emission over time and an increase in PL emission, as the CdSe QD surface is being passivated by the CdS (Fig. 3.36).

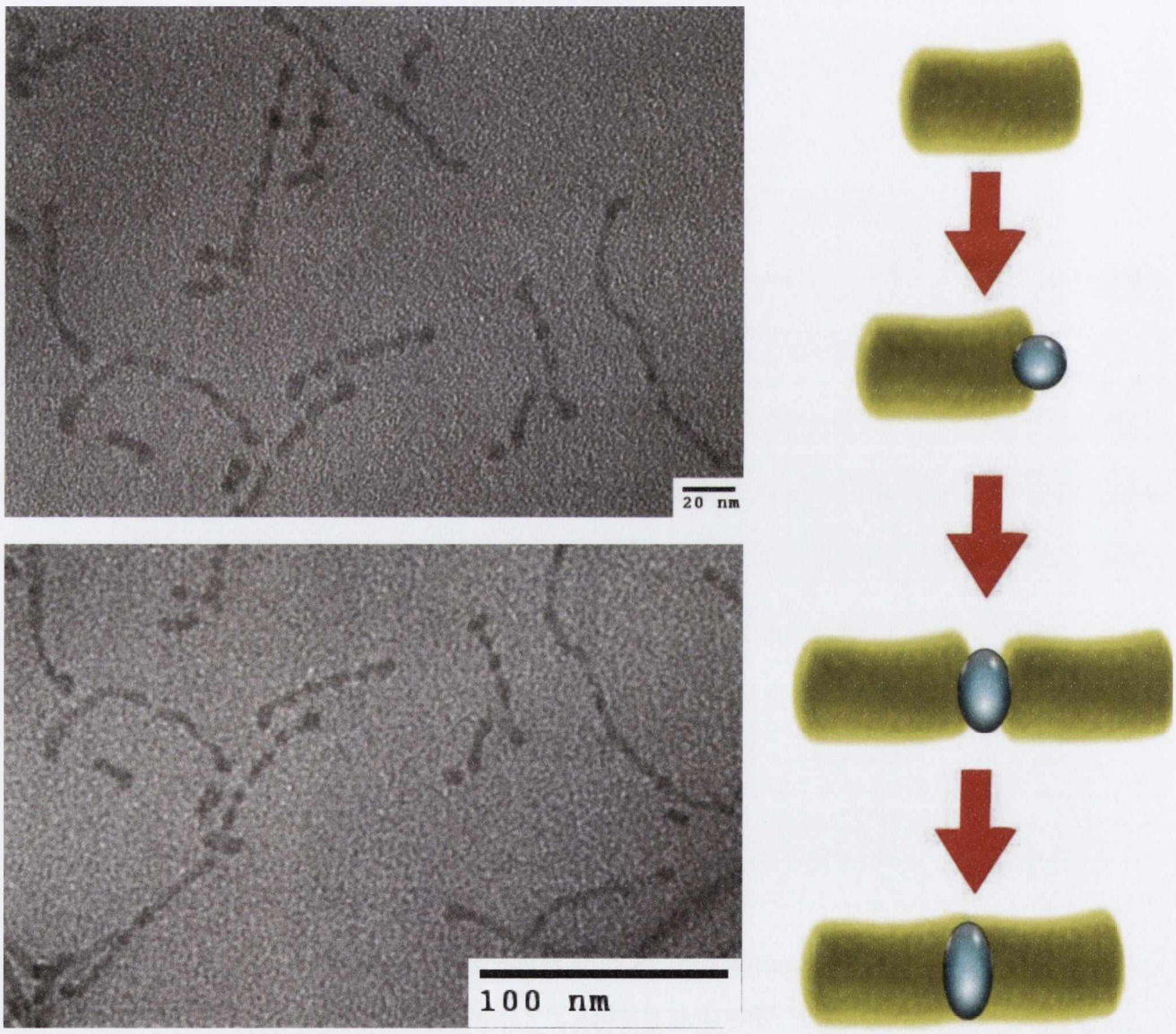

Fig. 3.39. CdS rods joining at lower temperature synthesis after addition of Cd/Se precursors.

At lower temperature a different growth regime is observed, where instead of the CdS rods rearranging to create CdSe/CdS core-shell particles, the rods link up to form chains, using CdSe QDs grown at the ends of the chains (Fig. 3.39).

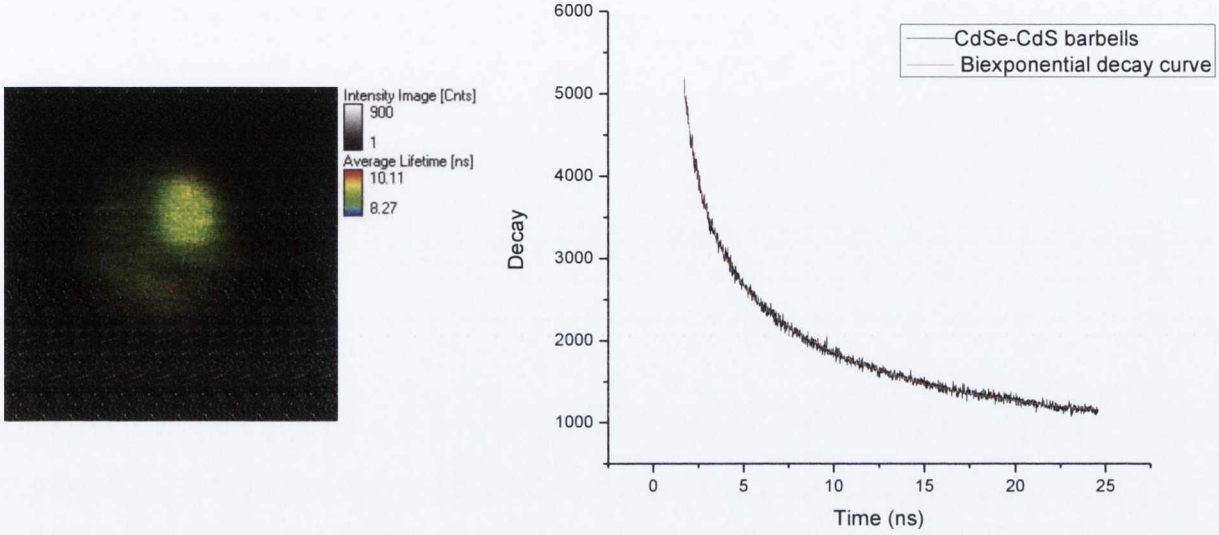

Fig. 3.40. FLIM carried out on a single dot-rod and corresponding lifetimes.

FLIM was also performed on some of the CdS-CdSe structures (Fig. 3.40). Fast lifetimes of $\tau^1 = 1.2\pm0.3$ ns and $\tau^2 = 8.3\pm0.4$ ns were seen, which correspond to other previously reported similar barbell structures[18,19].

3.8 Conclusions

Thus in this part of my work I have developed the synthesis of new CdSe, CdZnSe core-shell nanoparticles and CdSe-CdS based nanostructures.

I have found that microwave synthesis is very fast and convenient way to prepare CdSe and CdSeZn alloyed QDs. Microwave reactions produced CdSe and alloyed CdZnSe quantum dots at temperatures from 80 ^{o}C, which is considerably lower than that of a typical hot-injection synthesis. Reaction times were also greatly reduced, along with preparation time for the reactions, with my quickest reaction to form QDs at less than two minutes due to rapid microwave heating. Microwave heating was shown to be a versatile method to produce a range of CdSe nanoparticles with precise control over their size by varying precursors.

I demonstrated that the addition of Zn to CdSe nanostructure resulted in an increase of PLQY from 21.1 % to 58.37 % using a hot-injection synthesis. This clearly indicates that not only has the CdSe core been fully alloyed, but that a ZnSe shell has effectively pacified the surface, eliminating surface traps. However, the microwave approach has some issues with the reproducibility and stability of resulting QDs. Hot injection synthetic approach provided more reliable and reproducible results and also enabled us to produce QDs with very high PLQY (up to 82 %).

I have also prepared a range of various CdSe-CdS nanostructures using the hot injection technique. My ultimate goal was to produce dual emitting barbell like structures (e.g. CdS rod with CdSe bells). I have successfully prepared a range of CdS rod-like structures of various lengths, but it was extremely challenging to produce corresponding CdSe-CdS-CdSe barbells. In my studies I have found that this system is extremely labile and very hard to control. The nanostructures were changing rapidly during the reaction, storage and even on TEM grids during the sample preparation. As result I have prepared a range of CdS-CdSe rod-dot nanostructures of various sizes and found that many of them transform into the most stable nanostructures in this system such as CdSe/CdS core shell spherical nanoparticles. I have suggested some mechanisms for these transformations, but more detailed and time demanding studies are necessary to understand and explain all processes which take place in CdSe-CdS system. I believe that this research should be of fundamental importance for further development of widely used II-VI QD nanostructures.

References:

(1) Haynes, W. M. *CRC handbook of chemistry and physics*; CRC, 2010.
(2) Javier, A.; Magana, D.; Jennings, T.; Strouse, G. F. *Applied Physics Letters* **2003**, *83*, 1423.
(3) Lee, W. Z.; Shu, G. W.; Wang, J. S.; Shen, J. L.; Lin, C. A.; Chang, W. H.; Ruaan, R. C.; Chou, W. C.; Lu, C. H.; Lee, Y. C. *Nanotechnology* **2005**, *16*, 1517.
(4) Yu, W. W.; Qu, L.; Guo, W.; Peng, X. *Chemistry of Materials* **2003**, *15*, 2854.
(5) Wang, X.; Ren, X.; Kahen, K.; Hahn, M. A.; Rajeswaran, M.; Maccagnano-Zacher, S.; Silcox, J.; Cragg, G. E.; Efros, A. L.; Krauss, T. D. *Nature* **2009**, *459*, 686.
(6) Murray, C. B.; Norris, D. J.; Bawendi, M. G. *Journal of the American Chemical Society* **2002**, *115*, 8706.
(7) L.E Brus, D. J. N., M. G Bawendi In *Molecular Electronics*; Jortner, J., Ed.; Blackwell Science: 2010, p 293.
(8) Reiss, P.; Bleuse, J.; Pron, A. *Nano Letters* **2002**, *2*, 781.
(9) Li, J. J.; Wang, Y. A.; Guo, W.; Keay, J. C.; Mishima, T. D.; Johnson, M. B.; Peng, X. *Journal of the American Chemical Society* **2003**, *125*, 12567.
(10) W, A. N. *Physical Review A* **1991**, *43*, 3161.
(11) Wang, X.; Ren, X.; Kahen, K.; Hahn, M. A.; Rajeswaran, M.; Maccagnano-Zacher, S.; Silcox, J.; Cragg, G. E.; Efros, A. L.; Krauss, T. D. *Nature* **2009**, *459*, 686.
(12) Hotje, U.; Rose, C.; Binnewies, M. *Solid State Sciences* **2003**, *5*, 1259.

(13) Su, H.; Xu, H.; Gao, S.; Dixon, J.; Aguilar, Z.; Wang, A.; Xu, J.; Wang, J. *Nanoscale Res Lett* **2010**, *5*, 625.
(14) Lesnyak, V.; Dubavik, A.; Plotnikov, A.; Gaponik, N.; Eychmuller, A. *Chemical Communications* **2010**, *46*, 886.
(15) Sun, J.; Goldys, E. M. *The Journal of Physical Chemistry C* **2008**, *112*, 9261.
(16) Lakowicz, J. R.; Gryczynski, I.; Gryczynski, Z.; Murphy, C. J. *The Journal of Physical Chemistry B* **1999**, *103*, 7613.
(17) Zou, Y.; Li, D.; Yang, D. *Nanoscale Res Lett* **2011**, *6*, 374.
(18) Hewa-Kasakarage, N. N.; El-Khoury, P. Z.; Tarnovsky, A. N.; Kirsanova, M.; Nemitz, I.; Nemchinov, A.; Zamkov, M. *ACS Nano* **2010**, *4*, 1837.
(19) Halpert, J. E.; Porter, V. J.; Zimmer, J. P.; Bawendi, M. G. *Journal of the American Chemical Society* **2006**, *128*, 12590.

Chapter 4. Quantum Dots and Optical Microcavities

4.1. Introduction

Optical microcavities, which confine the propagation of light in all three dimensions, are extensively studied due to their microscopic size, high quality factor and the possibility of achieving low threshold lasing[1-8].

These systems exhibit novel features arising from the ability to tailor the electromagnetic field and the photon density of states in a prescribed manner, such as to concentrate and guide light on the micrometre scale, couple light between different components, and inhibit or enhance spontaneous emission. Optical microcavities can be used in many applications including strong-coupling cavity quantum electrodynamics (QED), enhancement and suppression of spontaneous emission, as optical sensors, novel sources, and dynamic filters in optical communication.

Quantum dots are supreme as a fluorescent light source for various photonic applications because of their tuneable and narrow emission spectra, short lifetimes, and resistance to photobleaching and greater processability compared to organic dyes[9-13]. Previously QDs have been incorporated into polymer microspheres by swelling in organic solvents, or by layer by layer (LbL) deposition onto the surface[14-17]. The addition of the QDs by swelling and subsequent electroactive polymer layers leads to additional surface roughness however, decreasing the Q-factor of the cavity[18]. Whispering gallery modes (WGMs) have been observed in cylindrical and spherical microcavities using QDs as a fluorescent light source, showing promising results for applications in sensing and low power lasing platforms. Hollow cavity spherical microspheres are more difficult to synthesize and dope with QDs however. In this chapter I show my results of doping polystyrene microspheres with QDs, synthesising polymer microspheres with QDs, my synthesis of microtube arrays and the synthesis of hollow PMMA microspheres as well as demonstrating their ability to display WGM resonances through solid state emission spectroscopy.

4.2 QD loaded polystyrene microspheres

4.2.1 QD loaded PS microspheres

In my experiments I used polystyrene (PS) microspheres with a size distribution of 5.19 μm +/- 0.5 μm which were supplied by Phosphorex. Highly luminescent CdSe/ZnSe QDs were incorporated into these polymer microspheres by the swelling of polymer spheres in the QD solution in mixtures of organic solvents under ultrasound. The spheres may absorb the organic solvent becoming a solvent swollen gel. The swelling may deform the spheres during this process, decreasing the efficiency of light being confined inside the sphere[19]. This affects the WGMs resonance, reducing or eliminating the resonant modes. In my work the polymer microspheres were placed in a sonic bath for varying times in chloroform/propanol, hexane/propanol and toluene/propanol solutions at different concentrations. At high concentrations of chloroform in the solution, the microspheres were deformed and started to coagulate, as seen under SEM (Fig. 4.1). Deformed and coagulated microspheres were found not to exhibit WGM resonances in the PL spectra when doped with QDs. The concentration of chloroform was therefore limited to a maximum of 5 % w/v of chloroform and sonication times to less than 10 minutes to avoid microsphere deformation. Because of its miscibility in propanol and solubility of my HDA/TOPO capped QDs, chloroform was chosen as my solvent to swell the microspheres[20]. The short treatment times resulted in the majority of QD to be incorporated in the surface and the top ~100 nm of the sphere. Using fluorescent confocal microscopy (Fig 4.2) it was confirmed that the QDs were successfully incorporated into the microspheres as I observed the strong emission from the spheres

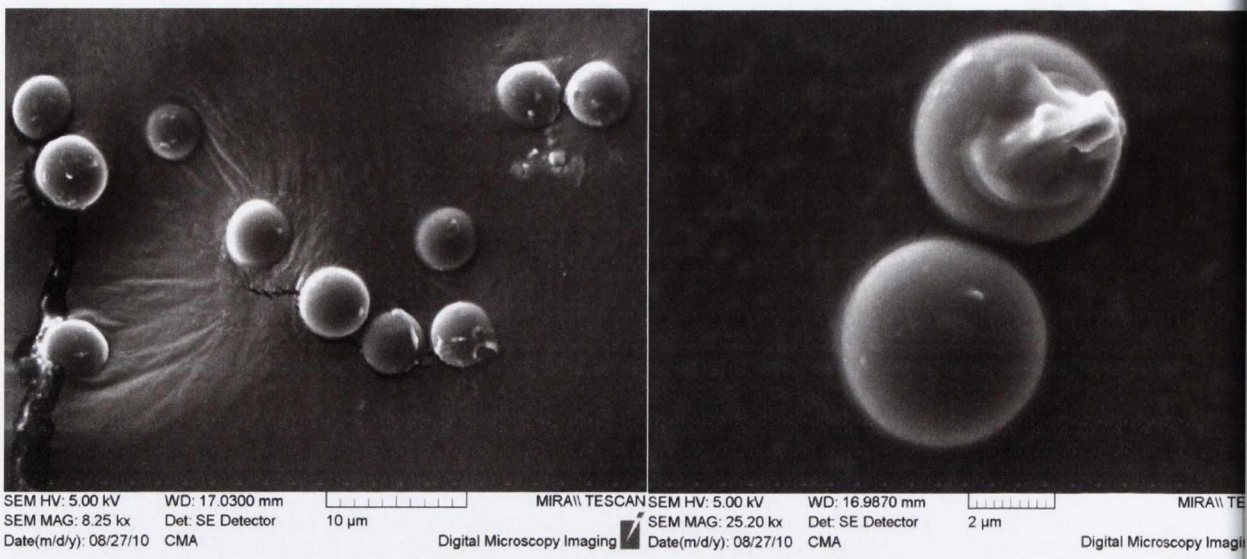

Fig. 4.1 SEM images of deformation of microspheres by sonication of PS microspheres in chloroform and propanol 10 % w/v solutions

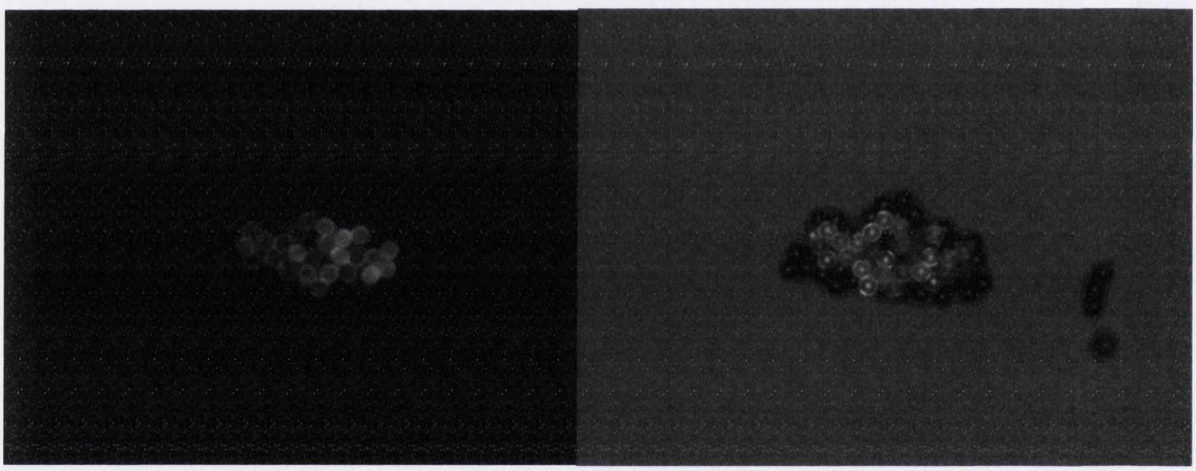

Fig 4.2. PS microspheres with CdSe QDs incorporated into them under UV light (left,) and white light (right). Magnification is at 50x.

Selected SEM images showed that some QDs have aggregated onto the surface of the PS sphere (Fig 4.3, left). This can lead to increased surface roughness of the sphere, which can potentially scatter light out of the microcavity and decrease the Q-factor of the microsphere. QDs aggregates can also be seen fully infiltrated beneath the surface (inside in microsphere), while still keeping their spherical shape (Fig 4.3 right). Although some QD aggregates were seen using SEM, according to fluorescent microscopy the microspheres appear to have a quite uniform coating of QDs at the

surface (Fig. 4.4). SEM samples were prepared by drop casting a sample onto a glass substrate, then gold coating the sample. I have found that microsphere deformation was minimal when using QD solutions in 5 % w/v chloroform and propanol mixtures for sonication times less than 10 minutes, while the swollen microspheres still showed bright PL emission under fluorescent microscope (Fig. 4.4).

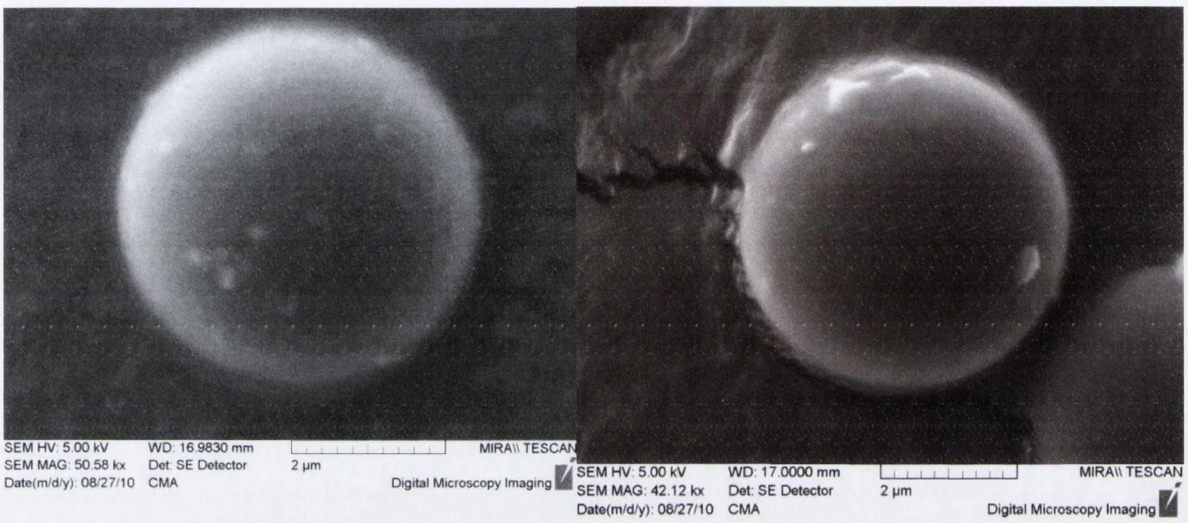

Fig. 4.3. SEM image of PS microspheres infiltrated with QDs.

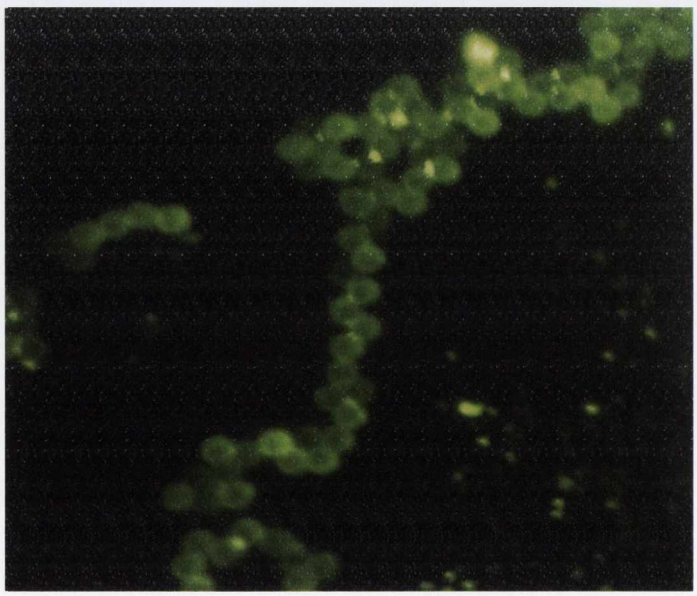

Fig. 4.4 Fluorescent microscopy image of PS doped microspheres.

Emission from the CdSe QDs can clearly be seen and WGM resonance peaks are strongest on the red side of emission (Fig. 4.5, top). WGM peaks seem to be the strongest at the maximum QD emission as expected. This is thought to be due to the Purcell effect, which states that the rate of spontaneous emission can be enhanced when in a resonant cavity. In some cases modes from other connected spheres may also be present in the spectra as the laser light passes from sphere to connecting sphere. Using optical microscopy I can focus the laser light into the sphere for more efficient laser light to sphere coupling (Fig. 4.5, bottom). The laser light can be seen to be guided around by the microsphere and exiting the opposite side, indicating good coupling between the light and the sphere which is necessary to observe the WGM resonances[21].

Periodic excitation modes are seen for the highly spherical PS microsphere. Light is easily coupled into the cavity and the sharpness and regularity of the modes shows a Q factor of up 3.5 x 10^4 to for the microsphere. QD emission is seen at 575nm, with stimulated emission from WGMs continuing on to 800 nm and beyond. The WGM peaks from 600 nm upwards may be due to the enhancement of PMMA autoemission spectra when using laser light at high intensities (above 10 % power)[22].

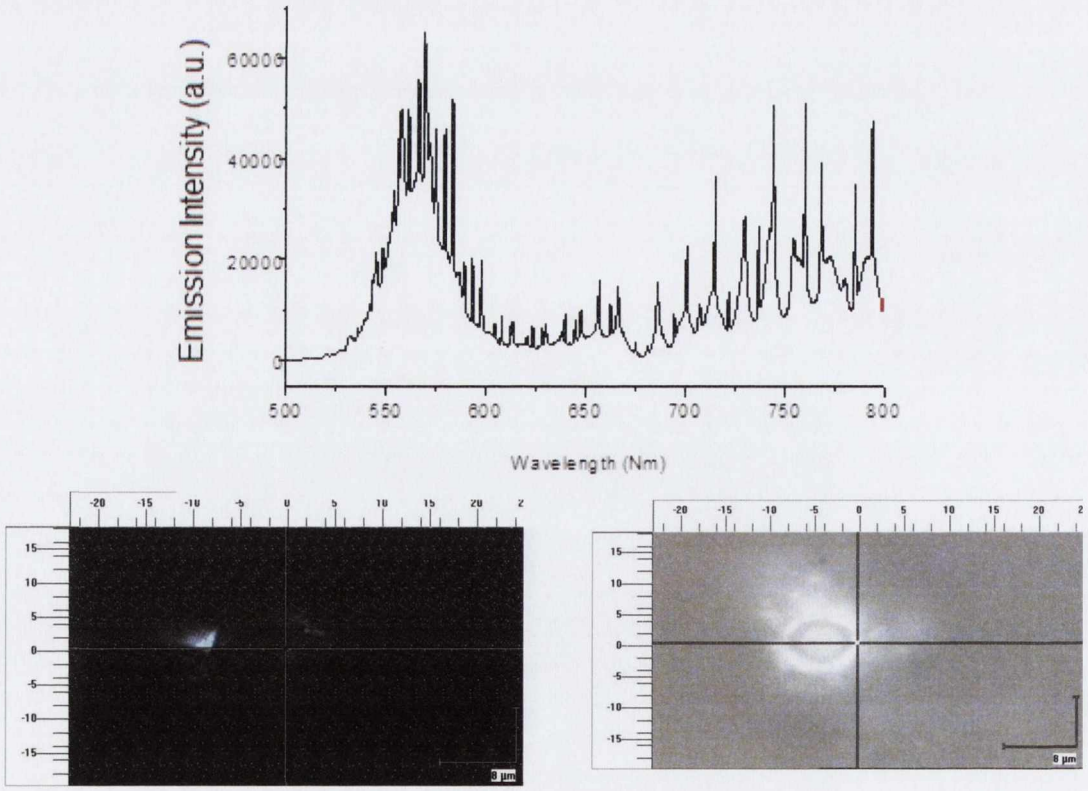

Fig 4.5 Steady state PL spectroscopy of PS microspheres infiltrated with QDs (top), with bright field (right, bottom) and laser light (left, bottom) microscopy images.

Quality factors for WGM spectra were calculated using equation (1)[23]:

$$Q = \frac{\lambda}{FWHM} \quad (1)$$

With λ being the resonant frequency, and FWHM being the full width half maximum of the peak a value of Q = 6.1 x 10^3 can be calculated from peak in Fig. 4.6, top (left). The peak was fitted using Origin 8, using a Gaussian fit (Fig. 4.6). Below are the results of my multiple peaks fitting for a typical PMMA microsphere:

Table 1: Results for multiple peak fitting for WGM resonance peaks shown in Fig, 4.6:

Peak	Area	Center (nm)	FWHM (nm)	Height (A.U)	Q Value
1	250.21543	607.47932	0.14249	1401.13183	$4.25x10^3$
2	426.92563	607.91681	0.18269	1864.53038	$3.32x10^3$
3	447.51997	608.33924	0.13543	2636.56252	$4.49x10^3$
4	500.33113	608.74947	0.12738	3134.06263	$4.78x10^3$
5	530.31105	609.1315	0.12168	3477.33874	$5.00x10^3$
6	555.08751	609.50567	0.12006	3689.07996	$5.07x10^3$
7	456.49392	609.85529	0.10609	3433.19187	$5.75x10^3$
8	316.40335	610.18301	0.09548	2643.93122	$6.39x10^3$
9	120.20774	610.49439	0.07268	1319.56584	$8.40x10^3$

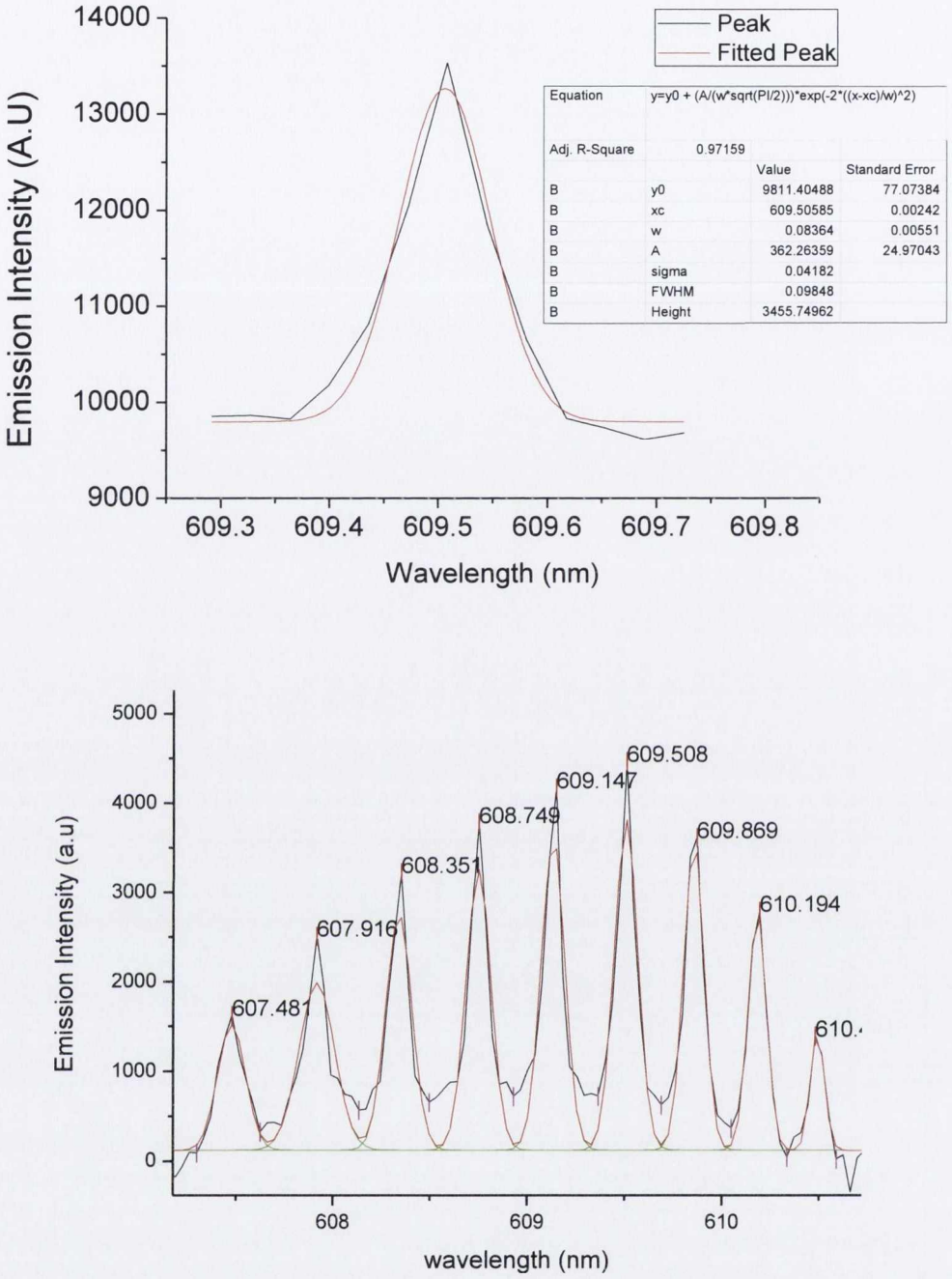

Fig. 4.6 WGM resonance peaks fitted using a Gaussian curve for a single peak (top) and multiple peaks (bottom).

4.2.2 QD loaded PMMA microspheres

PMMA microspheres were synthesised by a microemulsion polymerisation of methyl methacrylate (MMA) in a 75 wt % solution of methanol and water. The polymerisation process was performed at 75 ^{o}C for 8 hours using azobisisobutyronitrile (AIBN) as the

radical initiator. Exceeding of this polymerisation time led to degradation of the microemulsion and cross polymerisation of the microspheres into random polymer clumps. A broad distribution of microspheres of sizes 500 nm to 5.5 μm were synthesised using this procedure (Fig 4.7). Size separation of polymer spheres was achieved by centrifugation of the dispersions of microspheres at 100 rpm, 200 rpm and 500 rpm. This gave us a more focused size regime of microspheres to work with when doping with QDs by removing coagulated polymer spheres. Although the size dispersion of the initial spheres was quite high, they could be separated out to a narrower size distribution of <10 %, which were then doped using QDs.

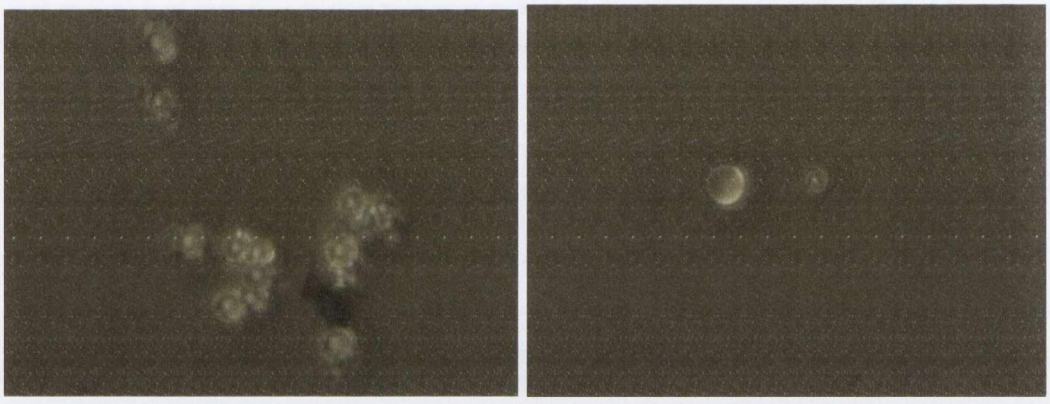

Fig. 4.7. Optical microscope images of PMMA spheres prepared without QDs (left) and with QDs (right). The magnification is at 150x.

During the polymerisation experiments it was found thatboth CdSe and core shell CdSe/ZnSe QDs prepared by hot injection synthesis were completely quenched when added to the MMA microemulsion solution. This could be due to a number of reasons including surface oxidation of the QDs in the methanol and aqueous media as well as the effects of the radical initiator on the surface ligands. Therefore the PMMA microspheres were doped with the same method as the PS microspheres a namely by swelling in a chloroform/propanol solution with CdSe/ZnSe QDs. Using fluorescent microscopy, I can see that swelling is an effective way to dope the PMMA microsphere without any visible loss of emission intensity from the QDs (Fig. 4.8).

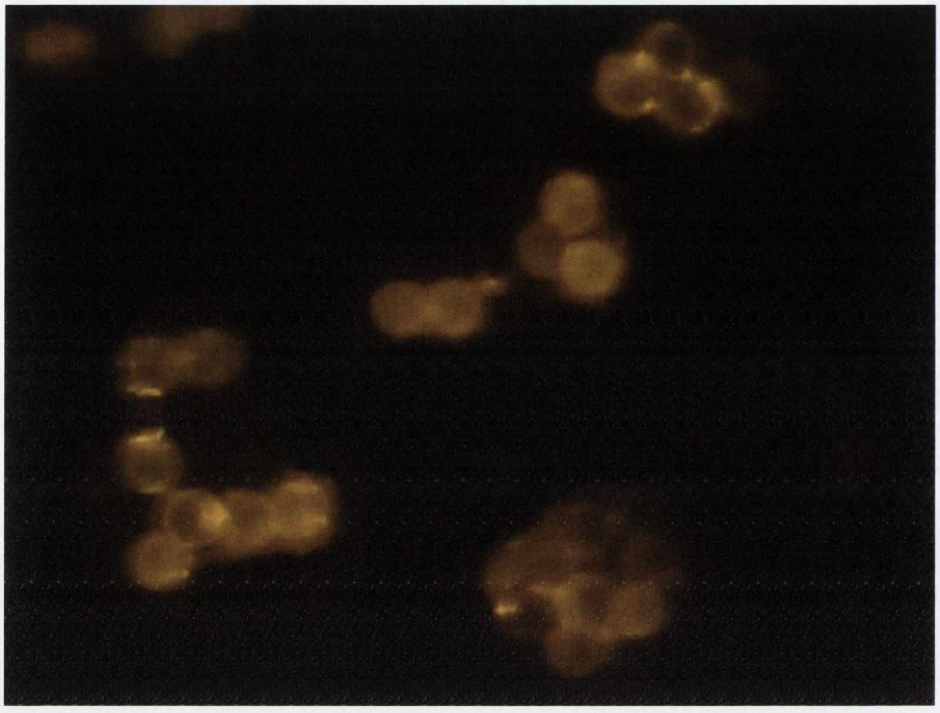

Fig.4. 8 Fluorescent microscopy image of QD loaded PMMA microspheres

In the PL spectra broad WGM can be seen between 700 nm and 775 nm indicating weak coupling to the modes of the PMMA sphere (Fig. 4.9). This may be due to surface roughness or the particle shape deviating from a perfect sphere. Multiple periodic peaks are related to different modes present in the microcavity. The peak at 550 nm and broad emission from 660 nm is typical for Raman spectra of PMMA.

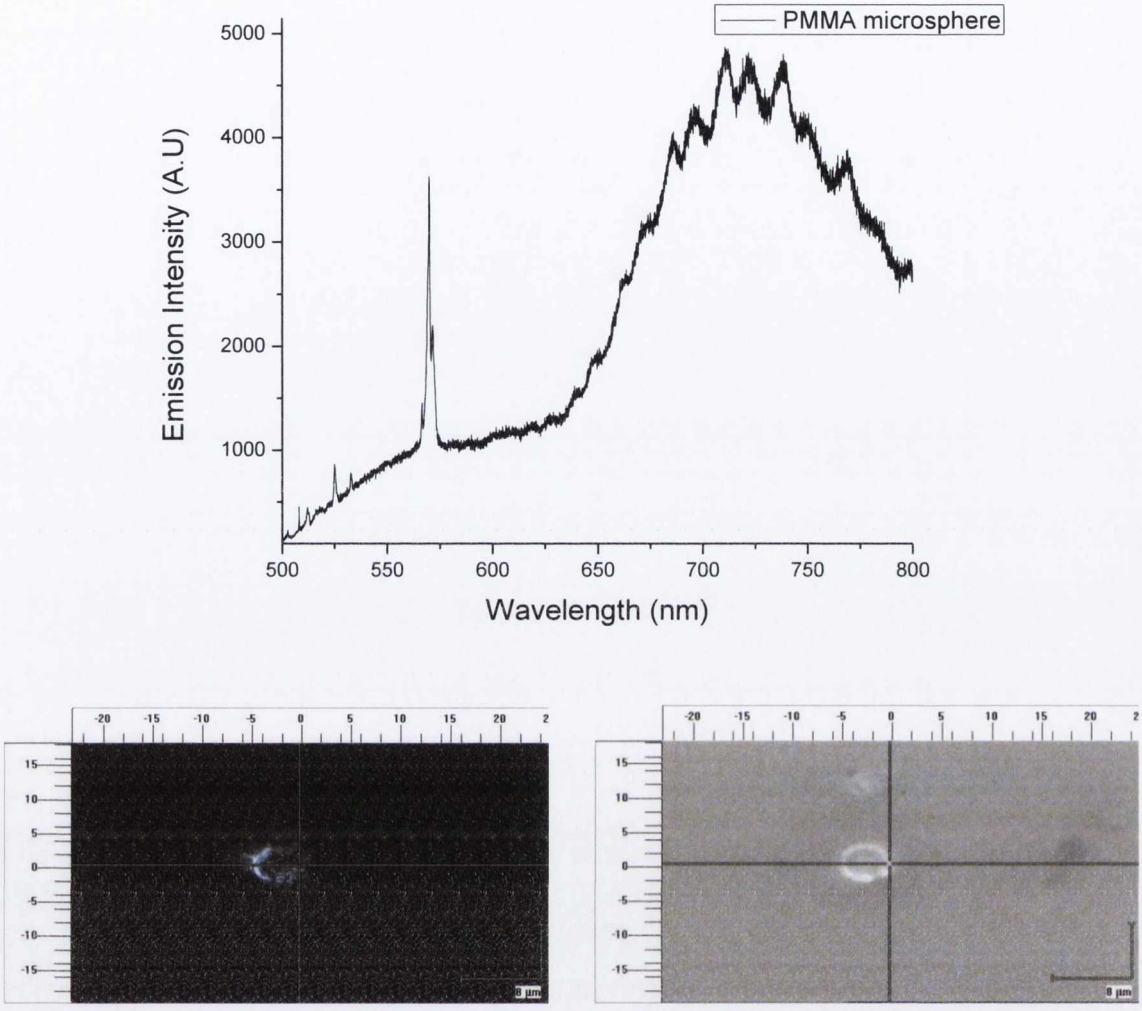

Fig 4.9. Top: PL spectra of PMMA microspheres showing characteristic Raman peaks of PMMA at 570nm and broad emission from 600nm to 800nm. Bottom: Bright field (right) and laser light (left) images of the microsphere.

The laser light is focused at the edge of the sphere, to ensure the strongest coupling of the laser light to the sphere. Light from the laser is guided around the sphere and exits the other side, suggesting the sample is of sufficient quality to trap and guide light effectively. Spheres doped with QDs with an emission centred at 570 nm were also tested using solid state PL for WGMs (Fig. 4.10).

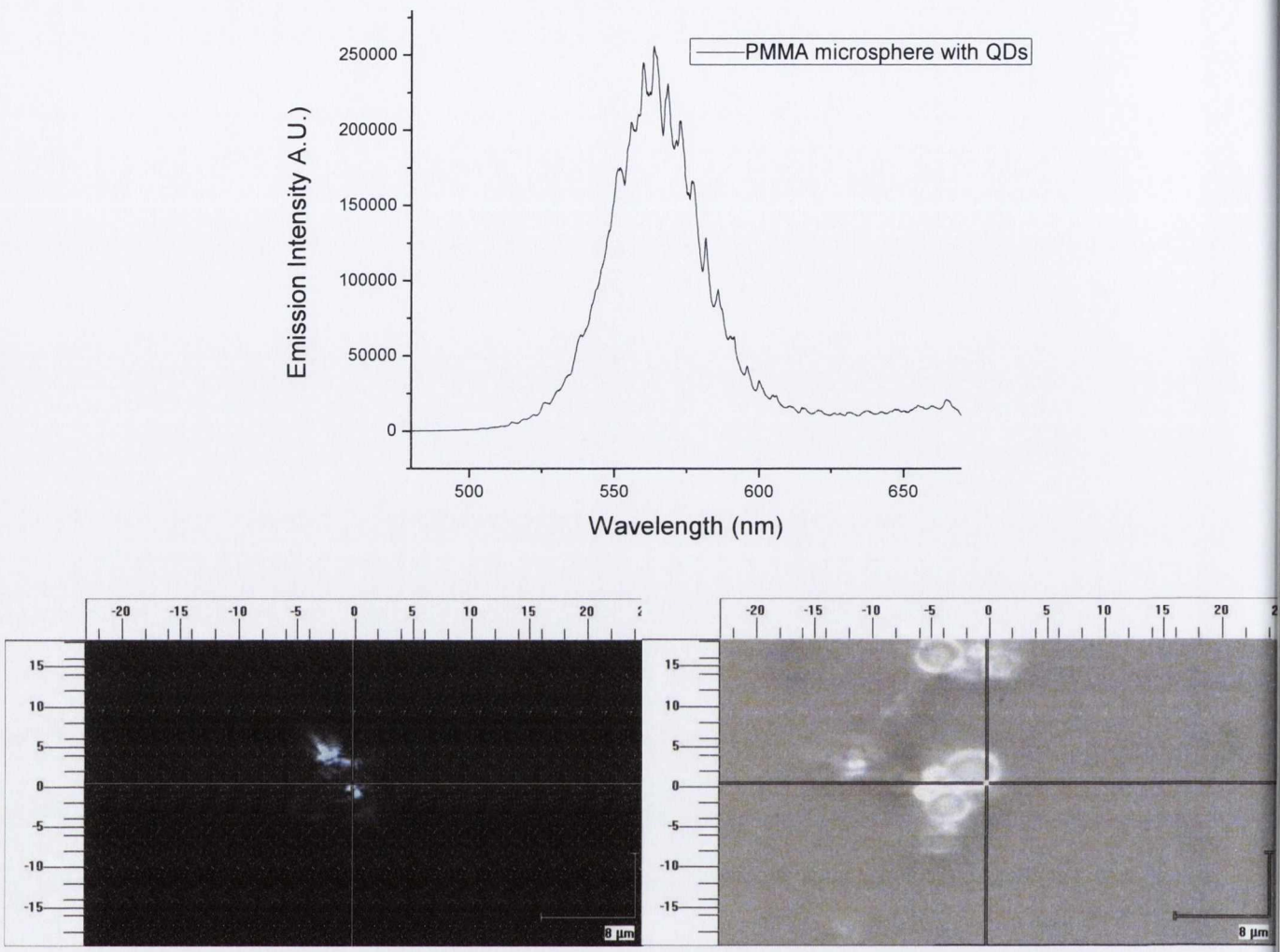

Fig. 4.10. Top: steady state PL emission spectrum of the QD loaded PMMA microsphere. Bottom : Bright field (right) and laser light (left) images of the microsphere.

Here I focused on an aggregate of four spherical microcavities to see the change in the WGM spectra. I focused on the largest of the spheres, with the laser light being guided out the opposite side of this sphere (Fig. 4.10, bottom). WGM resonances were weak, with broad peaks, indicating that light may be leaking into the other spheres or escaping due to the sphere not being perfectly spherical and also likely due to some surface defects.

4.3. Quantum dot loaded hollow PMMA microspheres

Synthesis of hollow microspheres has recently been an intensively explored area due their potential applications in drug delivery, cosmetics, insulating materials and sensors[24-28]. Preparation of uniform hollow spheres can be difficult however. Multi-pot synthetic routes require high temperatures and etching steps which increase the cost of synthesis. This prevents commercially available polymer spheres from entering the market at low cost as well as limiting the synthesis of spheres on a large scale[25,29,30]. For instance, hollow glass spheres are available with sizes from 10 μm and up and can be coated with a variety of metals for fillers for composite materials. The preparation of these spheres usually involves high temperatures of over 1000 ^{o}C using ultrasonic spray pyrolysis and sol-gel techniques with the resultant spheres prone to cracking and breakage due to their brittle nature [31].

The use of spray drying of polymer solutions has previously been reported as a versatile method for production of a range of polymer microspheres for biological applications. For example, polysaccharide microspheres were formed by spray drying a solution of chitosan, hyrdoxypropyl-B-cyclodextrin and polyethelyene glycol to form spherical microspheres to study the release of bovine serum [32]. Spheres prepared by this methods exhibit a large size distribution and rough surfaces, rendering them unusable for photonic applications. Manitol, trehalose and insulin solutions have also been used in spray-freeze-drying methods to create spherical shapes showing that a range of solutions may be used to form microspheres [33,34]. The easy addition of biological agents to these systems furthers the applications of microcavities as possible lab on a chip and sensing candidates, but so far it has not been shown that these methods can enable to manufacture microspheres with hollow cavities and sufficient quality for optical applications.

Solvent evaporation techniques for the formation of hollow microspheres have been previously reported using water-oil-water emulsions of polystyrene and acrylonitrile-butadiene-styrene/polycarbonate[35,36]. This method typically produces spheres with diameters of 100 μm. Hollow polyaniline/Fe_3O_4 spheres were also produced by emulsion polymerisation in a multistep process giving spheres of diameter ~1 μm[37].

In my work I developed a novel approach for production of hollow polymer microspheres that have several advantages over traditional polymer and silica hollow microspheres. My spraying technique allowed us to prepare uniform hollow PMMA microspheres which can incorporate quantum dots by *in situ* processing. In my method treating the glass with a oxidising solution of sulphuric acid and hydrogen peroxide ("Piranha etch") enables us to remove any organic contaminants and promotes the formation of OH groups at the glass

surface, making the substrate hydrophilic in nature. As result the PMMA spheres can be formed by simple spraying of polymer solution over the pre-treated glass substrate when the organic solvent evaporates off to leave spherical polymer microcavities. The size and concentration of spheres on the surface can be controlled by adjusting the solution concentration and nozzle aperture.

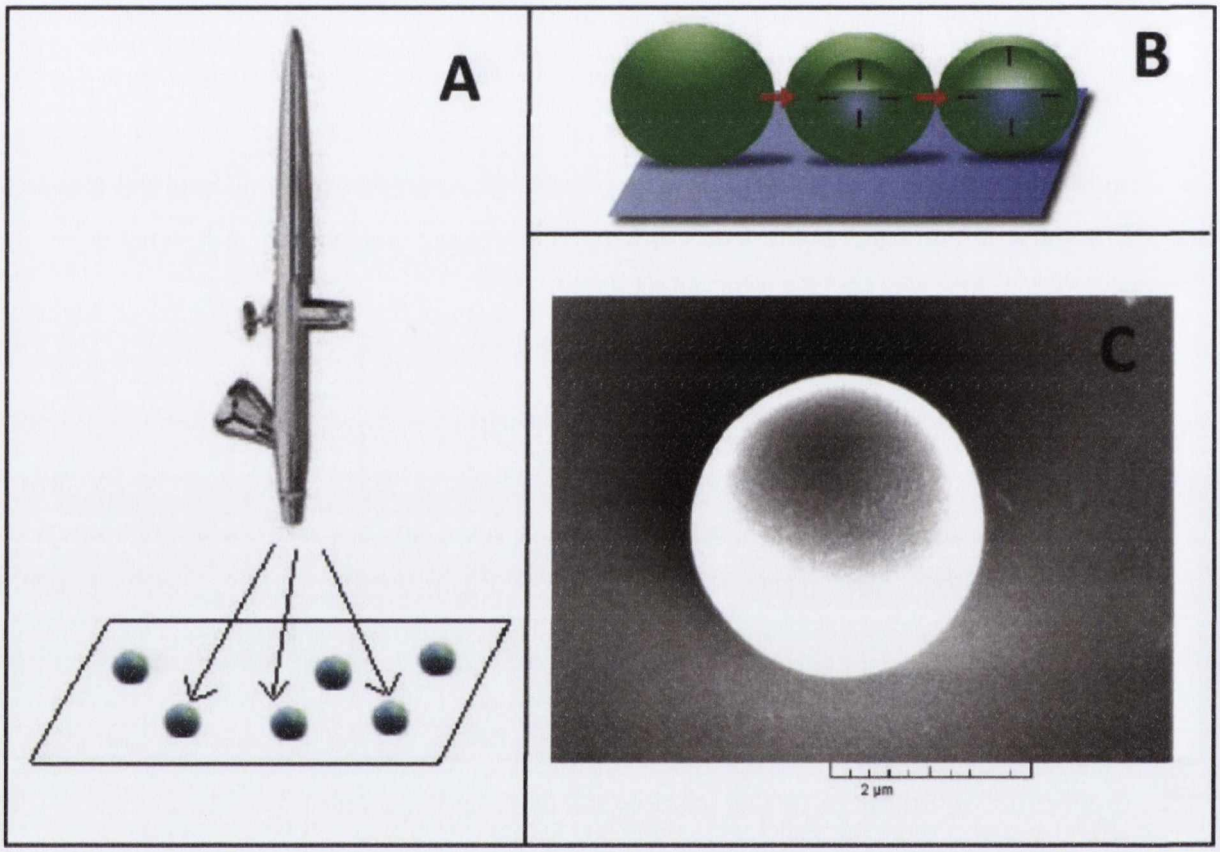

Fig. 4.11 Diagram of experimental set up (A), formation of hollow microsphere (B) and SEM of formed microsphere, 15° tilt (C).

The spherical microcavities have been produced by spray drying of PMMA dissolved in organic solutions which were blended with CdSe/CdS core shell QDs as fluorescent light sources. The experimental setup was constructed as it shown in Fig.4.11, A. An evolution air® gun with pressurised argon gas was used to spray the polymer-QD solution. Argon pressure, nozzle aperture, nozzle-substrate distance and solution viscosity were varied to find the optimum set up for the formation of spherical microcavities between 0.7-5 µm.

To form spheres the glass slides were cleaned with a solution of hydrogen peroxide and sulphuric acid to remove an organic contaminants and promote –OH bonds on the surface.

This is a well-known treatment for glass substrates and creates a hydrophilic surface that increases the wetting angle of polar solvents[38].

As the solvent evaporates on the surface of the glass slide, the polymer dries at the solution-air interface forming a hollow sphere on the substrate (Fig 4.10, B). The hydrophillicity of the glass slide determines the shape of the microsphere formed as well as the area of contact between the final sphere and the substrate. When the treated surface is smooth, well-shaped spherical microstructures are formed (Fig. 4.11, C and Fig. 4.12, A). Without acid treatment it was found that the hydrophillicity of the glass slide surface was not sufficient for microsphere formation (Fig. 4.12, B).

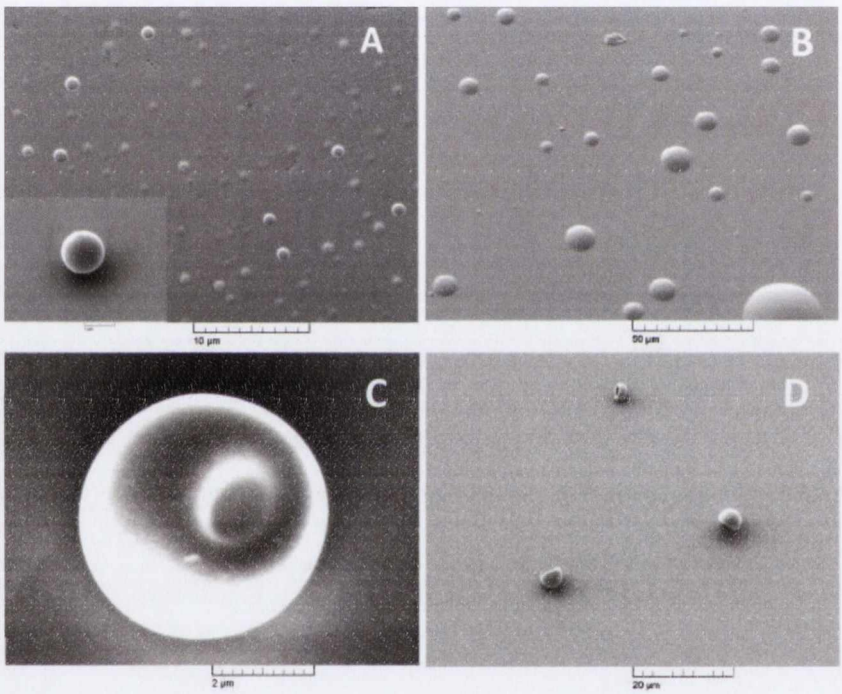

Fig. 4.12 A) Panorama SEM of PMMA spheres sprayed with a 5 % w/v solution of toluene/PMMA and (inset) close up of single sphere with 15° tilt. B) PMMA spray dried onto untreated glass surface, 15° tilt C) Electron beam damage of PMMA sphere by SEM, 15° tilt D) Collapsed spheres formed by spraying 10 w/v of toluene/PMMA solution, 25° tilt.

The PMMA microspheres were investigated using scanning electron microscopy and confocal microscopy to observe the morphology of the spheres and confirm their hollow structure. The QDs were used as fluorophores in confocal microscopy to observe the central cavity of the microspheres as well as in solid state photoluminescence spectroscopy where

whispering gallery modes were observed indicating the high quality of the hollow microspheres as optical microresonators.

PMMA microspheres were gold coated for SEM analysis, which sometimes resulted in the damage and collapse of the spheres due to melting under high energy electron beam (Fig. 4.12, C). Increasing the PMMA w/v solution above 7. 5% resulted in the formation of collapsed and half formed spheres (Fig 4.12, D). This can be attributed to the larger spheres formed due to the high viscosity of the polymer solution being sprayed. The thin shell of the spheres formed under certain conditions can lead to the buckling of the hollow spheres as they dry. This forms hemispheres with a small cavity in the centre (Fig. 4.12, C). Using confocal microscopy I can observe the hollow centre of the microspheres as I focus down the Z axis (Fig. 4.14). In Fig. 4.14 B we can see a thinner shell on the right side of the sphere indicating how the spheres can collapse due to a difference in shell thickness and from drying effects.

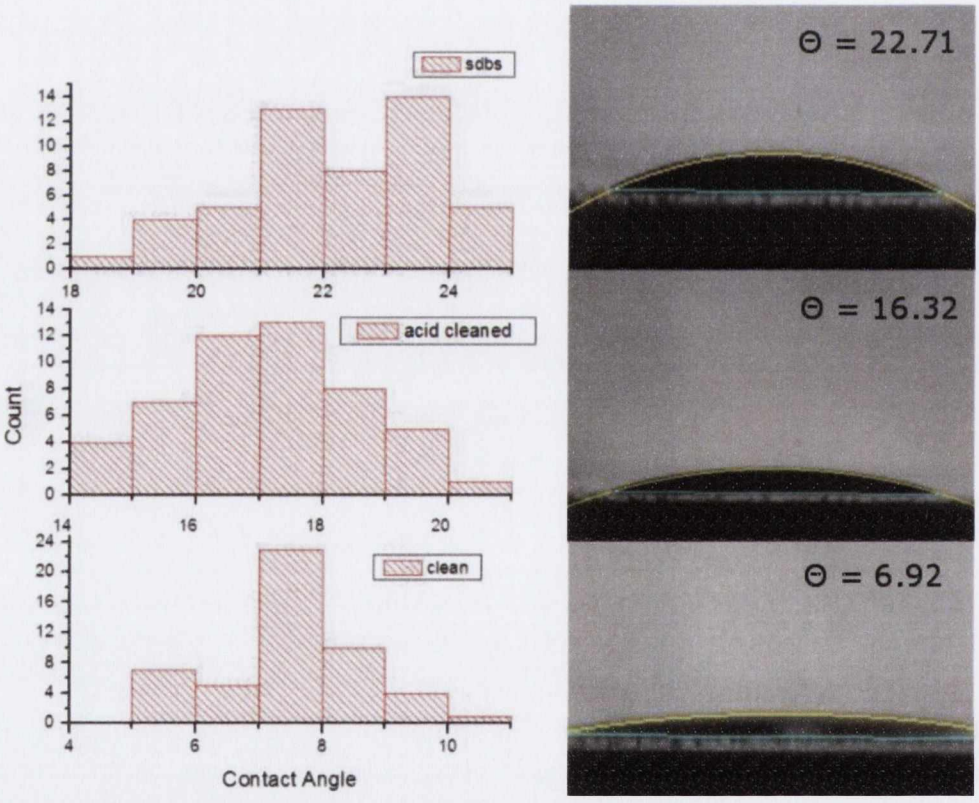

Fig. 4.13 Wetting angles of washed glass slides, treated with Pirhana etch and with SEBS. 1 µl of toluene was dropped onto the slide by a micro syringe. The wetting angles shown above are for the individual droplets in the image.

To further increase the hydrophillicity of the glass slide, an acid cleaned side was dip coated in a 0.01 M solution of SDBS in water (Fig. 4.13). The contact angle of cleaned,

piranha etched and SDBS dip-coated slides were measured by dropping 1 µl of toluene onto the slide. The contact angle of 50 1µL drops was measured for each substrate and was found to increase from 7.52^0 ±1.24 for untreated slides to 17.27^0 ±1.42 and 22.2^0 ±1.56 for piranha etched and SDBS treated slides respectively.

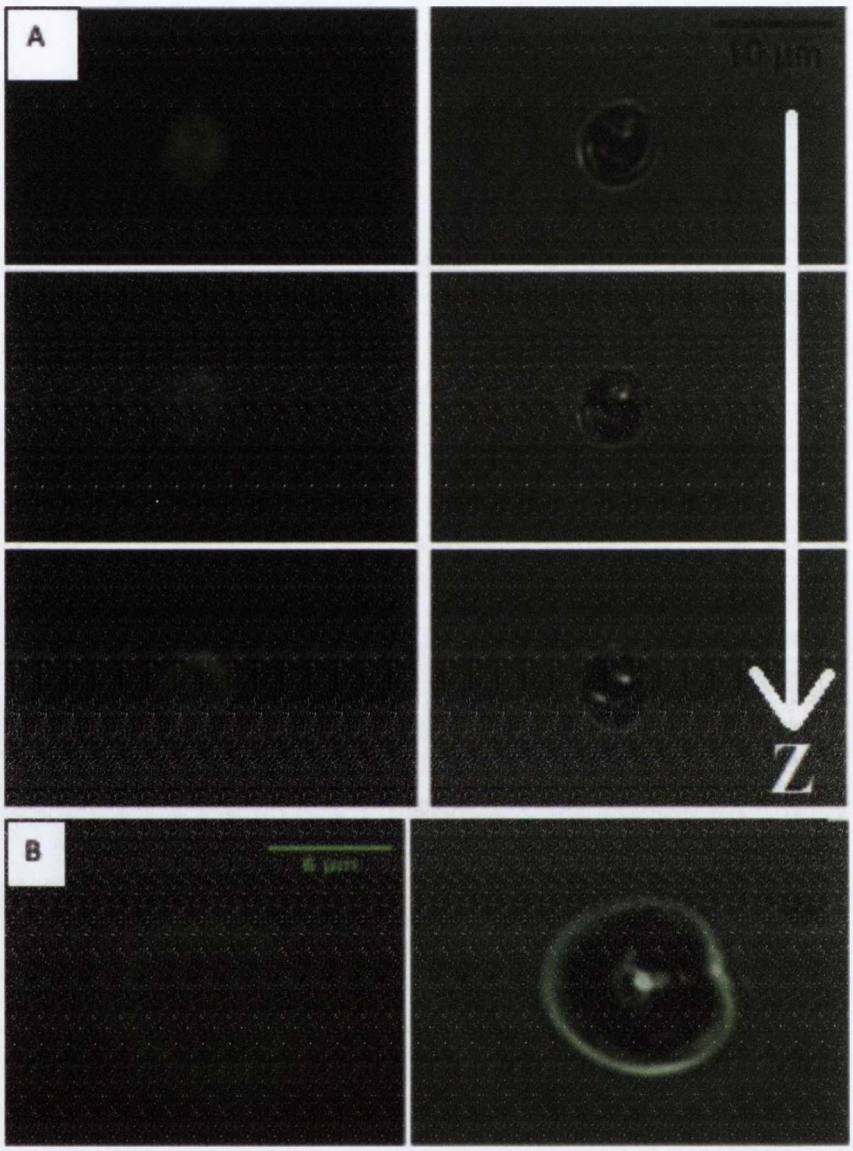

Fig. 4.14 (A) Confocal microscopy of PMMA microspheres (left under UV right under white light, going down the Z axis to show hollow centre. (B) Confocal microscopy of a larger sphere with bucking on the right hand side of the sphere.

Table 4.2. Fluorescent lifetimes of original QDs and QD loaded PMMA microspheres.

Sample	Amp 1	τ_1 (ns)	Amp 2	τ_2 (ns)	χ^2
CdSe/CdS	82%	14.9±0.6	18%	2.4±0.1	1.05
PMMA sphere	33%	10.4±0.6	67%	1.91±0.07	1.14

FLIM of CdSe/CdS QDs in a polymer matrix and of doped PMMA spheres shows a change in the lifetimes of the sample. PL decay was fitted by two-exponential function.

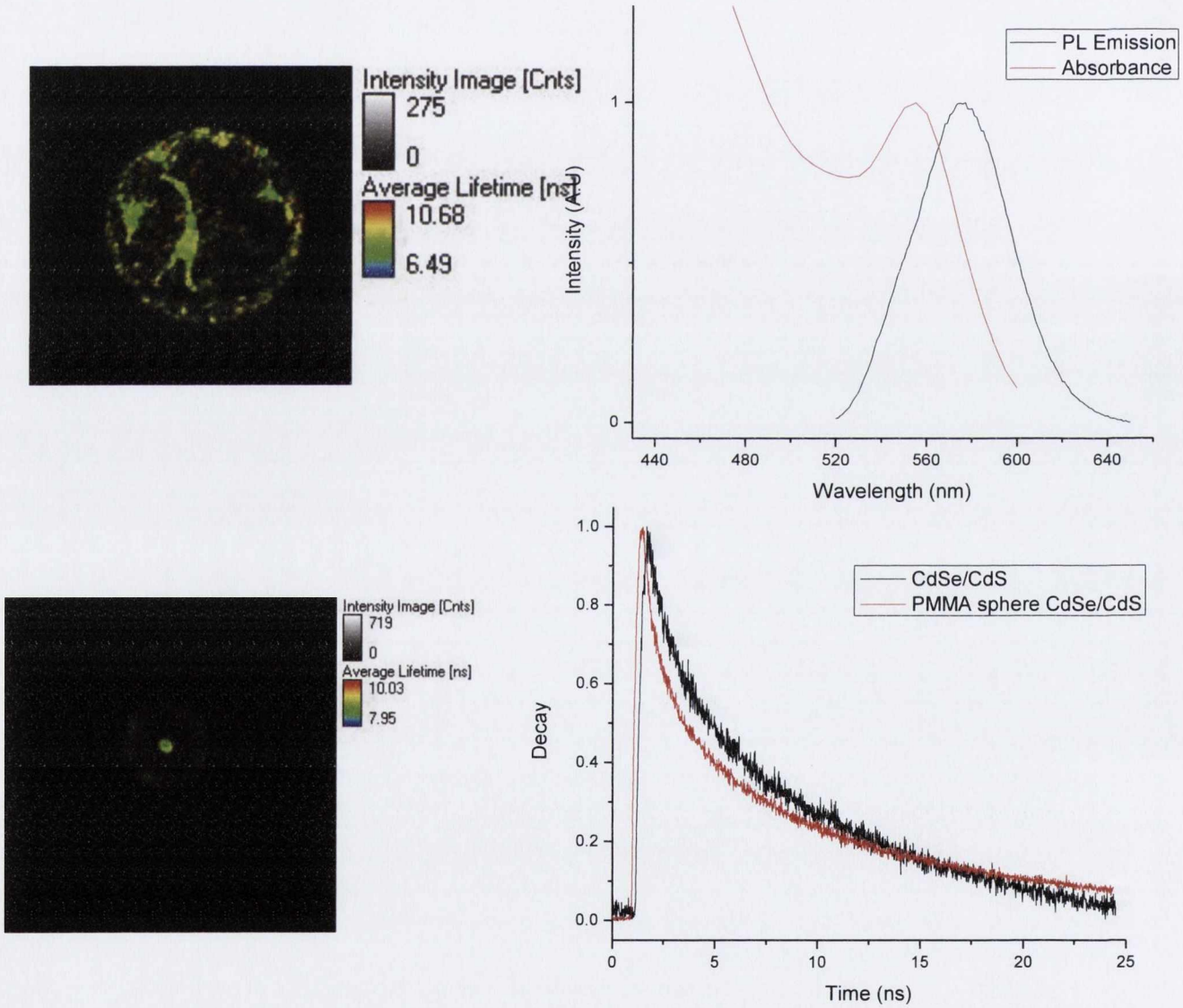

Fig. 4.20 Fluorescent Lifetime Imaging Microscopy (FLIM) image (top) and biexponential lifetime results for a single microsphere compared to CdSe/CdS QDs in a polymer matrix (bottom).

It was found that not only were the fluorescent lifetimes faster by 30.5 % for t_1 and 19.7 % for t_2 than those for original free CdSe/CdS QDs , but there was a greater contribution to the shorter lifetime (t_2) for the doped spheres too (Table 4.2 and Fig. 4.20).

Steady state PL of the spheres was measured using a Reinshaw micro-Raman setup, exciting the spheres with a 488 nm laser. Well defined WGM resonant peaks were observed in multiple spray dried particles (Fig. 4.23, Fig. 4.21). The specific structure of the WGM varied from particle to particle. A typical spectrum from a spherical particle is shown in Fig.4.22. The observed WGM peak structure is a result of coupling of electronic states in the QDs and photon states of the microsphere. The placement and spacing between WGM peaks are determined by the size and refractive index of the microsphere, while the spectral intensity distribution depends on the parameters of the QDs. For these samples both Transverse electric (TE) and Transverse magnetic (TM) modes were observable demonstrating a random orientation of nanoparticles in the PMMA matrix. The FSR was shown to correspond well with the SEM measured diameter of the particles. Particles with slight deformation break the degeneracy of the WGMs in a perfect sphere and result more complex broader features. These broad features are in fact a collection of narrow high Q modes with spacing below the spectral resolution of the spectrometer used.

A lower bound for the quality factor of the modes can be obtained by fitting the modes and extracting the FWHM. The spheres showed a quality factor (Q-factor) of 5.4×10^3 limited by the spectrometer resolution, demonstrating that these microspheres are of high optical quality and could potentially be used as optical microresonators (Fig. 4.21).

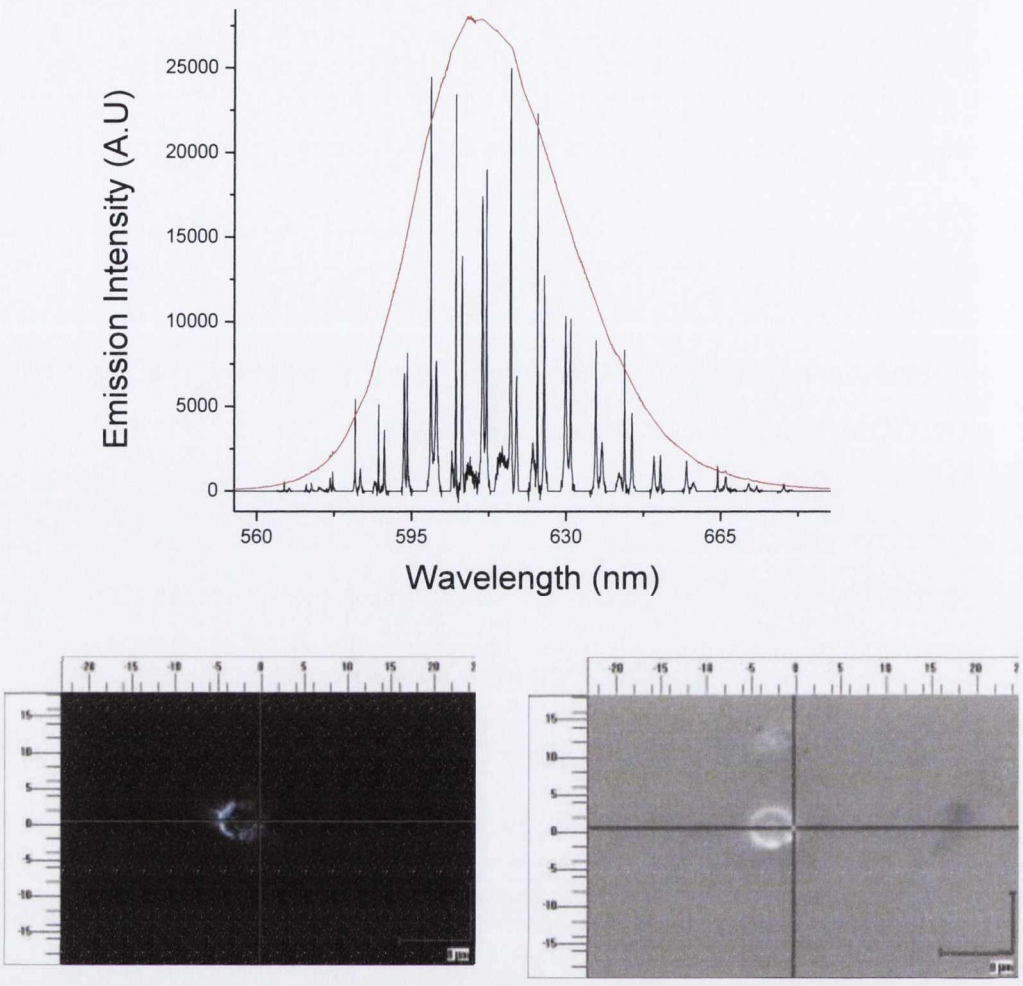

Fig. 4.21 Steady state PL showing WGM resonances (top), Bright light and laser light images of microsphere (bottom, right and left).

From additional measurements done on a variety of spheres it becomes clear that the size and shape of the microspheres influence the WGM spectra to a degree that no two spectra are completely similar (Fig. 4.22). This contrast can be seen in Fig 4.22, top right and bottom left, where the degeneracy in WGMs in the top right results in a broad WGM peak, whereas in the bottom left the peaks are well defined and spaced.

It has been shown that the spray drying method can be used for organic fluorophores whilst maintaining the WGM spectra in the sample (Fig. 4.22, bottom right). WGM resonances are more pronounced on the red side (longer wavelengths) of the emission max of the fluorophore. Coumarin dye 153 was used for this as it gave a broad PL emission, has a high PLQY and emits close to my QD samples. This illustrates the versatility of the system to incorporate not only QDs, but a range of organic dyes and nanoparticles that can

influence the effect of the emission spectra while still maintaining the optical quality needed for WGM resonances to occur.

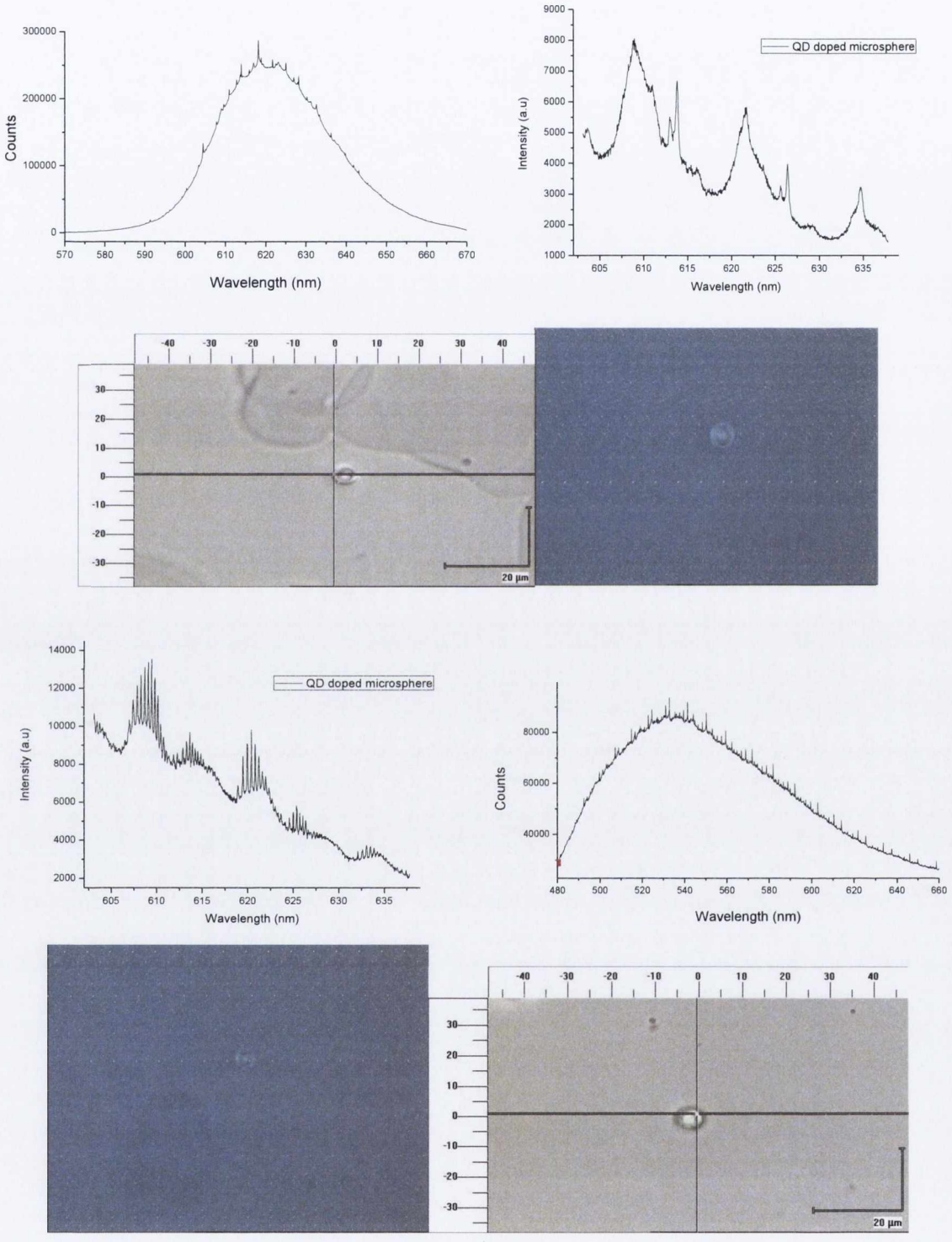

Fig. 4.22. PL emission and corresponding bright light image of hollow microsphere with QDs and coumarin 153 dye (bottom right) showing WGM resonances

4.4 PMMA microcylinder arrays

PMMA microcylinder arrays were synthesised by infiltration of a PMMA/toluene or PMMA/THF solution through a Ni metal membrane from Tecan Ltd (Fig. 4.23). A 10 % w/v solution of PMMA dissolved in toluene and THF was prepared and vacuum infiltrated through the substrate. The substrate was allowed to dry over night and the PMMA microcylinder arrays were stripped from the Ni substrate using an SEM stub. It was found that the PMMA/toluene solution provided higher quality microcylinder and therefore toluene was used as a preferred solvent in my experiments.

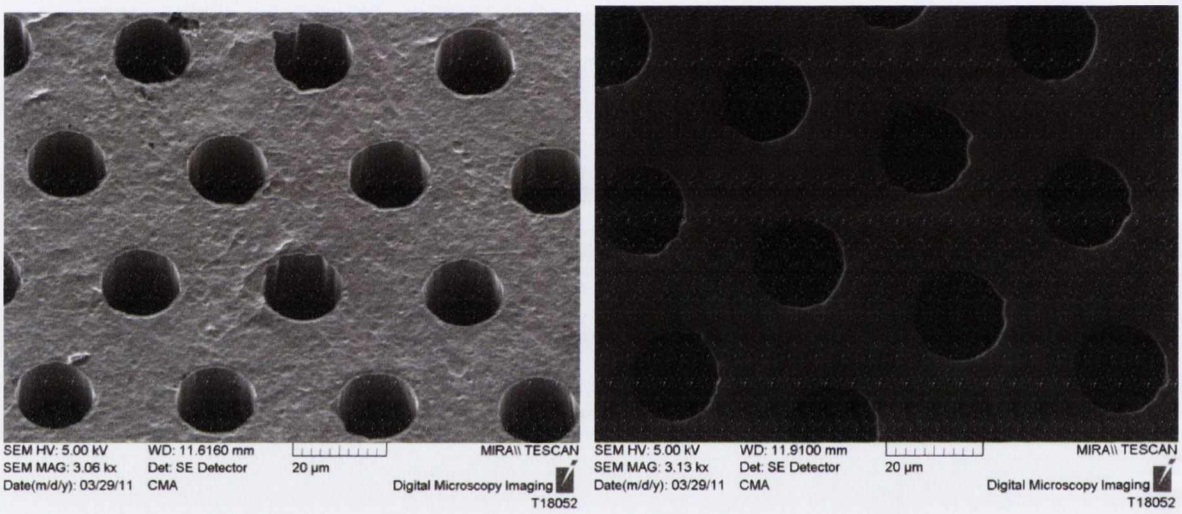

Fig. 4.23 SEM images of Ni template used to make PMMA microcylinders.

Two types of Ni template were infiltrated with PMMA solutions. The 10 µm template has straight pores all the way through, while the 5µm template has a 10µm pore that ends in a 5µm hole at one side. The 5 µm hole results in microcylinders having a small 5 µm x 5 µm head at the top of the cylinder (Fig 4.24, top right and Fig. 4.25, top left).

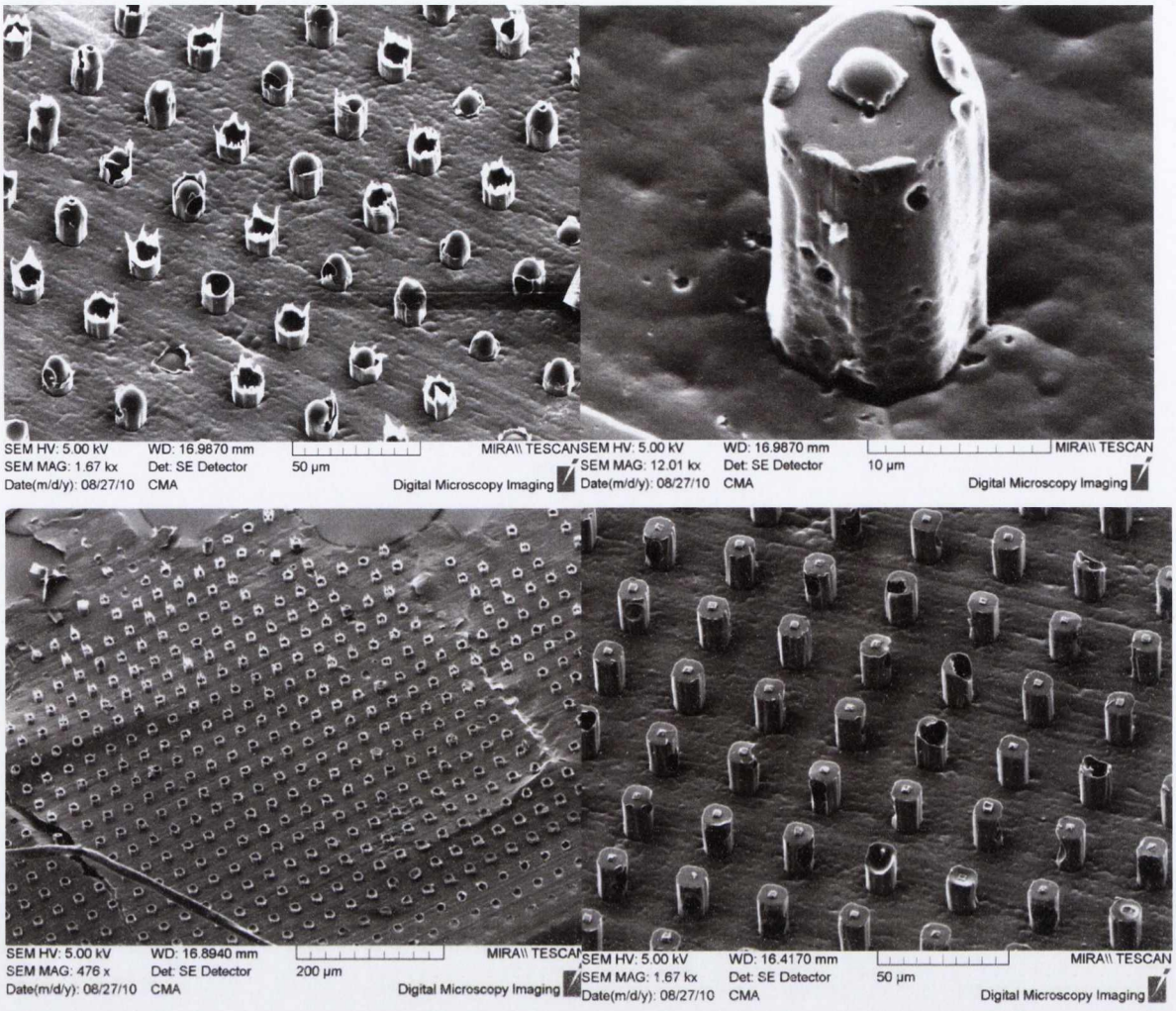

Fig. 4.24 Microcylinders prepared with varying PMMA/toluene concentrations solutions and time.

Infiltration into the porous template and subsequent removal of pillars from the porous template often resulted in broken microcyclinders (Fig. 4.24, bottom left). This was often the case when the pores were not filled enough, which sometimes created hollow and fragile microcyclinders (Fig. 4.24, bottom right, Fig. 4.25, bottom right). Hollow microcylinders were often deformed by the SEM electron beam, which damaged the surface (Fig. 4.23, top right). Solutions of less than 10 % w/v of PMMA and toluene did not result in fully formed microcyclinders (Fig. 4.24, top left), as the viscosity of the solution was too low to allow the PMMA to deposit correctly with the Ni matrix.

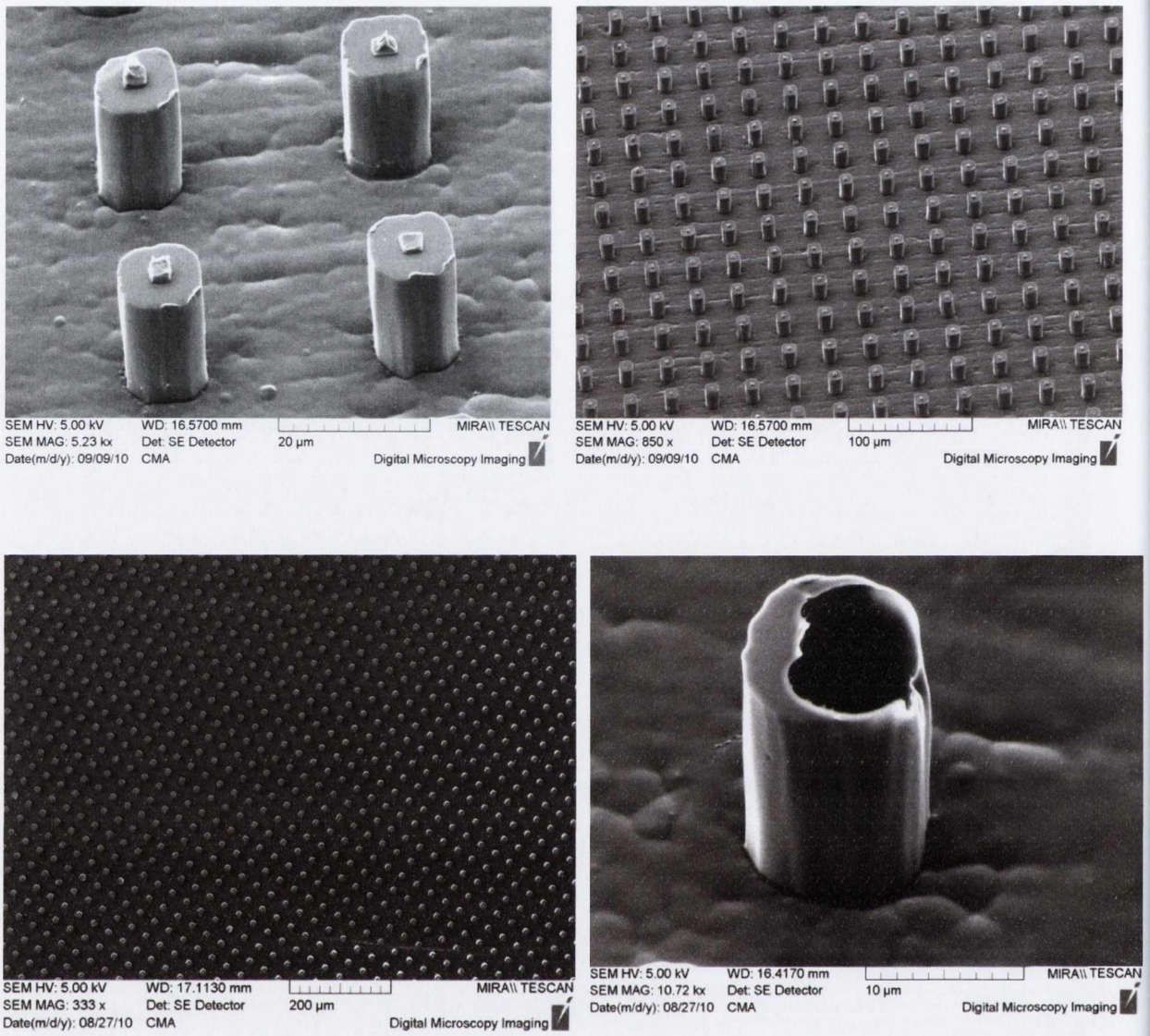

Fig. 4.25. SEM of PMMA microcylinders which were produced by the infiltration of the polymer solution through 10µm pores with a 5µm tip. Infiltration of the pores results in a uniform array of microtubes, although when not infiltrated fully can form fragile hollow microcylinders.

A solution of QDs in toluene and PMMA was infiltrated through the Ni template and imaged under a flourescent microscope (Fig. 4.26). QD aggregates were seen in some samples, with the brightness varying slightly for indivual microcylinder. This could be due to partial QD aggregation in the polymer solution and not even distribution of QDs in the polymer matrix.

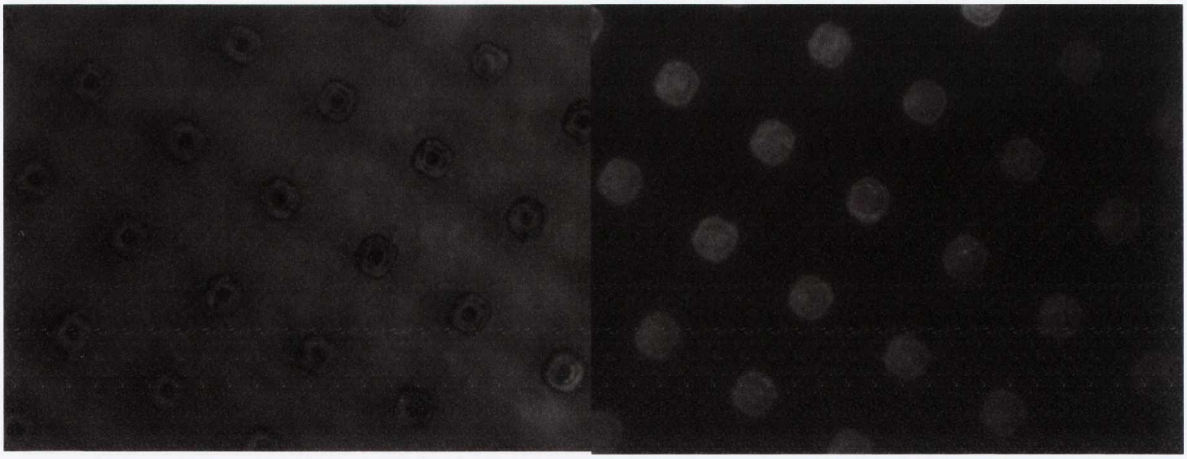

Fig. 4.26. Bright field (left) and UV (right) confocal imagesof PMMA microcylinder, synthesised using a 5μm porous Ni template

Using the same set up as for the spherical microcavities, steady state PL spectroscopy was performed to study the PMMA microcylinder arrays (Fig. 4.27). Unfortunately, no WGMs were observed. There may be several reasons for this. Firstly, the surface of mocrocylinders could be too rougth for WGM to occur. Secondly, the laser light is shone directly onto the top of the microcylinder. This would lead to very inefficent coupling to the microcavity. Laser light may also pass directly through the cylinder, instead of reflecting off the walls. Finally, the octagonal shape of the microcylinders may not be able to set up a standing wave becasue of the irregular sides. This would result in no resonant modes being created. However, the strong luminescence from pillars is still observed though.

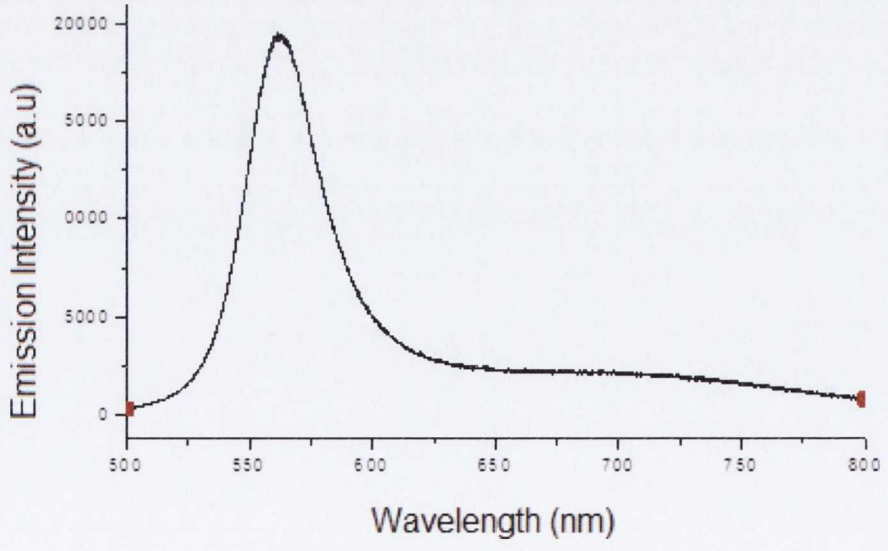

Fig. 4.27. Steady state PL of a single PMMA microcylinder. Bright emission is seen from the incorporated QDs, although no WGM resonant peaks are observed.

4.4.1 Preparation and investigation of liquid microdroplets using PMMA microcylinder arrays

The main aim of this part of my work was to explore if the PMMA microcylinder arrays could be used to create liquid optical microcavities which are based on water and glycerol. I was expecting that micropillar array could serve as a template holder for droplets due to surface tension. In this case the droplets potentially could serve as optical microcavities.

A solution of glycerol in millipore water was made using 5 % v/v glycerol to water. A water soluble organic dye, sulpharhodamine 101 was used as an emission source in the water. The solution was sprayed onto both flat PMMA surfaces and the PMMA micropillars to create microdroplets. Glycerol acted as a stabilising agent for the water droplets to prevent evaporation of the liquid spheres and increase their stability on the substrate. Steady state PL and optical images were taken for the water droplets sprayed onto the flat PMMA surface. Although circular droplets are seen, the hydrophobicity of the PMMA was not enough to form water spheres capable of sustaining WGM resonances. The water droplets could guide the laser light however, which led us to believe that if a more spherical droplet could be formed, WGM resonances could be seen from the PL emission of the doped PMMA pillars.

To do this I sprayed the same solution onto the QD doped PMMA micropillars. The decreased and roughened surface area has been shown in previous studies to decrease the wetting angle for water droplets. Indeed, it was found that spheres formed by resting on top of four PMMA pillars, and smaller spheres were formed on the PMMA base between pillars (Fig. 4.28). Solid state PL of these spheres still showed no sign of WGM resonances however, although the size distribution of water droplets were decreased dramatically because of the PMMA pillar matrix only allowing certain size droplets between pillars or resting on top of them.

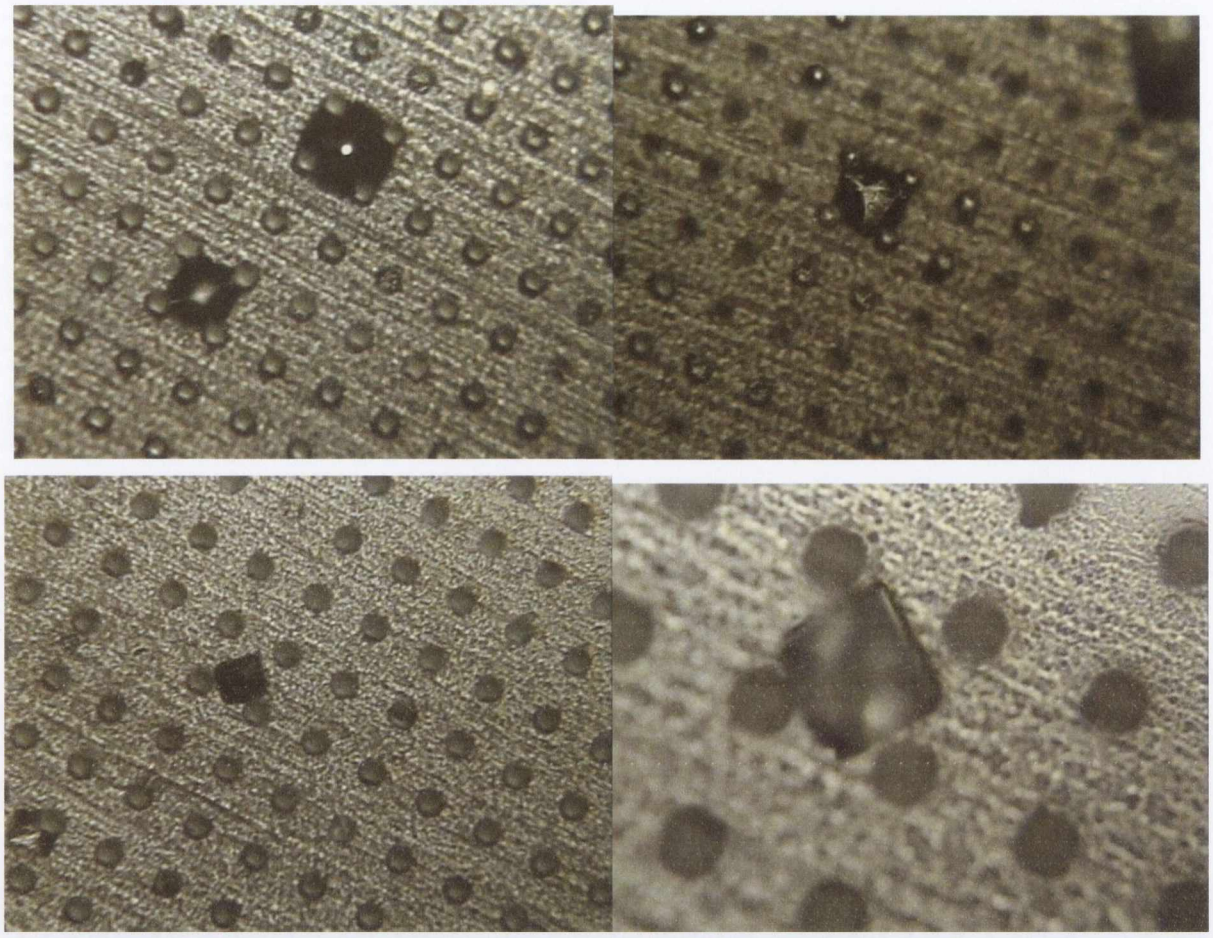

Fig. 4.28 Water on PMMA pillars substrate (above) and with the addition of salt (below).

To further test the effect of the water droplets on the PMMA pillar matrix, NaCl salt was added to the water solution and glycerol was taken out. This was to lower the surface tension of the water droplet to form different shapes between the PMMA pillars. Salt was added to the water solution in increasing amounts of 0.01M, 0.02 M, 0.05 M, 0.1 M and 0. 2M. It was found that at low concentrations, when focusing the optical microscope on water droplets sitting on top of the pillars, the droplets are quickly rearranged to sit inside the pillars, effectively minimising their surface energy (Fig. 4.28, bottom). This could also be due to slight evaporation of the water droplet while focusing the white light of the optical microscope, resulting in the droplet sitting inside the pillars. At higher concentrations, square boxes instead of spherical water droplets were formed. This was thought to be an effect of the crystalline nature of the salt in solution and lowered surface tension of the solution.

However, further more detailed studies are necessary to achieve the formation of controlled liquid optical microcavities using my cylindrical micropillar arrays.

4.5 Conclusions

In summary using various approaches I have produced a range of optical polymer based microstructures, which were loaded with QDs. Spherical polymer based microcavities demonstrated quite good optical quality, WGM and could be promising as optical microresonators. I have also developed a novel approach to produce hollow QD loaded polymer microspheres by using a spray drying technique. These spheres are formed by solvent evaporation on glass slides, leading to thin shelled microcavities that display WGMs at the emission band of the incorporated QDs. The Q-factor for these spheres was calculated to be 5.4 x 10^3 and a reduction in lifetime of the QDs was observed when incorporated into the PMMA matrix. It was demonstrated that microsphere size can be controlled by adjusting the nozzle aperture to give high quality spherical microspheres with the deviation in size distributions below ± 19 %. However, buckling and deformation of microspheres larger than 3 μm was common, due to the thin shell of the hollow microspheres. In addition I have developed a novel approach for fabrication of microcylindrical polymer arrays using commercially available Ni metal based membranes. Despite this, my PMMA microcylinder arrays were of not sufficient optical quality to demonstrate WGM, but these microstructures are still quite promising for other applications. I believe that my approaches can be further developed and optimized for a large scale production of new optical microstructures with a range of potential applications including microencapsulations, optical sensing, lab on the chip and photonics.

References:

(1) Rakovich, Y. P.; Donegan, J. F.; Gaponik, N.; Rogach, A. L. *Applied Physics Letters* **2003**, *83*, 2539.

(2) Ilchenko, V. S.; Matsko, A. B. *Selected Topics in Quantum Electronics, IEEE Journal of* **2006**, *12*, 15.

(3) Matsko, A. B.; Ilchenko, V. S. *Selected Topics in Quantum Electronics, IEEE Journal of* **2006**, *12*, 3.
(4) Vahala, K. J. *Nature* **2003**, *424*, 839.
(5) Klitzing, W. v.; Long, R.; Ilchenko, V. S.; Hare, J.; Lefèvre-Seguin, V. *New Journal of Physics* **2001**, *3*, 14.
(6) Moon, H.-J.; Chough, Y.-T.; An, K. *Physical Review Letters* **2000**, *85*, 3161.
(7) Moon, H.-J.; Park, G.-W.; Lee, S.-B.; An, K.; Lee, J.-H. *Optics Communications* **2004**, *235*, 401.
(8) Arnold, S. *American Scientist* **2001**, *89*, 414.
(9) Resch-Genger, U.; Grabolle, M.; Cavaliere-Jaricot, S.; Nitschke, R.; Nann, T. *Nat Meth* **2008**, *5*, 763.
(10) Gaponik, N.; Hickey, S. G.; Dorfs, D.; Rogach, A. L.; Eychmuller, A. *Small* **2010**, *6*, 1364.
(11) Rakovich, Y. P.; Jackel, F.; Donegan, J. F.; Rogach, A. L. *Journal of Materials Chemistry* **2012**, *22*, 20831.
(12) Komarala, V. K.; Bradley, A. L.; Rakovich, Y. P.; Byrne, S. J.; Gun'ko, Y. K.; Rogach, A. L. *Applied Physics Letters* **2008**, *93*.
(13) Purcell-Milton, F.; Gun'ko, Y. K. *Journal of Materials Chemistry* **2012**, *22*, 16687.
(14) Meissner, K. E.; Allen, A. In *Sensors, 2005 IEEE* 2005, p 4 pp.
(15) Rakovich, Y. P.; Yang, L.; McCabe, E. M.; Donegan, J. F.; Perova, T.; Moore, A.; Gaponik, N.; Rogach, A. *Semicond. Sci. Technol.* **2003**, *18*, 914.
(16) Rakovich, Y. P.; Gerlach, M.; Bradley, A. L.; Donegan, J. F.; Connolly, T. M.; Boland, J. J.; Przyjalgowski, M. A.; Ryder, A.; Gaponik, N.; Rogach, A. L. *Journal of Applied Physics* **2004**, *96*, 6761.
(17) Rakovich, Y. P.; Donegan, J. F.; Gerlach, M.; Bradley, A. L.; Connolly, T. M.; Boland, J. J.; Gaponik, N.; Rogach, A. *Physical Review A* **2004**, *70*.
(18) Gómez, D. E.; Pastoriza-Santos, I.; Mulvaney, P. *Small* **2005**, *1*, 238.
(19) Gomilšek, M. http://mafija.fmf.uni-lj.si/seminar/files/2011_2012/wqm.pdf **2011**.
(20) Miller-Chou, B. A. K., Jack L. *Prog. Polym. Sci* **2002**, *28*, 1223.
(21) Cai, M.; Painter, O.; Vahala, K. J. *Phys. Rev. Lett.* **2000**, *85*, 74.
(22) Piruska, A.; Nikcevic, I.; Lee, S. H.; Ahn, C.; Heineman, W. R.; Limbach, P. A.; Seliskar, C. J. *Lab on a chip* **2005**, *5*, 1348.
(23) Paschotta, R. *RP Photonics Consulting GmbH* **2010**, http://www.rp-photonics.com/q_factor.html.
(24) Kawashima, Y.; Niwa, T.; Takeuchi, H.; Hino, T.; Itoh, Y. *Journal of Pharmaceutical Sciences* **1992**, *81*, 135.
(25) D Gagnebien, B. D. *US Patent 5,219,561 Google Patents*

1993.
(26) Cochran, J. K. *Current Opinion in Solid State and Materials Science* **1998**, *3*, 474.
(27) Zhu, H.; Wang, J.; Xu, G. *Crystal Growth & Design* **2008**, *9*, 633.
(28) Soppimath, K. S.; Kulkarni, A. R.; Aminabhavi, T. M. *Drug Development and Industrial Pharmacy* **2001**, *27*, 507.
(29) Han, J.; Song, G.; Guo, R. *Advanced Materials* **2006**, *18*, 3140.
(30) Artemyev, M. V.; Woggon, U.; Wannemacher, R. *Applied Physics Letters* **2001**, *78*, 1032.
(31) Bertling, J.; Blömer, J.; Kümmel, R. *Chemical Engineering & Technology* **2004**, *27*, 829.
(32) Gayakwad, S. G.; Bejugam, N. K.; Akhavein, N.; Uddin, N. A.; Oettinger, C. E.; D'Souza, M. J. *Journal of Microencapsulation* **2009**, *26*, 692.
(33) Rochelle, C.; Lee, G. *Journal of Pharmaceutical Sciences* **2007**, *96*, 2296.
(34) Schiffter, H.; Condliffe, J.; Vonhoff, S. *Journal of the Royal Society Interface* **2010**, *7*, S483.
(35) Jie, L.; Hongyan, L.; Shujun, W. *Materials Letters* **2011**, *65*, 2696.

(36) Cai, P.-j.; Tang, Y.-j.; Wang, Y.-t.; Cao, Y.-j. *Materials Chemistry and Physics* **2010**, *124*, 10.
(37) Yang, C.; Li, H.; Xiong, D.; Cao, Z. *Reactive and Functional Polymers* **2009**, *69*, 137.
(38) Penfold, J.; Staples, E.; Tucker, I. *Langmuir* **2002**, *18*, 2967.

Chapter 5: Dielectric Elastomers and Quantum Dots

5.1 Introduction

Dielectric elastomers (DEs) are a new group of polymeric materials that can deform under electrical stimulation due to Maxwell forces exerted upon the film. Because of this characteristic, the interest in dielectric elastomers as artificial muscles, sensors and novel mechanical devices has increased in recent years. In particular dielectric elastomers can be used as actuators for light-weight, compact, energy-efficient and large-displacement electromechanical transducers[1-4]. An elementary dielectric elastomer actuator (DEA) consists of a thin elastomeric layer with compliant electrodes on each side. When an electric potential difference is applied between the electrodes, an electrostatic stress (Maxwell stress) causes the film thickness to reduce and the electrode area to expand[1]. Electrically tuneable optical devices represent an emerging field of application of dielectric elastomers where they show one of the greatest potentials today[4]. They are being developed for different kinds of uses, such as laser speckle reducers[5], diffractive transmission grating[6] and optical lenses[7].

Advances in high actuation properties with low voltage are key to realising some of these new applications. Using charge separation to deform an elastomer film along its x and y axis by Maxwell forces is a well-documented effect[1,8,9]. 3Ms acrylic elastomer has been used as the quintessential elastomer to compare new materials to due to its low cost, reproducible results, high processability and high elastic strain when actuated. The main aim of this part of my project is to integrate QDs within a dielectric elastomeric structure which can be electrically deformed (actuated). An actuation of the QD-doped elastomer is expected to vary the distances among each QD and its neighbours in the structure, modifying the volume and/or surface density of QDs, and thus leading to variable interactions among them and so variable absorbance and fluorescence of the whole system. I expect to use the dielectric elastomers and QDs to conceive new optical devices with electrically tuneable absorbance and fluorescence. This work also involves the development of transparent flexible electrodes for applications such as components of electrically tuneable lenses.

5.2 Actuation of Prestretched Elastomers

Initially I investigated actuation of 3Ms acrylic prestretched elastomers in order to see the effects that might influence the properties of my future DE composites.

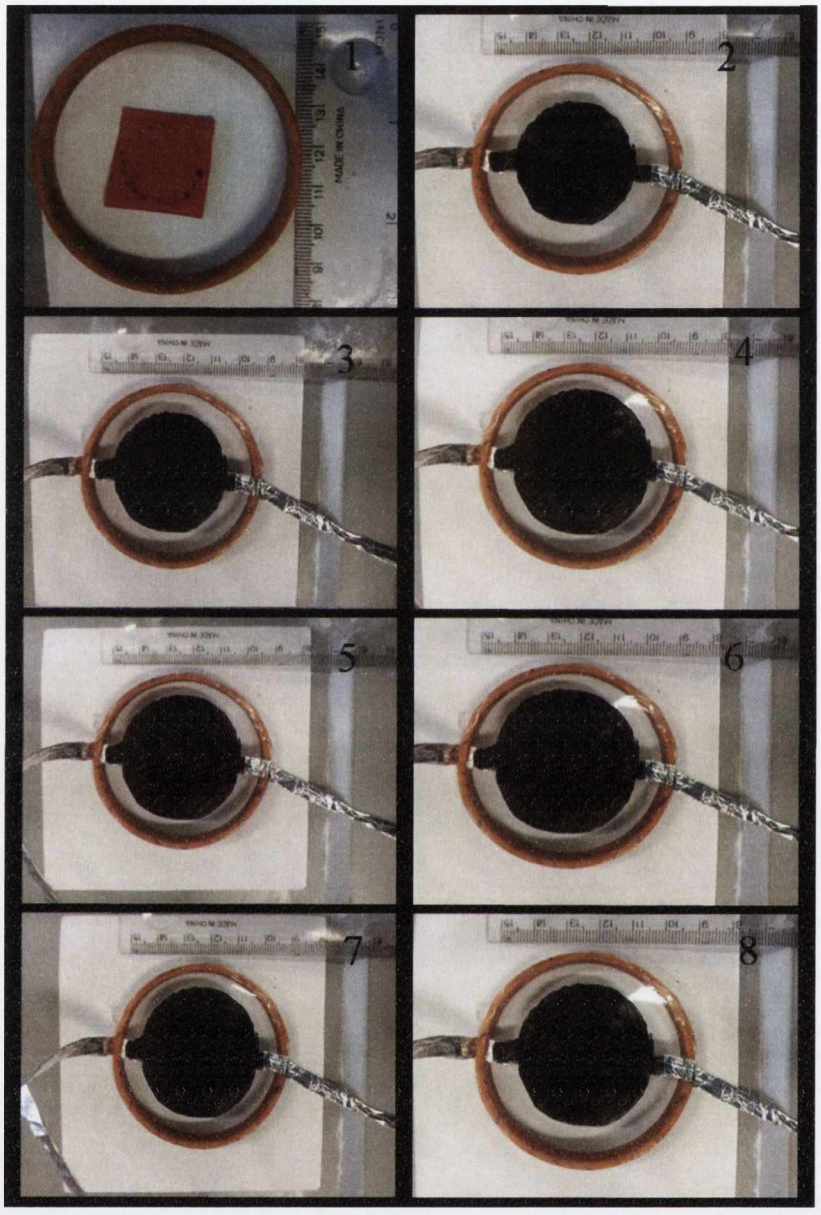

Fig. 5.1 VHB elastomer before stretching, after stretching with carbon black electrodes and with increasing voltage from 1.5 kV to 5 kV (dielectric breakthrough).

Normally actuation effects are greatly enhanced by prestretching elastomer material. My devices were built by prestreching VHB elastomer by up to four times over a circular frame (Fig. 5.1). Compliant electrodes were than painted on using a brush and carbon black paste. Voltages of 1 kV to 5 kV were passed through these devices and the

actuation measured by observing the change in the xy displacement of the film until dielectric breakdown of the film occurred (Fig. 5.1-8). Several configurations of this device were made by varying the electrode pattern (Fig. 5.2). Consistency of thickness of the prestretched film is essential for getting reproducible results, as a change in thickness can cause a loss in actuation movement and dielectric breakdown at lower voltages. The thickness of the films was found using a micrometre screw gauge before testing.

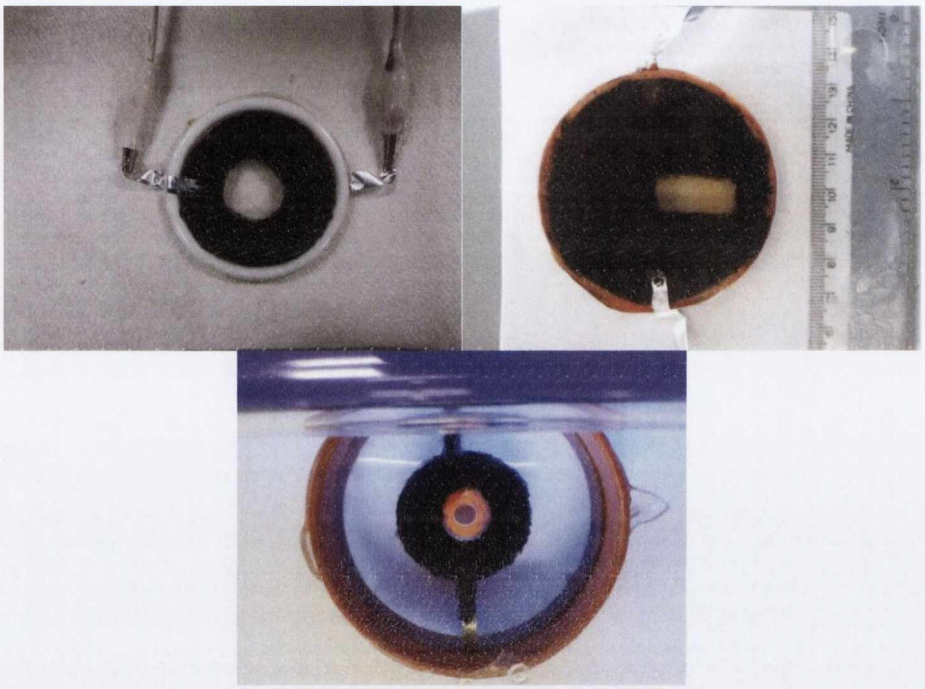

Fig. 5.2. DEA devices with different electrode configurations. Top left, shrinking hole in the centre, top right, for use with a spectrometer, bottom left, QD doped in centre ring, bottom right, expanding inner ring.

It was found that doping the elastomer by swelling in a QD (CdSe/CdS) solution gave the most evenly doped sample. Doping the sample before prestretching also minimises the chance of the film tearing or deforming during actuation. A circular actuator with no centre electrode (Fig. 5.2, top left) was found to be the most suitable for my experiments. This is as bucking of the thin film was minimal in this configuration, as well as a uniform expansion of the area under the electrode in all directions. The clear centre in the middle made it optimal for optical studies using FLIM.

5.3 Development of stretchable transparent electrodes and prototypes of electrically controlled lenses

In order to prepare transparent lenses I needed to produce stretchable transparent electrodes first. In my project these electrodes were made by spray drying PEDOT:PSS onto prestretched VHB over a heated substrate. PTFE rings were used instead of the original plastic ones to withstand deforming whilst on the heated substrate. Spray drying was done using an automated sewing machine, redesigned to hold an airbrush and configured to loop a pattern of spraying (Fig. 5.3).

.

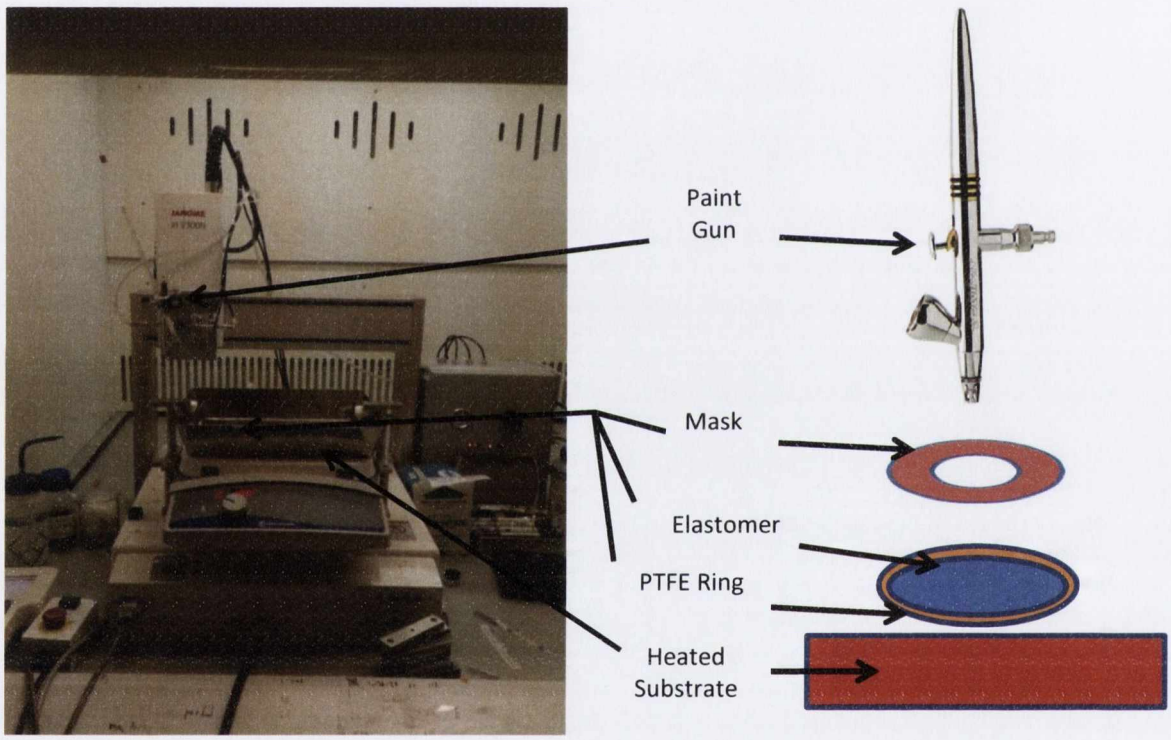

Fig. 5.3 Spray Drying apparatus with heated substrate

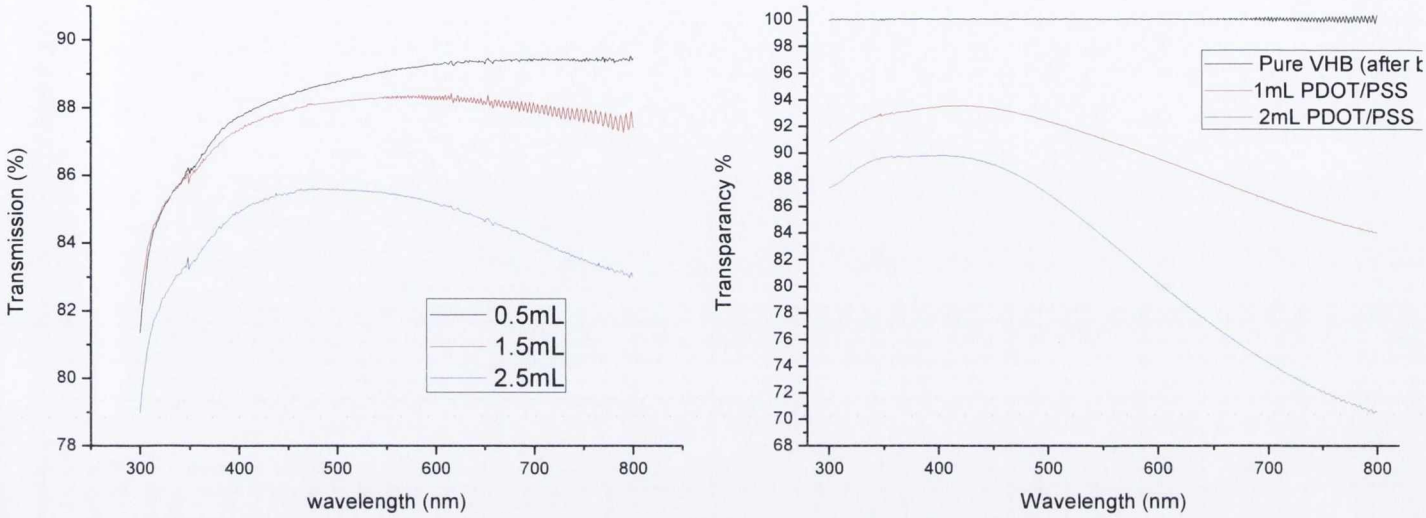

Fig. 5.4 Transparency of single PEDOT:PSS VHB film using different volumes of PEDOT:PSS (1 mg/ml)

In order to prepare transparent lenses I needed to produce stretchable transparent electrodes first. In my project these electrodes were made by spray drying PEDOT:PSS onto prestretched VHB over a heated substrate. PTFE rings were used instead of the original plastic ones to withstand deforming whilst on the heated substrate. Spray drying was done using an automated sewing machine, redesigned to hold an airbrush and configured to loop a pattern of spraying (Fig. 5.3).

Nozzle width was controlled by adjusting a screw at the top of the airbrush for fine or course spraying. The airgun used a pressurised source of nitrogen for spraying a solution of PEDOT:PSS in water onto the substrate. Initially the VHB elastomer was prestretched over a PTFE ring and held in place on a hot plate set to 110 ^{o}C. It was necessary to heat the substrate as slow drying of the solution on the surface might result in uneven distribution of the PEDOT:PSS layer, leading to cracks in the electrode and lower conductivity. This effect can be seen in Fig. 5.5.

In my experiments PEDOT:PSS was diluted from 1mL to 22.5 ml with deionised water for spray drying. The transparency of the films was then tested using a Cary UV-VIS spectrometer (Fig. 5.4). Transparency of the films is important for use as a lens and to observe QD emission and absorption through the lens when the elastomer is loaded with QDs. It was found that the maximum transparency for my films and electrodes occurred

in the window between 400-500 nm, with the transparency dipping below 85 % for films sprayed with 2.5 ml of solution.

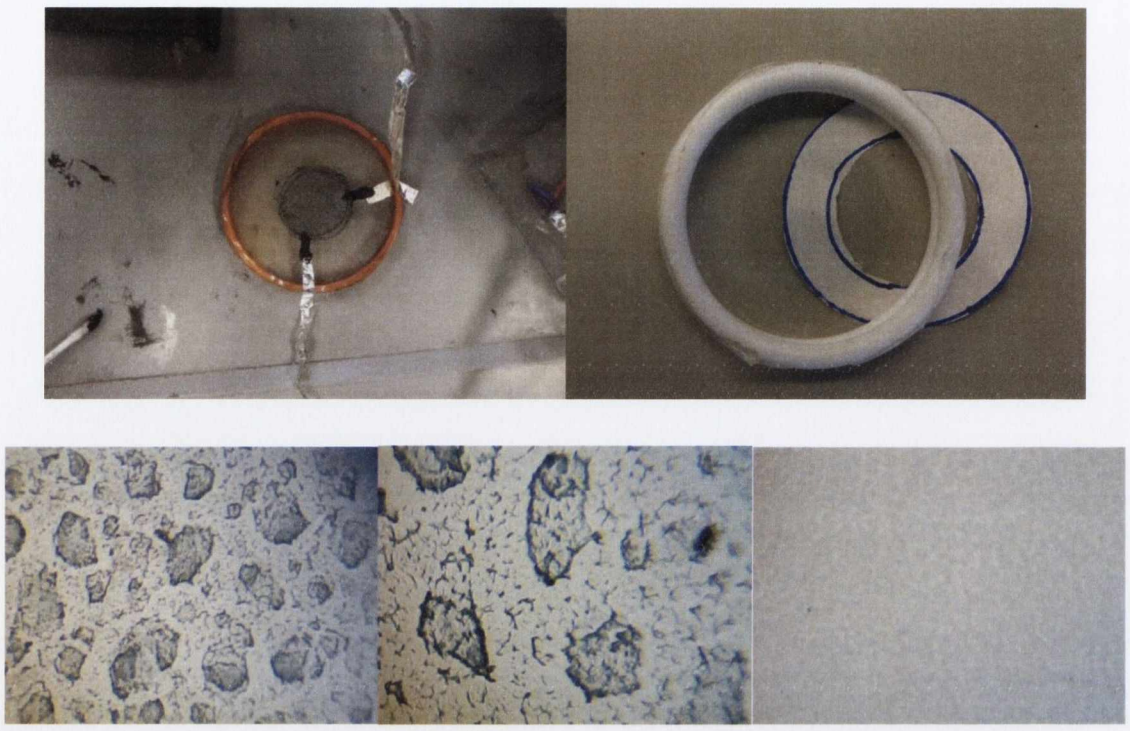

Fig 5.5. Comparison between air dried PEDOT:PSS electrode and spray dried (top, left and right) and 10x magnification of PEDOT:PSS without a heated substrate (bottom, left), air dried overnight (bottom, centre) and spray dried (bottom, right)

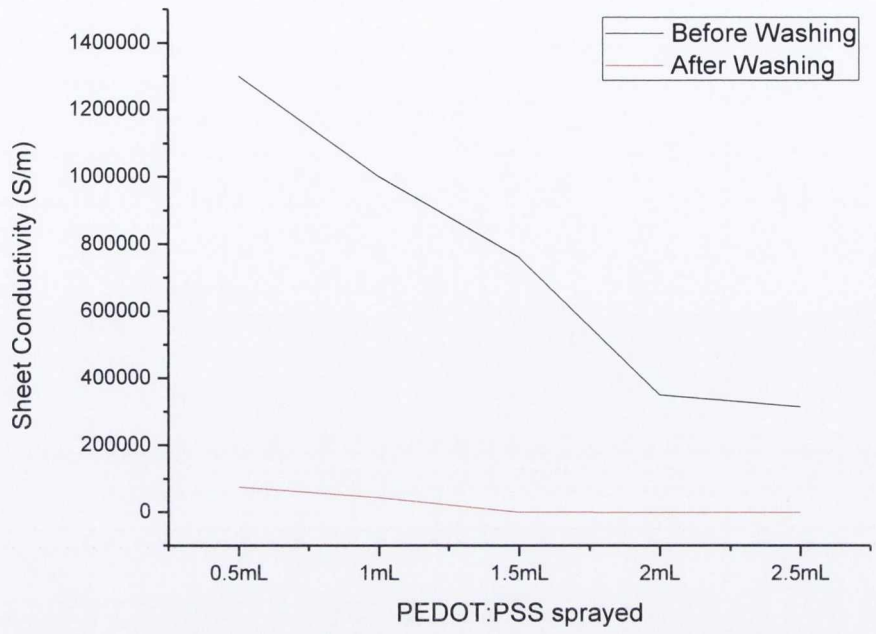

Fig.5.6 Sheet conductivity of PEDOT:PSS electrode before and after washing in methanol.

Conductivity of the PEDOT:PSS compliant electrodes was measured using a two point probe across a fixed distance of 4 cm on the film for all samples before and after washing in methanol (Fig. 5.6). It has been shown that treating PEDOT:PSS electrodes with methanol[10] can increase the conductivity of the films by an order of magnitude, which could increase the actuation properties of the devices.

PEDOT:PSS electrodes with 1mL and 2mL thick electrodes were tested before and after washing with methanol to see the change in actuation behaviour with increased conductivity. It was found that after washing the actuation properties worsened, expanding less. This could be because washing with methanol partially damages the DE film, reducing the effectiveness of the double layer needed for an efficient capacitor, as well as weakening the stretched elastomer film. Although the electrodes had a lower resistance after methanol treatment, the actuation decreased by up to 27 %, as well as the elastomer films breaking while drying.

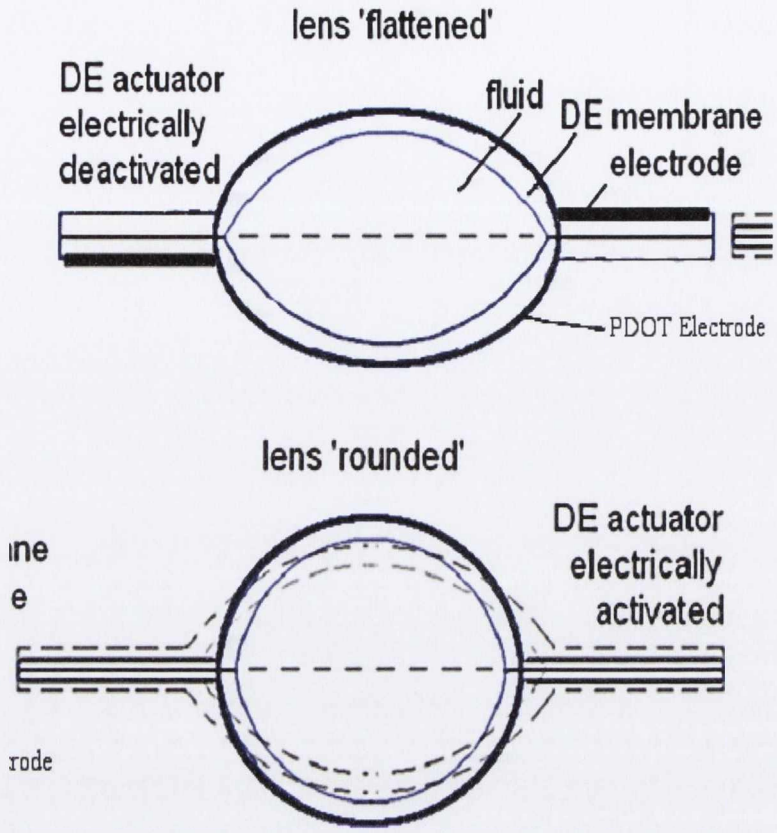

Fig. 5.7. DEA lens created by using PEDOT:PSS electrodes and silicone gel sandwiched between the two layers.

DEA based lenses were fabricated by putting two prestretched elastomer lenses together with a clear silicone gel in between to act as a lens (Fig. 5.7). PEDOT:PSS was used as a transparent electrode so that images could be magnified by the lens or used as a variable projector. 1.5 ml of transparent silicone gel was placed on top of the bottom electrode into a crevice made by depressing the centre of the elastomer film using an airtight syringe and holder. The top elastomer film was then placed on top of this and sealed to create the DEA lens. Because the acrylic elastomer is semipermeable, any air bubbles trapped between the two films dissipated within 48 hours.

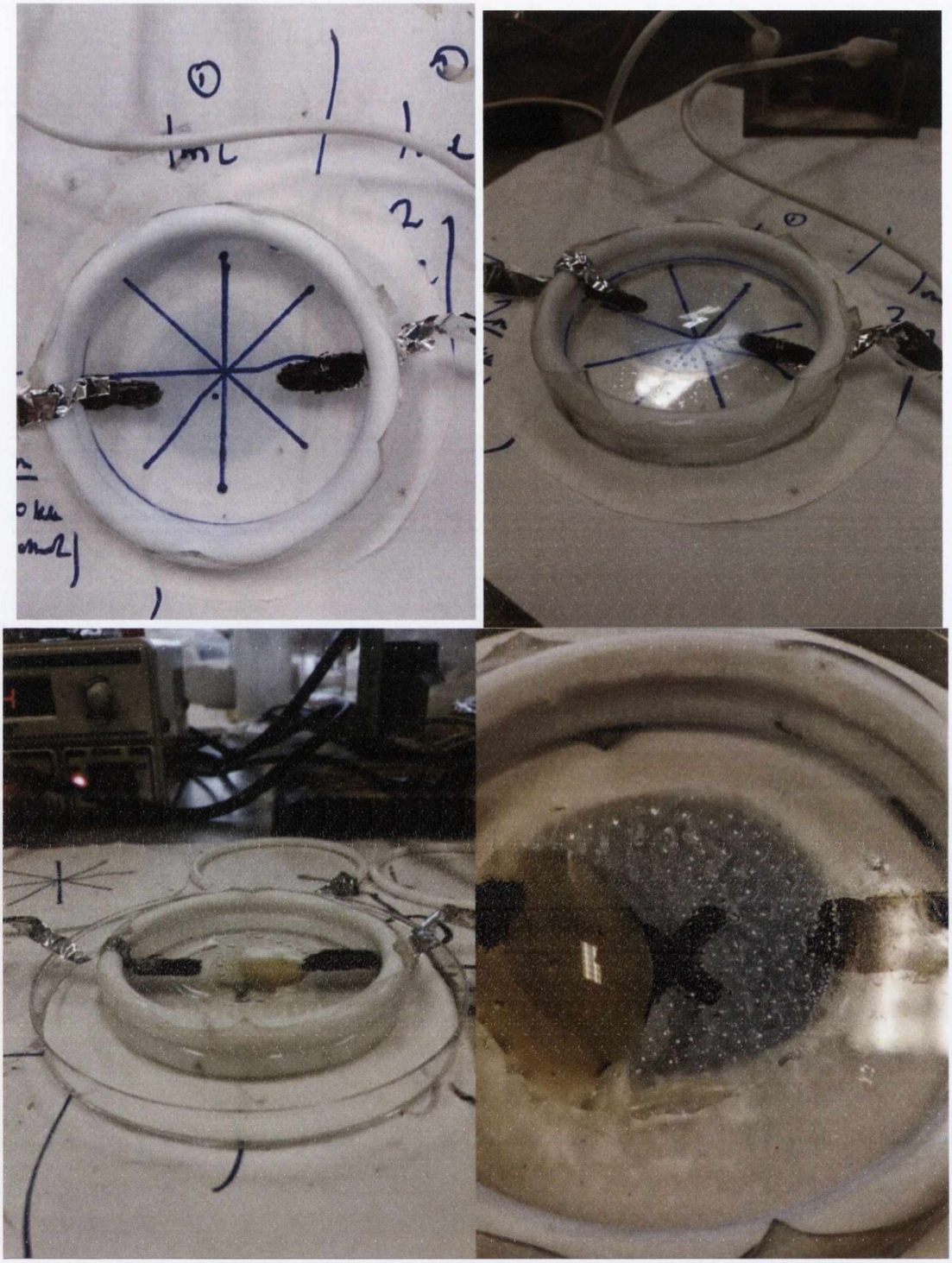

Fig. 5.8 Morphology effects of lenses with PEDOT:PSS electrodes with low to high current

Depending on the current supplied, the rate of actuation can be controlled, from fast actuation (<1 s) to slow actuation (<6 s). When the DEA lenses undergo quick actuation from a high current source, the silicone gel may become trapped between the two electrodes in isolated pockets, making smaller droplets over the electrode area.

Applying a lower current to the same configuration results in all the silicone gel being squeezed into one localised area, eliminating the mini-droplets (Fig. 5.8). If the lens is not sealed perfectly, the fluid may move preferentially to one side as is seen in Fig.5.8, bottom.

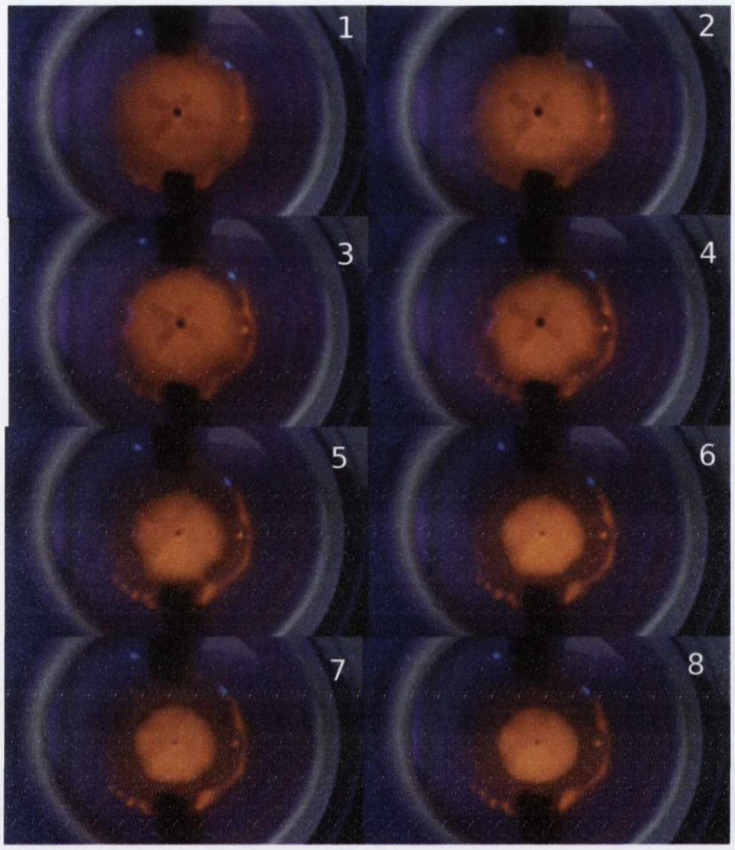

Fig. 5.9 QDs in silicone gel between two transparent PEDOT electrodes undergoing actuation (2 kV). An X was drawn on the substrate below the lens to demonstrate transparency

Then, CdSe/CdS core shell quantum dots were added and mixed with the silicone gel in the lens configuration to observe their effects during actuation (Fig. 5.9). It was found that QDs in silicone gel retained their luminescent properties. Pictures were taken over a period of 2 seconds to observe the movement of the QD solution in the lens under UV light.

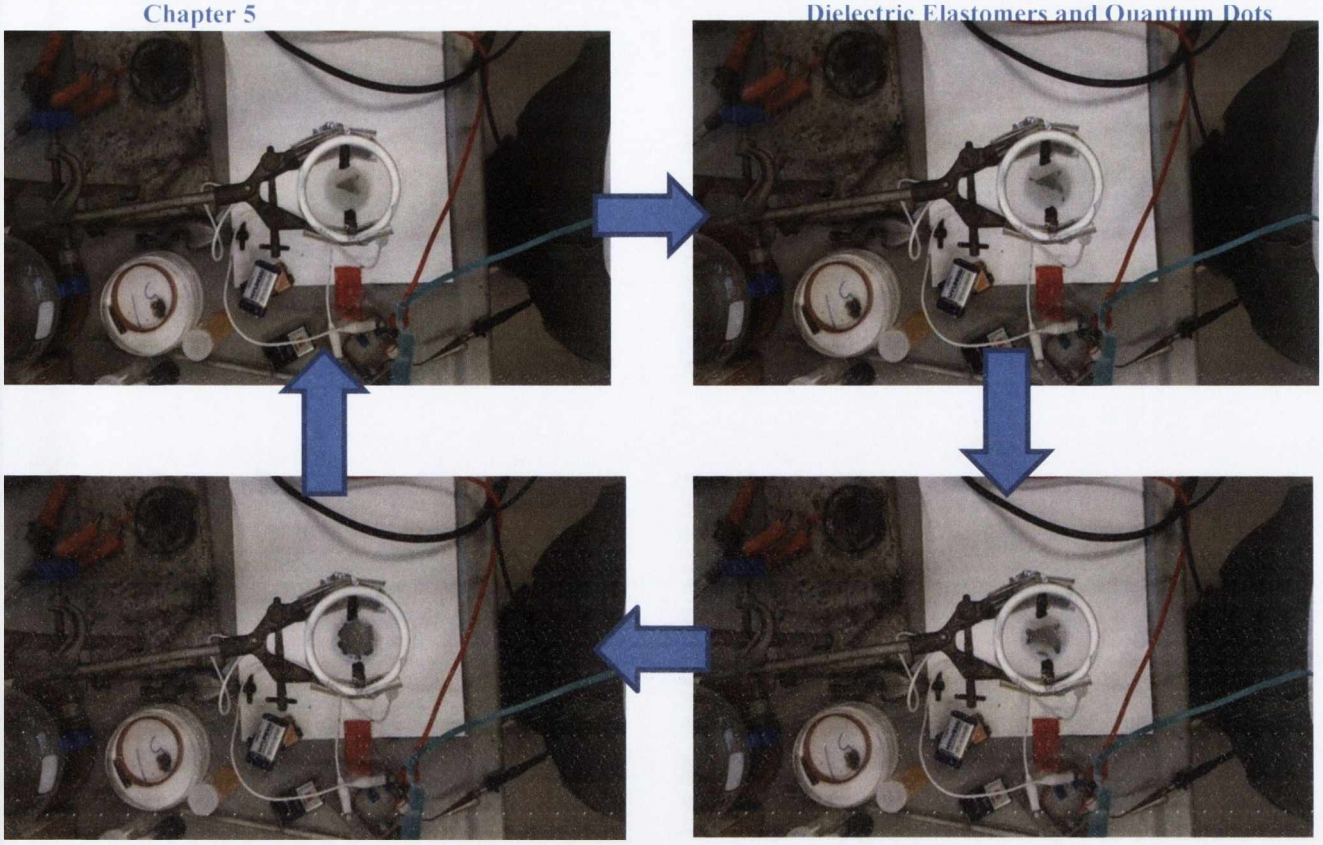

Fig. 5.10 Focusing effects of transparent lenses undergoing actuation at 2 kV.

The lenses may be used to focus and defocus on an image using the electric actuation in the device. In Fig. 5.10 the letter **A** was drawn on a sheet of paper and the lens device held above it. The device was then actuated using 2 kV to compress the silicone gel into the centre of the lens, defocusing the letter **A** on the sheet. When the voltage is turned off, the device returns to its original configuration, resulting in the refocusing of the image. Using this, I can calculate the power of the lens, as well as its magnification strength. Magnification of an object is demonstrated in Fig. 5.11. Using three simple lens equations:

$$M = -\frac{S_2}{S_1} \qquad \frac{1}{f} = \frac{1}{S_1} + \frac{1}{S_2} \qquad P = \frac{1}{f}$$

Where M is the magnification, S_1 is the distance from the centre of the lens to the object, S_2 is the distance of from the centre of the lens to the virtual object, f is the focal length and P is the power of the lens. Using this I calculated the power of the lens in Fig. 5.11 to be P = 0.12 dioptre.

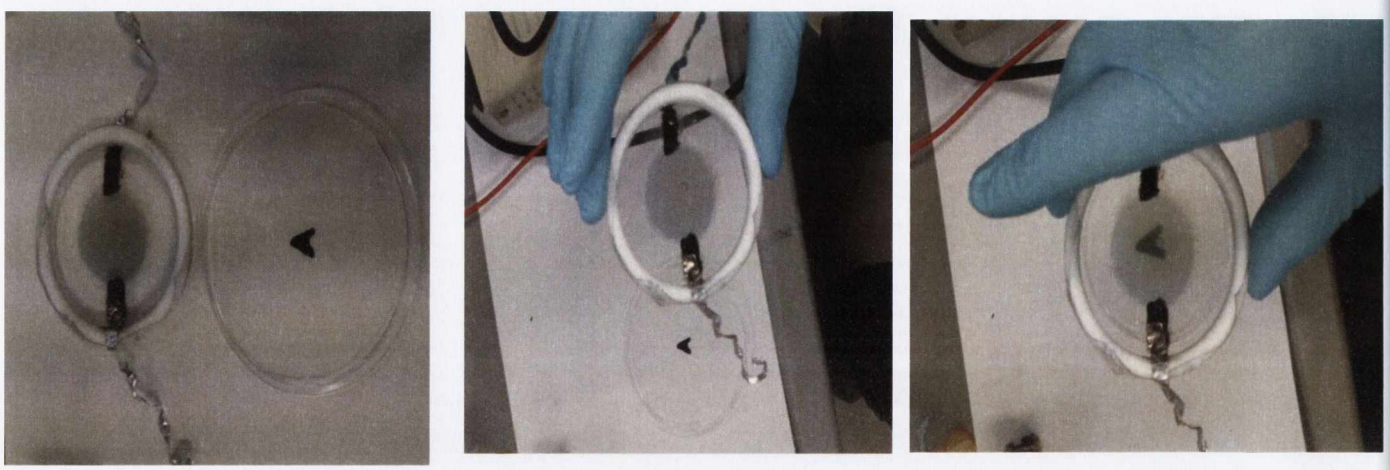

Fig. 5.11 Magnification of an object by silicone lens

5.4 Swelling of VHB and investigation of solvent effects on the DE polymer

The main goal of this part of the work was to observe changes in the actuation properties of the VHB or the emission/absorption properties of the QDs when actuation is induced. To observe the QDs in the VHB film we had to incorporate the QDs into the VHB minimising strain on the film to ensure that actuation was still possible after QD loading.

VHB film was loaded with CdSe, CdSe/ZnSe, CdSe/CdTe and CdSe/CdS QDs by swelling the polymer in solutions with varying concentrations of QDs.

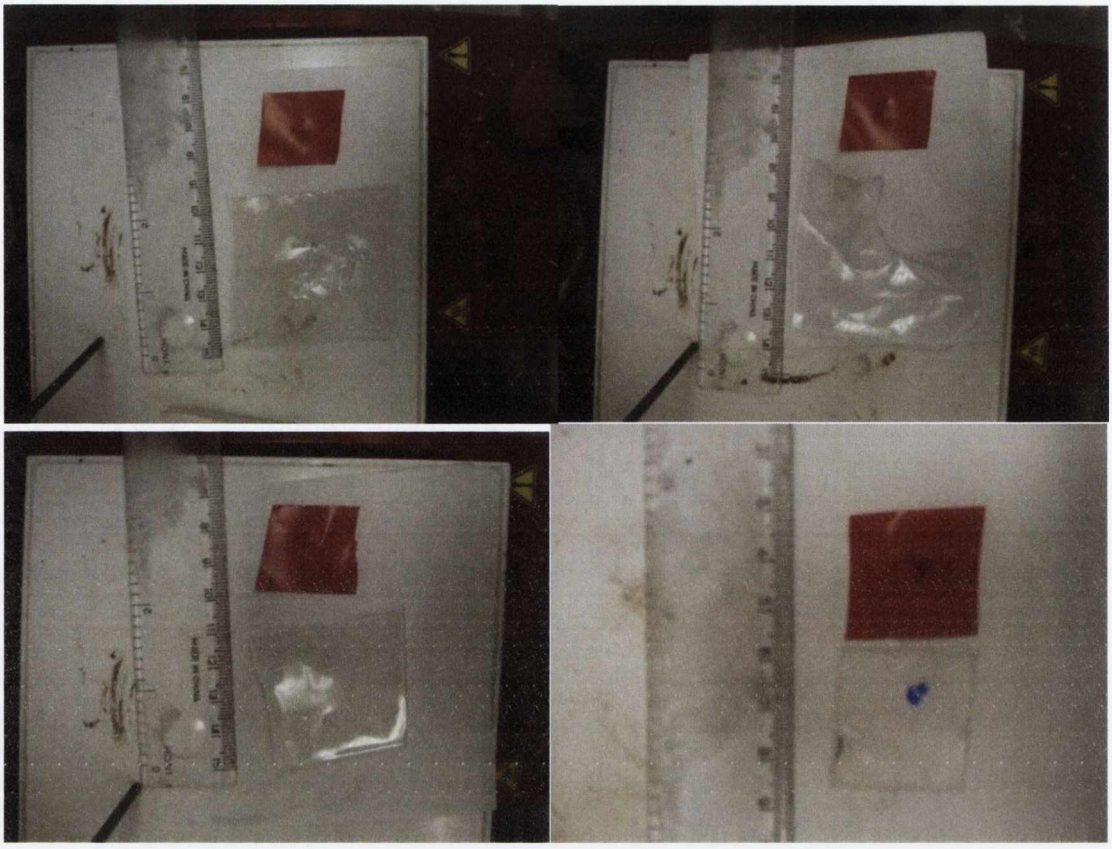

Fig. 5.12 Swelling of VHB in toluene (top left), Chloroform (top right), DCM (bottom left) and hexane (bottom right),

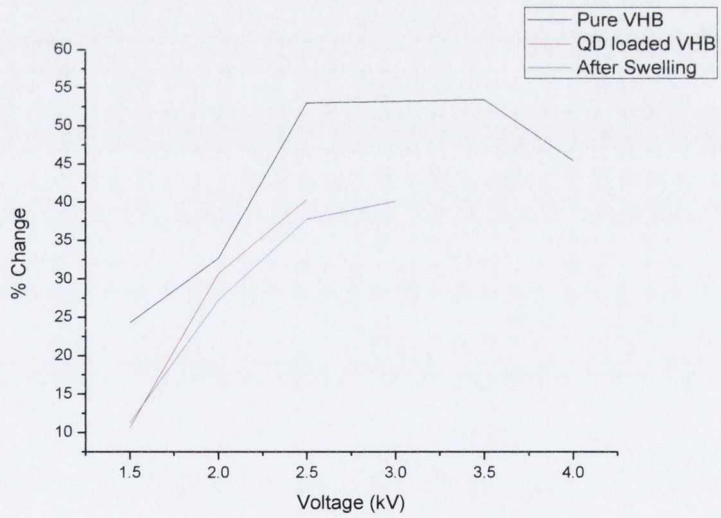

Fig. 5.13. Actuation effects of prestretched elastomer after QD loading and swelling in toluene

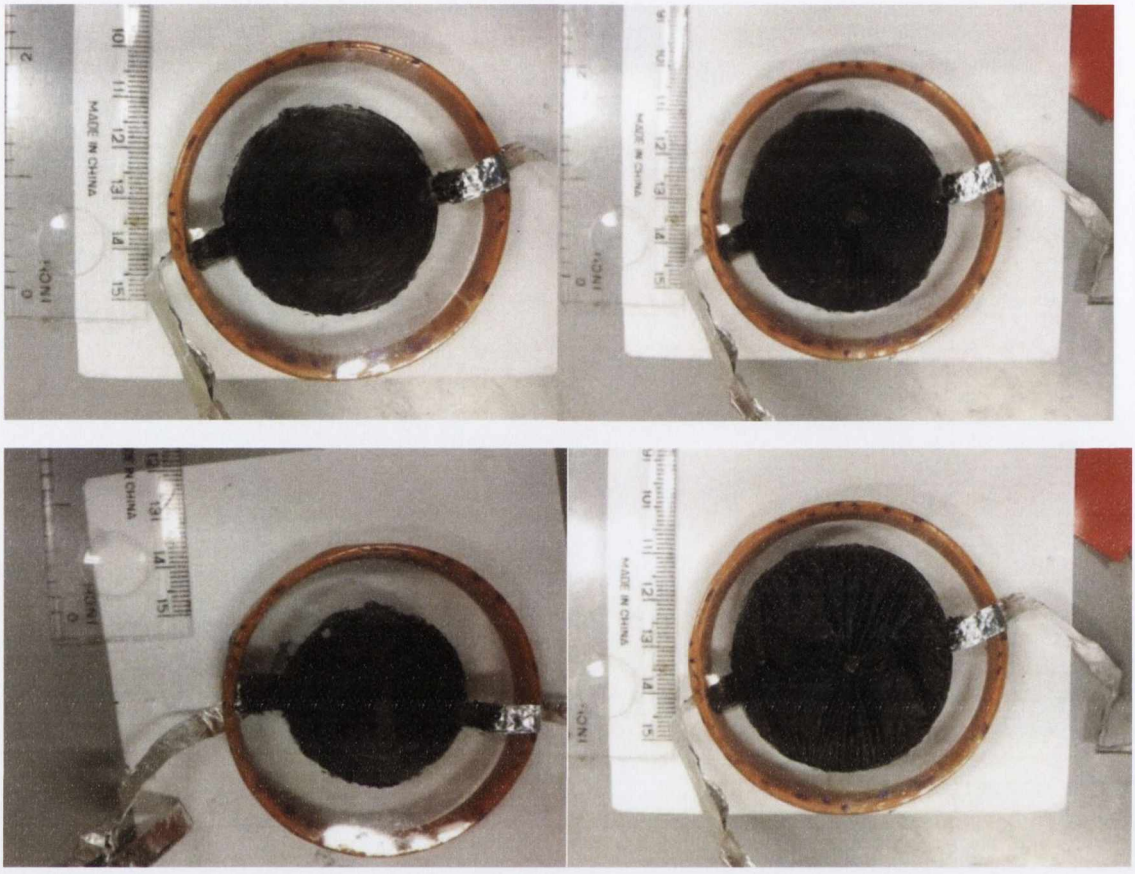

Fig. 5.14 Effects of solvents after swelling and deswelling on the actuation properties of VHB actuator devices.

It was found that when immersed in the organic solvents the acrylic elastomer can swell up to an 87 % increase in volume (Fig. 5.12). VHB was swelled in a variety of organic solvents to find the most suitable solvent for QD loading. Hexane, chloroform, toluene and dichloromethane were chosen for their ability to effectively dissolve my TOPO/HDA capped QDs without coagulation of the QDs or decrease in PLQY. Elastomer was swollen and QDs were incorporated before prestretching the film over a frame as swelling of the elastomer when strained could result in the breaking of the elastomer film and/or unreliable actuation results.

10mL of each solvent was placed in a sample tube with a 1cm x 1cm square of VHB elastomer and sonicated for a period of 1 hour. After sonication the swollen elastomer film was taken out of the remaining solution and dried for 12 hours at ambient conditions. After drying, the elastomer recovered its original size and could thus be reswollen to further incorporate more nanoparticles if necessary. This made the 3M VHB elastomer a suitable candidate for the incorporation of CdSe/CdS organic-phase QDs with high loading.

After a number of trials, toluene was chosen as my preferred solvent to swell the polymer and incorporate QDs into the elastomer as swelling of VHB in toluene resulted in an 87 % increase in volume of the VHB, compare to that of 70 % for chloroform, 65 % for dichloromethane and 45% for hexane. Toluene was also an excellent dispersant of TOPO capped QDs and could be easily degassed to reduce oxidation of QDs and preserve their PLQYs.

Elastomers that had been swollen in organic solvents were then tested to see if their actuation properties had been affected by the swelling process. I used the same electrode configuration. (Fig. 5.14) as one shown in Fig. 5.1 to compare the actuation of swollen and unswollen elastomer films as well as QD doped elastomer. It was observed that the actuation strain values were lower than that of pure VHB for swollen elastomer films with applied voltages up to 2.5 kV (Fig. 14). Above this, buckling of the film was observed(commonly referred to as electro-creasing[11], and a lower dielectric breakdown current recorded (2.5-3.0 kV) comparing to that of pure VHB elastomer.

5.5 Preparation and investigation of VHB - QDs composites

5.5.1 Loading of QDs into DE films

As described in the previous section VHB elastomer was loaded with CdSe and CdSe/CDS QDs by swelling the polymer sample in toluene and by using sonication and a vortex to ensure even QD distribution in the films. Varying concentration of QD solutions as well as doping times was used to find the most effective and even distribution of QD in the elastomer. Elastomer which was swollen for longer periods changed morphology of the film that could be seen under fluorescent optical microscope (Fig. 5.15). This is due to the swelling and subsequent drying effects which

resulted in the formation of a grooved surface on the elastomer film. I found that these effects can be reduced by shortening swelling times and it only becomes prevalent after swelling for more than 24 hours.

Backscatter detection was used for SEM analysis of the VHB to avoid charging of the sample. Light areas correspond to regions doped with CdSe/CdS QDs, whereas darker regions are areas with low QD concentrations. A cross sectional area was examined to analysis the extent of QD penetration of the film. As can be seen, quantum dots penetrate through the elastomer, but have slight aggregation in areas possibly due to drying of the solvent after doping (Fig. 5.16).

Fig. 5.15 Pure VHB elastomer (left), after swelling in CdSe/CdS QD/toluene solution for 12 hours (middle), and after swelling in QD solution for two days (right) under UV light.

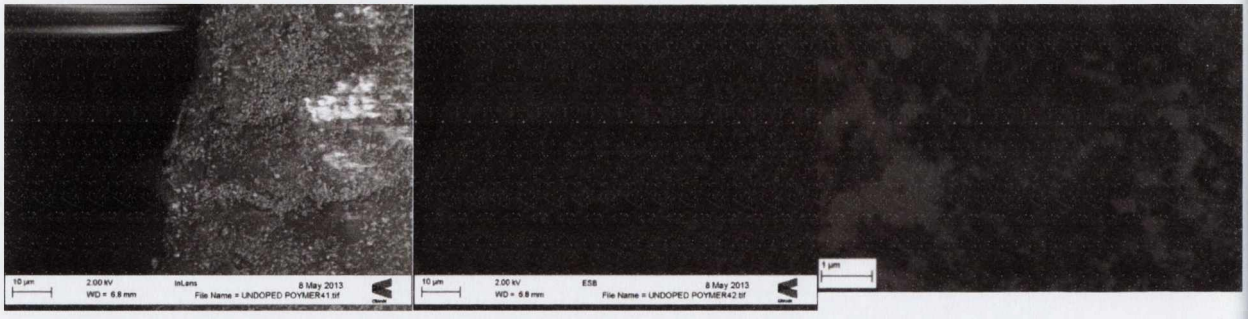

Fig. 5.16 SEM image of CdSe/CdS doped VHB using backscattered electrons.

Fig. 5.17 shows that the QD loaded elastomer film had good optical transparency (Fig. 5.17.1), and under UV light it was luminescent with a rather uniform distribution of

QDs (Fig. 15.17.2). As visible in Fig. 5.17 a central region of the film was left uncoated by the electrode material, so as to be used to record PL spectra and measure PL intensities and fluorescent lifetimes, as well as absorption spectra (with and without a voltage applied between the electrodes).

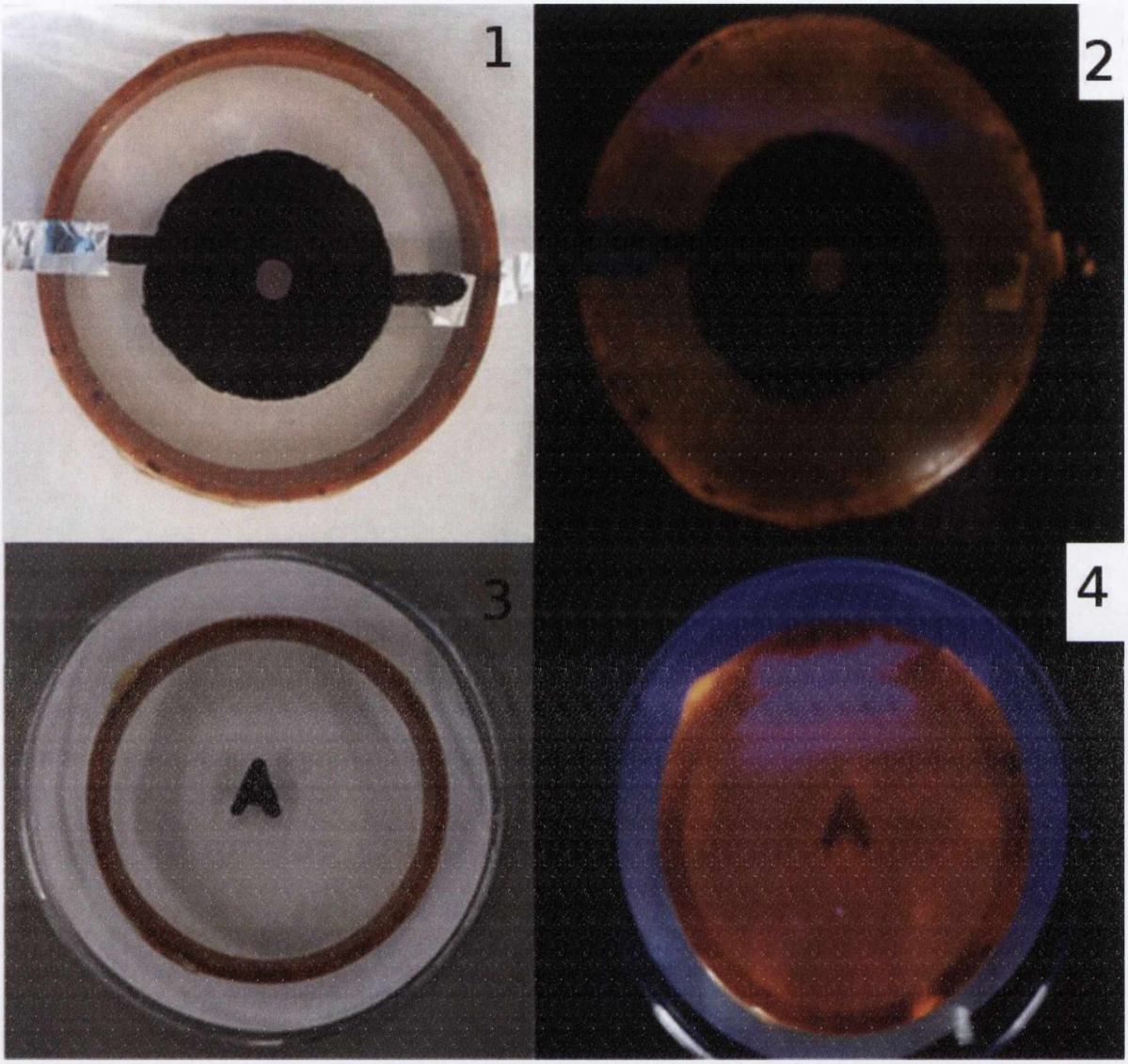

Fig. 5.17 CdSe/CdS quantum dot loaded dielectric elastomer actuator under bright light (1, 3) and UV (365 nm) light (2,4).

Initially CdSe core QDs were used to be loaded into the film. 10mL of a stock solution of $4x10^{-7}$ mmol/l of CdSe QDs in solution was used to dope a 1 cm x 1 cm square of VHB elastomer and allowed to dry. During the swelling and drying and processes the QDs are still visibly fluorescent under UV light, but after solvent evaporation the QD fluorescence was quenched completely. The same QDs when incorporated into a

PMMA matrix were still fluorescent after several weeks; therefore it is believed that the acrylic elastomer was quenching the CdSe QDs. The elastomer was swollen again using the same method to further load the elastomer with QDs. The QDs were quenched again, although the time to quench the QDs took 12 hours to complete. Loading the elastomer a third time with QDs results in partial quenching of the QDs in the elastomer, although the resultant film when stretched had inhomogeneous doping of QDs and collection of absorption and emission spectra were too scattered to give definitive results. Therefore it was decided to try CdSe/ZnSe core-shell QDs, as the ZnSe shell could protect the CdSe core and preserve the PLQY of the QDs in the elastomer. Using the above method, the elastomer was again loaded with QDs and allowed to dry. I have found that the elastomer film was luminescent under UV lamp and emission and absorption spectra was collected from the QDs in solution and in the elastomer. Although the ZnSe shell provides protection for the core, the acrylic elastomer still quenched the emission of the QDs. To combat the aggressive nature of the elastomer, CdSe/CdS core-shell QDs were used with a thick CdS shell for better protection. After loading with these CdSe/CdS QDs, the emission profile was still intense enough to be observed using standard spectroscopic techniques.

5.5.2 Mechanical properties of the composite films

Mechanical testing of the VHB elastomer was done using a Zwick tensile tester. Elastomer was swollen and dried up to 3 times to test degradation of mechanical properties of the elastomer. After total drying of the elastomer, strips of 1.5 cm were cut and compared to pure VHB elastomer as well as VHB elastomer doped with QDs and after swelling in toluene (Fig. 5.18). Treatment with toluene improved the elastomer's mechanical properties slightly, as can be seen. This may be due to the swelling and drying effects on the elastomer as the morphology of the surface changes when the elastomer shrinks back to its original size, making subsequent stretching easier.

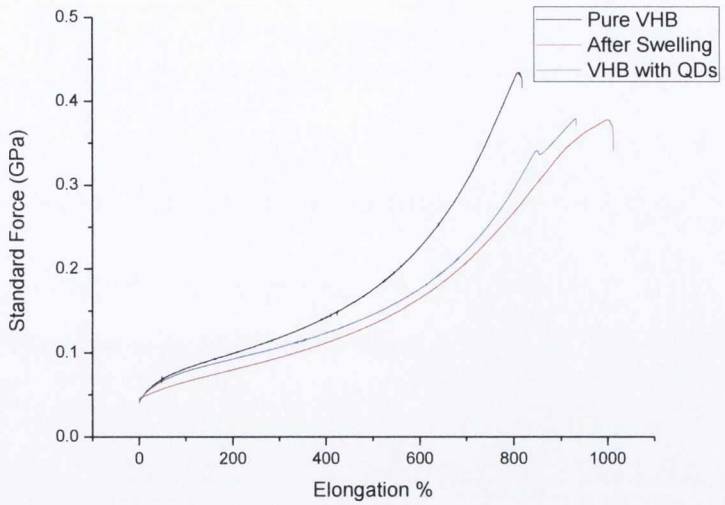

Fig. 5.18 Mechanical testing of VHB and VHB composites

Table 1. Mechanical Properties of VHB after swelling in toluene and doping with CdSe/CdS QDS

Property	original	QD Doped	After Swelling
Young's Modulus (GPa)	$7.18x10^{-5}$±1.06	$8.87x10^{-5}$±1.12	$8.99x10^{-5}$±1.1
Ultimate Tensile Strength (GPa)	0.434±0.012	0.379±0.017	0.369±0.01
Amount stretched%	880	980	1010

High concentrations (up to 10^{-3} m per cm^3) of CdTe/CdSe QDs were made and loaded into the VHB film. Because of the potential creation of excitons and charge separation properties of QDs it was anticipated that the electrical double layer formed when actuating could be affected by a high doping concentration of these nanoparticles. 10 mL of a known concentration of CdTe/CdSe QDs was added to a 1 cm^2 piece of VHB and swollen until the maximum amount of swelling was achieved. The VHB was allowed to dry then re-swollen again to increase an uptake of more QDs from the solution. After swelling I could calculate the concentration of QDs absorbed by the VHB. A 10mL QD solution of concentration 5.98 x 10^{-6} m is used to dope a 1 cm x1 cm x 0.1 cm VHB elastomer piece. The elastomer is swelled and dried multiple times to integrate all of the QDs in the 10mL solution, using sonication to ensure an even doping

throughout the film. Assuming that all the QDs in the solution are incorporated into the elastomer, this would give a concentration of 5.98×10^{-5} m per cm^3

5.5.3 Behaviour QD-VHB composite under UV light

To see if the QDs could affect the properties and behaviour of the VHB under irradiation of the QDs using UV lamp, fluorescent microscopy was performed on the sample (Fig. 5.20). Usually a high voltage of above 1 kV and current of over 3 μA is needed to visibly see actuation in a VHB sample by the naked eye. Therefore, the VHB was cut with a serrated blade to expose these strips of VHB that may be easier to actuate because of their thin and small size. Initially the sample of VHB elastomer loaded with CdTe/CdSe type II QDs was observed under microscope under low intensity light exposure. The sample was then exposed to a UV lamp of wavelength 365 nm and imaged over 1 minute. The light source was switched back to normal white light and imaged again over 1 minute. CdTe/CdSe QDs were first analysed by UV-Vis and PL spectroscopy as well as TEM (Fig. 5.19). As the CdSe shell was grown on the CdTe cores I saw a decrease in luminescence, typical for type II quantum dot structures. TEM found that the particles were spherical, crystalline and had a low size distribution.

Over films, the focus of the picture could be seen to change, but because all movement was in the Z-axis, it was difficult to observe and determine the any size changes under the influence of the UV light. The same tests were performed with pure VHB and VHB with organic dyes to rule out expansion of the film due to heating or other effects. As no visible size changes was observed for these samples, it was concluded that the size changes in the CdTe/CdSe loaded VHB film was due to the QD effects under the UV lamp. This action was reversible and movement of the VHB thread was quick, with movement observed within 1 second and stopping after ~30 seconds. Thermal heating is usually a slower process that takes place over minutes to hours in elastomers[12]. I also found that thermal expansion did occur in the VHB elastomer by heating it in an alkene which did not swell the VHB, octadecane.

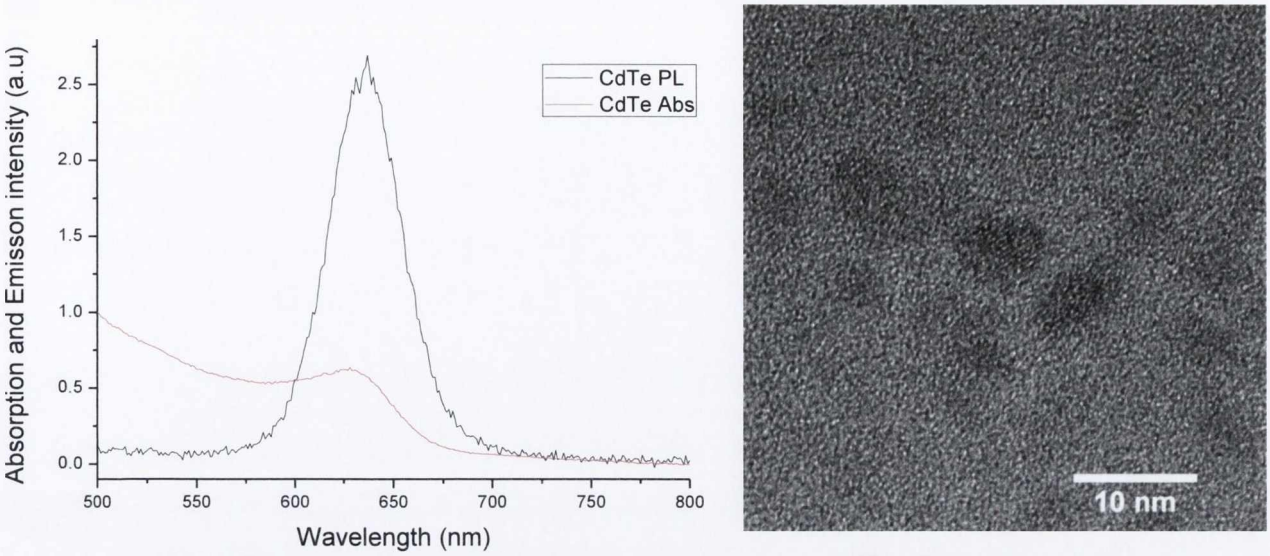

Fig. 5.19 Absorption and Emission spectra of my CdTe/CdSe QDs (left) and HRTEM on lacy carbon grids.

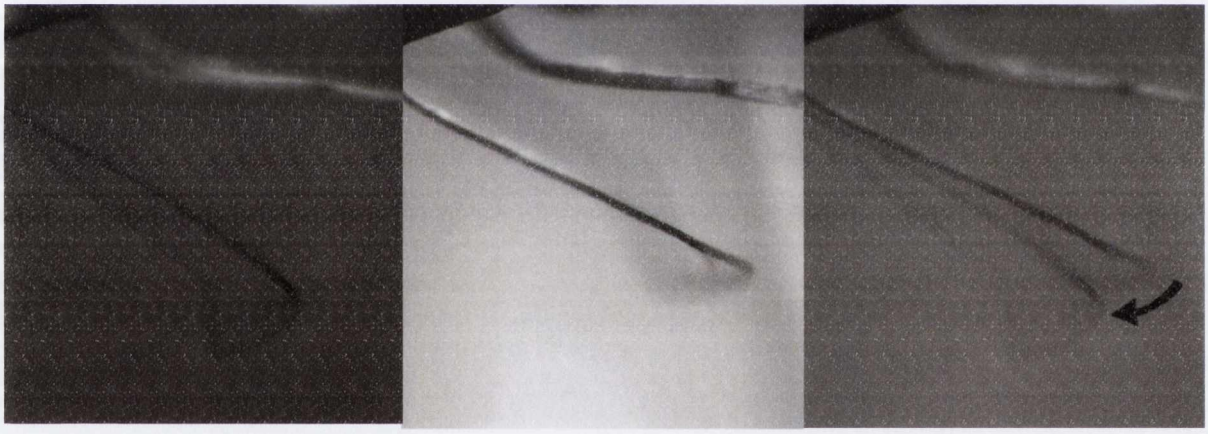

Fig. 5.20 Movement of elastomer strip when exposed to UV irradiation. The strip was seen to move up (left, UV light on) and down (middle, UV light off) with a reversible and reproducible action. Right Image showing on/off configurations overlaid

5.5. 4. Thermogravimetric analysis of the quantum dot loaded dielectric elastomer film

When immersed in the organic solvent the acrylic elastomer resulted in a swelling of up to about 87 % of its original size. After drying, the elastomer recovered its original size. This made the 3M VHB elastomer a suitable candidate for the incorporation of CdSe/CdS organic-phase QDs with high loading.

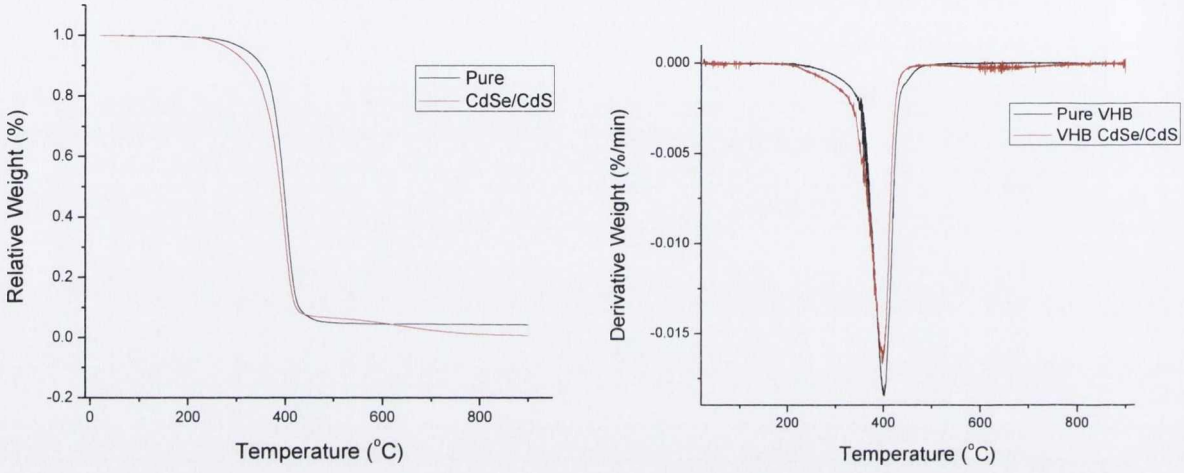

Fig. 5.21. Thermogravimetric analysis of the undoped and doped elastomer film and the derivative (right)

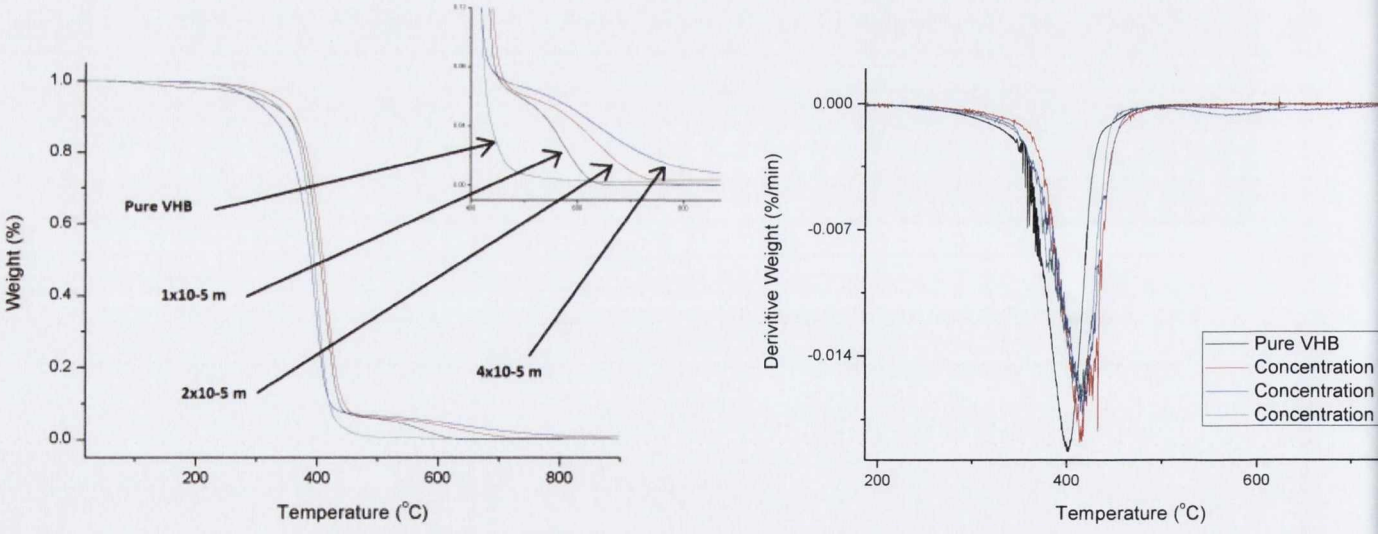

Fig. 5.22 Thermogravimetric analysis of VHB elastomer doped with different concentrations of QD solutions (left) and the derivative curve (right). TGA analysis was performed under nitrogen.

Fig. 5.21 shows results of the thermogravimetric analysis performed on the undoped and doped elastomer film under nitrogen flow (20 ml/min). The main peak at 400 ^{o}C of the derivative curve was attributed to the elastomer decomposition. In the pure sample the decomposition started at a slightly lower temperature than in the doped sample. This may be due to residual solvent in the elastomer following the incorporation of the QDs. A small peak at 630 ^{o}C for the doped elastomer confirmed the presence of the CdSe/CdS QDs and their hydrocarbon ligands, which decomposed at higher temperatures. The remaining weight of the doped sample showed that the achieved QD loading in the elastomer was 6.7 wt %. Although an increase in weight can be seen for doping with increasing concentration an accurate estimation of QD concentration inside the VHB cannot be done this way. A 10mL QD solution of concentration 5.98 x 10^{-6} M is used to dope a 1 cm x1 cm x0.1 cm VHB elastomer piece. The elastomer is swelled and dried multiple times to integrate all of the QDs in the 10 ml solution, using sonication to ensure an even doping throughout the film. Assuming that all the QDs in the solution are incorporated into the elastomer, this would give a concentration of 5.98x10^{-5} M per cm^3 assuming uniform uptake.

Further tests were done to see if I could control the amount of QDs incorporated into the elastomer. A solution of QDs with known concentration was diluted several times and used to dope pieces of elastomer to vary the doping concentration. As seen in Fig. 5.22, the difference in doping can clearly be seen as the dilute samples have a lower % weight and thermally decompose at lower temperatures.

5.5.5 Absorption spectra of the quantum dot loaded dielectric elastomer actuator

Fig. 5.23 shows UV-Vis absorption spectra recorded from the QD doped dielectric elastomer actuator, with and without an applied voltage (1.5 kV), as compared with the QDs in a toluene-based colloidal solution.

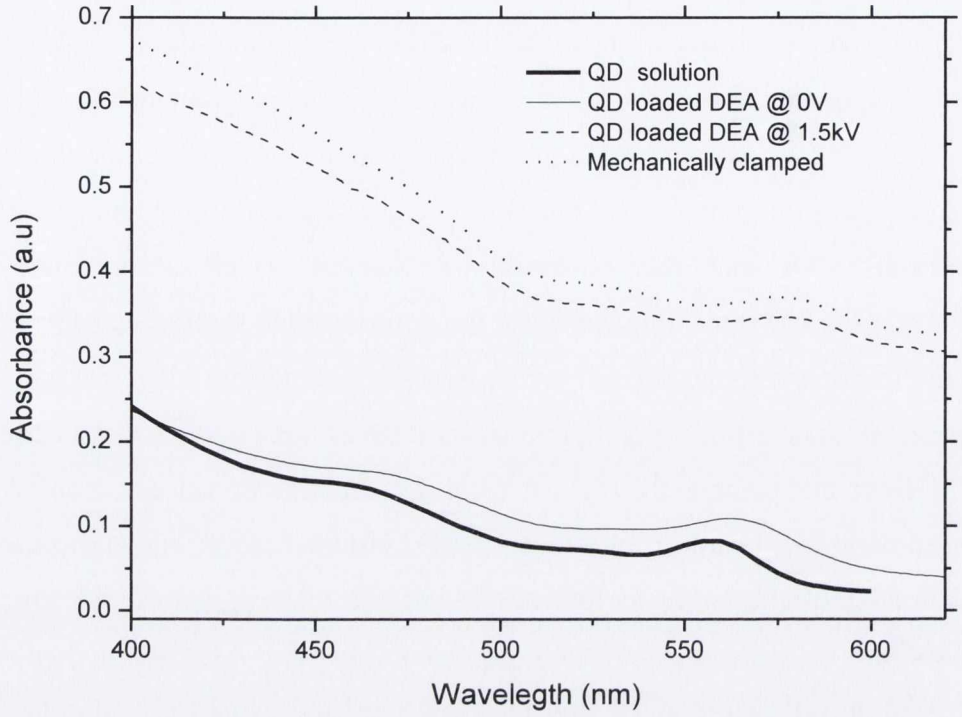

Fig. 5.23 UV-Vis absorption spectra of the QD doped dielectric elastomer actuator with and without an applied voltage, and comparison with the spectrum exhibited by a QD solution.

The UV-Vis absorption spectra showed following main features (Figure 5.23). First, there is a red shift (~10 nm) in the position of the first absorption peak of QD loaded DEA in comparison with QDs in solution. This can be explained by the aggregation of CdSe/CdS QDs in the DEA matrix after the processing. Second, there is a significant increase in absorbance and a further significant ref shift (~23 nm) observed in the QD loaded DEA samples under 1.5 V and in the mechanically compressed (clamped) sample with the same elongation. These observations can be attributed to the further aggregation of QDs due to the mechanical compression. This is a demonstration of one of the desired optical effects: an electrically tuneable absorbance of QDs. Indeed, as the d, there is a indow' in the middle of the device contracts with an applied voltage, the QD concentration per unit area increases, resulting in an increased absorption (Fig. 5.23). Third, I have found that in absorbance spectra of the sample under 1.5 V and mechanically compressed (clamped) sample with the same elongation have an identical peak position but the sample under voltage has a slightly lower intensity (within an experimental error). From these observations I can conclude that the sample absorption

is not really affected by electrical field and the increase in absorption found is only due to the rise of QD concentration per unit area as result of the compression of the elastomer film. Indeed the position of absorbance band should not be affected by external factors including electric fields as this is an intrinsic property of the material which relies on the size of the QD. Although absorbance shifts can be caused by changing conditions (e.g. from colloidal to solid state) and severe temperature changes, these are often extreme changes in conditions that lead to the aggregation of nanoparticles resulting in clusters of nanoparticles and red shift the absorbance spectra[13]. These findings should enable the potential development of QD loaded DEA materials of various colours where both absorbance and transmittance can be controlled by an applied electromagnetic field.

5.5.6 Photoluminescence spectra of the quantum dot loaded dielectric elastomer actuator

Fig. 5.24 presents the recorded photoluminescence spectra of the QD loaded dielectric elastomer actuator. CdSe/CdS QDs in solution showed a maximum PL at 591 nm and a Full Width at Half Maximum (FWHM) of 26 nm, indicating a narrow size distribution. When the PL was measured in the QD doped actuator a slight red shift of 8nm was observed (Fig. 5.24). Such an effect is typical when QDs are transferred from colloidal into solid phases. After applying a voltage of 1.5 kV, the PL was found to reduce to 27 % of its original intensity (Fig. 5.24). The PL was found to revert back to its original intensity when the voltage was turned off. When a voltage of 2 kV was applied, the signal became too weak to be observed over the background noise.

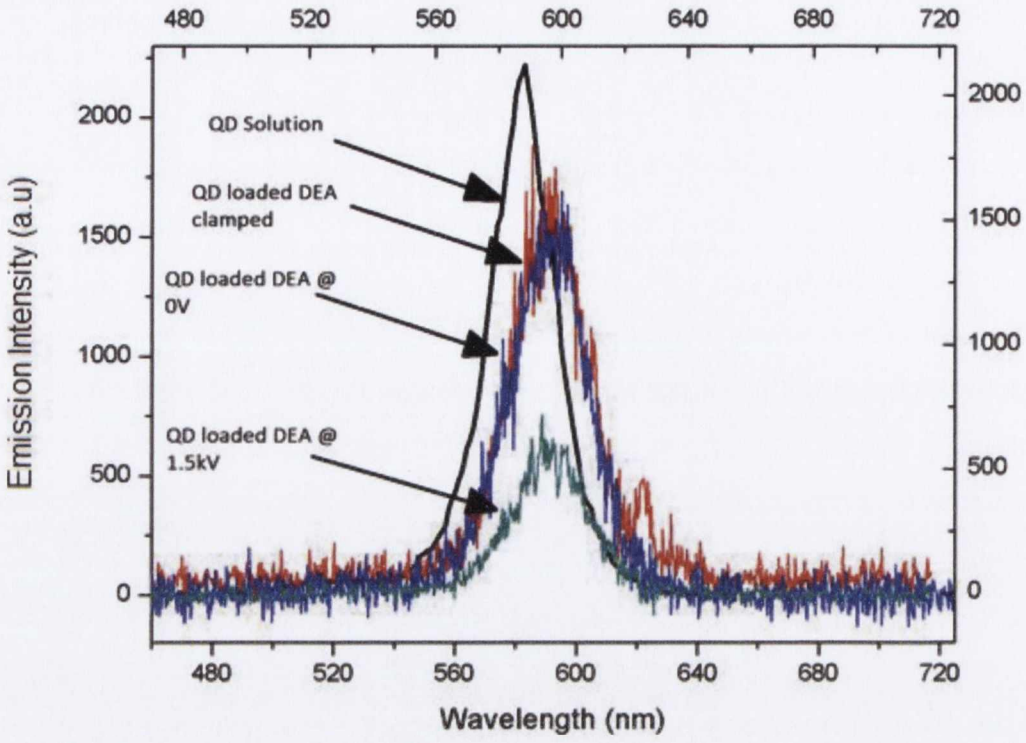

Fig. 5.24. Photoluminescence spectra of the QD doped dielectric elastomer actuator with and without an applied voltage, and comparison with the spectrum exhibited by a QD solution.

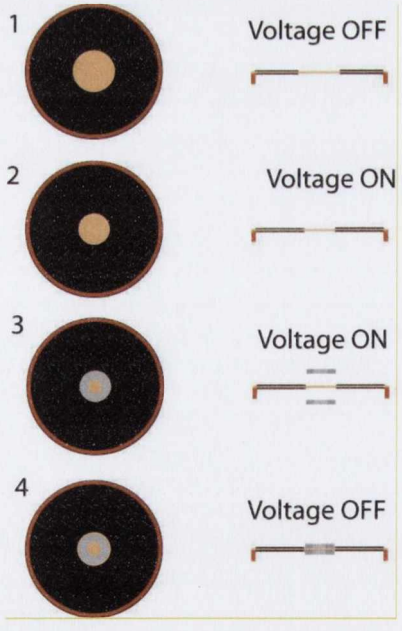

Fig. 5.25. Schematic presentation of clamping the DEA while applying a voltage. When the voltage is off, the DEA remains in its compressed state.

The observed decrease of PL while increasing the voltage might have at least the following two possible interpretations.

The most likely reason might be attributed to enhanced interactions between adjacent QDs as the film contracts. In fact, an applied voltage reduces the area of the central transparent window of the device, and thus it tends to increase the QD concentration per unit area (the radial and tangential distances among QD clusters tend to decrease). The closer the QDs come to each other, the higher the likelihood of energy transfer between them. It has previously been shown that this effect can cause the QDs to quench each other, leading to a decrease of both the PL intensity and the fluorescent lifetime[14]. Indeed, I have measured a progressive reduction of PL emission lifetime when the film contracts under electric field.

The PL quenching effect might also have an electrical nature, which is caused by the high fringe electromagnetic field that comes out of the capacitor and invest the QDs. Indeed, previous studies have demonstrated that electromagnetic fields can decrease the PL of CdSe/ZnS QDs[15].

A control experiment was conducted using a purely mechanically actuated QD-loaded elastomer sample, while observing the fluorescence intensity to see if the same effect takes place without any electromagnetic fields. In this experiment the DEA was actuated with a potential of 2.5 kV and mechanically clamped in position using two rings, so that the when the voltage was turned off, the elastomer remained mechanically compressed as it is in the electrically actuated state (Figure 5.25).

No PL intensity and lifetime change was observed when the sample was mechanically actuated this way. Thus it can be concluded that when actuation of the elastomer is performed by using the compliant electrodes, the electromagnetic fields play a crucial role in the reduction of the PL intensity despite an increasing QD concentration per unit area. In this case the drop in PL intensity can be caused by the interaction of the electromagnetic field with the defects in QDs that may result in a splitting of the energy levels in the defect[15]. This can result in trapping of an electron at a metastable level and following irradiative recombination. This should lead to the reduction of the number of radiative recombinations in QDs and drop of photoluminescence life time and intensity. Meanwhile there is no any significant quenching of QDs due to the mechanical compression and reduction of the distance between QDs in the DEA matrix.

Fig. 5.26 presents the PL emission decays measured from the QD doped actuator at different applied voltages. Data were fitted with a bi-exponential decay curve, obtaining lifetimes of 8.6 ns, 7.34 ns and 6.48 ns at 0 kV, 1.5 kV and 2 kV, respectively (X^2 values were 0.98, 1.0 and 1.03 for the fitting curves at 0 kV, 1.5 kV and 2 kV, respectively).

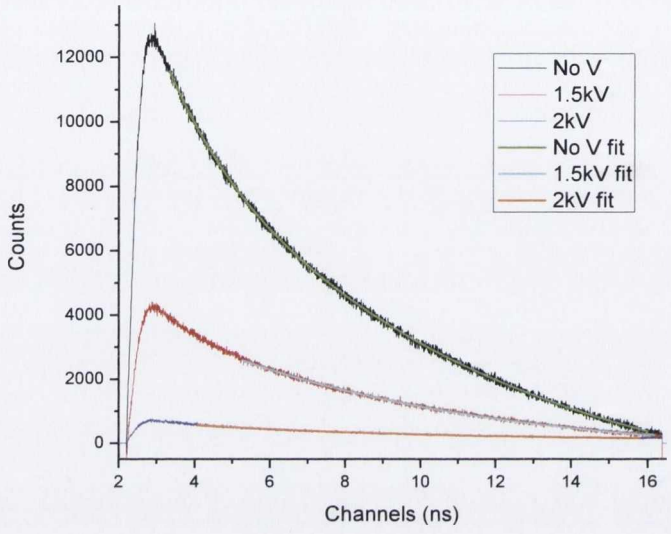

Fig. 5.26. Photoluminescent emission lifetime decays measured on the QD doped dielectric elastomer actuator at different applied voltages. Experimental data were fitted with bi-exponential decay curves.

The decrease of fluorescence lifetime with the increasing voltage most likely can be interpreted by the splitting of the energy levels in QD defects which occur in the system under electromagnetic field as I discussed above[15]. In addition I cannot rule out that some decrease of lifetime is due to an increase in clustering of CdSe QDs that results in the enhancement of energy transfer process between QDs[14]. In the device shown here, the shrinking of the window in the middle of the membrane as the voltage increases corresponds to an increase of QD concentration per unit area. This means that adjacent QDs have a shortened QD-QD distance, which can enhance energy transfer processes and thus reduce the fluorescence lifetime.

5.6 Conclusions

Thus in this work CdSe/CdS QDs were successfully incorporated into a dielectric elastomer actuator, obtaining a proof-of-concept demonstration of new stretchable optical devices with electrically tuneable absorbance and fluorescence.

The QD doped actuator showed a voltage or mechanically (compression) induced increase of the QD concentration per unit area that resulted in an increased UV-Vis absorption. However there was a decrease in photoluminescence intensity and shortened fluorescence lifetimes after the electric field application. Control experiments, when QD loaded dielectric elastomer actuator was also compressed mechanically to the same size and geometry using a mechanical clamp, has not shown any visible quenching of QDs in DEA matrix. Thus I observed opposite trends in the absorption and luminescence intensities during the electric actuation. The decrease in photoluminescence intensity can be explained by the splitting of the energy levels in QD defects which occur in the system under electromagnetic field[15]. This leads to trapping of an electron at a metastable level and following irradiative recombination, thus resulting in a luminescence quenching. This seems to be consistent with the observed decrease of fluorescence lifetimes. While an increase in the UV-Vis absorption can be entirely attributed to the rise of QD concentration due to the electrical or mechanical sample compression. In this case an increase in QD absorption is quite small and it does not compensate strong quenching of QDs by electromagnetic field. Although the emission of QD loaded DEA was quenched by an applied voltage, these results are still useful for the prospective development of new stretchable photoluminescent materials where both size and emission can be gradually controlled by an application of electromagnetic field. For example this can be potentially used in some sensing devices with a photoluminescent response.

I have found that QD loaded DE demonstrate very interesting behaviour by reversibly expanding under UV light. This phenomenon should be investigated in more details as it could potentially enable to harvest light and transfer this energy directly into mechanical movement.

I have also developed new stretchable transparent electrodes and used those to produce new prototypes of lenses with electrically controlled shape curvature and focus. These devices could potentially find many important applications.

In overall this explorative work provided an initial assessment of the potentials and challenges of QD-loaded dielectric elastomer actuators as new kinds of stretchable optical systems. I believe that the possibility to tune electrically spectral and mechanical parameters of QD loaded dielectric elastomers opens up new horizons in the development of novel optical devices, where absorption, transmittance, emission, size and shape can be simply controlled by an applied voltage. These devices could find a range of applications in electrically controlled micro-lenses, micro-lasers, optical amplifiers, sensors, filters, demultiplexers, switches, routers and optical logic gates. Further and more detailed investigations are necessary to fully elucidate the interplay of electrical, mechanical, chemical and optical variables, as well as to explore the full potential of this methodology for applications in photonics and optical sensing.

References:

(1) Pelrine, R.; Kornbluh, R.; Pei, Q.; Joseph, J. *Science* **2000**, *287*, 836.

(2) Carpi, F.; Bauer, S.; De Rossi, D. *Science* **2010**, *330*, 1759.

(3) Brochu, P.; Pei, Q. *Macromolecular Rapid Communications* **2010**, *31*, 10.

(4) Carpi, F., De Rossi D., Kornbluh R., Pelrine R. and Sommer-Larsen P *Oxford: Elsevier* **2008**.

(5) Giger J., S. M., Aschwanden M *Proc. EuroEAP 2012 – Second International Conference on Electromechanically Active Polymer Transducers & Artificial Muscles, Potsdam, Germany,* **2012**.

(6) Aschwanden, M.; Beck, M.; Stemmer, A. *Photonics Technology Letters, IEEE* **2007**, *19*, 1090.

(7) Carpi, F.; Frediani, G.; Turco, S.; De Rossi, D. *Advanced Functional Materials* **2011**, *21*, 4152.

(8) Kofod, G.; Sommer-Larsen, P.; Kornbluh, R.; Pelrine, R. *Journal of Intelligent Material Systems and Structures* **2003**, *14*, 787.

(9) McMeeking, R. M.; Landis, C. M. *Journal of Applied Mechanics* **2004**, *72*, 581.

(10) Alemu, D.; Wei, H.-Y.; Ho, K.-C.; Chu, C.-W. *Energy & Environmental Science* **2012**, *5*, 9662.

(11) Qiming Wang, M. T., Lin Zhang and Xuanhe Zhao *Soft Matter* **2011**, *7*, 6583.

(12) Richards, J. M.; Wostenholm, G. H.; Yates, B.; Darby, M. I.; Phillips, L. N. *J Mater Sci* **1990**, *25*, 721.

(13) Vossmeyer, T.; Katsikas, L.; Giersig, M.; Popovic, I. G.; Diesner, K.; Chemseddine, A.; Eychmueller, A.; Weller, H. *The Journal of Physical Chemistry* **1994**, *98*, 7665.

(14) Higgins, C.; Lunz, M.; Bradley, A. L.; Gerard, V. A.; Byrne, S.; Gun'ko, Y. K.; Lesnyak, V.; Gaponik, N. *Opt. Express* **2010**, *18*, 24486.

(15) Vece, M. D.; Kolaric, B.; Baert, K.; Schweitzer, G.; Obradovic, M.; Vallée, R. A. L.; Lievens, P.; Clays, K. *Nanotechnology* **2009**, *20*, 135203.

Chapter 6: Conclusions and Future Work

6.1 Conclusion

In this work, a series of new nanoparticles and polymer nanocomposite materials based on cadmium II-VI semiconducting quantum dots have been prepared and investigated. These materials could have a broad range of potential applications in the areas of nanotechnology, chemistry, biosciences and solar technology.

CdSe TOPO/HDA capped QDs were successfully synthesised and characterised in detail. Using a CEM star system microwave, we have shown that CdSe nanoparticles could be synthesised at temperatures as low as 80 ^{o}C due to activation of specific precursors through microwave radiation. It was found that reaction times and heating times were shortened compared to a hot-injection synthesis using similar precursors. Additionally, CdZnSe ternary core QDs were synthesised using microwave heating, showing the versatility of the system. Precise size control of the QD nanostructures was demonstrated using varying reaction times and temperatures. The QDs synthesised by microwave heating were found to have lower PLQYs than that of their hot-injection synthesised counterparts. This may be due to the fast reaction times and lower reaction temperatures leading to unpassivated surface defects on the surface of the QD. Higher temperatures or more polarizable ligands may be needed to increase the PLQY of organic QDs synthesised by microwave irradiation. This paves the way for potential application of a scalable, cost-effective and controllable synthesis of luminescent QDs for various applications.

CdSe/ZnSe and CdZnSe/ZnSe have been synthesised by hot-injection synthesis of organometallic precursors. These core-shell nanocrystals were found to have PLQYs above 80 %, with good resistance to phtobleaching and oxidation when put into a polymer matrix. It was shown that the ternary core CdZnSe/ZnSe quantum dots had faster fluorescent lifetimes of ~4 ns compared to that of CdSe/ZnSe quantum dots (~20ns), which is typical of non-blinking quantum dots. FLIM of CdSe/ZnSe QDs showed on/off states when a point scan was carried out with the QDs in a PMMA matrix. Using the same technique, it was shown that the alloyed CdZnSe/ZnSe QDs displayed continuous emission. Using XRD and optical characterisation of the alloyed

QDs, it was shown that we could successfully control the composition and ratio of the Cd-Zn in the ternary core QD.

A range of novel high aspect ratio CdS and CdSe nanostructures were prepared with the use of selective stabilisers to provide a directional growth of the nanostructures. The CdS seeds were used as a precursor for controlled grow of CdS rods of varying length dependant on the CdS seed concentration at the start of the reaction. HPA and ODPA were used to selectively bind to the (111) facet of the CdS seed particle for growth along that axis. CdS seed concentration was found to be critical in controlling the CdS rod length, which were synthesised in the ranges of 10-100 nm. We have also developed a range of new CdS/CdSe nanostructures. It was found that CdSe QDs formed on the ends (tips) of the CdS rod when Cd and Se organometallic precursors added in a hot-injection synthesis. When the synthesis was performed at temperatures over 250 ^{o}C, it was found that the CdS/CdSe barbell and match-stick like structures were transformed into CdSe/CdS core shell particles. Evidence for this includes TEM at several key stages of CdS rod deformation, as well as emission and absorbance profiles indicating the formation of CdSe QDs and their subsequent capping. Below 250 ^{o}C the formation of another nanostructures was observed: CdSe QDs grew onto the ends of CdS rods that then were linked together to form chain-like structures. When the multiple Cd/Se precursor amounts were injected slowly over time to the CdS rod solution the growth of CdSe QDs was observed, indicating that initially CdSe QDs grow onto high energy facets of the CdS rods.

A range of QDs were incorporated into polymer matrixes and the properties of these new materials have been investigated. Initially highly luminescent CdSe QDs were added to commercially available PS microspheres by swelling of the PS sample in organic QD-containing solvents. The doped PS spheres displayed strong luminescence and WGM resonances. In addition we have prepared new QD-loaded PMMA microspheres using a micro emulsion technique in the presence of QDs in a similar method. These PMMA microspheres also displayed WGM resonances, making them suitable for various photonic applications.

A novel method of the production of hollow PMMA microspheres with high Q values was also developed in our work.. This involved a spray drying processing of

polymer solutions onto treated glass substrates to form hollow microspheres. FIB microscopy was used to confirm that the spheres were hollow, as well as we demonstrated loading of the microspheres with QDs and organic fluorophores, showing the a versatility of this system and our approach..

Finally, for the first time we have successfully incorporated QDs into a dielectric elastomers whilst maintaining the QDs luminescence. The new QD-elastomer composite was actuated and the emission and absorbance profiles of the QDs in the elastomer were observed under the electric field actuation. The QD loading concentration was found to be controllable by swelling of the elastomer in a fixed concentration of QD solution in toluene and by the swelling time. A QD- loaded silicone gel lenses was also produced, using a transparent PEDOT:PSS thin film as a compliant electrode. We demonstrated that these lenses could be used for magnification as well as focusing of an image.

Overall, we expect that the range of new QD- based materials developed in this project will find a variety of potential applications. We believe that our research should contribute to further progress of relevant areas of nanotechnology, chemistry, biosciences, photonics, optoelectronics and solar cell technology.

6.2 Future Work

As has been shown in this work, the QD based materials synthesised and investigated here may have a great potential. Several areas of interest have emerged from the research undertaken for this thesis as potential avenues for future work.

6.2.1 Development of microwave synthesis of QDs

Work on developing of appropriate precursors with polar bonds for more efficient microwave heating and corresponding QD synthesis should be explored. We believe that using more ligands with highly polar bonds as starting materials could lead to more efficient microwave heating for organic phase QDs with higher PLQYs.

6.2.2. Further development and investigation of non-blinking QDs and hybrid QD nanostructures

We have performed preliminary studies of our CdZnSe/ZnSe non-blinking quantum dots on single QDs using cross-correlation photon counting methods and the FLIM set up (Fig. 6.2). The results were very promising, but due to the fast decomposition of single QDs in the matrix, it was very challenging to collect necessary data and reproduce the results. We think that multi-shell protection should be used to preserve individual single ternary core QDs with varying Cd/Zn compositions and investigate their lifetimes and emission in details. This may yield new information on the mechanism of blinking in QD systems and lead to the development of more stable, non-blinking QD systems. New ternary core QDs could be explored (e.g. CdSeS and CdTeSe) to find if a new range of non-blinking QDs may be synthesised.

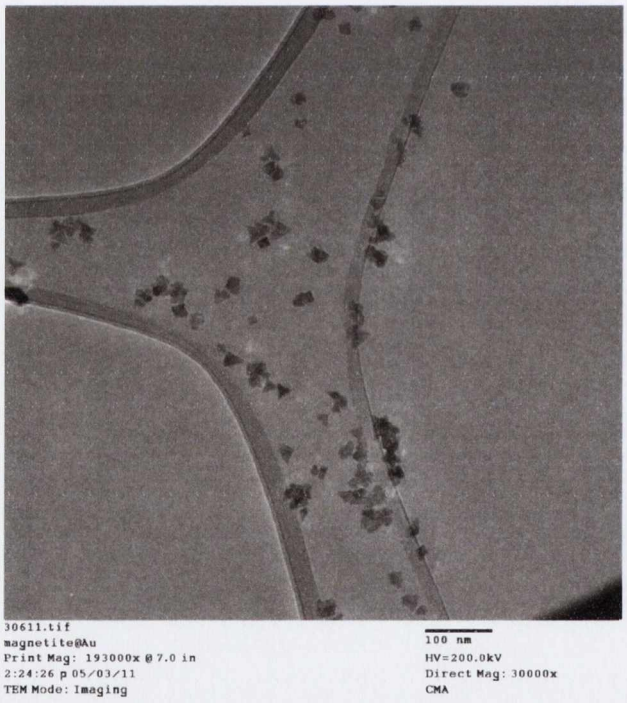

Fig. 6.1 CdS triangles synthesised using a variation of CdO and OA precursors.

Future work on hybrid CdS - CdSe nanostructures should involve further studies and understanding of growth mechanisms and reasons of the formation of complex

nanostructures. We think that stable CdSe/CdS/CdSe barbell-like nanostructures may be synthesised by the optimisation of the growth conditions. We believe that these nanostructures would present a great interest as dual emitters with unique optical properties. Further work could also be done with CdS rods and the addition of CdTe to see if similar structures are formed. CdS nanoparticles with triangle morphology have also been synthesised (Fig. 6.1). This was done by hot injection synthesis using CdO with varying amounts of OA. Increasing the amount of OA in the reaction results in a change in morphology of the CdS QDs from spherical to that of a triangular morphology. TOPS was used as the sulphur source.

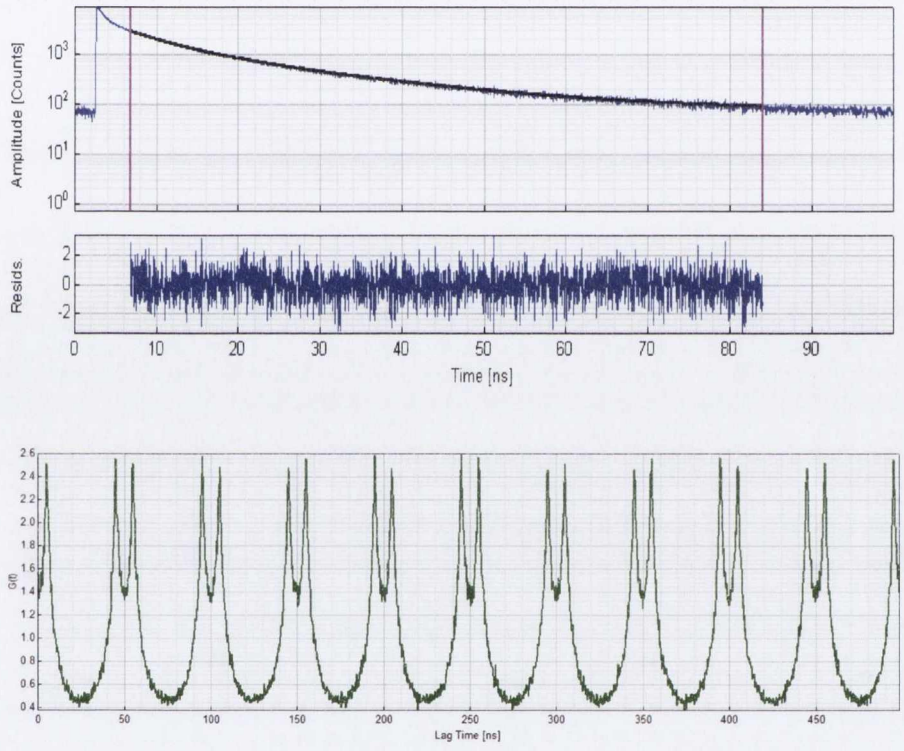

Fig. 6.2 Top: fluorescent life time decay curve recorded using our FLIM system. Bottom: anti-photon bunching with a characteristic dip in the lag time when looking at a single emitter.

6.2.3. Further development and studies of QD loaded optical microcavities

We have also developed a new approach to produce optical quality micropillar structures using sol-gel infiltration into the porous Ni membrane to give silica microcylinders that could potentially serve as optical microcavities and demonstrate WGM resonances (Fig. 6.3).

In our preliminary studies we have also found that the addition of glycerol to the water on the PMMA microcyclinder arrays may make the droplets stable and spherical enough to trap light effectively. This research should be continued as it can potentially lead to new "lab in the drop" methods.

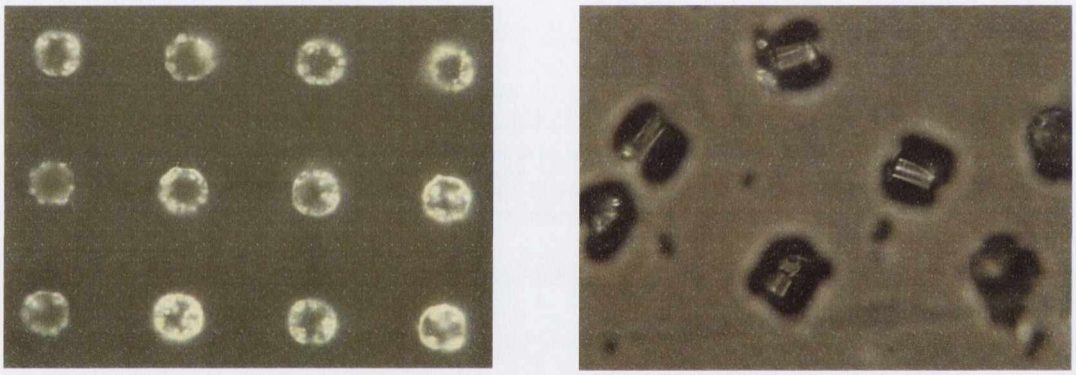

Fig. 6.3 Silica microspheres imaged by optical microscopy (50x mag). An aluminosilicate sol-gel was used to infiltrate our porous Ni template.

We also think that the production of our hollow PMMA microspheres can be refined to produce microstructures with narrow size distribution of spheres on the glass substrate. Additionally, superhydrophillic coatings may be applied to the glass substrate to increase the percentage of microspheres formed and to improve their quality. The method may also be further developed for water soluble polymers and a hydrophobic substrate.

The Q-face tor of the WGM peaks for our hollow PMMA microspheres were analysed and graphed for the TE and two TM modes from the spectra and was found to be dependent on wavelength (Fig. 6.4). No clear explanation for this behaviour is currently

available. We presume that the set originates from the hollow microsphere giving two separate WGM resonances from the air-polymer interface on the outside and on the inside.

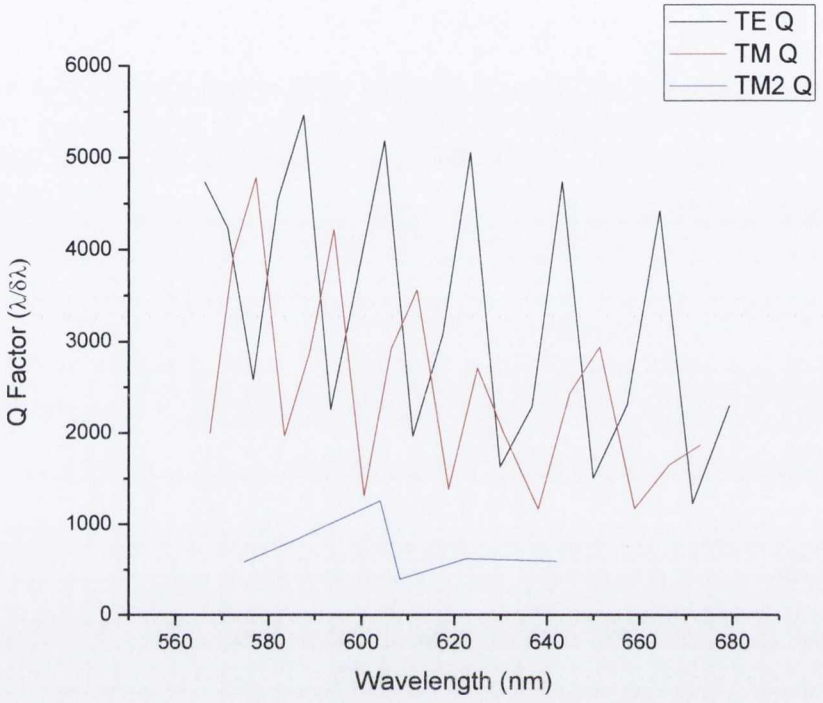

Fig. 6.4 Q-factor for the WGM peaks from the microsphere emission. The peaks were labelled TE, TM and TM2.

6.2.4. Further development and studies of QD loaded electroactive polymers

For the first time the preparation of dielectric elastomer –QD composite was perused in our work. Because of VHBs resistance to dissolution in a variety of solvents, we looked for other elastomer composite that can be moulded with QDs in solution. One of the potential dielectric elastomers for this could be SEBS. In our preliminary work we have made attempts to produce SEBS films for use in actuation, as well as to prepare SEBS-QD composites. SEBS was dissolved in chloroform and toluene to be cast as elastomer films for new actuator devices. It has been shown previously that SEBS and silicone oil can be cast into films and used as actuating devices[1,2]. VHB was

not a candidate for dissolving and recasting into different shapes as it is not soluble in common organic solvents. We found that the VHB elastomer did not dissolve under sonication and heating in hexane, chloroform, toluene, dichloromethane, THF and methyl ethyl ketone. Meanwhile SEBS has a very good solubility in the most of organic solvents, hence 1 %, 2.5 %, 5 % and 10 % SEBS in chloroform and toluene were prepared. Several methods were employed to create a uniform film that we could paint electrodes onto to build an actuator. A glass slide was used as a substrate for spin-coating a thin layer of SEBS using the 5 % and 10 % solutions. Below 5 % the film created was not thick enough for use as dielectric breakdown occurred even at very low voltages. Using 10 ml of the 5 % solution, with a ramp speed of 10 seconds, a rpm speed of 2000, and a deceleration speed of 10 s we coated a clean glass slide and a silicone greased glass slide of area 1 cm^2. Silicone grease was added to the slide so that the resultant film could be peeled off the glass without damaging the film (Fig. 6.5, right, bottom). Dilute solutions of SEBS in toluene were also used and allowed to dry slowly over 12 hours to create a film on a silicon wafer. Unfortunately the resultant film cracked while drying, with the remaining pieces too small to be used for actuator devices (Fig. 6.5, left).

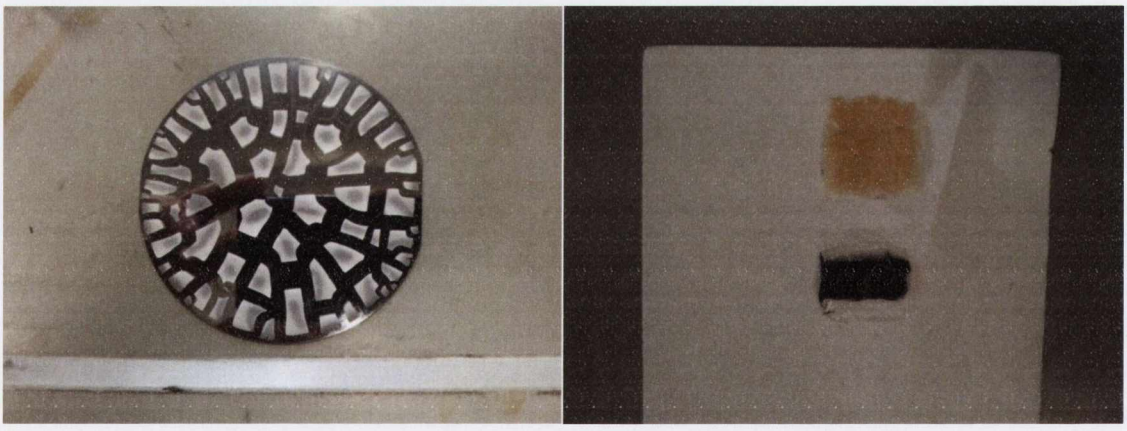

Fig. 6.5. SEBS dried on a silicon wafer (left), with 1% silicone oil and doped with QDs (right, top) and spin coated (right, bottom) with carbon black electrodes.

Imaging of doped VHB using He Ion microscopy should also be performed. Because of its high dielectric properties, SEM imaging is difficult to do for acrylic elastomers as the sample charges quickly. He Ion microscopy may provide a way to look at how the

QDs are distributed in the elastomer due to its high resolution and ability to image non-conducting polymer composites.

Fig. 6.6 Alternative Actuator design for UV-VIS absorption measurements (it is shown at the voltage off (left) , @ 2kV (middle) and under UV light (right).

QD-elastomer design is still being developed. We have made a luminescent QD-elastomer actuator with a contracting window for studies using UV-Vis and PL (Fig. 6.6). The new design makes it more suitable for recording spectra in our UV-Vis spectrometer.

Finally, QD doped elastomer lenses can further be studied using FLIM to observe changes in optical properties of QDs when voltage is applied to transparent PEDOT:PSS electrodes. A variety of type I and type II quantum dots as well as donor-acceptor quantum dot systems could be incorporated into the silicone lens for the further studies. We believe that this research should lead to a range of new optoelectronic devices in which shape and optical properties can be controlled using an electric field.

References:

(1) Stoyanov, H.; Kollosche, M.; McCarthy, D. N.; Kofod, G. *Journal of Materials Chemistry* 2010, *20*, 7558.

(2) Kim, I. J.; Jung, J.; Hong, S. M.; Koo, C. M. *Molecular Crystals and Liquid Crystals* 2012, *566*, 135.